

Novel Photovoltaic Solar Power Generating Diode

BY

ZIAD YOUEL BANYAMIN

A thesis submitted in partial fulfilment of the requirements of

Manchester Metropolitan University for the Degree of Doctor of Philosophy



Manchester
Metropolitan
University

Manchester Metropolitan University,

Manchester, UK

Faculty of Science and Engineering

School of Engineering

(Surface Engineering Group)

December 2014

Table of Contents

TABLE OF CONTENTS	I
LIST OF FIGURES	VII
LIST OF TABLES	XI
LIST OF EQUATIONS	XVII
DECLARATION	XIV
ABSTRACT	XV
ACKNOWLEDGMENT	XVI
1 INTRODUCTION	1
1.1 Background.....	1
1.2 History of solar cells.....	3
1.3 Recent development in solar cells.....	9
1.4 Aim and objective.....	11
1.5 Structure of thesis.....	12
2 SEMICONDUCTORS AND TCO THIN FILMS	14
2.1 Introduction.....	15
2.2 Concept of the semiconductor.....	18
2.3 Optical properties of semiconductors.....	20
2.4 Electrical properties of semiconductors.....	24
2.5 Dopant effect on semiconductors.....	27

2.5.1	Fluorine doped tin oxide.....	28
2.5.2	Antimony doped tin oxide.....	30
2.5.3	Copper aluminium oxide	30
2.6	Trends in the development of TCO materials.....	32
2.7	Industrial applications of TCOs.....	36
2.8	TCO deposition approach	37
2.9	Summary and outlook	38
3	<i>P-N DIODE</i>	40
3.1	History of p-n junctions.....	41
3.2	p-n junction device theory	42
4	PHYSICAL VAPOUR DEPOSITION	50
4.1	Fundamentals of PVD process.....	51
4.2	Vacuum evaporation	54
4.3	Glow discharge plasma	56
4.4	Ion plating.....	61
4.5	Sputter deposition process.....	62
4.5.1	Magnetron sputtering deposition.....	64
4.5.2	Unbalanced magnetron sputtering	68
4.5.3	Closed-field unbalanced magnetron sputtering.....	70
4.6	Reactive sputter deposition	74
4.7	Plasma characteristics	78

4.8	Film growth and formation	82
4.9	Structure zone models	85
4.10	Summary and outlook	89
5 POWDER TARGETS		91
5.1	Introduction	92
5.2	Discharge stability	93
5.2.1	Pulsed-DC reactive sputtering of dielectric powder targets	96
5.2.2	Pulsing parameters and discharge behaviour	98
5.3	Target to substrate distance comparison	107
5.4	Effect of pulse frequency and duty cycle parameters on electrical property of FTO	110
5.5	Crystallographic analysis of powder targets	112
5.5.1	Target composition Vs sample composition	116
5.5.2	Target composition Vs discharge voltage of CAO target	118
5.5.3	Hysteresis studies of copper aluminium powder targets	121
5.5.4	Hysteresis study of titanium dioxide	127
5.6	Effect of base pressure on target voltage of titanium target	130
5.7	Effect of oxygen flow rate on titanium target discharge voltage	132
5.8	Deposition rate in a titanium/oxygen system	133
5.9	Summary and outlook	134
6 ANALYTICAL TECHNIQUES		137
6.1	Introduction	138

6.2	Analysis of electrical properties	138
6.2.1	Hall effect measurement system	142
6.2.2	Van der Pauw technique	142
6.3	Analysis of optical properties.....	145
6.4	Structural analysis	149
6.4.1	Scanning electron microscopy	149
6.4.2	X-ray diffraction	151
6.5	Summary and outlook	158
7	EXPERIMENTAL DETAILS	159
7.1	Introduction	160
7.2	Preparation of the powder targets	160
7.3	Deposition techniques	168
7.3.1	Substrate cleaning	168
7.3.2	Sputtering equipment	168
7.3.3	Deposition conditions	170
7.4	Fabrication of p-n junction diodes.....	173
7.5	Summary and outlook	176
8	CHARACTERISATION OF THIN FILMS	178
8.1	Fluorine doped tin oxide	179
8.1.1	Introduction	179
8.1.2	Elemental analysis of SnO ₂ :F thin films	179

8.1.3	Structural properties of SnO ₂ :F thin films	181
8.1.4	Electrical properties of SnO ₂ :F thin films	185
8.1.5	Optical properties of SnO ₂ :F thin films	188
8.1.6	Morphological properties of SnO ₂ :F thin films	192
8.1.7	Conclusions	193
8.2	Antimony doped tin oxide	194
8.2.1	Introduction	194
8.2.2	Electrical properties of antimony doped tin oxide	196
8.2.3	Optical properties of ATO thin films.....	199
8.2.4	Structural properties of ATO thin films	200
8.2.5	Conclusion	202
8.3	Copper aluminium oxide.....	203
8.3.1	Introduction	203
8.3.2	Elemental analysis of the CAO thin films	204
8.3.3	Deposition growth rate	206
8.3.4	Structural properties of CAO thin films.....	208
8.3.5	Electrical properties of CAO thin films.....	213
8.3.6	Optical properties of CAO thin films	219
8.3.7	Conclusion	224
8.4	Photovoltaic response of p-n junction.....	225
8.4.1	Conclusion	233

9 OVERALL CONCLUSIONS	235
10 RECOMMENDATIONS FOR FUTURE WORK.....	240
APPENDIX: A PUBLICATIONS AND CONFERENCE CONTRIBUTIONS	242

List of Figures

Figure 1.1:1 Simple schematic layout of a conventional p-n junction diode solar cell depicting the creation of an electron-hole pair.....	2
Figure 1.2:1 First photovoltaic design setup by Becquerel in 1839 [1].....	3
Figure 1.2:2 Device configuration used by Adam and Day (1876) for the investigation of the photoelectric effects in Selenium [3].....	4
Figure 1.2:3 Se thin film device demonstration by Frits (1883) [3].	5
Figure 1.2:4 Copper-cuprous oxide photovoltaic cell made by Grondahl (1930) [3].	6
Figure 1.2:5 Thallous sulphide photovoltaic device structure developed in 1930's [3].	6
Figure 1.2:6 First semiconductor p-n junction constructed using recrystallised Si melts, developed in 1941 [3].	7
Figure 1.2:7 Silicon structure solar cell developed in 1970 [3].	8
Figure 1.2:8 Thin film stack cell using two p-n junctions connected using tunnelling junction [3].....	8
Figure 1.3:1 The evolution of the PV- market over the last two-decades [9].....	9
Figure 3.2:1 The band diagram of a p-n junction at thermal equilibrium [100].	43
Figure 3.2:2 Sharing of valence electrons in outer shell between atoms.	44
Figure 3.2:3 Formation of energy bands [20].	45
Figure 3.2:4 Top two band structures in a metal, a semiconductor and an insulator [20].	45
Figure 3.2:5 Current-Voltage characteristic graph of a typical p-n junction solar cell.....	47
Figure 3.2:6 p-n junction under forward and reverse bias [100].....	49
Figure 4.1:1 (a) Pathway of a scattered particle between collisions and (b) Boltzmann distribution of mean particle velocities.	53
Figure 4.2:1 Schematic representation of vacuum evaporation system [104].....	56
Figure 4.3:1 Schematic representation of ionisation and formation of the glow discharge plasma 58	58
Figure 4.3:2 Formation of visible glow discharge plasma in an magnetron sputtering process. 59	59
Figure 4.4:1 Schematic representation of an ion plating process [112]. 62	62
Figure 4.5:1 Schematic representation for the propagation momentum and particle movement of the Ar ion hitting the target surface. 63	63
Figure 4.5:2 Schematic of DC-sputtering system..... 64	64
Figure 4.5:3 Representation of plasma in unbalanced and conventional magnetrons [85]. 70	70
Figure 4.5:4 Dual Magnetron Configurations [85] 71	71
Figure 4.5:5 Measured magnetic field B_n , at 1 cm from the above the copper backing plate surface. 73	73
Figure 4.5:6 (a) typical configuration of a complete magnetron sputtering system (b) typical discharge in a magnetron sputtering system. 74	74
Figure 4.6:1 Hysteresis characteristics of the discharge voltage (top) and the total pressure (bottom) as a function of the reactive gas flow. 77	77
Figure 4.7:1 The formation of the plasma sheath during (a) initial n_i and n_e and electric potential, (b) densities (n_i , n_e) electric field and potential during post formation of sheath [121]. 79	79
Figure 4.7:2 Typical I-V characteristic of a Langmuir probe..... 81	81

Figure 4.8:1 Three fundamental modes of thin films growth processes.....	83
Figure 4.9:1 Structure zone model relating to evaporated films, after Movchan and Demchishin [106].	86
Figure 4.9:2. Structure zone model of sputter deposited materials.....	86
Figure 4.9:3 Novel SZM of the CFUBMS system, relating coating structure to the homologous temperature, ion-to-atom ratio and bias voltage [133].	88
Figure 5.2:1 Effect of tamping of the powder target, (a) target tamped with very light steel rod, (b) target tamped with 1 kg steel rod.	94
Figure 5.2:2 Discharge voltage stability as function of deposition period of loosely packed powder targets sputtered in argon and oxygen atmosphere.	95
Figure 5.2:3 Copper aluminium powder target surface state after being sputtered with 550 W.	96
Figure 5.2:4 Schematic of an asymmetric bipolar-pulse DC waveform to power dielectric surface	97
Figure 5.2:5 power supply trials conducted using different pulse frequency, pulse off time and duty cycle on FTO powder target.	99
Figure 5.2:6 SEM fracture sections showing the effect of pulse frequency on structure and deposition thickness of the FTO thin films.	99
Figure 5.2:7 Effect of pulse frequency on FTO powder target voltage waveform 90% duty cycle using constant power mode at 400 W of sputtering power, in 10 sccm of Ar and 4.5 sccm of O ₂ , coating pressure of 0.55 Pa.	100
Figure 5.2:8 Effect of pulse frequency on the deposition rate of a FTO powder target (duty cycle = 90%).	101
Figure 5.2:9 Effect of duty cycle on the FTO target voltage using 50, 70 and 90% duty cycle at 200 kHz pulse frequency.	102
Figure 5.2:10 Effect of pulse time on the growth thickness of the FTO thin films using sputtering power of 400 W, sputtering period of 20 minutes using a variety of pulse frequency and a variety of pulse off time in 10 sccm of Ar and 4.5 sccm of O ₂ , coating pressure of 0.55 Pa.	103
Figure 5.2:11 Effect of sputtering power on the FTO target voltage using a 90% duty cycle and 200 kHz pulse frequency in 20 sccm of Ar chamber pressure of 0.55 Pa.	104
Figure 5.2:12 Average target voltage of FTO powder target conditioning measured across a period of 2 hours.	105
Figure 5.2:13 Chamber pressure variations during the FTO powder target-conditioning period of 2 hours.	106
Figure 5.2:14 Effect of oxygen flow on the SnO ₂ target voltage.....	107
Figure 5.3:1. The effect of target-to-substrate separation (d_{t-s}) on the thickness of the coatings.....	109
Figure 5.3:2 The effect of the target-to-substrate distance on the electrical resistivity of the FTO coatings.....	109
Figure 5.4:1 The effect of the pulse frequency of (a-b) 300 kHz (c-d) 200 kHz and duty cycle 50, 70, 90 % on electrical property of FTO thin films.....	112
Figure 5.5:1 X-ray diffraction pattern for the powder targets used in this project.....	116
Figure 5.5:2 Average target voltage of a copper/aluminium target as a function of Cu at.% concentration deposited in oxygen environment.....	119
Figure 5.5:3 Deposition rate and the average target voltage as a function of oxygen partial pressure using a Cu:Al powder target.	121

Figure 5.5:4 hysteresis analysis of pure metal powder target of (a-b) Al (c-d) Cu and (e-f) Cu:Al blended powder target.	127
Figure 5.5:5 Hysteresis study of Ti metal base powder.	130
Figure 5.6:1 Effect of chamber pressure on target voltage for titanium powder.	131
Figure 5.7:2 Effect of frequency on time averaged target voltage for titanium powder target.	132
Figure 5.7:1 Target voltage Of Ti target at different oxygen flow rates.	133
Figure 5.8:1 Deposition rate of a titanium target at different oxygen flow rates.	134
Figure 6.2:1 Schematic of the Hall effect.	140
Figure 6.2:2: Ohmic contact placement on TCO thin film.....	142
Figure 6.3:1. The instrumental setup for measuring the Transmission, absorption and the reflection of the coating.....	146
Figure 6.4:1 Schematic representation of X-ray diffraction operating in the θ -2 θ mode.....	152
Figure 6.4:2 GIXRD device setup	155
Figure 7.4:1 Schematic fabrication process of p-n junction solar diode	174
Figure 7.4:2 Cross section schematic diagram of multi p-n heterojunction diode configuration.....	175
Figure 7.4:3 (a) The mask design and (b) the corresponding copper metal contact for the n-type FTO thin film.....	175
Figure 8.1:1 EDS analysis of fluorine and oxygen atomic content in the FTO films as a function of fluorine atomic content in the target.	180
Figure 8.1:2 XRD diffraction pattern for (a) all FTO diffraction patterns (b) diffraction pattern of SnO ₂ , SnO ₂ :F1 and SnO ₂ :F4.....	183
Figure 8.1:3 Average grain size as a function of fluorine atomic content in the FTO thin films.	185
Figure 8.1:4 Variation of (a) resistivity in logarithmic scale, (b) mobility and (c) absolute carrier concentration of FTO thin films as a function of fluorine atomic content.	188
Figure 8.1:5 The optical transmittance of FTO thin films as a function of fluorine atomic content. The insert shows the variation in optical band-gap and the average transmittance across the 300 $\leq\lambda\leq$ 900 nm with change in fluorine concentration in thin film.....	191
Figure 8.1:6. The direct allowed transition of FTO thin films as a function of fluorine atomic content... ..	191
Figure 8.1:7. (a) Surface and (b) Cross-sectional SEM morphologies of SnO ₂ :F2 thin film.	193
Figure 8.2:1 Discharge of power–current curve for a working pressure 0.5 Pa for a ATO powder target.	195
Figure 8.2:2 Variation of the electrical (a) resistivity, (b) hall mobility and (c) carrier concentration of SnO ₂ :Sb thin films with varying target power.....	198
Figure 8.2:3 Optical transmittance of ATO thin films as a function of the discharge power.	199
Figure 8.2:4 The XRD pattern for ATO thin films as function of discharge power.....	201
Figure 8.2:5 Average grain size for the ATO thin films as a function of the discharge sputtering power.	202
Figure 8.3:1 The effect of pulse frequency on the atomic ratio of a CuAlO ₂ thin films.	206
Figure 8.3:2 Deposition rate of Cu-Al-O thin film as a function of various pulse frequency and discharge sputter powers.....	207
Figure 8.3:3 Effect of the oxygen flow rate on the film thickness of the CuAlO ₂ coatings.	208

Figure 8.3:4 XRD pattern of the CAO thin films deposited using various discharge power (a) 250 W and (b) 350 W using various pulse frequency of DC, 100, 225 and 350 kHz.	212
Figure 8.3:5 Effect of Cu-to-Al ratio on the electrical resistivity of the CAO thin film.	214
Figure 8.3:6 Electrical properties (a) resistivity, (b) Hall mobility and (c) carrier concentration of CAO thin films using various pulse frequency and discharge sputtering power.	217
Figure 8.3:7 Effect of the oxygen flow rate on the CAO thin films.	218
Figure 8.3:8 Optical transmittance of CAO thin films grown using (a) 350 W (b) 250 W sputter discharge power (c) average transmittance across 350-900 nm at various pulsed frequency and discharge sputter power.	221
Figure 8.3:9 The direct optical band-gap of CAO thin films as a function of discharge power at (a) 350 W and (b) 250 W with varying pulse frequencies.	223
Figure 8.4:1 The equivalent electrical circuit of a real pn-junction solar cell.	230
Figure 8.4:2: Electrical I-V characterisation of the p-n heterojunction device in dark and under illumination.	231
Figure 8.4:3 I-V curve and the parameters used to calculate the device performance.	231
Figure 8.4:4 n-FTO Ag electrical contacts (a) Mask design (b) complete Ag contact design, (c) problems encountered after FTO deposition onto the Ag contacts	233

List of Tables

Table 1.3:1 PV world production in terms of technology (MW) [9].	10
Table 2.6:1 TCO compounds and dopants [11].	32
Table 5.3:1 Comparison experiments using different separation distances.	108
Table 5.5:1 The Compositional analysis of (a) SnO ₂ and (b) SnF ₂ powder targets prior to blending. ...	117
Table 5.5:2 Compositional analysis of the powder targets and subsequent tin oxide and fluorine doped tin oxide.	118
Table 5.5:3 Experimental parameters during the hysteresis study of Cu-Al powder target.	122
Table 5.5:4 Power supply experiment conditions during the Ti hysteresis study.	128
Table 5.7:1 Experimental parameters of oxygen partial pressure affect on target voltage.	132
Table 7.2:1 Atomic percent ratio of the dopants for the SnO ₂ :F and Cu:Al powder targets.	161
Table 7.2:2 Calculation for mass % of elements in SnO ₂ :F3 powder target.	164
Table 7.2:3 The total mass of the blended powder targets (a) fluorine doped tin oxide, (b) copper aluminium oxide and (c) titanium and antimony doped tin oxide.	166
Table 7.2:4 Purity, particle size and hazard of the powder targets.	167
Table 7.3:1 Deposition conditions and corresponding deposition rates of CuAlO ₂ thin films.	171
Table 7.3:2 Standard deposition parameter for (a) antimony doped tin oxide powder target and (b) titanium metal base powder target.	172
Table 7.3:3 Standard deposition parameters for Cu and Ag targets.	173
Table 8.1:1 Compositional analysis of the powder targets and subsequent tin oxide and fluorine doped tin oxide.	179
Table 8.1:2 Diffraction angle (2θ), the miller indices (<i>hkl</i>), grain size (D) and the texture coefficient (P) of FTO thin films.	184
Table 8.3:1 Composition analysis of CAO thin films produced using different powder targets.	204
Table 8.3:2 Composition of Cu-Al-O thin film deposited using various discharge sputtering power.	205
Table 8.3:3 Effect of pulse frequency on the composition ratio of CuAlO ₂ thin films sputtered at 350 W.	206
Table 8.3:4 Dependence of CuAlO ₂ thickness on the O ₂ flow rate.	208
Table 8.3:5 The grain size of the as-deposited CAO thin films.	213
Table 8.3:6 Average optical transmittance and energy band-gap of CAO thin films grown using various pulse frequency and discharge sputtering power.	224
Table 8.4:1 Photovoltaic parameters of n-FTO/p-CAO p-n junction solar cell device.	228

List of Equations

$E_\lambda = \frac{hc}{\lambda} = hv = \hbar\omega$ Eq. 2.2:1	18
$\sigma = q_n\mu_n + q_p\mu_p$ Eq. 2.2:2	19
$N \approx n - ik$ Eq. 2.3:1	20
$\alpha = \frac{4\pi k}{\lambda}$ Eq. 2.3:2	21
$\varepsilon = \varepsilon_0 e^{-(i2\pi N_x)/\lambda}$ Eq. 2.3:3	21
$\varepsilon = \varepsilon_0 e^{-2\pi kx/\lambda} \cdot e^{-i2\pi nx/\lambda}$ Eq. 2.3:4	21
$I/I_0 = e^{(-\alpha d)}$ Eq. 2.3:5	21
$T_{\min} = 4n^2 n_{\text{sub}}(1 + n^2)(n^2 + n_{\text{sub}})$ Eq. 2.3:6	22
$T_{\text{corr}} = (100 \times T\%)/(100 - R\%)$ Eq. 2.3:7	23
$\alpha = 1/d[\ln(\frac{100}{T_{\text{corr}}})]$ Eq. 2.3:8	23
$\alpha h\nu = A(h\nu - E_g)^{1/n}$ Eq. 2.3:9	23
$\mu = e\tau/m^*$ Eq. 2.4:1	25
$P = nmv^2/3$ Eq. 4.1:1	52
$v_2 = (8kT/\pi m)^{1/2}$ Eq. 4.1:2	53
$\lambda = (kT)/(\sqrt{2\pi\sigma^2 N_A P})$ Eq. 4.1:3	53
$\text{Ar} + e^- \rightarrow \text{Ar}^+ + 2e^-$ Eq. 4.3:1	57
$\text{Ar} + e^- \rightarrow \text{Ar}^* + e^-$ Eq. 4.3:2	58
$\text{Ar}^{*-} \rightarrow \text{Ar} + h\nu$ Eq. 4.3:3	58
$F = q(v \times B)$ Eq. 4.5:1	66
$R = mv_\perp/qB$ Eq. 4.5:2	66
$\sigma = E/J$ Eq. 6.2:1	139
$\rho = R \times \left(\frac{b \times t}{l}\right)$ Eq. 6.2:2	139
$\rho = Rt = \rho_S$ Eq. 6.2:3	139
$F = -e \cdot V \cdot B$ Eq. 6.2:4	140
$E_H = V_d \cdot B$ Eq. 6.2:5	141
$v_d = \mu \cdot E$ Eq. 6.2:6	141
$E_H = \mu \cdot E \cdot B$ Eq. 6.2:7	141
$R_A = V_{43}/I_{12}$ Eq. 6.2:8	143
$R_B = V_{14}/I_{23}$ Eq. 6.2:9	143
$e^{(-\pi R_A/R_S)} + e^{(-\pi R_B/R_S)} = 1$ Eq. 6.2:10	144
$\rho = R_S d$ Eq. 6.2:11	144
$n_s = IB/q V_H $ Eq. 6.2:12	144
$n = n_s/d$ Eq. 6.2:13	145
$T + R + A = 1$ Eq. 6.3:1	145
$T = (S - D)/(R - D) \times 100\%$ Eq. 6.3:2	147
$A = -\log[(S - D)/(R - D)]$ Eq. 6.3:3	147

$R = (S - D)/(R - D) \times 100\%$ Eq. 6.3:4	148
$AB + BC = n\lambda$ Eq. 6.4:1	151
$n\lambda = 2d_{hkl}\sin\theta_{hkl}$ Eq. 6.4:2	152
$D = 0.9 \times (\lambda/\beta\sin\theta)$ Eq. 6.4:3.....	153
<i>crystallite size (average)</i> $= K\lambda/(B_{size}\cos\theta)$ Eq. 6.4:4.....	157
<i>Lattice strain mean lattice distortion</i> $= B_{strain}/(4\tan\theta)$ Eq. 6.4:5	157
$B_{(size)} = B_{obs.} - B_{std.}$ Eq. 6.4:6.....	157
$B_{(size)} = (B_{obs.}^2 - 2B_{std.}^2)$ Eq. 6.4:7.....	157
at. % $= n(F)/(n1(Sn) + n(O) + n2(Sn) + n(F))$ Eq. 7.2:1	162
$n1(Sn) = 0.5n(O)$ Eq. 7.2:2	162
$n2(Sn) = 0.5n(F)$ Eq. 7.2:3	162
$m(SnO_2) = n(SnO_2) \times M(SnO_2)$ Eq. 7.2:4.....	163
at. % $= n/n_T$ Eq. 7.2:5.....	165
$m(Cu) + m(Al) = 50g$ Eq. 7.2:6.....	165
$m(Cu) = n(Cu) \times M(Cu)$ Eq. 7.2:7	165
$m(Al) = n(Al) \times M(Al)$ Eq. 7.2:8	165
Ratio of Gas 1 $= (\text{flow rate of gas 1})/((\text{flow rate of gas 1}) + (\text{flow rate of gas 2}))$ Eq. 7.3:1	169
$TC_{(hkl)} = \frac{I_{(hkl)}}{I_{o(hkl)}} \times [\frac{1}{n} \sum_{i=1}^n I_{hkl}/I_{o(hkl)}]^{-1}$ Eq. 8.1:1	183
$T \approx e^{-\alpha t}$ Eq. 8.1:2.....	189
$\alpha h\nu = C(h\nu - E_g)^{1/2}$ Eq. 8.1:3	189
$FF = P_m/P_o = [V_m \times I_m][V_{oc} \times I_{sc}]$ Eq. 8.4:1	227
$\eta = \frac{P_m}{P_{rad}} = (FF \times V_{oc} \times I_{sc})/P_{in}$ Eq. 8.4:2	228

Declaration

This is to certify that the material contained in this thesis has been produced by the author, has not been accepted in substance for any other degree and is not currently submitted in candidature for any other academic award.

ABSTRACT

Thin film solar cells are based on semiconductor materials which are configured together to form a single p-n junction. The p-n junction diode is effectively a simple device that has the capacity to absorb part of the sunlight spectrum and deliver the absorbed photon energy to carriers of electrical current known as electrons and holes. A simple p-n junction solar cell device consists of a p-n junction, a metallic grid and a back contact. The aim of this project was to develop and fabricate a p-n heterojunction diode that is robust, developed with low cost and suitable for large surface area. The device attains a heterojunction configuration, consisting of two thin films, each exhibiting different semiconducting behaviour, namely n-type and p-type semiconductors that are brought together to form a p-n junction diode device.

The initial stage of this research was to make and characterise a range of oxide coating compositions that can be sputtered from blends of loosely packed powder targets, using the pulsed DC magnetron sputtering technique. These compositions include fluorine doped tin oxide, antimony doped tin oxide and titanium oxide. The different coatings should be transparent conductive oxides (TCO) that exhibit an n-type semiconductor material characteristic.

The second objective was to characterise and develop a p-type semiconductor namely copper aluminium oxide to investigate the optimum compositional ratio and the effect of deposition power on the structure of the thin films. The thin films were characterised in terms of their structural,

morphological, optical (transmission and band-gap) and electrical (resistivity, mobility and carrier concentration) conditions.

The collection of the charge carriers generated from the incident light was achieved through metal ohmic contacts. This was deposited onto both sides of the device using copper and the silver grids/contacts that are deposited onto the n-type layer and the p-type layers, respectively. The design layout of the grid was optimised in order to increase the device efficiency.

The final part of this project was to construct the p-n junction device, test the electrical (current-voltage characteristics) performance and investigate the rectifying behaviour and the formation of the p-n junction.

ACKNOWLEDGEMENT

First of all, I would like to thank my project supervisor Professor Peter James Kelly for his continuous support and guidance throughout the project.

I would like to thank my second supervisor Dr. Glen West for his valuable advice and help in the research laboratory. Many thanks go to all my other colleagues in the research laboratory and especially my very good friend Lukas Seidelmann who really gave me the friendship and support during my project.

I would like to thank the analytical team Dr. Hayley Andrews for training me on the SEM and the EDS, also Helen Sutton and Lee Harman for training me on the XRD machine.

I would like to thank Dr. Andrew Clayton from Glyndŵr University for providing the technical assistance to measure the electrical performance of the p-n junction device.

I would like to dedicate this thesis to my parents and to my aunt to express my gratitude for giving me the strength to overcome the obstacles that I encountered throughout this project.

I also would like to dedicate this thesis to my brothers and sisters for being my best friends and for giving me continuous encouragement and support.

*“The more I learn, the more I realise
how much I don’t know”*

Albert Einstein

INTRODUCTION

1.1 Background

There has been vast progress in the manufacturing scale to generate electricity through the use of solar power technology. An example of solar power technology is thin film solar cells, also known as photovoltaic cells, which convert the solar energy into electrical energy. Thin film solar cells are based on semiconductor materials which are configured together to form a single p-n junction.

The p-n junction diode is effectively a simple device that has the capacity to absorb part of the sunlight spectrum and deliver the absorbed photon energy to carriers of electrical current known as electrons and holes. The p-n junction separates and conducts the current carriers through two regions known as the n-region and the p-region. The n-region consists of atoms that are capable of easily donating an electron, while the p-region contains atoms that are capable of binding an electron. These atoms or dopants are termed donors and acceptors, respectively. A simple p-n junction solar cell device consists of a p-n junction, a metallic grid and a back contact. As light shines onto the top surface of the device, it passes through the metallic grid, which forms one part of the electrical contacts and falls onto the semiconductor, thus absorbed and

converted to electrical energy. The other electrical contact, is formed by a metallic layer deposited at the back of the solar cell. A simple schematic layout for a p-n junction solar cell device showing the creation of electron-hole pair is depicted on Figure 1.1:1.

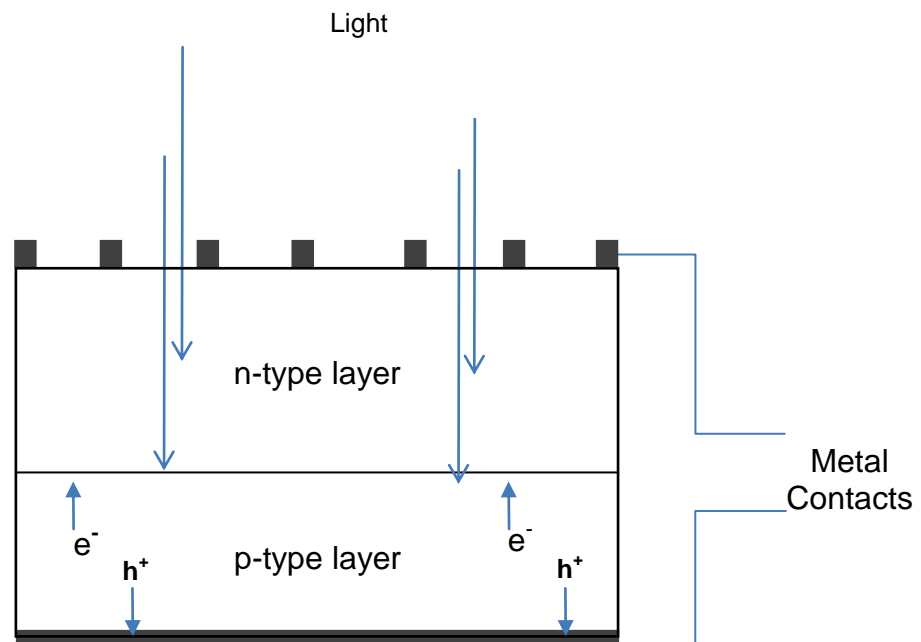


Figure 1.1:1 Simple schematic layout of a conventional p-n junction diode solar cell depicting the creation of an electron-hole pair.

Thin film solar cells are deposited onto a variety of substrates including transparent, opaque, and flexible substrates using different deposition technology including physical vapour deposition (PVD), chemical vapour technology (CVD), spray pyrolysis etc.

The subject of this chapter is a historical overview of solar cell technology. A road map of this technology, describing important findings of some of the pioneer scientists in the field is presented in order to understand the important evolution of thin film solar cells.

1.2 History of solar cells

The word photovoltaic describes a way of providing an electric direct current (DC) by the influence of light or similar radiation. In 1839, the French physicist Alexandre-Edmond Becquerel (1820-1891) was the first person to study the photovoltaic effect and was able to generate electricity by illuminating one electrode (usually he used platinum but he also managed to get a response by using silver electrodes) that was coated with a light sensitive material, such as silver-chloride (AgCl) or silver bromine (AgBr). The electrodes were inserted into an acidic solution [1]. This configuration is shown in Figure 1.2:1.

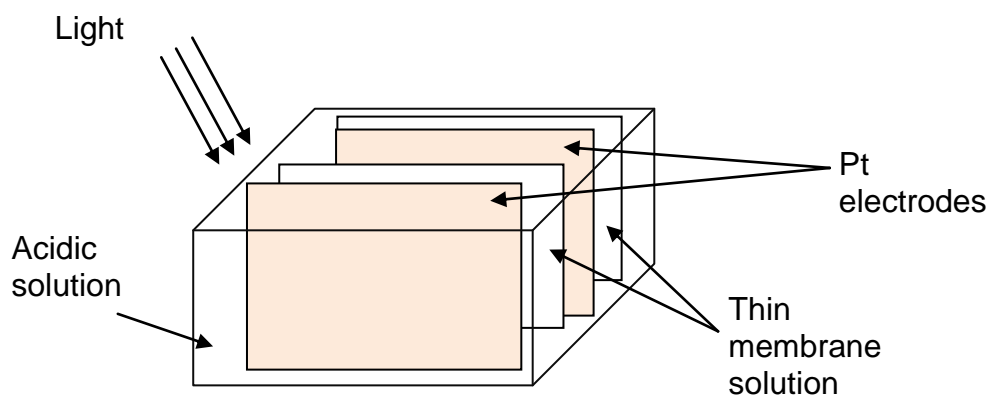


Figure 1.2:1 First photovoltaic design setup by Becquerel in 1839 [1].

The next generation of photoconductive materials was introduced by Adam and Day in 1876. The object of their experiments, was to examine the electric conductivity of selenium when kept in the dark and also to determine whether light could actually generate an electric current in the selenium [2]. The results were positive and were able to demonstrate the photovoltaic effect in a solid state system. The device configuration is shown in Figure 1.2:2 [3].

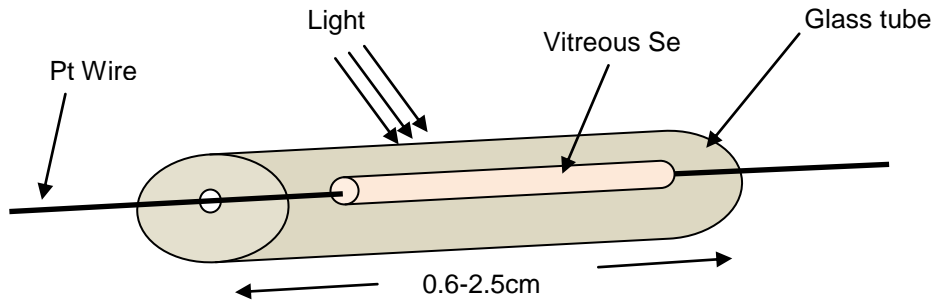


Figure 1.2:2 Device configuration used by Adam and Day (1876) for the investigation of the photoelectric effects in Selenium [3].

Seven years later, the first thin film selenium (Se) solar cell was fabricated by Frits in 1883 [4]. Frits was able to adhere a thin layer of Se to one plate but not to the other. He used a thin leaf of gold, which he pressed onto the Se thin layer, thereby making the first thin film device. He was the first person to recognise the potential of photovoltaic devices and noted that these devices can be manufactured at a low cost. He also suggested that, “if the current is not wanted immediately, it can either be ‘stored’ where produced (in storage batteries) or transmitted to a distance (and there used, or stored)”.

The thin film gave an efficiency of 1%, owing to the electrical properties of Se. The device is demonstrated in Figure 1.2:3. The results of this experiment paved the way for the study of solar cells during the 19th century.

The photovoltaic field saw a very slow growth, and the most efficient materials used as an absorbing layer were either Se, Cu_2O or Ti_2S which were adhered onto a metal contact, a design very similar to Frits layout.

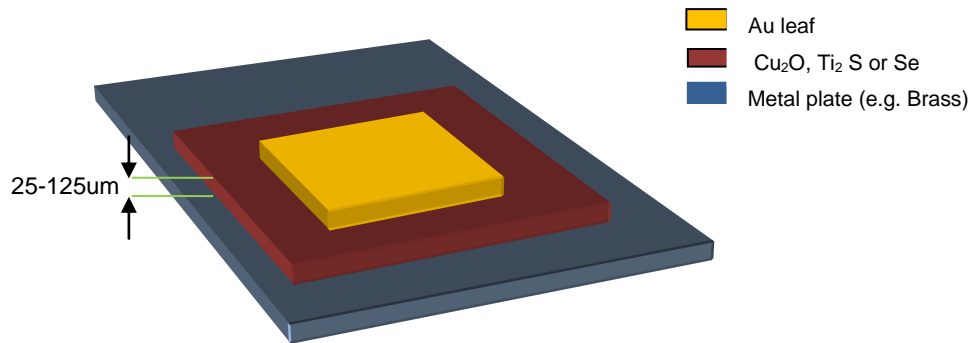


Figure 1.2:3 Se thin film device demonstration by Frits (1883) [3].

Another novel finding was made in 1930 by Grondahl who was able to develop rectifiers and photovoltaic cells using III-V semiconductors and their alloys [5]. The copper-cuprous oxide layers were grown on copper substrates. The rectifying action of the copper-cuprous junction was discovered and applied to solar cell technology [5]. The cell structure was based on sputtering a thin grid contact of lead (Pb) onto the illuminated side of the cell. Figure 1.2:4 outlines the Grondahl initial cell layout [5]. The use of materials from groups III-V pioneered band-gap engineering for use in photovoltaic cell technology.

The work of Grondahl on selenium brought great interest especially from Bergman who in 1931, managed to produce a more effective and efficient selenium device that was suitable for photovoltaic solar cell technology [5].

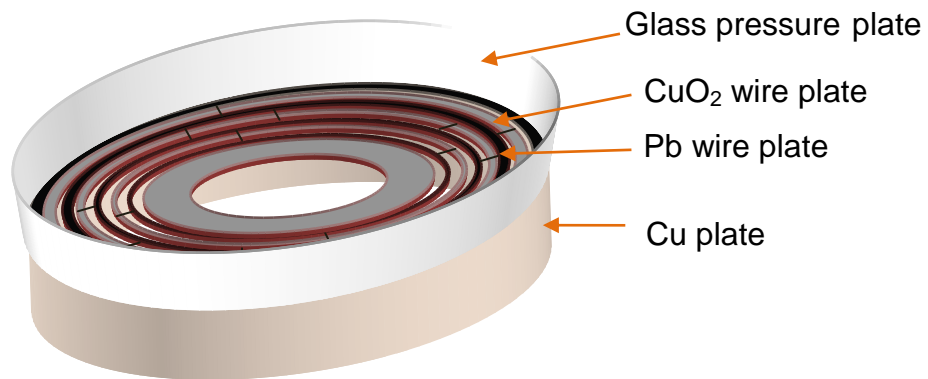


Figure 1.2:4 Copper-cuprous oxide photovoltaic cell made by Grondahl (1930) [3].

In 1939, Nix et. al, managed to get similar results by using thallos sulphide with a similar device structure to that of Grondahl. The device structure is shown in Figure 1.2:5 [3].

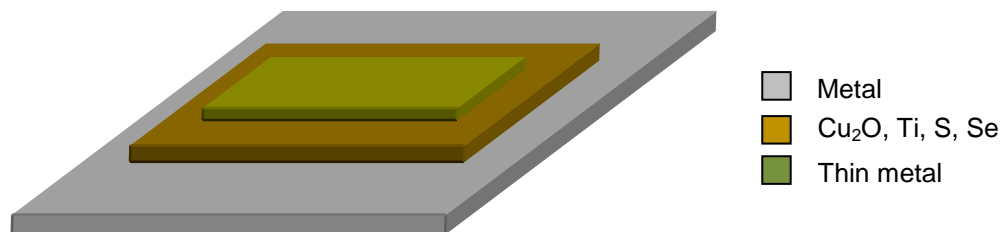


Figure 1.2:5 Thallos sulphide photovoltaic device structure developed in 1930's [3].

In 1941, there was another interesting finding made by Russel Ohl in the Bell Laboratories. He was able to create the first semiconductor p-n junction solar cell [6]. The p-n junction layout is shown in Figure 1.2:6

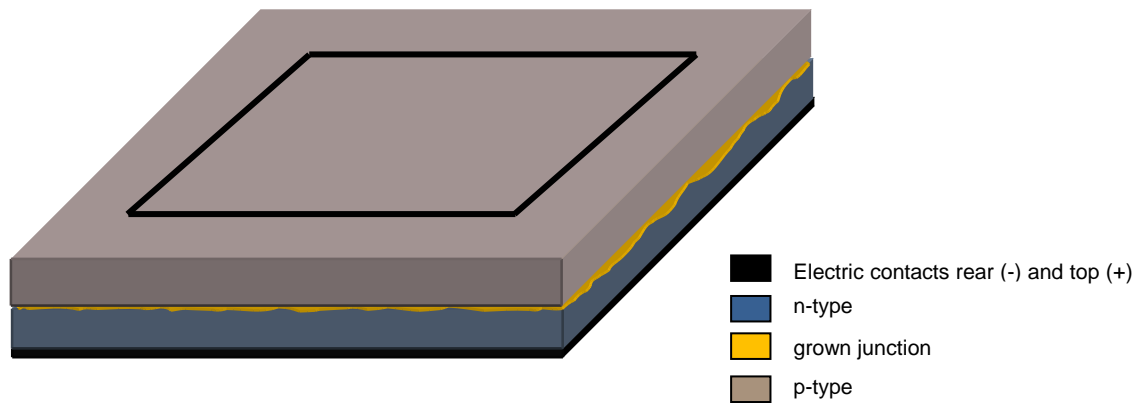


Figure 1.2:6 First semiconductor p-n junction constructed using recrystallised Si melts, developed in 1941 [3].

The cell was formed using a high purity silicon (99% pure) ingot which is provided with a conductive terminal (low resistance conductive terminals which are secured on both sides of the silicon ingot). Circuit connections are then secured to the terminals using soldering or friction contacts. The ingot is made by fusing metallic silicon in powdered form in a silica (SiO_2) crucible in an electric furnace which is then slowly solidified [6]. Investigation of the properties of the junction led to the understanding of the role of the 'p' and the 'n' type dopants in controlling semiconductor properties and hence creating a microelectronic revolution [3, 7].

In the late 1970s, solar cell design changed to that shown in Figure 1.2:7. In 1975, the top surface of the design was changed to a crystallographic textured surface in order to reduce light reflection. The design incorporated other features which were adapted from the field of microelectronics [8].

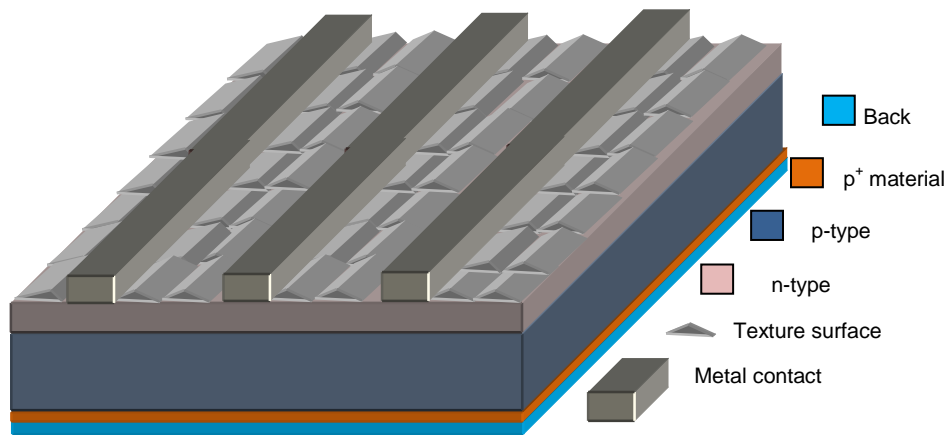


Figure 1.2:7 Silicon structure solar cell developed in 1970 [3].

Different device configurations have been implemented in order to incorporate the stacking of multi-junction thin films, such as the double and triple device setup, to allow for each layer to collect a small portion of photon energy (energy suitable for the material's band-gap), resulting in an increase in the cell efficiency. Figure 1.2:8 outlines the structure of such technology.

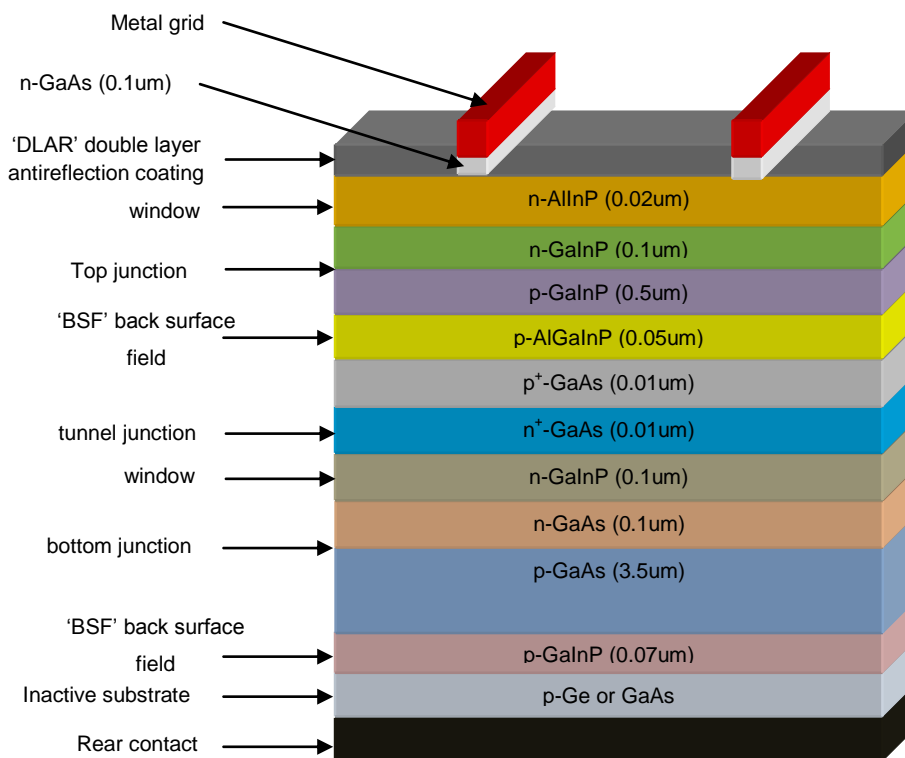


Figure 1.2:8 The structure of a multi-junction solar cell [3].

1.3 Recent development in solar cells

The average energy consumption the world uses today is 10 TW per year and it will escalate to 30 TW per year by 2050. Global warming issues that the world faces today has pushed the need to create 20 TW of non-CO₂ producing energy to supply the advancing world. The major market segment served by PV cell comprises consumer applications, remote industrial systems, developing countries and grid-connected systems.

The PV industry is flourishing in countries such as Japan, China, Taiwan, Germany and the United states. The evolution of the PV-market around the world is shown below [9].

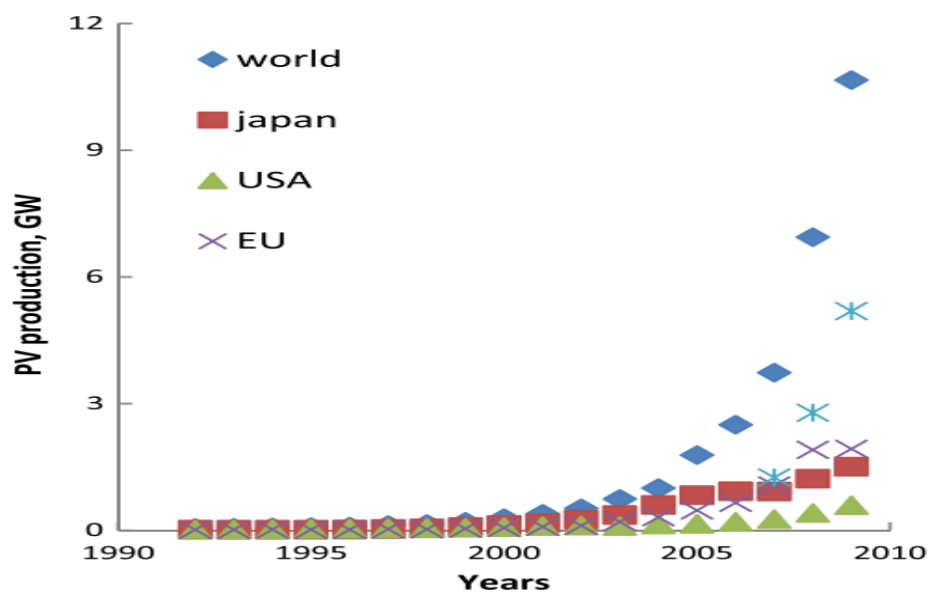


Figure 1.3:1 The evolution of the PV- market over the last two-decades [9].

With the increase in demand for PV cells, raw materials such as silicon cannot supply the demand because of an expected Si shortage. Therefore, the need for the thin-film solar cells to expand into the world PV market is required. In

terms of PV production, almost 80% of world production is based on crystalline silicon (c-Si) and polycrystalline silicon (pc-Si) wafer technology. Other PV technologies including cadmium telluride (CdTe), copper indium gallium selenide (CIGS) and amorphous silicon (a-Si) are in the beginning stages of large-scale production and will expand soon. It is expected that thin-film PV technology will play a huge part in the PV industry in the future. The world production for PV cell technologies is presented below,

Table 1.3:1 PV world production in terms of technology (MW) [9].

Technology	World production (MW)	Cell efficiency (%)
c-Si (wafer)	8.678	22
CdTe	1.017	7.3
CIGS	166	10.2
a-Si	796	13.7

1.4 Aim and objective

The aim of this project was to develop and fabricate a p-n heterojunction diode that is robust, developed with low cost and suitable for large surface area. The device attains a heterojunction configuration, consisting of two thin films, each exhibiting different semiconducting behaviour, namely n-type and p-type semiconductors that are brought together to form a p-n junction diode device.

The initial stage of this research was to make and characterise a range of oxide coating compositions that can be sputtered from blends of loosely packed powder targets, using the pulsed DC magnetron sputtering technique (described in detail in Chapter 5). These compositions include fluorine doped tin oxide, antimony doped tin oxide and titanium dioxide. The different coatings should be transparent conductive oxides (TCO) that exhibit an n-type semiconductor material characteristic.

The second objective was to characterise and develop a p-type semiconductor namely copper aluminium oxide to investigate the optimum compositional ratio and the effect of deposition power on the structure of the thin films. The thin films were characterised in terms of their structural, morphological, optical (transmission and band-gap) and electrical (resistivity, mobility and carrier concentration) conditions.

The collection of the charge carriers generated from the incident light was achieved through metal ohmic contacts, which are deposited onto both sides of the device using copper and the silver grids/contacts that were deposited

onto the n-type layer and the p-type layers, respectively. The design layout of the grid was optimised in order to increase the device efficiency.

The final part of this thesis reports on the construction the p-n junction device and the electrical verification (current-voltage characteristics) showed the rectification and the formation of the p-n junction.

1.5 Structure of thesis

This thesis has been divided into a number of chapters, a review is detailed below;

Chapter 2: an overview of semiconductor thin films is presented, and the understanding behind the optical and electrical properties and the effect of dopant behaviour is given. It also presents the trends and the commercial availability of TCOs.

Chapter 3: presents the historical and also the device theory of p-n junctions and answers the question of what happens when light shines on to a junction.

Chapter 4: reviews physical vapour deposition processes and gives a description of glow discharge plasmas and the growth and formation of thin films. It also provides an overview of the sputtering technique and gives project descriptive overview of the rig used during the development of thin films in this thesis.

Chapter 5: reviews the characterisation of the single and compound powder targets. It presents the effect of the pulse frequency, duty cycle, discharge power, gas partial pressure on the target discharge voltage.

Chapter 6: describes the surface and the film analytical techniques used during this project for characterising the thin films, including the scanning electron microscopy (SEM), X-ray diffraction (XRD), optical spectrometry and Hall-effect measurements.

Chapter 7: describes the experimental process of the rig used during this project, and presents the sample preparation and experimental parameters of each thin film developed.

Chapter 8: presents the results and the discussion of the thin films developed during this project. It also presents the electrical characteristics of the p-n junction device.

Chapter 9: presents the overall conclusions of this thesis

Chapter 10: outlines the future work that might be undertaken to further improve the developed p-n junction solar generating device.

SEMICONDUCTORS AND TCO THIN FILMS

The coexistence of optical transparency and electrical conduction can be achieved in different types of materials. Once those two entities are optimised in a thin film, it is referred to as a transparent conductive oxide (TCO). These properties depend on the nature and the atomic arrangements of the metal cations in the crystalline structures and on the presence of intrinsic or intentionally doped defects. The most utilised TCOs are multi-component oxides with ZnO, SnO₂ or In₂O₃ as the host material, which is deposited. For recent applications, Sn doped In₂O₃, (ITO) F doped SnO₂ (FTO) and aluminium doped zinc oxide (AZO) are the most utilised.

2.1 Introduction

Metallic oxide thin films have been the centre of attention in technological industries for many years. These thin films are produced via a variety of techniques to make transparent conductive oxides (TCOs). They can be thought of as conjugate property materials that are comprised of two properties that strongly coincide with one another, one is conductivity and the other is the loss of the refractive index or/and the excitation coefficient. For instance, metals are highly conductive and opaque; meanwhile, glass is highly transparent and insulating. The challenge is to decouple these two properties, through the understanding of the structure and property relationships that enable the material to retain its transparency while becoming conductive.

In 1907, Badeker discovered the first TCO materials when he sputter deposited the first thin film made from CdO which went under incomplete thermal oxidation during the post-deposition in air [10]. The electrical properties of the developed TCO changed with time, owing to the oxygen deficiency that lend free carriers to associated metal defect energy levels near the bottom of the metal like conduction band of the oxide (discussed later in Chapter 3). The general finding was that it is possible to produce n-type conductivity by using reduced metal oxide materials. This finding led to other TCO thin films being produced via different deposition techniques and based on oxides of two or three metallic elements that exhibit good optical transparency and electrical resistivity.

There are a number of applications that TCO thin films are utilised for including, transparent electrodes for flat panel displays, transparent

electrodes for photovoltaic cells, light emitting diodes, transparent transistors and semiconductor lasers. The most popular TCOs are aluminium doped zinc oxide (AZO) [11], indium doped tin oxide (ITO) [12] and fluorine doped tin oxide (FTO) [13]. Typical electrical resistivity values for TCOs are as low as $10^{-4} \Omega \cdot \text{cm}$ with optical transparency greater than 80% in the visible light spectrum [14]. The optical transparency is attributed to the wide band gap $E_g \geq 3.0 \text{ eV}$ corresponding to the wavelengths which are shorter than the visible range (380 nm to 750 nm). Therefore, any photons with an energy that is lower than the band gap are not absorbed by these materials, but are transmitted instead.

One of the ways to enhance the electrical and optical properties of any intrinsic material is to create electron degeneracy either by exploiting the deviation of the stoichiometry (such as through structural defects), or introducing native donors (such as oxygen) or introducing donor elements into the oxide matrix. An example of donor impurities in oxides includes fluorine in tin oxide, tin or antimony in indium oxide. However, it is important to understand, that there is a limitation of how many impurity atoms can be introduced to the metal oxide [15]. This will increase the carrier concentration and affects the coulombs charge between the free electrons and the ionised donor centres from which they are generated and can therefore provide a scattering to the doped material, hence degrading the optical properties of the thin film [16].

The TCO thin films developed in this research will be tuned to utilise the electromagnetic radiation in the visible range only. The optical and the electrical behaviour of the developed TCO thin films must be considered and

careful balance between the two required properties of transmission and resistivity is required. In order to achieve a TCO material with such characteristics, the composition should either be non-stoichiometric or should be doped with other elements. The cost and the availability of other elements should be considered together with its stability in use.

The usefulness of TCO thin films depends on a number of factors such as the opto-electrical properties, environmental stability, surface adhesion and suitability for the substrate. By considering all the above factors, the functionality of the TCO can be maximised. It is also important to consider the economical means when developing a TCO by choosing the raw material and the deposition method for growing the films.

The most utilised TCO, especially in electronic and photovoltaic applications is ITO owing to its great opto-electrical properties (electrical resistivity, $\rho=10^{-4}$ $\Omega\cdot\text{cm}$, optical band-gap, $E_g \geq 3$ eV, Transmission >90% at 100 nm thick film and sheet resistance 10 Ω). With the high price and the scarcity of indium, there is much interest in finding an alternative TCO. Currently, the best candidate that is inexpensive and nontoxic is AZO which can have a low electrical resistivity in the order of $\rho=10^{-4}$ $\Omega\cdot\text{cm}$ and an optical transparency higher than 85% [17-18].

During this chapter, the concept of n-type and p-type semiconductors is given. In addition, the optical behaviour, electrical behaviour and the affect of dopants on n-type TCO is studied. The trends, commercial development and availability of TCO thin films are presented.

2.2 Concept of the semiconductor

A semiconductor is a transitional staged material between an insulator and a conductor material [15]. It attains the optical behaviour of an insulator (such as glass) and related dielectric materials that accommodate and guide light waves, and electrical properties (such as metal conductors) that do not allow light to travel through.

The flow of the electrical current depends on the electrons, which act as charge carriers. The electrons that are responsible for carrying the electrical current are called conduction electrons. In general, the majority of the electrons are attached to single atoms and cannot move freely. However, some electrons are loosely bound and can be released to become a conduction electron, leaving positive charged atoms (ions) behind and the net charge zero. The valence electrons are responsible for moving the positive charges from one atom to the other and therefore creating a path through which electrical current can travel.

There is an energy gap, E_g , which separates the conduction electrons from the valence electrons, and in semiconductors, this energy gap is in the order of 1eV. In some semiconductors, this energy gap can capture the electromagnetic radiation from sunlight, which carries its energy via particles called photons, which have a wavelength, λ , of less than the gap wavelength, λ_g . A photon also exhibits a wavelike character and its energy, E_λ , can be determined across a wavelength, λ , by [15],

$$E_\lambda = \frac{hc}{\lambda} = h\nu = \hbar\omega \quad \text{Eq. 2.2:1}$$

Where h is Planck's constant and, c , is the speed of light, ν , is the frequency, $\omega=2\pi\nu$ and $\hbar=h/2\pi$ is the reduced Planck's constant. The generation of electron-hole pairs is only possible with photons that have greater energy than the band-gap (E_g). Therefore, to design an efficient solar cell, it is important to consider this physical mechanism.

In a semiconductor, the outermost shell of a single atom is fully occupied by the valence electrons and there is no possibility of accepting an electron of the same energy level. As the atoms in a semiconductor crystal are joined together, their outer shells begin to interact with one another forming a slight gap in the valence energy. The electrons are able to exchange places within this valence energy band but since there are no holes available, no charge flow is possible. Generating holes is only possible, if the electrons can be promoted to a higher energy band, also termed the conduction band, which is initially empty. The electrical conductivity of a semiconductor is governed by the electrons' concentration in the conduction band and holes' concentration in the valence band, and can be summed by the following equation [15],

$$\sigma = q_n\mu_n + q_p\mu_p \quad \text{Eq. 2.2:2}$$

Where q is the elementary charge, n is electron concentration, p hole concentration, μ_n and μ_p are the mobility of the electron and hole, respectively.

2.3 Optical properties of semiconductors

To develop TCO thin film coatings, it is important to study the optical properties and how they behave in the visible range of the spectrum in terms of the interaction of the electromagnetic radiation with the electrons of the material. In the ideal world, a TCO thin film coating should absorb 100% of the photon energy across the whole spectrum range. However, this is not possible, due to reflection and interference effects such as scattering and surface imperfections arising from porosity, pinholes and microcracks, which affect the transmission. In the ultra-violet (UV) range, the transmission is limited due to the band gap as photons with higher energy than the band-gap are absorbed and at the near-infra-red (NIR) a second transmission exists due to the free-carrier plasma resonance frequency.

The electromagnetic radiation propagates differently in TCO thin films compared to free space due to the charge occupancy found in thin films. This intolerance has an affect on the intensity and the wave velocity of the radiation described by the complex index of refraction, N , derived by Heavens [19],

$$N \approx n - ik \quad \text{Eq. 2.3:1}$$

Where, n , is the real refractive index, and, k , is the imaginary portion of the complex index of refraction, also known as the extinction coefficient. A value that is usually associated with the extinction coefficient is the absorption coefficient, presented by, α , and given by the following equation [20],

$$\alpha = \frac{4\pi k}{\lambda} \quad \text{Eq. 2.3:2}$$

The electric field of the propagating wave in the x direction travelling through space is expressed as follows [20],

$$\varepsilon = \varepsilon_0 e^{-\left(\frac{i2\pi N x}{\lambda}\right)} \quad \text{Eq. 2.3:3}$$

Where, ε_0 , is the amplitude of the field, and, λ , is the wavelength. During the propagation through space, the index of refraction is unity and the wave velocity is equal to the speed of light, c . However, as the wave propagates through a medium, these quantities change to, n , and, c/n , respectively. As the wave propagates through the material, absorption processes takes place, so a real function is added to Eq. 2.3:3 to represent the damping effect or the attenuation of the wave [20],

$$\varepsilon = \varepsilon_0 e^{-\frac{2\pi k x}{\lambda}} \cdot e^{-\frac{i2\pi n x}{\lambda}} \quad \text{Eq. 2.3:4}$$

The second expression in Eq.2.3:4 contains n and represents the propagation without absorption. All materials exhibit a varying complex index of refraction N , for example, the extinction coefficient, k , of a glass substrate is vanishingly small compared to its refractive index, n . On the other hand, for highly absorbing material such as metals, n , is usually small compared to, k . The imaginary phase, i , of Eq 2.3:4 can be eliminated by multiplying by the complex conjugate. The attenuation of a beam of light in an absorbing material can then be calculated as follows [21],

$$I/I_0 = e^{(-\alpha d)} \quad \text{Eq. 2.3:5}$$

Where, I , is the emergent intensity, I_o , is the incident intensity, α , is the absorption coefficient given in Eq 2.3:5 and, d , is the thickness of the material.

The intrinsic optical properties of the TCO's including the transmission (T), Reflection (R) and absorption (A) are influenced by the refraction index (n), optical band-gap (E_g) and the extinction coefficient (k). The intrinsic properties are strongly dependent on the chemical composition and the structure of the thin film. The geometric features that influence the optical properties of the TCO thin film are; film thickness, thickness uniformity, film roughness and film defects [22].

It is possible to deposit TCO thin films onto different substrates, including glass, polymers and ceramics [23]. However, TCO are usually deposited onto glass substrates, which have a refractive index (n_{sub}) of 1.45 for silica base glass and 1.6 for other various types [24]. Depending on the film thickness and the wavelength of the light, if the film thickness is greater than 100 nm then interference bands can occur and this will cause the transmission to have maximum and minimum values.

The refractive index, n , of most TCO thin films in the visible range of the spectrum is between 1.8 to 2.8 and using the equation below, it is estimated the minimum transmission, T_{min} , is between 0.5-0.8 [24],

$$T_{min} = \frac{4n^2 n_{sub}}{(1+n^2)(n^2+n_{sub}^2)} \quad \text{Eq. 2.3:6}$$

The optical band gap (E_g) of the TCO thin film is estimated from the transmittance (T%) and the reflection (R%) spectra. The optical absorption coefficient, α , data can be initially calculated from the following equation,

$$T_{\text{corr}} = \frac{100 \times T\%}{100 - R\%} \quad \text{Eq. 2.3:7}$$

And

$$\alpha = \frac{1}{d} \left[\ln \left(\frac{100}{T_{\text{corr}}} \right) \right] \quad \text{Eq. 2.3:8}$$

T_{corr} (%), is the transmittance corrected for the reflection losses at the air-film and film-substrate interface, d is the thickness of the film measured in nanometres. The optical band gap (E_g) can then be obtained from the following equation,

$$\alpha h\nu = A(h\nu - E_g)^{\frac{1}{n}} \quad \text{Eq. 2.3:9}$$

A is a constant, $n=0.5$ for direct and $n=2$ for indirect allowed transitions. Data is plotted graphically for $(\alpha h\nu)^{n/2}$ against $h\nu$, which is of the form 'y = mx + c' and then a linear fit of the data to Eq.2.3:9 will give the allowed transition and optical absorption edge, E_g [25].

During the study of the developed TCO thin film, the total transmission, total reflection and band gap measurements were considered. These parameters significantly depend on the film thickness, the refractive indices of the substrate and the film as well as the dopant percentage level. A USB2000+ spectrometer sourced from Ocean Optics was used to determine the transmission and the reflection of the TCO thin film coatings.

2.4 Electrical properties of semiconductors

TCO semiconductors are comprised of a wide band-gap ($E_g > 3$ eV) that has a typical conductivity in the range of 1×10^2 to 1×10^6 S [24]. Typical TCO materials are known to exhibit an n-type conductivity, such materials include In_2O_3 , SnO_2 , CdO , ZnO [26-27]. Some p-type materials have been developed, such as CuAlO_2 [28], AgGaO_2 [29], however, their properties remain inferior to that of the n-type TCO materials. The conductivity of a TCO material can be enhanced by co-doping the intrinsic material.

The n-type conductivity that is present in indium tin oxide (ITO) or fluorine doped tin oxide (FTO) is related to the presence of the shallow donors that are located close to the conduction band that are introduced by the chemical doping [12]. At room temperature, the excess electron undergoes thermalisation into the conduction band. Further doping the intrinsic material, will result in the increase in the donor electrons, which form a current carrying degenerate gas that gives rise to the electrical conductivity.

The conductivity in a semiconductor is the result of the energy absorption that comes from the light directed onto the semiconductor, which causes the carriers to transit from the valence and conduction bands.

High conductivity in semiconductors is achieved through the overlap of the s-orbital band electron states between large radii metal ions, especially when the counter anion state is small (such as oxygen). Research has shown that the electron conductivity in indium oxide is attributed to the 5s-orbital overlap. Moreover, recent studies on zinc oxides which has a 4s-orbital, confirmed that the extent of this s-orbital overlap is the driving factor to higher conductivity in semiconductors [30]. If the overlap between the s-orbitals is sustained in the conduction band, free carrier mobility populates the conduction band.

The electrical conductivity in TCO semiconductor depends on two factors: the carrier density in the conduction band and the carrier mobility. This is illustrated by $\sigma = \mu n e$, where, μ , is the electron mobility, n , is the electron density, e , is the electron charge [31],

$$\mu = \frac{e\tau}{m^*} \quad \text{Eq. 2.4:1}$$

Where, τ , is the mean time between collision and, m^* , is the effective mass of an electron. Eq.2.4:1 presents the relationship between the scattering time and mobility. It is assumed that after each scattering time, the carrier motion is randomised, so it has a zero average velocity, after which it accelerates uniformly in the electric field until scattered again.

In intrinsic materials, the electrical conductivity can be enhanced by populating the area close to the conduction band with shallow donors and impurity states using donor centres such as metallic interstitials or oxygen vacancies. Kilic and Zunger studied the electron energy band structure using the ab initio density functional theory (DFT) calculations to study the effect of dopants on the band structure of SnO₂ [32]. The interstitial state of Sn populating the conduction band, and the O₂ vacancies dominating the defect structure of SnO₂, due to the multivalence of Sn, was investigated. The study showed that the defect structure of the SnO₂ provides a theory for the coexistence of conductivity with transparency which produce shallow donor levels (introducing impurities in a semiconductor which are used to set off free electrons in the conduction band), turning the material into an extrinsic semiconductor [32].

TCO thin films with relatively high carrier concentrations have limited electrical conductivity, i.e. high carrier density limits the carrier transport due to the coulomb interaction between the electrons and the dopant. This attraction is also known as the ionised impurity scattering effect. Increasing the dopant concentration above a saturation limit will dramatically reduce the carrier mobility and therefore limit the conductivity and the resistivity and reduce the optical transmission near the infrared edge [33]. All the recently developed TCOs from doped or undoped compounds suffer from these limitations. Research conducted by Bellingham et al. reported the electrical resistivity and mobility of TCOs including indium tin oxide (ITO) and tin oxide (SnO₂) have a limited mobility and resistivity above a carrier concentration of $1 \times 10^{20} \text{ cm}^{-3}$ due to the ionised impurity scattering constraint [16]. Ellmer and Mientus

studied the effect of the deposition technique on the electrical properties of ZnO and found that resistivity and the mobility were nearly independent of the deposition technique used and were limited to $2 \times 10^{-4} \Omega \cdot \text{cm}$ and $50 \text{ cm}^2/\text{Vs}$ [34].

2.5 Dopant effect on semiconductors

Doping is a process whereby an insulating material becomes a semiconductor by introducing foreign impurities into the crystal lattice. The energy levels of the electrons orbiting the dopant atom are different to that of the metal oxide. The dopant can either donate electrons (free carriers) to the conduction band of the metal oxide creating an n-type semiconductor or accept electrons from the valence band of the metal oxide creating a p-type semiconductor. For a metal oxide, the conduction band consists of unfilled metal cation energy levels, while the valence band consists of oxygen anion energy levels. If the introduced dopant has an energy level that is just below the conduction band minimum (CBM), this means a small energy is required to free the dopant electrons into the conduction band and therefore allowing free carriers to populate the conduction and therefore increasing the electrical conductivity. Semiconductors that are manufactured that way are called n-type because the free carriers are of negative charge (electrons). An example of an n-type semiconductor is zinc oxide doped with aluminium. The energy level of aluminium lies very close to the CBM of zinc oxide, therefore promoting free carriers in the conduction band and effectively enhancing the electrical properties of the semiconductor. By introducing the defect levels near to the bottom of the conduction band, increases the band-gap energy, leading to a blue-shift in the high energy absorption edge which is also known as the

Burstein-Moss effect [35]. This shift correlates with the magnitude of the carrier density.

An alternative method to make a semiconductor is by introducing a dopant that has empty energy levels just above the valence band maximum (VBM) of the metal oxide. This promotes the electrons in the valence band to hop onto these new levels, leaving a population of positive charge (holes) to conduct in the valence band. Dopants that act in such way are termed accepters. Semiconductors manufactured in such a way are called p-type because the conduction can only take place when holes move in response to an applied field. An example of a p-type semiconductor is the delafossite oxide copper aluminium oxide CuAlO_2 .

2.5.1 Fluorine doped tin oxide

Un-doped tin oxide (SnO_2), is a wide band-gap semiconductor ($E_g > 3 \text{ eV}$) that exhibits high optical transparency ($T \geq 85 \%$) and an n-type character due to oxygen vacancies [36]. The electrical conductivity of the material can be largely enhanced by doping with foreign impurities. The most favoured dopants are antimony which substitutes the tin cations or by fluorine via substituting the oxygen atoms [36].

Fluorine doped tin oxide (FTO) exhibits good visible transparency owing to its wide band-gap, while retaining a low electrical resistivity due to the high carrier concentration (N_d) caused by the oxygen vacancies and the substitutional fluorine dopant [37]. FTO is mechanically, chemically and electrochemically stable [38], and it is utilised in numerous technologies including; thin film solar cells [39], dielectric layers in low emissivity coatings

for windows [40], in gas sensors applications [41] and in liquid crystal displays [42]. There are a number of methods/techniques to grow SnO₂ (either doped or undoped) films, including chemical vapour deposition [43], pulsed laser deposition [44], DC reactive sputtering [45] and spray pyrolysis [46].

Some techniques require a high substrate temperature to deposit the film, which can often cause the formation of intermediate semiconductor oxide layers at the film boundary [47]. Any post-treatment of the films, such as annealing, also poses additional operational costs and reduced throughput. A few attempts have been made to sputter FTO from solid targets using techniques such as RF magnetron sputtering [48]. More recent work deals with DC reactive magnetron sputtering using a metallic tin target and various plasma atmospheres such as Ar/O₂/CF₄ [45], Ar/O₂/Freon [49].

This project presents a unique alternative way to deposit FTO by mid-frequency (100-350 kHz) pulsed DC magnetron sputtering (explained in Chapter 4) from loosely packed (as opposed to sintered or pressed) blended powder targets. Thin films have been produced at a low deposition temperature (~170°C process heating and no post deposition treatment) and a relatively high deposition rate of 27 nm·min⁻¹. This technique has further advantages over conventional DC or RF sputtering from solid metallic or ceramic targets such as employing a closed field unbalanced magnetron configuration and pulsed sputtering to enhance the sputtering rate, benefit from low deposition temperatures, suppress arcs and produce dense homogenised films [50]. The powder target is loosely packed (as opposed to sintered or pressed), so target cracking is avoided and, most importantly, the target composition can be readily varied. The powder target approach is a

cheap and efficient means of investigating and optimising the properties of multi-component materials, compared to using metallic or ceramic targets [51].

2.5.2 Antimony doped tin oxide

Transparent conductive oxide (TCO) thin films and their remarkable applications as electrodes is dependent on the material used to make a sweeping strides. However, the availability of the raw materials and the economics of the deposition method are big significant factors in choosing the appropriate TCO material. The recent and the scarcity of the high price of ITO, the most popular TCO material has pushed research and development to find a substitute [52].

Research has shown that fluorine and antimony are the most favourite element to compensate the electrical properties of the tin oxide thin films without degrading the optical properties. ATO is a TCO which has been the focus of R&D studies due to its technological importance in the field of energy saving and energy generation [23, 53], and also because of its environmental stability [54] and its electrochemical stability [53], as well as its low cost and easy fabrication [55].

2.5.3 Copper aluminium oxide

In general, TCOs are n-type semiconductors, which are doped intrinsically via native donors such as oxygen atoms or interstitially via metal atoms in order to achieve high opto-electrical properties. Some of the materials that combine the above stated conditions include indium tin oxide (ITO), fluorine doped tin oxide (FTO), and aluminium doped zinc oxide (AZO) [56-58]. These materials

have a limited electrical conductivity because at certain carrier density threshold, the Coulomb interaction between the accessible free electrons and the ionized donors provide a scattering effect in the doped material; this in turn reduces the mobility. Metal oxides with high carrier concentration can absorb part of the incident radiation via the electron gas interaction that takes place around the electron plasma frequency, which increases with the increase in the carrier concentration [50]. Literature suggests that when the carrier density is $> 2 \times 10^{23} \text{ cm}^{-3}$, the transparency of the TCO films is degraded in the visible spectrum due to a shift in the plasma frequency from absorbing infrared wavelength, to visible light. Generally, the deposition of a conductive p-type TCO is difficult due to the electronic structure of the oxide. More recently, research has taken a great depth to generate p-type TCO films that retain similar opto-electrical behaviour of an n-type semiconductor. In order to achieve a p-type conductivity, materials are required to have a defect energy that lies close to the valence band of the metal oxide [59]. Electron promotion to these defect levels, promotes hole generation in the valence band edge, hence increasing the electrical conductivity.

Research has recently investigated different deposition techniques to grow the CuAlO_2 coatings, including sputtering [18, 51, 60], pulsed laser deposition [61-63] and plasma-enhanced chemical vapour deposition (PECVD) [64]. Among these techniques, reactive sputtering is one of the main techniques used to develop binary compounds thin films due to its process reliability, strong adhesion between film and substrate [65], working pressure [60], sputtering power [66] elemental content [67] and substrate temperature [68].

2.6 Trends in the development of TCO materials

The development of a novel TCO material is dictated by low resistivity and high transmittance in the visible spectrum. There are two strategies that can be used to obtain the desired TCO thin film. The first is to dope the TCO compounds with other elements, which will increase the electron density [56].

Table 2.6:1 outlines different TCOs and their possible dopants.

Table 2.6:1 TCO compounds and dopants [11].

TCO	Dopant
SnO ₂	Sb, F, As, Ta, Nb
ZnO	Al, Ga, B, In, Y, Sc, F, V, Si, Ge, Ti, Zr, Hf, Mg, As, H
In ₂ O ₃	Sn, Mo, Ta, W, Zr, F, Ge, Nb, Hf, Mg

T.Minami produced and characterised more than 20 different TCO compounds and dopants, and found that ITO (indium tin oxide) performed best in terms of low resistivity and high transmittance in the visible region. It was also noted that doping the TCOs with low metallic ion concentration can generate shallow donor levels, forming a carrier population at room temperature [56]. Doping indium oxide (In₂O₃) with tin (Sn) can increase the electrical conductivity because Sn⁺⁴ ions substitute for In⁺³ ions and this provides more electrons as the Sn⁺⁴ acts as a one-electron donor [69]. Doping zinc oxide with other impurities such as aluminium, gallium or indium from group 3 and tin or germanium from group 4 is also possible. However, doping zinc oxide with aluminium produced relatively high conductivity [70].

Other examples that have been reported include the deposition (including magnetron sputtering and chemical vapour deposition) of aluminium zinc oxide doped with germanium, AZO:Ge (GZO), tin oxide doped with fluorine, SnO₂:F (FTO) and tin oxide doped with antimony, SnO₂:Sb (ATO) [69, 71]. When doping SnO₂ with F, the O⁻² ion is replaced with a F⁻ ion, creating a new donor level, therefore increasing the mobility and carrier concentration, and effectively reducing the resistivity [72-73]. The fluorine doping level should be carefully determined and not exceed the maximum limit, as doing so will increase the F⁻ carrier scattering and effectively deteriorate the electrical properties of FTO. Doping SnO₂ with Sb will introduce Sb⁺⁵ ions that act as donor levels. If the doping saturation limit is exceeded, it will effectively increase the resistivity because the Sb⁺³ substitutes the Sn⁺⁴ ions leading to an increase in the acceptor level that compensates the donors, resulting in resistivity retardation [74]. The best electrical properties for doped zinc oxide were achieved by Agura et al. They deposited AZO solid films and reported a low resistivity of 8.5X10⁻⁵ Ω·cm [75] and Park et al when depositing GZO and achieving a resistivity of 8.1X10⁻⁵ Ω·cm [76].

For an effective TCO, the lowest conduction band should be wide enough so that when doping occurs, the carriers will be highly mobile. A second condition which must be satisfied is that the TCO material must accommodate the dopant and populate the conduction band in such a way that the mobility or the transmittance are not degraded [30, 77].

In n-type semiconductors, the electrons are the majority carriers and therefore the carrier density '*n*' is denoted by '*N_d*'. Since the majority of the TCO

materials are n-type semiconductors, the majority of the electron density is in the conduction band.

Research carried out on TCO materials to study the electron mobility in the conduction band, showed that the electrons are connected by an electronic structure and that the mobility of the electron is proportional to the band gap size [77].

The conductivity of a TCO material is limited by two factors, the carrier density and the electron mobility. If the TCO material has a large electron density, the carrier transport of the electrons is limited because of the Coulomb interaction between the electrons and the dopants. Increasing the dopant level in the TCO material will result in a decrease of the carrier mobility and at some stage the conductivity cannot be increased any further. This will have a negative impact on the optical transmittance window near the infrared spectrum.

Another effect that reduces the electron mobility in a TCO material is the scattering effect, which is due to the ionised dopant levels that are distributed evenly in the semiconductor. Increasing the dopant concentration level will considerably increase the scattering of the ionised dopant atoms. All the TCO materials suffer from such a problem.

Another effect associated with increasing the dopant level, is the clustering of the doped ions which can limit the conductivity due to the increase in the average scattering time, τ , [78-79].

During this investigation, it was important to study and characterise the resistivity of the coating against the mobility and the carrier concentration at different experimental conditions in order to find the optimum process conditions that gave the least resistivity at the maximum possible transparency. The carrier concentration and the mobility should be in the range of 1×10^{19} to $1 \times 10^{21} \text{ cm}^{-3}$ and 10 to $50 \text{ cm}^2/\text{Vs}$, respectively, in order to be able to optimise the resistivity.

The trend in p-type semiconductor materials has an interesting future especially in the field of transparent electronics. However, it is proving to be difficult to deposit p-type semiconductors that attain the required properties. The poor electrical conductivity and mobility of carriers arises from the fact that the positions of the oxygen $2p$ levels are lower than the valence orbit of the metallic atoms, creating a deep acceptor level. The holes are therefore restricted and would require high energy to overcome the barrier height in order to move freely within the crystal lattice, therefore this behaviour results in poor hole mobility and high electrical resistivity [28].

However, this situation was improved by Kawazoe in 1997 who reported a P-type TCO using CuAlO_2 with a wide bandgap of 3.5 eV, electrical conductivity of $10.52 \Omega \cdot \text{cm}$ and electrical mobility of $10.4 \text{ cm}^2/\text{Vs}$ at room temperature [62]. With the emphasis on the production of p-type thin films, more recent work was carried by Alkoy et al who reported CuAlO_2 p-type thin films with resistivity of 5-10 $\Omega \cdot \text{cm}$ [51] and by Ping et al. who reported p-type properties with an electrical resistivity of $1.9 \text{ k}\Omega \cdot \text{cm}$ [66].

2.7 Industrial applications of TCOs

TCOs thin films are used in many applications, the largest three in terms of surface area covered includes electronics [80], photovoltaic technologies [81] and architectural glass [82]. In the electronics industry, the TCOs are used as transparent electrodes in LCDs (liquid crystal displays of a flat panel display). The optical transparency allows for the backlighting to pass through and at the same time, the electrical property allows the voltage to be applied to the various pixels. The most favourable TCO in the electronic industries is ITO due to excellent opto-electrical properties.

TCO thin films play an important role in photovoltaic cells. They are used as a transparent electrode owing to excellent optoelectrical and environmental properties.

TCO thin films are generally applied as part of a multi-layer stack in architectural glass. Low-E windows use the transparency of the TCO in order to transmit the light through in the visible spectrum, but filters the infrared spectrum, therefore minimising heat transmission. This property will minimise air conditioning cost during summer and the heat cost during winter.

The majority of solar cell technologies use TCO thin films as the transparent electrode. The major advantages of using a TCO is; compatibility with the other layers in the solar cell and environmental stability. Usually, fluorine doped tin oxide is used as a TCO layer due to its cheap cost and environmental stability [83].

Other applications that TCOs are used in include; transparent heating elements that can be act as defrosters in vehicular windscreens; shielding to

decrease the electromagnetic radiation on sensitive electronic devices; applied to surfaces in clean rooms used for electronics assembly to prevent static discharge build-up [84].

2.8 TCO deposition approach

TCOs are deposited on transparent or non-transparent substrates with an average thickness range between 10 nm to 1 µm via a vast range of deposition technologies, below are the most utilised in industry;

Magnetron sputtering is a form of physical vapour deposition that is widely used to make uniform coatings on glass, polymers, metals, and other substrates (described in later section). There are a number of techniques, such as direct current (DC) sputtering, radio frequency (RF) sputtering and reactive sputtering [85]. Essentially, plasma is initiated in a low pressure of an inert or a reactive gas, and the energetic ions in the plasma sputter the atoms off the raw material (known as the target) which are deposited as a uniform film on the surface of the substrate. This deposition technique appears to be the most popular technique in film deposition due to its cost effectiveness and the capability for deposition on large surface area substrates, therefore from a practical point of view, the fabrication of TCO films is done in this manner [85]. TCOs that have fabricated using this technique include n-type; ITO [86-87], ZnO [88-89], FTO [90-91], p-type; CuAlO₂ [51, 67], NiCo₂O₄ [92], NiO [93].

Pulsed laser deposition (PLD) is a PVD technique that is used to grow a variety of oxide films, including TCO's [94]. PLD is a process that requires medium to high vacuum conditions. A reactive gas is added to the chamber to create oxides films. During a typical PLD process, a laser beam is focused

onto a target surface such as an oxide powder or a metal target, and it ablates target material off the target. The substrate is heated to a high temperature (typically ~ 400-700 °C). Typical TCO fabricated using this technology include; ZnO:F [94], ITO [95], TiO₂ [96], and p-type TCOs NiO:Li [97].

Other techniques such as sol gel, spray coating, chemical vapour deposition and spray pyrolysis are also used to deposit TCO thin films. These techniques do not require the need for a vacuum environment, however instead they require high deposition temperatures. Sol gel, involves immersion of the substrate in a chemical solution, then the withdrawal at a controlled rate and seemingly controlled heat treatment. Alternatively, the chemical solution can be flame sprayed onto the substrate. Chemical vapour deposition (CVD) uses high temperature substrate holders to decompose the evaporated vapour from the precursor to make the thin film with the right compositional ratio. Spray pyrolysis uses the same principles of CVD, the only difference is the fluid containing the precursors is sprayed onto the hot substrate.

2.9 Summary and outlook

The subject of transparent conductive oxides films has gained a very important role in the field of optoelectronics, smart windows, and solar cell technologies, due to their unique combination of optical and electrical properties. An example for TCO application is in energy savings especially in buildings, as TCOs have low infrared emittance and can therefore be used to improve the thermal properties of modern buildings. Other applications rely on the optical and electrical properties such as in p-n junction power diodes, in

which the n-type TCO allows the light to penetrate to the p-type layer, and concurrently collecting the charge carriers. ITO is currently the most utilised TCO in the opto-electronic industry however; the scarcity and the high price of indium drives the research to search for alternative TCOs to replace ITO and to understand the physics and chemistry of TCO materials. The physical effect on the optical transparency and the electrical conductivity, in particular the effect of oxygen vacancies and effect of dopants in the formation of shallow donor levels is well established. In summary, the AZO, FTO and GZO coatings are the present TCOs that have close electrical conductivity to that of the ITO and high optical transparency in the UV-VIS-NIR range.

P-N DIODE

A p-n diode is a semiconductor device that is based on a p-n junction configuration that generates the electrical energy by absorbing energy from sunlight and converting it to a direct current that flows in one direction. The device consists of two regions, namely the n-region and the p-region. The n-type and the p-type regions are created by varying the doping level within a single semiconductor crystal or using two materials. The physical principles underlying the operation of the p-n junction diode are the subject of this chapter.

3.1 History of p-n junctions

In March 1940 at the Bell Telephone Laboratories, an important finding was observed by Ohl when he observed the photovoltaic effect when a flashlight was shone onto a silicon rod and recorded a voltage reading of almost 0.5 V [6]. This was by far the best result anyone had gained in the photovoltaic field. During that period, crystals had different purities and therefore a natural p-n junction was formed unintentionally.

During Ohl's electrical tests on much purified silicon rods, he noted that at some parts of the rod, the rectification properties were opposite to what he expected. Ohl and the research group decided that the two-types of silicon needed to be named differently as they both exhibit different behaviour. They named them p-type (positive) and n-type (negative). This is because the bottom part of the slab gave a negative voltage while the top part gave a positive voltage when light was shone onto it. The mid-section, which exhibited high resistance, was termed a p-n junction.

The unusual behaviour of silicon was further investigated by another solid state physicist named William Shockley who was very interested in the p-n junction barrier of the silicon. He was interested in using this technology in amplifying a signal, which he termed a "solid state valve". Shockley recorded the first signal amplification and his work led to the first point-contact transistor which Bell Labs claimed in 1947 and this caused Shockley to further investigate the matter and manage to control the flow of electrons between the surrounding n-type regions. He managed to create the first p-n junction transistor in January 1948 [98].

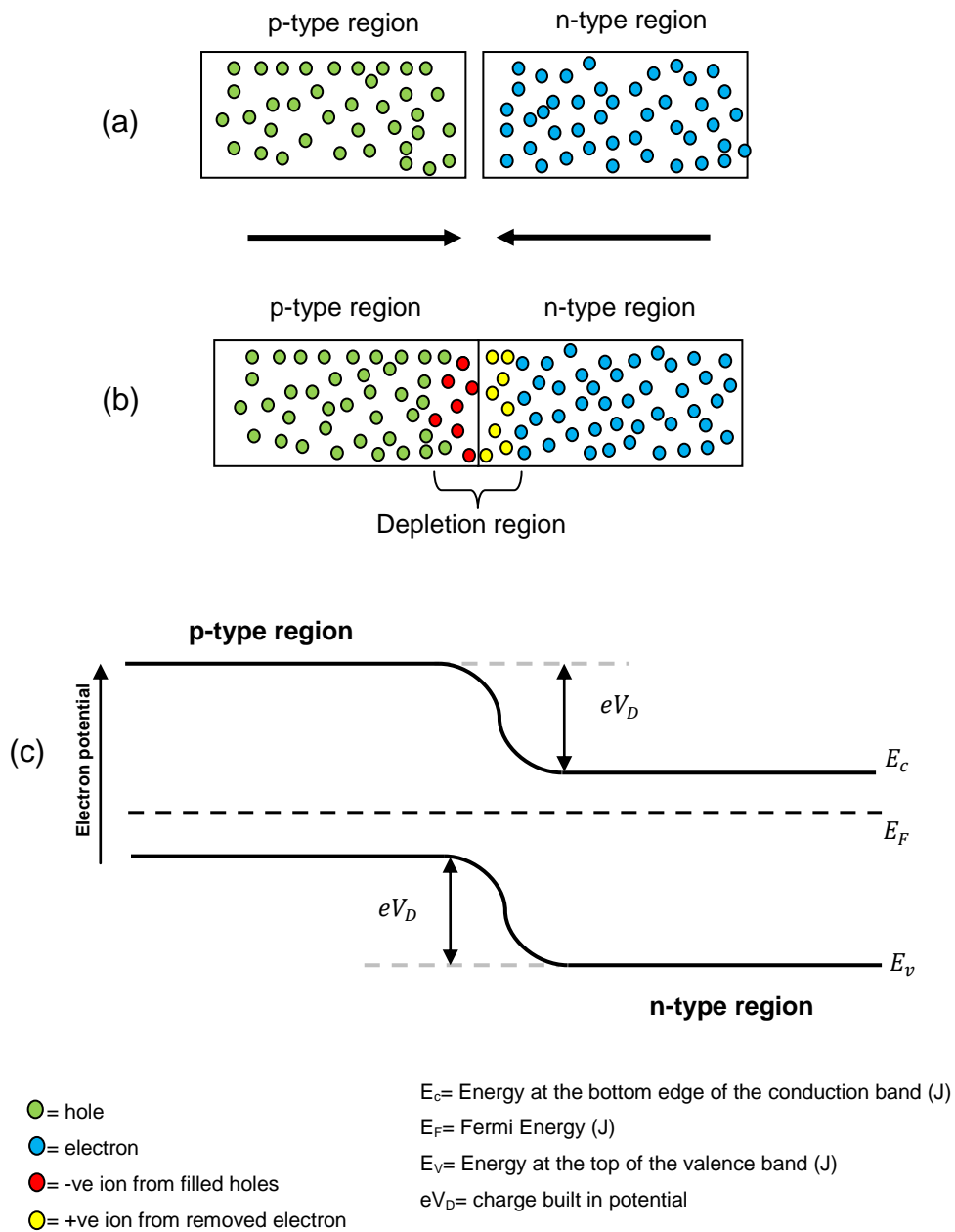
3.2 p-n junction device theory

Figure 3.2:1 outlines how a p-n junction is formed by bringing together the p-type and the n-type regions and also outlines the energy levels and a junction barrier [99]. When a p-type and n-type materials are placed in contact with each other, the junction behaves very differently than either type of material alone, and it is termed the p-n junction, as shown in Figure 3.2:1 (a-b). When the p-n junction is formed, some of the electrons in the n-region diffuse across the junction and combine with the holes to form negative ions. A hole can be treated as a particle with a positive mass and a positive charge that is exactly equal in absolute value to an electron, this is depicted by the yellow and the red circles in Figure 3.2:1 (b) . The n-region contains positive donors and a large amount of electrons, while the p-region contains negative accepters and positive holes. The n-region contains more free electrons, which diffuse to the p-region while the holes in the p-region migrate to the n-region. The flow of carrier from one region of higher concentration to lower concentration results in a diffusion current.

If these particles had no charge, the diffusion process would stop once their concentration becomes equal and no electric field would exist because there will be no electrostatic attraction between them. However due to their opposite charge and the distance between them, an electric field is established and the drift current causes the carriers to flow in the opposite direction to that of the diffusion current.

While in thermal equilibrium no external voltage is applied between the *n*-type and *p*-type material, there is an internal potential, which is caused by the work

function difference between the *n*-type and *p*-type semiconductors. This potential equals the *built-in* potential, eV_D .



- (a) = electrons and holes in the two halves
- (b) = flow of carriers to equalise the electrochemical potential difference and formation of depletion region
- (c) = energy level and junction barrier

Figure 3.2:1 The band diagram of a p-n junction at thermal equilibrium [100].

Bringing together a large number of atoms (in the order of 10^{20} atoms or more) will produce molecular orbitals, which are proportional to the number of atoms. This will make the energy difference between them very small. The band that contains the valence electrons is termed the valence band and the next permitted band is termed the conduction band [101].

The energy band structure is a series of a forbidden and allowed energy bands. The allowed energy bands associated with different atomic orbital can overlap to produce a single large energy band. The space between the allowed bands is called the forbidden energy gap because the electrons cannot have these energies.

The band structure determines the electrical and optical behaviour of the material. A typical structure of the outer shell of electrons in a solid is shown in Figure 3.2:2. A common characteristic of a solid is that they contain only a few electrons in the outer shell, the bond between these electrons and the nucleus is relatively weak, so for example, when Al atoms are brought together in a block of metal, the valence electrons leave the atoms to become part of a common electron cloud. With this arrangement, the valence electrons have high mobility and are therefore able to conduct electricity.

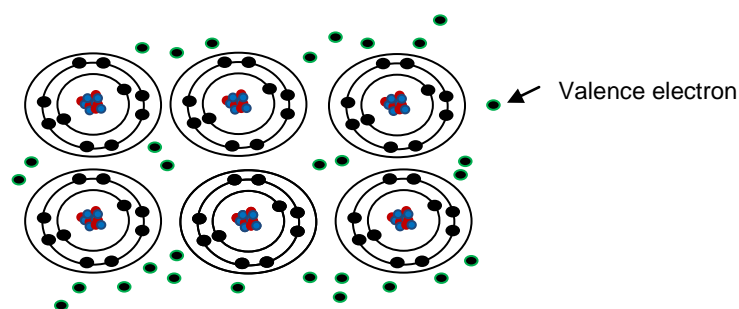


Figure 3.2:2 Sharing of valence electrons in outer shell between atoms.

The locations of the allowed and forbidden gaps in the atom are shown in Figure 3.2:3.

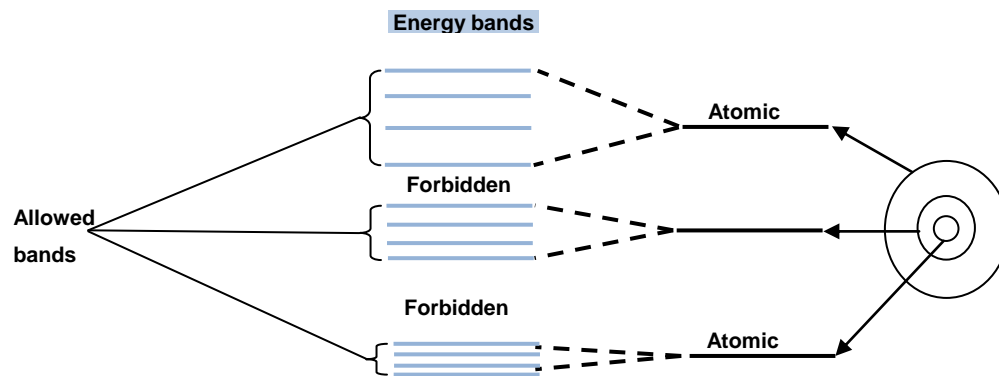


Figure 3.2:3 Formation of energy bands [20].

For an electron to pass from one energy band to the next, it requires energy that is sufficient enough to excite it to the next energy state, provided the nearby states are not full, or else the electron will not respond.

The band diagram model is a useful model in describing the difference between metal, semiconductor and insulator materials. The following diagram outlines this,

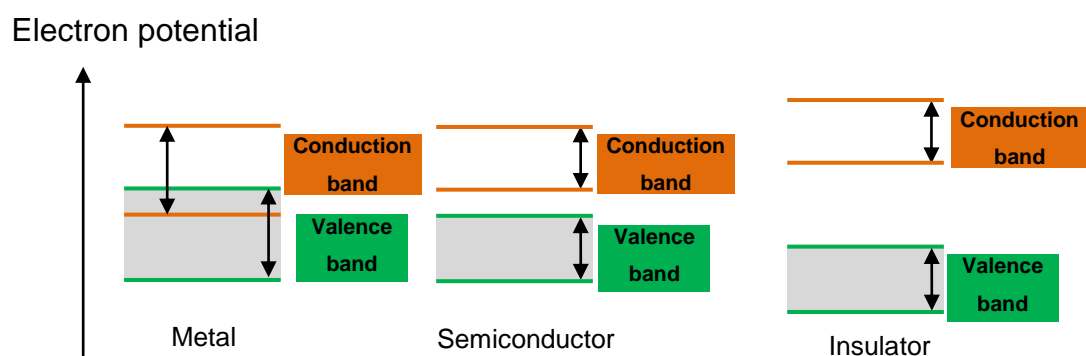


Figure 3.2:4 Top two band structures in a metal, a semiconductor and an insulator [20].

In a metal structure, there is no band gap, so the top region has an empty state. When an electric field is applied, the electrons gain energy from the

field and can move easily from the valence band to the conduction band producing an electric current. This implies that a metal structure has a very large free carrier density.

In a semiconductor material such as silicon, the valence band is 1 eV (10^{-19} J) [102] below the conduction band, so an electron can be emitted by a small amount of energy (thermal, photoemission, field or secondary emission) to break its bonds and become an unlocalised free electron. This minimum required amount of energy is called the work function, $e\phi$.

In an insulator material, the valence band is filled and the electrons have no contribution towards the current flow unless it can cross the band gap of magnitude 5×10^{-19} J (~ 5 eV) [102], this is a large gap for an electron to cross without external assistance. This leaves the conduction band in an empty state, which can be seen in Figure 3.2:4.

Every photon that has energy above the band gap energy is absorbed by the p-n junction material. However, photons with lower energy than the band gap energy causes a mismatch between the specific band gap absorption spectrum and the solar spectrum, this leaves the photon not being absorbed, hence its energy not being used.

The photon excites the electron in the valence band and promotes the electron into the conduction band. However, the excited electron quickly loses energy due to the lattice of the material in the form of heat; this process is termed thermalisation. The kinetic energy gained by the thermalised electron is determined by the temperature of the lattice and since

the thermal energy is not used as electrical current, therefore it is a significant loss process.

The excited electron can either be extracted as electrical current or recombined back with the valence hole and give energy in terms of light (luminescence). At this point, no current can be extracted because all the electrons are radiated to the valence band and also the energy of the electron at that point is much lower than that of the excited electron.

Electrical current can only flow if the built-in voltage is lower than the open circuit voltage (V_{OC}) and operating the cell at its maximum efficiency i.e. at its maximum power point (MPP) induces losses which are termed the fill factor (FF) loss, which is attained from the current-voltage characteristics. A typical I-V characteristic of a p-n junction diode is shown in the figure below, which outlines the important points mentioned earlier;

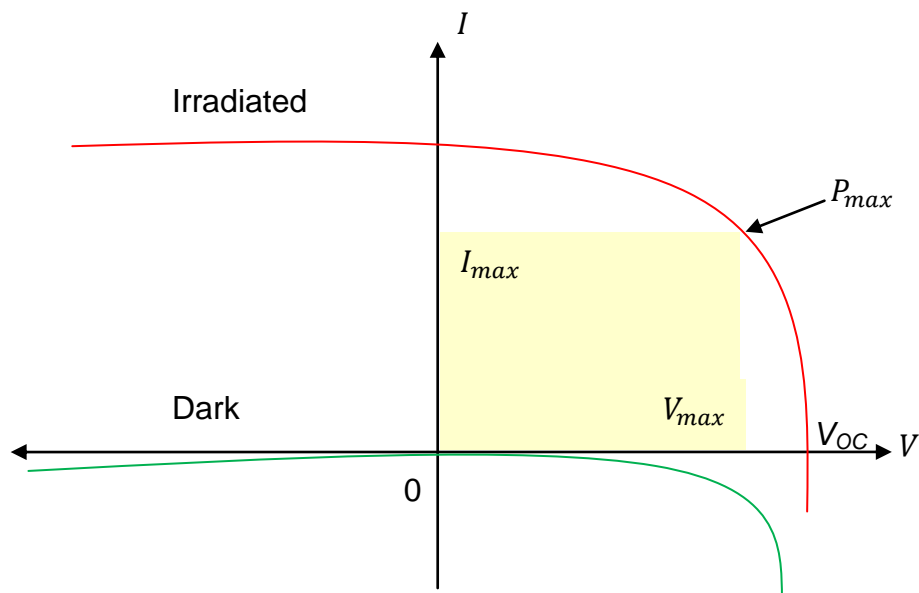


Figure 3.2:5 Current-Voltage characteristic graph of a typical p-n junction solar cell.

There are two ways of applying a voltage (bias) across a p-n junction, either from the p-region to the n-region or vice versa, this is called *forward bias* and *reverse bias* respectively.

In a forward bias arrangement (applying positive bias voltage to the p-region), the charge carriers are pushed to the depletion region and recombined continuously allowing current to flow. In a reverse bias arrangement (applying positive bias voltage to the n-region), the charge carriers are exhausted and the depletion region is polarised and hence, no current can flow, this is shown in Figure 3.2:6.

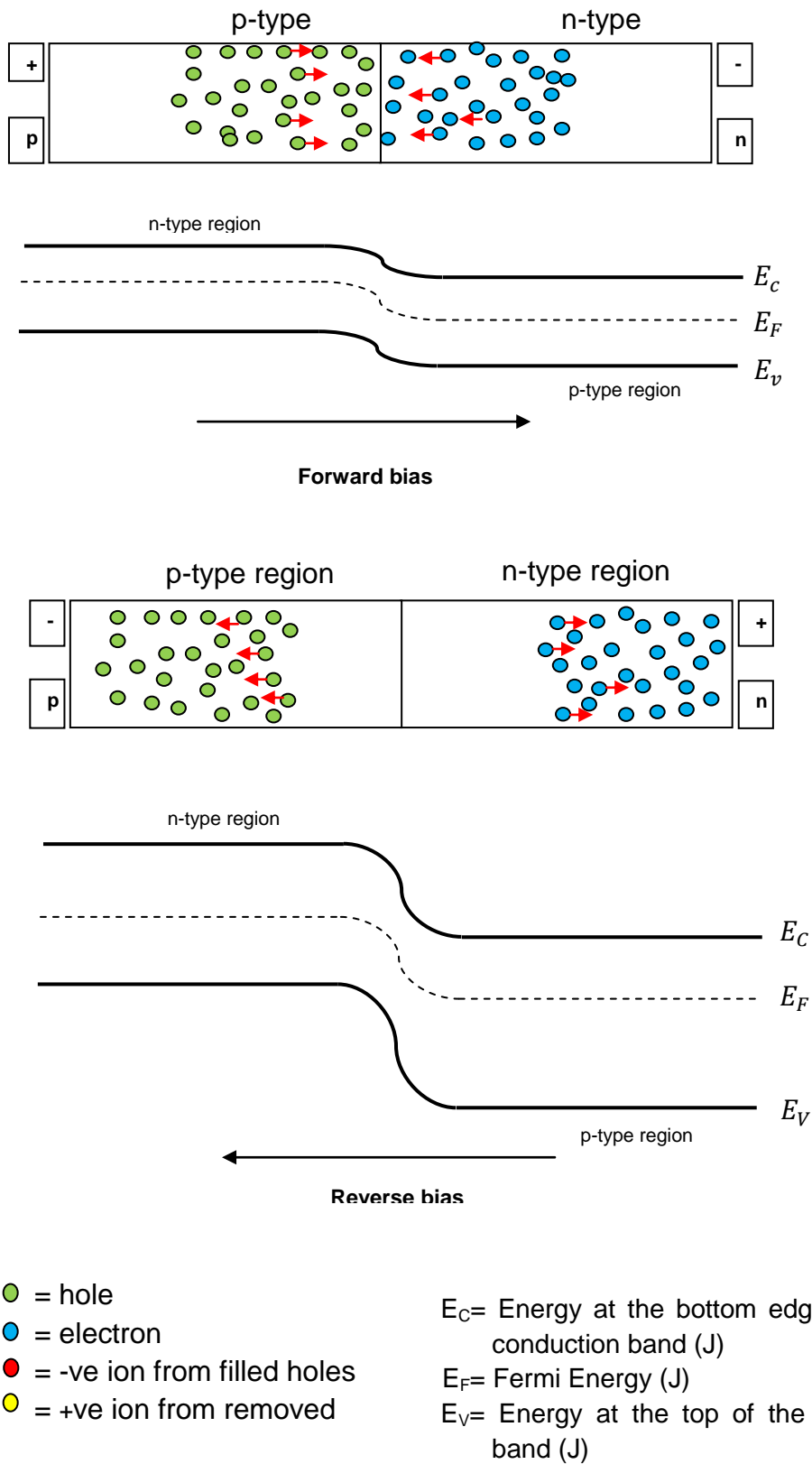


Figure 3.2:6 p-n junction under forward and reverse bias [100].

PHYSICAL VAPOUR DEPOSITION

Physical vapour deposition (PVD) is a generic term given to a group of atomistic deposition processes in which the atoms or molecules of a material are physically vaporised from a liquid or a solid and then transported to the substrate surface via a vapour through a vacuum or a plasma environment. The main categories of PVD processes are vacuum evaporation, sputter deposition and ion plating. PVD process can be used to deposit films of elements, alloys and compounds using reactive deposition processes. PVD processes are used to deposit multilayer thin films, on substrates of different shapes and complexity or in a range of size from very small to very large glass substrates such as 6 m × 3 m architectural glass.

In this chapter, an emphasis on the PVD processes is considered along with characteristics and structural formation of thin films.

4.1 Fundamentals of PVD process

Historically, most solid and ceramic materials were produced by melting and solidification technologies. Surface engineering became a valuable technology for conceiving both surface and bulk properties simultaneously. PVD technologies advanced and new techniques were introduced, which promoted the production of a diversity of materials. This is a key motivation for industrial application such as the energy, microelectronics and optoelectronics, etc [103]. Some of the key and motivation parameters include [104],

- Wide range of coating thickness from few nano meters to tens of micrometers is achievable.
- Multi-layered coatings can be deposited in a single deposition run.
- Layer uniformity and reproducibility of coatings is high.
- Substrate deposition temperature can be between room temperature to 350°C.
- Deposition parameters varied to achieve the desired coating properties.
- The substrates can range in size from very small to very large such as the 18 m² glass panels used for architectural glass.
- Typical PVD deposition rates are 10 to 100 Å (1–10 nm) per second.

In PVD processes, the flux of atoms that forms a coating can be generated from a solid source of the required material (in the form of a target plate or placed in a crucible) using thermal energy (also known as evaporation) or using kinetic energy from ions (known as sputtering). In a reactive deposition process, the coating is formed by the reaction of the coating atoms

(deposition material) with the gaseous environment, e.g. nitrogen or oxygen. The nucleation and growth modes of the condensing thin films determine its microstructure and crystallography.

PVD is the most commonly used deposition process for metals and metal oxide in semiconductor processing by using thermal evaporation energy or kinetic sputtering energy of ions to remove the material from the target/crucible source and transported in the form of a vapour through a vacuum or low-pressure gaseous (plasma) environment to the substrate.

Varying the parameters of a PVD process can have great influence on the properties of the coated surface, this includes;

- Specific resistance
- Temperature of coefficient resistance (TCR)
- Adhesion
- Structure
- Composition
- Density
- Refractive index

Since PVD processes are vacuum processes, it is important to understand the fundamental concept of vacuum physics like pressure and mean-free-path. The pressure can be described as gas particles with concentration, n , per unit volume, mass m , and mean velocity ν , colliding with the container wall [104],

$$P = \frac{nm\nu^2}{3} \quad \text{Eq. 4.1:1}$$

The average velocity of the gas molecule, depend on two factors, the molecular mass, m^* , and the temperature, T . Assuming the particle distribution follows that of Boltzmann distribution (see Figure 4.1:1) [104],

$$v_{ave} = \left[\frac{8kT}{\pi m^*} \right]^{1/2} \quad \text{Eq. 4.1:2}$$

Where, k , is the Boltzmann constant.

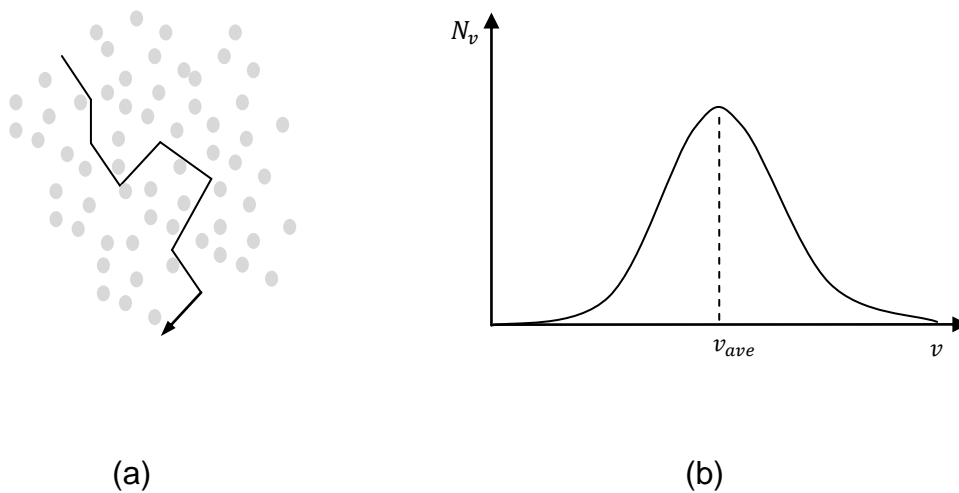


Figure 4.1:1 (a) Pathway of a scattered particle between collisions and (b) Boltzmann distribution of mean particle velocities.

The mean-free-path of molecules between collisions is therefore [104],

$$\lambda = \frac{kT}{\sqrt{2}\pi\sigma^2 N_A P} \quad \text{Eq. 4.1:3}$$

Where, N_A , is Avogadro's number and σ is the collision cross section

It is imperative that the mean free path of the particle to be larger than the distance between the target and the substrate in order to obtain coatings with chemical compositions that closely match the composition of the target. The chemical composition of the deposited coating depends on the purity of the target and the gas type used in the vacuum chamber.

4.2 Vacuum evaporation

Vacuum evaporation is a PVD process, which works by the principle of thermal vaporisation of the source material in a vacuum environment until a sufficient vapour pressure for net evaporation of the source material has reached. The vaporised material reaches the substrate in a line-of-sight configuration with little or no collision with gas molecules in the space between the source material and the substrate. The vacuum chamber is evacuated to a typical pressure of 10^{-2} to 10^{-4} Pa in order to create a large mean-free-path bigger than 5 m [105], for the vapour particles to prevent reaction of the source material with the residual gas and prevent contamination from the deposition system [106].

The key feature of this process is that the source material is heated to very high temperatures using a heated source such as resistive heater or e-beam evaporation gun, while the substrate temperature can be freely changed in order to influence the structure of the coating. The resistive heater is usually tungsten wire wrapped around a ceramic ingot. The drawback of using a resistive heater of the vapour source is the evaporation of the actual heater, which can lead to contamination in the coating. In addition, this process does not allow for the evaporation of high melting temperature materials such *W*, *Mo* and *Ta*. To ensure an even coating, the substrate holder is moved in a concentric motion to ensure constant layer thickness is achieved across the substrate.

The e-beam is used to achieve efficient local heating of the source material. Typical deposition rates vary from 100 nm/min to 5 μ m/min [107]. The core

parameter to achieve good coatings is to keep the residual gas pressure approximately 10^{-2} Pa in order to stop any collisions between the vaporised particles and the gas particles. The evaporation rate is controlled by varying the electron density of the e-beam. The disadvantage of using e-beam is the ability to bubble the source material, which can lead to the danger of splattering of the source material onto the substrate surface [107].

The vacuum evaporation process is generally used for the deposition of metallic coatings. However, it is also possible for deposition in reactive and non- reactive atmospheres of alloys, ceramics and chemical compounds. Alloys are difficult to evaporate because not all elements have the same evaporation temperature. This makes other PVD techniques such as sputtering, a more favourable technique for alloy deposition. The evaporation of chemical compound can produce dissociation (i.e. the breaking of the chemical compound to simpler components); therefore sputtering can be a better PVD process to use. Reactive evaporation is possible via the use of reactive gas such as oxygen or nitrogen, which can lead to metal oxide or nitrides. Sputtering can provide better process control and is therefore often used in preference [104].

The vacuum deposition process is used to form a variety of coatings such as; mirror coatings, decorative coatings, packaging materials, wear resistant coatings, corrosion resistive coatings, etc [106].

In order to improve the structure and properties of the coatings, energetic bombardment from a glow discharge plasma is used. As mentioned earlier, ion plating and sputtering are other forms of PVD processes, but it is

important to describe in the next section the glow discharge plasma more clearly in order to give better understanding for the reader.

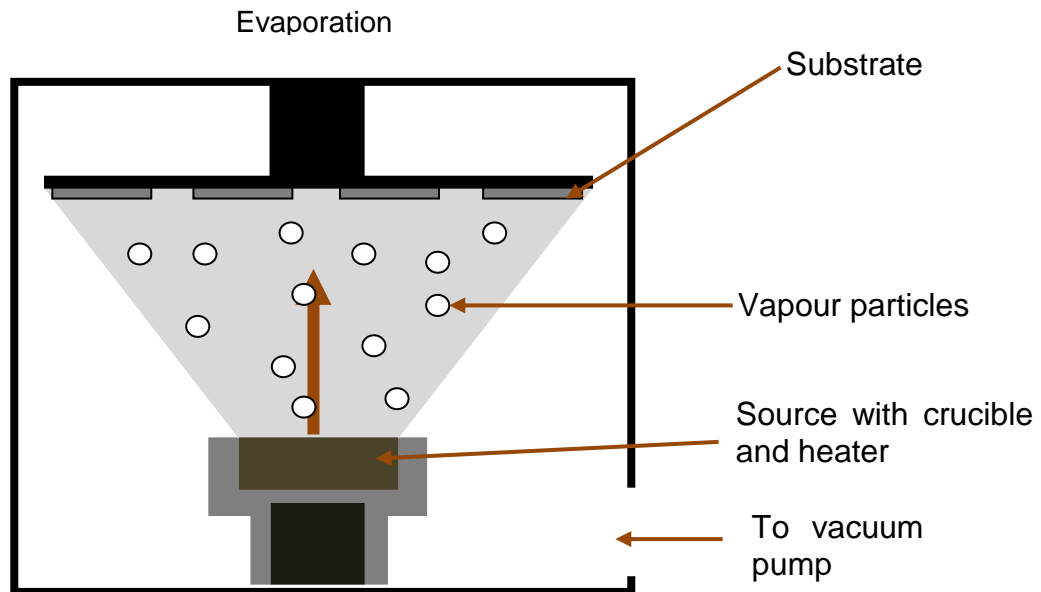


Figure 4.2:1 Schematic representation of vacuum evaporation system [104].

4.3 Glow discharge plasma

The term plasma is defined as a partially ionised gas, which contains ions, electrons and atoms that is produced by applying an external electric field [108]. Gas discharges were studied over a century ago by Irvine Langmuir as a result of developing a small area plasma probe [109]. Traditionally discharges were utilised in switching equipment such as gas valves and lighting.

Glow discharge plasma utilised in deposition processes consists of a low pressure (typically in the range of 0.1 to 70 pa) partially ionised gas that contains the same number of electrons as the number of ions, also referred to as quasineutral [110]. The kinetic energy transfer between the electron and

the heavy particles such as an ion or an atom or even a molecule during an elastic collision is proportional to the mass difference between the electrons and the heavy particles, therefore it is attributed to have a small value (10^{-5}) [111].

At low-pressure atmospheres, the electrons can gain high kinetic energy to have a high probability to produce sufficient ionisation or excitation during the collision with other heavy particles. The production of these excited species and their interaction on the growth of the deposited film has made glow discharge plasma treatments become the main process in material processing. A few examples of systems that employ glow discharge plasma include; sputter deposition, Ion plating and plasma assisted chemical vapour deposition.

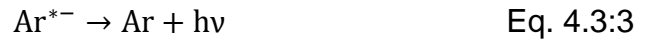
The discharge in a deposition system, such as magnetron system is created by applying a negative voltage to the magnetron target, which is in a vacuum chamber backfilled with a low pressure of discharge gas such as argon. This causes electrons that are close to the target surface to accelerate away from the surface, causing the electron to have sufficient kinetic energy to ionise the gas atoms. This can be described by the equation below;



Collisions of particles with insufficient energy for ionisation will cause the gas atoms to release energy in terms of light (emitting a photon), this gives the characteristic glow of the discharge plasma, as can be seen from the equation below;



This leads to;



The process of ionisation and the glowing of the plasma are visualised in the following Figure 4.3:1 and Figure 4.3:2.

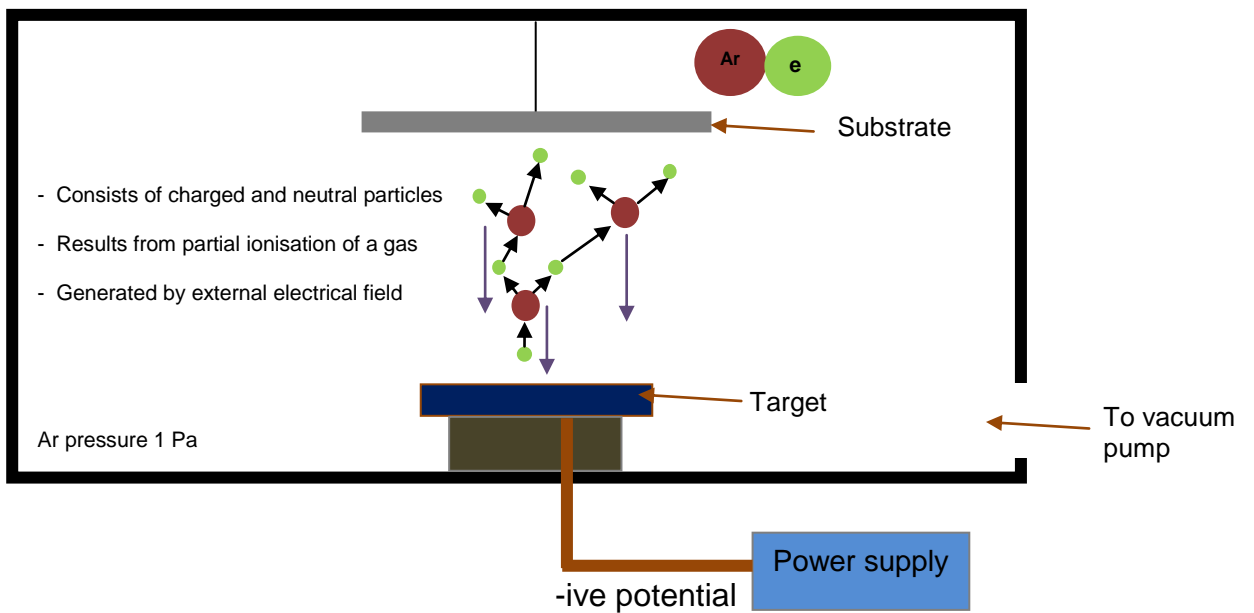


Figure 4.3:1 Schematic representation of ionisation and formation of the glow discharge plasma

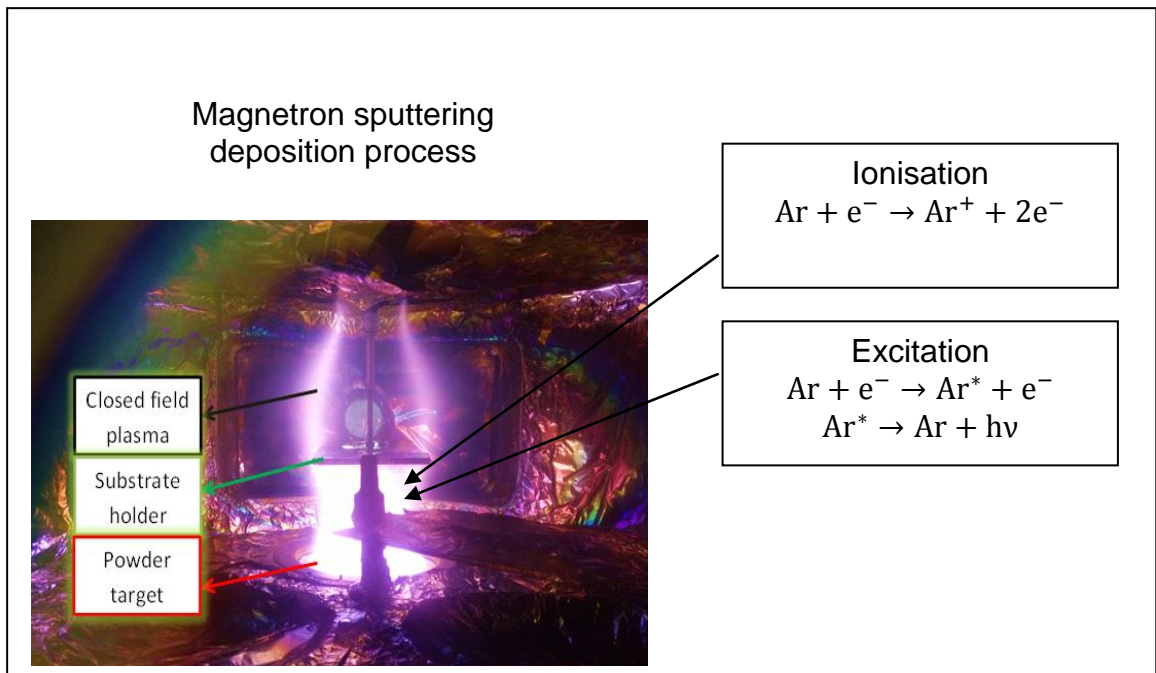


Figure 4.3:2 Formation of visible glow discharge plasma in an magnetron sputtering process.

In a low pressure plasma (0.1 Pa), the mean free path of the electron is high. This allows the electron to obtain high kinetic energy as it travels for longer periods of time, so the collisions between the electron and the gas particles are not sufficient to allow thermal equilibrium to be established so the temperature $T_{electron} \gg T_{ion} \gg T_{gas}$, this type of plasma is referred to as a *cold plasma* [110].

In a high pressure plasma, thermal equilibrium is achieved as the rate of the collisions between electrons and ions is increased. This type of plasma is referred to as a *hot plasma* where $T_{electron} \approx T_{gas}$ [110].

Glow discharge plasmas are utilised in many PVD technologies including DC sputtering, RF sputtering and ion plating. During a plasma discharge, three regions can be identified;

- Townsend discharge
- Breakdown discharge
- Glow discharge

At low voltage, the electrical field generated is very low, due to the low amount of current being drawn. The electrons will have no energy to cause ionisation of the gas particles, hence few ions will be present, this is termed the *Townsend discharge*.

As the voltage is further increased, the electrons gain sufficient energy to cause ionisation of the gas particles, which increases the current. This region is termed the *breakdown discharge*. Further increase in the voltage creates more charged particles (positive ions) which will have enough kinetic energy to strike the cathode surface and as a result, more secondary electrons are emitted away from the cathode surface and collide with other gas particles, as a result, a self-sustaining discharge is created.

By further increasing the voltage, the bombardment of the ions will cover the whole cathode surface and the current intensity becomes uniform at constant pressure. This region is termed *abnormal glow discharge*, which is the point at which sputtering is normally carried out. As the voltage is further increased, more ions collide with the cathode surface and a layer of ions will cover the surface and breakdown can occur in the form of an arc.

4.4 Ion plating

Ion plating is another group of PVD process in which the discharge is carried out in a mixture of the evaporated flux and an inert working gas (usually argon) pressure in the range of 0.1-1 Pa, with the substrate holder biased negatively relative to the plasma potential in order to sustain the plasma discharge. The glow discharge plasma is kept close to the surface of the substrate by applying a high negative potential (-2 to 5 kV) to the substrate holder using either a DC or RF power supply. The high energetic ions from the discharge bombard the surface prior and during the deposition [112].

The source material is vaporised in the similar way to the vacuum evaporation process, however, the evaporated atoms pass through the plasma discharge and get ionised from the plasma and bombard the surface at higher energies. Prior to deposition, the substrate surface is bombarded by high-energy gas ions which sputter away any impurities on an atomic scale, which can then improve the adhesion and lower impurity content of the films onto the substrate. However, the disadvantage of ion bombardment is that it can decrease the deposition rate as some of the deposited particles are sputtered off, it can also cause the increase in the substrate temperature due to the high energetic ion bombardment, which is undesired for applications such as microelectronics components [112]. A schematic representation of the ion plating process is shown in Figure 4.4:1.

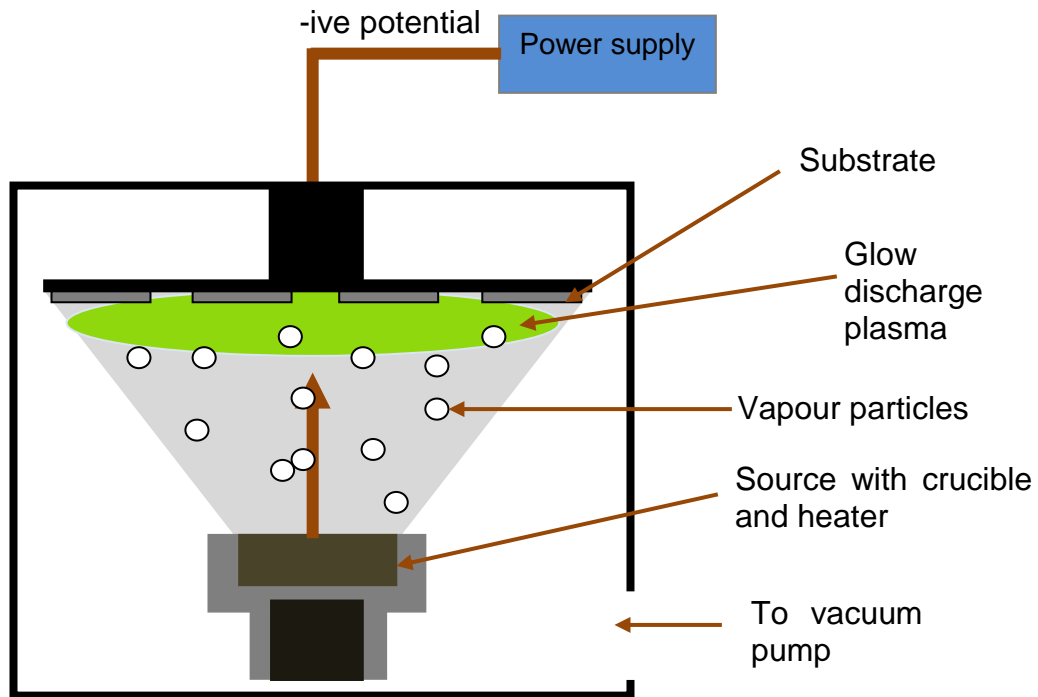


Figure 4.4:1 Schematic representation of an ion plating process [112].

4.5 Sputter deposition process

Sputtering is plasma based PVD process in which noble gas ions such as argon (Ar^+) are attracted towards the target surface and cause the removal of particles from the target surface. The removed particles then travel through the plasma and collide with the gas atoms. This results in their arrival of the substrate surface from various directions where they condense to form a coating. The condensation rate of the sputtered particles at any sputtering power is controlled by the target-substrate distance. The average distance between the target and the substrate is typically 5-35 cm [104].

In a typical sputtering process, the chamber is evacuated to a high vacuum, (typically 10^{-3} Pa) and backfilled by inert gas such as argon to 1 Pa of pressure. The gas atoms are then partially ionised by the electric discharge

and are ready to bombard the target surface. A schematic representation for the propagation momentum and particle movement of the Ar ion hitting the target surface is shown in Figure 4.5:1.

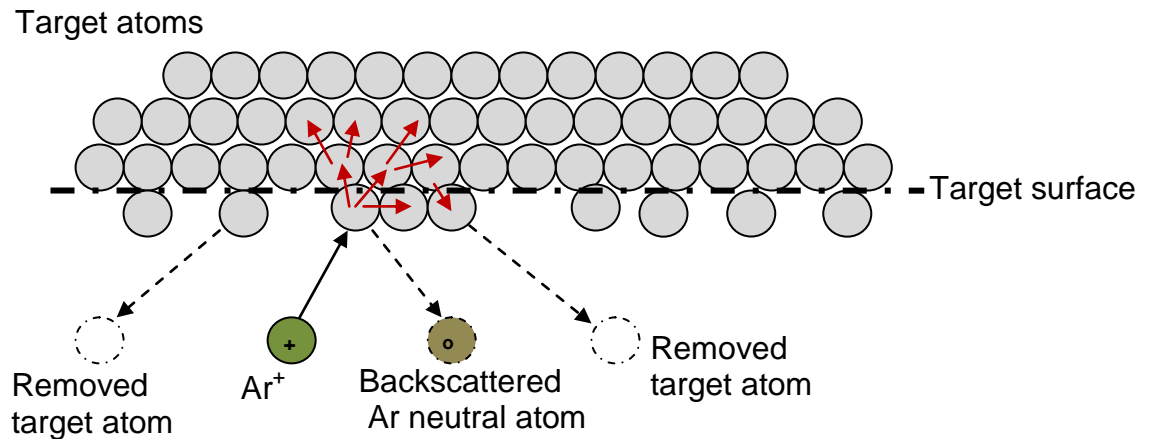


Figure 4.5:1 Schematic representation for the propagation momentum and particle movement of the Ar ion hitting the target surface.

Sputtering equipment is widely available for the different sputtering processes. Ion beam sputtering ablates the material from the target using an ion beam, which then condense onto the substrate surface. Glow discharge plasma sputtering is the most commonly used from the sputtering processes systems. The most common system used in plasma sputtering is either DC sputtering or RF sputtering [104]. In a DC system, the target holder is generally cooled using a water cooling facility in order to minimise radiant heat from the target surface and also to prevent any diffusion which could change the composition in the target surface when alloy targets are used. This can act as an advantage over the thermal evaporation process [106].

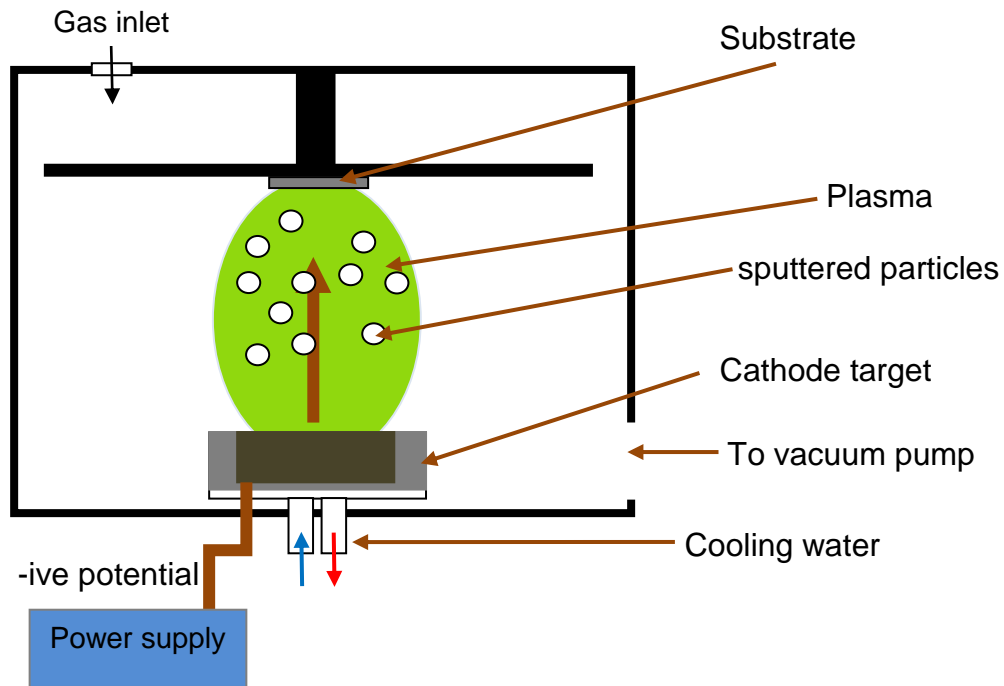


Figure 4.5:2 Schematic of DC-sputtering system

4.5.1 Magnetron sputtering deposition

Magnetron sputtering is a technique, which has evolved over the past 3-4 decades to an industrial standard used to deposit commercially important coatings. The main advantages offered by this technique are the high quality of the coatings produced and the versatility of the technique, compared to other PVD techniques. Magnetron sputtering has a great impact on manufacturing areas including [108],

- Decorative coatings
- Wear-resistant coatings
- Corrosion-resistant coatings
- Low friction coatings
- Optical and electrical coatings

As in a conventional sputtering system, in a typical magnetron configuration, the pressure in the vacuum chamber is reduced to typically 10^{-4} Pa after which argon gas (typically 0.2 Pa) is introduced into the chamber. Discharge plasma is induced by applying a negative voltage (typically 200 V to 1 kV) to the target. The primary electrons found close to the target are accelerated away from the negatively charged target. When the applied target voltage is large enough, the electrons gain enough energy to begin to ionise the argon neutrals, which are then accelerated to a negatively biased target plate causing the bombardment and the sputtering of atoms from target surface, which condense as a thin film on a substrate surface. The bombardment of the target by the ions also causes the ejection of secondary electrons from the target surface into the dense plasma, which is important in maintaining the plasma. The number of electrons that are emitted per incoming ion is called *secondary electron emission yield*, γ_{see} . This parameter depends greatly on the condition of the target surface and on the ion energy. These secondary electrons are again repelled away from the target surface and may also ionise the argon atom. One ion creates enough secondary electrons to ensure one ionisation, the discharge achieves a breakdown and it becomes self-sustaining. Some of the electrons do not have the sufficient energy to create argon ions, because the transferred energy is less than the ionisation energy, however, the argon neutral do get excited, but then lose their energy and go back to their ground state by emitting a photon, which is observed during a typical glow discharge of a plasma.

The initial sputtering process was limited by its low deposition rate, high substrate heating temperature and low ionisation efficiency in the plasma

[113]. These limitations were overcome with the development of the magnetron configuration and later the unbalanced magnetron configuration in the late 1980s and its further improvement in the 1990s into a multi-source closed-field system [85].

The magnetic field in a magnetron is, therefore, employed in order to increase the deposition rate, this is done by configuring the magnets in such a way that one pole is placed in the centre of the target axis and the other pole is formed by placing other magnets around the outer edge of the target in a ring shape. By employing such a configuration, provides a magnetic field, B , which is applied to the discharge in addition to the electric field, E , the secondary electrons are trapped near the target surface and are governed by the Lorentz force, F .

$$F = q(v \times B) \quad \text{Eq. 4.5:1}$$

Where, q , and, v , are the electron charge and velocity respectively and, B , is the magnetic strength of the magnetic field. If the force (electric field) applied on the charge particle is perpendicular to a magnetic field, the charged particle will change its path to that around the magnetic field line. The orbit radius of the charge particle can be determined by,

$$R = mv_{\perp}/qB \quad \text{Eq. 4.5:2}$$

Where, m , is the mass of the charged particle, v_{\perp} , is the component of the velocity that is perpendicular to the magnetic field. It can be observed from the above equation, that heavy charged particles have a larger circular radius orbit. Therefore, a magnetic field can significantly influence the charged particle within a plasma and the degree of the influence is governed by the

mass of the charged particle. In a plasma atmosphere, the effect of the electron is normally considered, and the ion ignored.

The electric field causes the electrons to travel in the direction perpendicular to both the magnetic and the electric field, this is called the $\mathbf{E} \times \mathbf{B}$ or Hall drift. The combination of the Hall drift and confinement of the electron significantly increases the mean free path of the electron in comparison to other conventional glow discharges. This increases the probability of an electron to atom collision, hence, increasing the ionisation efficiency. The result is a dense plasma and high sputtering rate at the target and high deposition rate at the substrate region.

In a typical magnetron configuration, the magnets are placed beneath the target in a north-south polarity arrangement in a balanced array (explained in the next section) and the field lines travel from the north to the south pole through the target to form a closed loop region. This configuration forces the electron to spiral along the magnetic field lines very close to the target surface and undergo many collisions before being lost to ground. The secondary electrons produced from the target are attracted by the field lines and confined close to target surface. This increases the ionisation rate in the plasma and creates a dense plasma in front of the target surface. This allows for more ions from the plasma to bombard the target surface with full discharge potential.

The implementation of magnets allow for sputtering and deposition at lower discharge voltages (-200 to -1000 V) in comparison to basic sputtering (-3000 V). Also reduced pressure of up to 100 times less in comparison to basic

sputtering allows for the sputtered species to have very little gas scatter, therefore increasing the deposition rate and increasing the coating flux and energy of the sputtered species [114].

The dense plasma of a conventional magnetron system is located very close to the target surface (60 mm). If the substrate is not located within the short distance, then the growing coating cannot benefit from the ion bombardment, which is proven to improve the physical and chemical properties of the grown coating [115]. This problem was tackled by the use of unbalanced magnetrons, which is explained in the next section.

4.5.2 Unbalanced magnetron sputtering

Window and Savvides were the first in appreciating the effect of altering the magnetic field in a conventional magnetron system. They managed to change the balanced magnetic array to the unbalanced magnetic array.

In a conventional balanced magnetron, the strength of the inner and the outer arrays are approximately equal and the magnetic flux is closely confined to the target region; this is termed 'balanced' magnetic array.

The design of the Window and Savvides was based on increasing the magnetic strength of either the inner array or the outer array and therefore the magnetic flux was no longer confined near the target region. This new design was termed an unbalanced array. Window and Savvides proposed two types of systems and termed them Type-I and Type-II [116]. Figure 4.5:3 outlines the differences in the balanced system and the unbalanced Type-I and Type-II systems.

In a typical Type-I system, the inner or central pole is made stronger than the outer pole which can be seen in Figure 4.5:3. This allows the plasma density to decrease near to the substrate region, as some of the magnetic field lines do not close in on themselves. As a results, the plasma flux travel to the chamber walls, giving a low ion current at the substrate.

In an unbalanced magnetron, the Type-II configuration is typically used, this can be seen in Figure 4.5:3, whereby, strong magnets are utilised on the outer side, which forces the plasma to expand away from the target surface towards the substrate surface. This will trap the secondary electrons that have escaped from the target surface and will eventually collide with the neutral gas atoms causing an ionisation effect to take place. The collision increases the number of ions and electrons in the region near the substrate. The increase in the plasma density near to the substrate will cause an ion current to be transported to the substrate surface without the need for biasing the substrate (referred to as self-biasing).

Unbalanced magnetrons have been routinely used by researchers and it was possible to produce substrate ion currents of 5 mA cm^{-2} , this is an order of magnitude higher than conventional magnetrons [117]. It was also found that the ion current produced is directly proportional to the target current and also directly proportional to the deposition rate, meaning constant ion-to-atom ratio [118]. A schematic representation of the plasma in conventional and unbalanced magnetrons is shown in Figure 4.5:3.

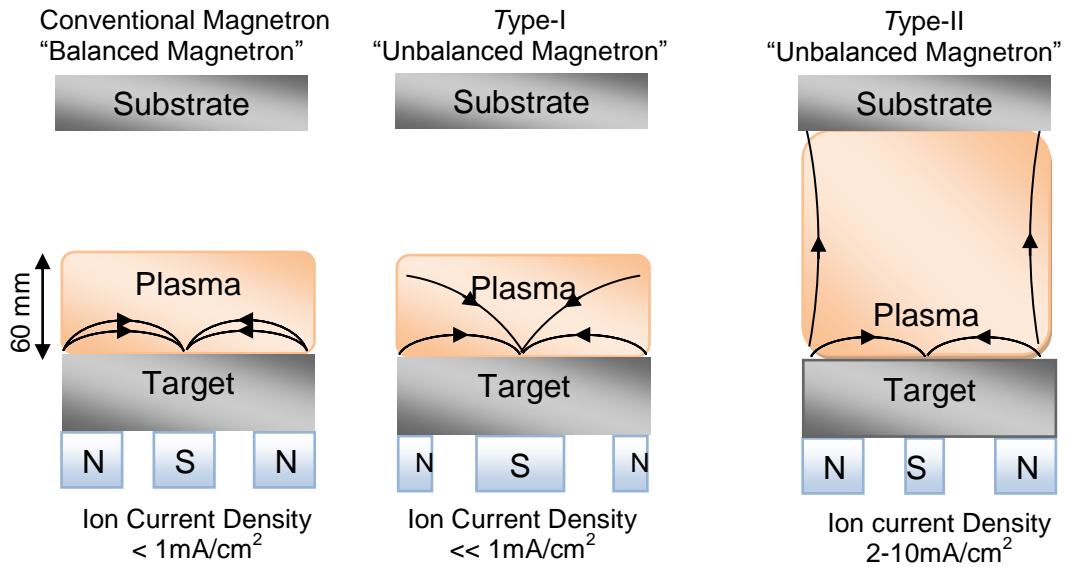


Figure 4.5:3 Representation of plasma in unbalanced and conventional magnetrons [85].

4.5.3 Closed-field unbalanced magnetron sputtering

To coat complex components, multiple magnetrons are required and any two magnetrons can be arranged in two different ways – same magnetic polarity (known as the mirrored configuration) or opposite polarity (known as the closed field configuration). Closed field unbalanced magnetron systems consist of multiple cascaded magnetrons, that consist of strong magnets which are configured to have opposite magnetic polarity to the neighbouring magnetrons. This design was introduced to overcome the problem of uniformly coating complex designs, which the single unbalanced magnetrons did not provide. The configuration can be seen from Figure 4.5:4. The mirrored configuration provide a weak plasma flux because secondary electrons are directed more towards the chamber walls hence providing a lower plasma density at the substrate.

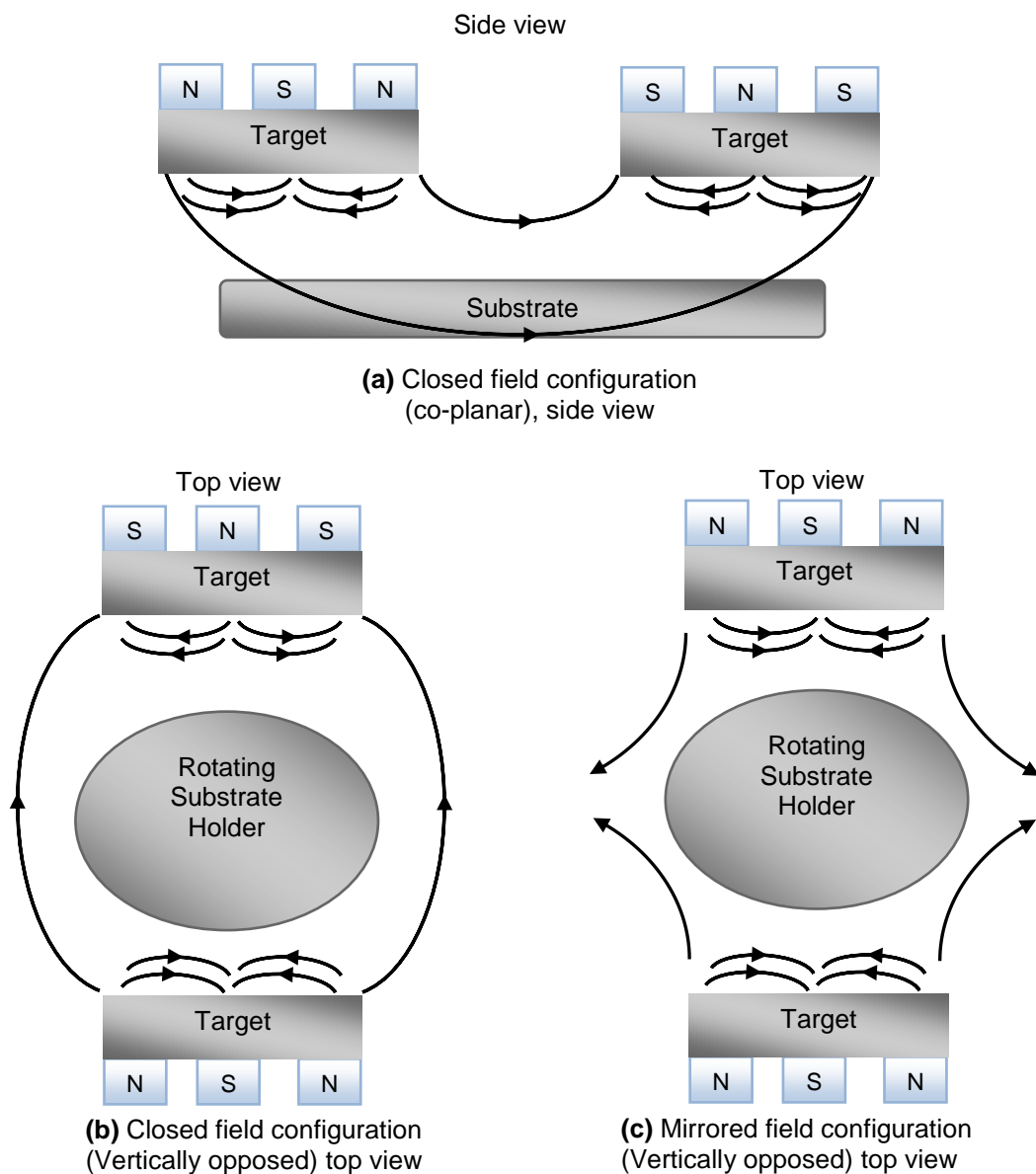


Figure 4.5:4 Dual magnetron configurations [85]

In the closed field arrangements, the field lines are closed due to the opposite polarity configurations, hence the secondary electrons are trapped within the plasma flux and this provides a higher plasma density near the substrate region, hence increasing the ion current drawn at the substrate. A study was carried by Kelly et al and it was shown that using the closed field configuration

provided an ion-to-atom ratio of 2 to 3 times greater than using the mirrored configuration [117].

The use of such multiple design configurations was first recognised by Teer Coatings Ltd in the early 1990s and were able to patent this configuration for commercial use [119].

With advancement in the design concept of closed field magnetrons, the use of rare-earth magnets (magnetic strength of up to 1 kilo Gauss) instead of the conventional ferrite magnets (with a magnetic strength of 300 to 500 Gauss) has been utilised. The change in the magnetic strength produced an improvement in the ion current density at the substrate surface, this was investigated by measuring the current-voltage characteristic of different Teer Coating magnetrons systems, which was presented by Kelly et al [85].

In this project, a closed field unbalanced magnetron sputtering system was used. The magnetic field of the system used was measured with a Gauss probe. The circular magnetron was unbalanced with the strength of the outer north ring stronger than that of the inner south pole. A dummy magnetron containing only the outer ring of south magnets was installed directly above the unbalanced magnetron to form closed magnetic field lines between the unbalanced magnetron and the substrate holder. High strength rare earth magnets were used for both magnetrons with a magnetic strength of 1.5 kG measured at 1cm above the copper housing of the magnets. The schematic layout of the unbalanced closed field magnetron system used in this project is shown along with the magnetron configuration in Figure 4.5:6 (a) and (b).

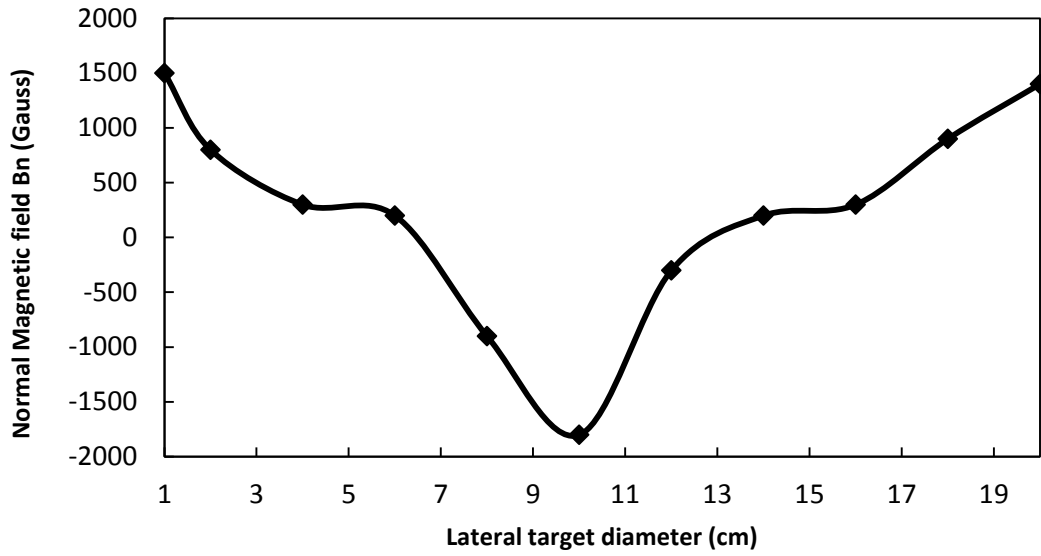
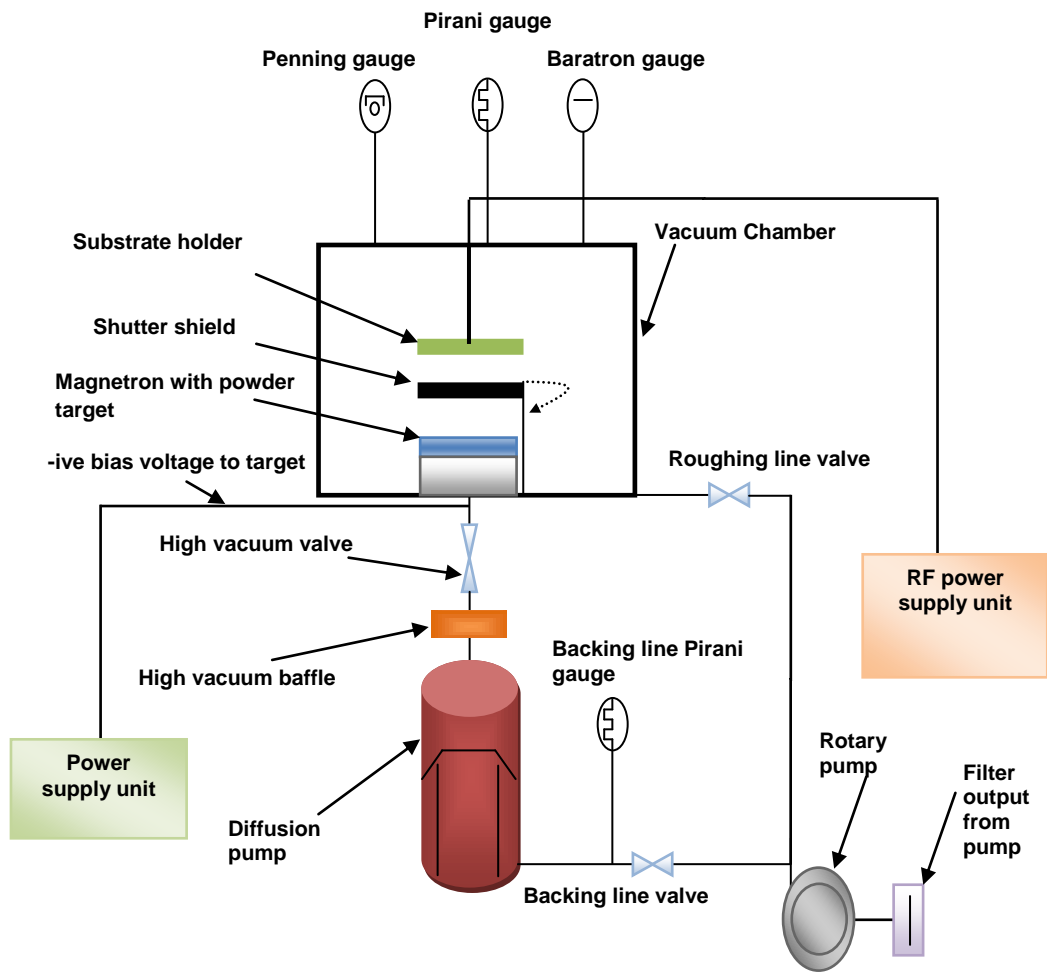
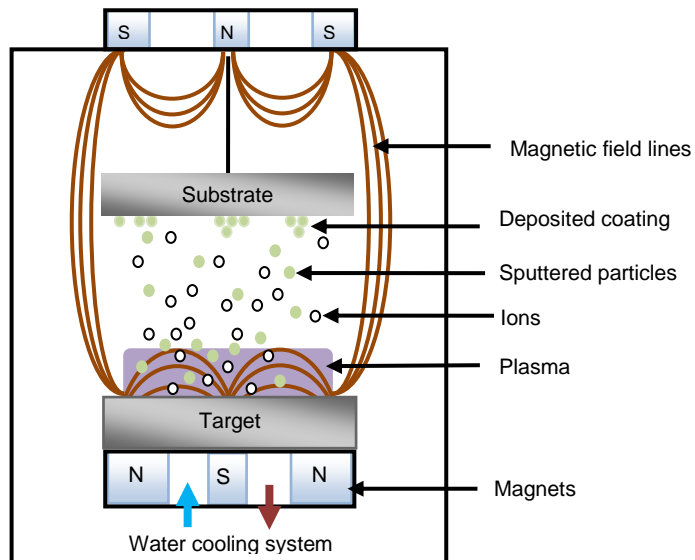


Figure 4.5:5 Measured magnetic field B_n , at 1 cm from the above the copper backing plate surface.



(a)



(b)

Figure 4.5:6 (a) typical configuration of a complete magnetron sputtering system (b) typical discharge in a magnetron sputtering system.

4.6 Reactive sputter deposition

Reactive sputter deposition is the physical sputtering of a metal, compound or alloy in a mixture of a reactive gas atmosphere in order to deposit a compound coating that is composed of the sputtered material and the reactive gas. The target can be of a pure metal (or metal alloy) or powder form target.

The advantages of using reactive sputtering are (i) insulating materials can be deposited via DC or Pulsed DC power supplies, (ii) possibility to use easy to fabricate targets to sputter compounds, (iii) films with sub-stoichiometry can be deposited. However, the relationship between the film properties and the gas injection rate is non-linear [113]. This is because the sticking probability of the reactive gas species onto the coating depends on many factors including the growth rate, target composition and temperature of deposition [120]. Other factors such as controlling the gas injection rate when chemical reactions

occur at the target surface, or at the substrate surface in order for reactive sputtering to be effectively used on a production basis [120].

A typical reactive sputter deposition system can be composed of a pure metal target such as Ti or Al or Sn sputtered in an inert gas such as Ar with typical pressure of 0.1-10 Pa, this yields a metallic coating. By introducing a reactive gas such as O or N, the reactive species will combine with the target atoms to form a compound coating. The partial pressure of the reactive gas will govern the reactivity of the species, so the coatings stoichiometry is controlled by the reactive gas partial pressure. However, high levels of the reactive gas species will introduce the formation of compounds on the target surface. This compound formation will persist as the reactive gas partial pressure is reduced until the metal target surface is exposed via the physical sputtering, this phenomena is known as the hysteresis effect.

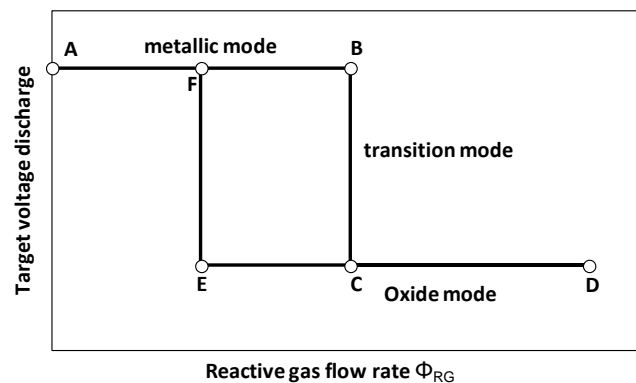
The hysteresis behaviour can be graphically represented, by monitoring the discharge voltage at the target and the partial pressure of the reactive gas during the discharge, as a function of the reactive gas flow. The discharge voltage is the most obvious parameter to measure because it is closely related to the target surface condition.

A schematic illustration of typical hysteresis behaviour for a reactive magnetron sputtering is shown in Figure 4.6:1. There are three modes that can be observed in a hysteresis modes, (1) metallic, (2) transition and (3) oxide, also referred to as poisoned. When the target is sputtered in pure argon mode, there is a constant flux of material being deposited on the substrate. At low partial flow of the reactive gas (interval A-B), no influence is

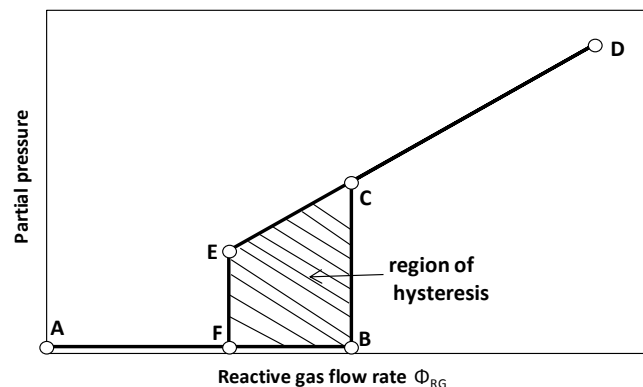
observed on the discharge voltage nor on the partial pressure, due to the reactive gas being gettered by the sputtered metal, i.e. the reactive gas introduced to the chamber is mainly absorbed by the deposited material. At point B the partial pressure of the reactive gas is equal to the gettering rate of the sputtered metal. A further increase in the reactive gas results in a critical point where a sudden change is observed: (1) increase in the chamber pressure, (2) a change in the target voltage, depending on the secondary electron coefficient of the target material. A further increase in the reactive gas flow (interval C-D) corresponds to a linear increase in the chamber pressure and a relatively constant value in the target voltage. Such behaviour is typical in the reactive mode of sputtering. As the reactive gas flow is step increased, it crosses a critical point of which there is not enough deposited material to react and consume the reactive gas. The excess reactive gas reacts with the target surface and forms a compound layer and raises the partial pressure. The formed compound layer will have different secondary electron emission rate and is more than likely to cause a change in the discharge voltage. With any further increase in the reactive gas flow, the chamber pressure increases linearly, as it is not possible to consume more oxygen in the deposition process. As the flow of the reactive gas is reduced again (interval D-E), the chamber pressure is also observed to decrease, but the return to a metallic mode (interval E-C) is delayed. This is because the chamber pressure remains high until the compound layer on the surface of the sputtered target is fully removed (point F). This results in the increase in the consumption of the reactive gas and the partial pressure of the reactive gas decreases to a background level. Further increase in the oxygen gas flow

will shift the metallic mode critical point to a poisoned mode as now only the compound material formed on the target surface is sputtered.

Another factor influenced by the change in the reactive gas flow is the sputter yield. As the sputter yield of a metallic material is higher than that of a compound material. The transition between a metallic to a poisoned mode drastically reduces the deposition rate due to the formation of an oxide layer on top of the metallic surface. The drastic drop in the deposition rate lowers the critical point to which metallic mode occurs during the decrease of the reactive gas flow rate. As the reactive gas flow is further reduced, the compound layer is then sputtered away and the metallic surface is exposed.



(a)



(b)

Figure 4.6:1 Hysteresis characteristics of the discharge voltage (top) and the total pressure (bottom) as a function of the reactive gas flow.

4.7 Plasma characteristics

In a glow discharge plasma, the electrons have a tendency to reach the plasma boundaries quicker than the heavier particles (ions). This is because the mass of the electron m is lighter than the mass of the ion, M , ($m/M \ll 1$) and therefore the thermal velocity $(eT_e/m)^{1/2}$ of the electron is 100 times the magnitude of the ion thermal velocity $(eT_e/M)^{1/2}$ [121]. This results in the plasma gaining a higher positive charge, which then restricts the losses of any more electrons. This leads to a stable state to which the loss rate of electrons is the same as the loss rate of ions. This leads to a plasma characteristic termed *quasi-neutral* ($n_i \approx n_e$). When the plasma bulk is quasi-neutral, the plasma boundaries (sheaths) appear where the plasma meet a solid surface such as a chamber walls, electrodes, substrate or probes. The actual structure of the sheath is greatly dependent on the potential difference between the solid surface and the plasma potential. Figure 4.7:1 describes the electric potential, Φ , of a DC diode set-up of a bulk plasma with length, l , at which $n_i = n_e$ that is confined in between a cathode and a grounded wall. Where, n_e , is defined as the amount of free electrons (that are not bound to an atom) available per a given volume, measured in cm^{-3} and, n_i , is the amount of available ions per given volume. Since the ion density, n_i , is equal to the electron density, n_e , the net charge density $\rho = e(n_i - n_e)$ is equal to zero, where, e , is the un-signed charge on an electron (1.602×10^{-19} C) and the electric potential and electrical field, E_x , is zero in all the region This is the floating potential, V_f , which occurs at a negative potential of -20 to -30 V in magnetron systems. Because the fast moving electrons are not confined, they are quickly lost to the surrounding walls, this is illustrated in Figure 4.7:1.

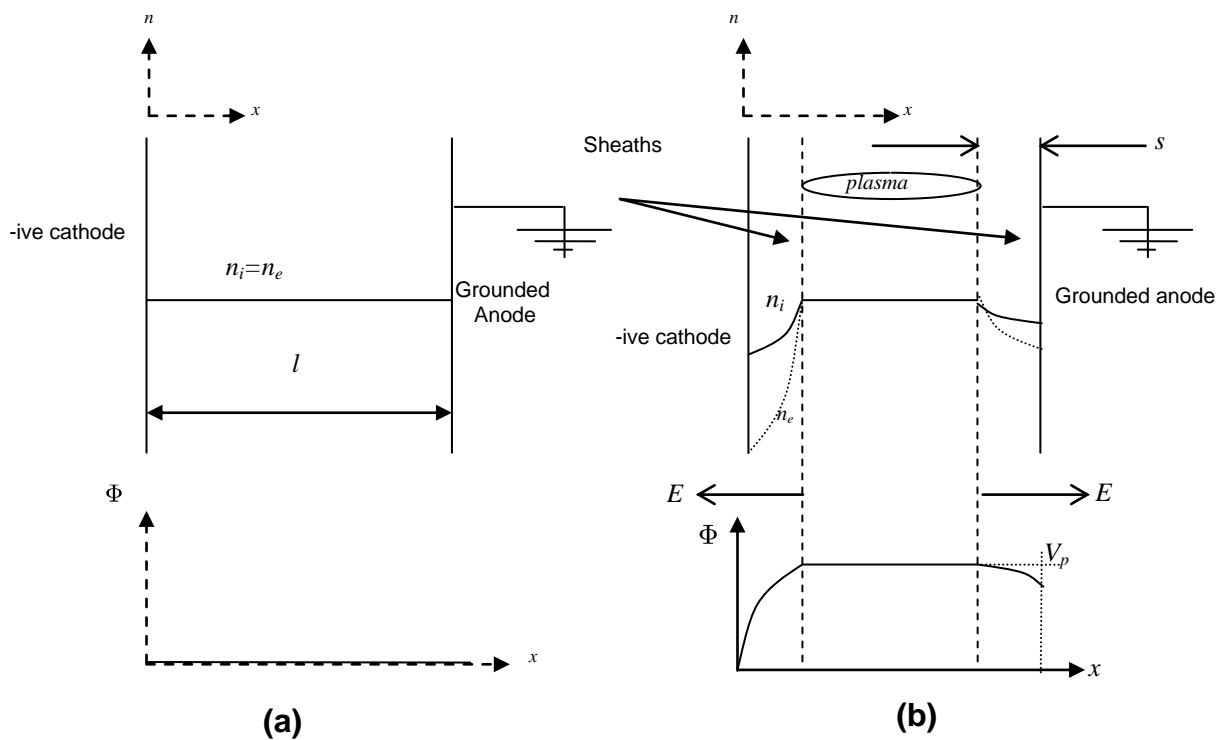


Figure 4.7:1 The formation of the plasma sheath during (a) initial n_i and n_e and electric potential, (b) densities (n_i , n_e) electric field and potential during post formation of sheath [121].

However, after a short timescale, some electrons near the walls are lost, leading to a mismatch between the ion to electron densities $n_i \gg n_e$. This leads to the formation of a thin positive ion sheath near each wall, this is graphically represented in Figure 4.7:1 (b). This forms a positive net charge density leading to positive potential, Φ_x , within the confined plasma and a sharp fall near the grounded anode. The ions from the plasma that enter the sheath are quickly accelerated to the walls. Conversely, the electrons in the plasma are confined and kept from entering the sheath, as the electric field within the sheaths is directed from the plasma to the walls. Therefore, the force acting on the electrons is directed towards the plasma, thus, reflecting any electrons

travelling to the walls back to the plasma. In order to confine most of the electrons within the plasma, the plasma potential must be high enough to keep the lost rate of the ions the same as that of electrons [121].

The plasma potential is measured by inserting a metal probe that is biased negatively or positively into the discharge, to draw electron or ion current. This technique is one of the oldest and still used tool to diagnose the plasma. These probes were introduced in 1926 by Langmuir and were extensively used by Mott-smith and Langmuir and are usually called the Langmuir probes. A typical current-voltage plot is shown in Figure 4.7:2 [122]. The probe is biased to a certain voltage, V_B , with respect to ground and the plasma is at a potential, Φ_p , with same ground reference. As the, V_B , increases in the positive direction, and becomes equal to the plasma potential, Φ_p , the ratio of the different charge species changes from the ion saturation to the electron saturation, which is associated with the positive current flowing from the probe into the plasma. As the bias voltage across the probe is increased above the plasma potential, the current saturates at the electron saturation current. The point where the current net flow is zero, is called the floating potential, Φ_f . In a magnetron sputtering system, the floating potential is of a negative bias, usually between -20 to -30 V. If the bias voltage is more negative, the plasma potential $V_B < \Phi_p$, the current is increasingly ion current, which saturates depending on the probe collection area of the probe. It is worth to note that the saturation of the ion current is much smaller than the saturation of the electron current due to the large ion mass in comparison to the electron mass.

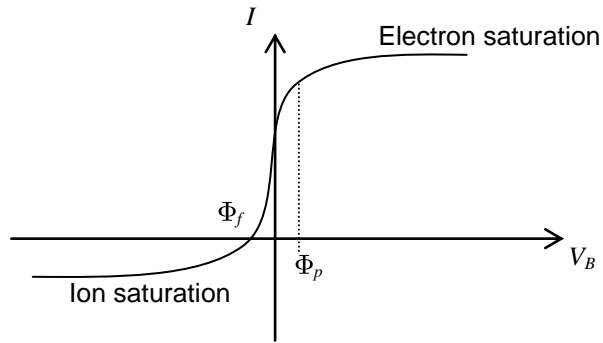


Figure 4.7:2 Typical I-V characteristic of a Langmuir probe.

Another important parameter used to characterise the plasma is the Debye length (λ_{De}) also called Debye shielding. It is one of the most important length scales in plasma physics. It is the screening distance over which a charge becomes unaware of other charges inside the Debye length [121]. The Debye length can be illustrated by considering the following; the charge in plasma (an ion or an electron) will attract opposite charge polarity and repel the like charges due to the Coulomb electrostatic field it creates. The electric field is screened by the charges it has attracted, so the particles outside the screening region are unaware of the presence of the interior charges.

The Debye length is estimated to $\lambda_{De} = 743 \times (T/n)^{1/2}$ where, T , is in eV and, n , is in cm^{-3} . In a typical magnetron sputtering system, the typical, λ_{De} , of the magnetron discharge is in the range of 0.5 mm to 0.02 mm [123]. It is clear from the, λ_{De} , equation what is the physical meaning of the Debye length. When the charge is inside the, λ_{De} , the charges feel the Coulomb electrostatic potential due to the central charge. Outside the, λ_{De} , the potential falls off exponentially and the charges are no longer aware of the presence of the central charge. This means that in the bulk plasma there are no long-range electrical fields

4.8 Film growth and formation

The initial stage of thin film growth begins when the substrate is exposed to the incident vapour molecules, at which, a uniform delivery of atoms begin to impinge on the substrate surface. As the deposited atoms condense onto the substrate, they bond together and become adatoms then diffuse across the surface as their lattice energy is lost and are trapped onto the surface and interact among each other to form 'clusters'. As the impingement rate of the mobile adatoms increases, the clusters begin to be more stable and grow in size and become thermodynamically stable. This stage is termed the 'nucleation stage'.

Clusters can grow in parallel by surface diffusion or perpendicularly by direct impingement of atoms onto the substrate surface. If the size of the clusters grow quicker parallel to the substrate, they begin to merge to form 'islands' by a phenomenon termed 'coalescence'. This phenomenon was observed in 1976 by Vook et al where coalescence growth of an Ag film on NaCl substrate was studied and monocrystalline and polycrystalline structures were observed [124].

The coalescence behaviour is best achieved when the substrate is at a high temperature, because the adatoms attain more thermodynamic energy to bond with neighbouring particles, hence accelerating the rate at which the islands bond together. As the deposition continues, different facets are formed with different orientations and geometry.

The coalescence of the adatoms continues and islands begin to form, leaving empty gaps and holes in between, and after some time, the empty gaps are filled and the film develops into a continuous network.

Depending on the thermodynamic stability of the target and the substrate surface used, the initial film growth can be characterised as follows [125];

- a) Island growth (also known as Vomer-Weber growth)
- b) Layer growth (also known as Frank-van der Merwe growth)
- c) Mixed growth (Also known as Stranski-Krastanov growth)

The initial three modes of thin film growth are represented schematically in the Figure 4.8:1,

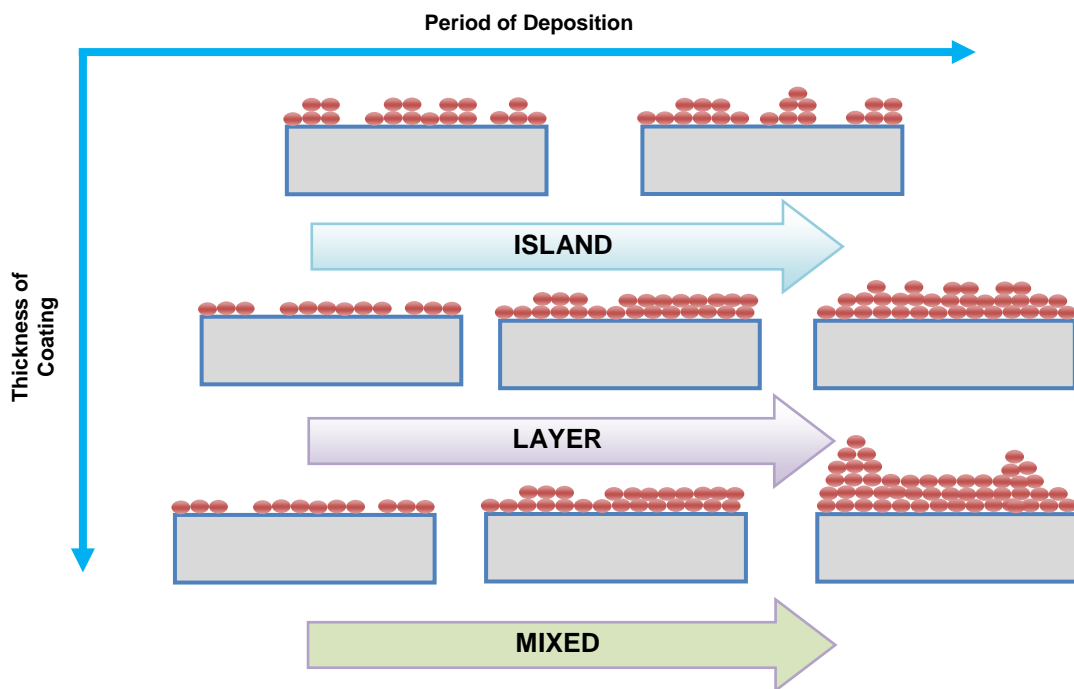


Figure 4.8:1 Three fundamental modes of thin films growth processes.

The growth format depends on the bonding of the vapour species to the substrate materials and themselves. Island growth can be observed if the adherence of the vapour species is greater. Therefore, small adatoms

accumulate together and coalesce to form the coating. This can lead to the formation of porous coatings. If the adherence between the adatoms and the substrate is greater, the coatings will grow layer by layer and the coating will be dense and free from defects. The third type of growth is the Stranski-Krastanov growth which combines the island and the layer growth.

If the orientation geometry of the different islands are similar throughout the thin film and are grown on a single crystal substrate using optimum deposition conditions, the thin film will have a structure of grains growing parallel to each other connected via small angle grain boundaries. This type of film is termed an *epitaxial single crystal film* [125]. The word epitaxy describes the formation of extended single crystals on top of crystalline substrate which was first discovered over a century ago and was first seen in literature in 1928 by L. Royer [126].

The surface morphology of a thin film can either be a smooth surface or a rough surface. This depends on the crystallographic growth rate, as some crystals will grow faster than others, and also depends on the substrate surface, as some parts of the substrate might be rough due to scratches or particle contamination.

The structure of a deposited thin film depends greatly on the sputtered material, the substrate chemistry and morphology, the preparation of the substrate surface, the deposition process and the deposition parameters. The surface roughness and the mobility of the adatoms can be used to determine the morphology of the coating.

Rough surfaces exhibit peaks and valleys, the peaks accumulate particles from different directions. If the mobility of the sputtered particles is low, then the peak will accumulate more adatoms and will geometrically shadow the valleys and also disturb the line-of-sight of the impinging atoms, therefore growing faster than the valleys [127].

4.9 Structure zone models

In order to study the characteristics and the behaviour of a deposited coating, it is important to understand the type of structure that may form to explain why some materials behave differently than others.

The relationship between adatoms energy and mobility and the resultant structure that forms has been studied by many researchers and is often expressed in the form of a structure zone model (SZM) which describes the different structures as a function of particular deposition parameters. The earliest study of zone models was first conducted in 1969 by Movchan and Demchishin (MD) who managed to deposit very thick coatings (circa 0.3-2 mm) by evaporating metals (Ti, Ni, W, Fe) and oxides (ZrO_2 and Al_2O_3) and managed to model three zone (zones 1, 2, 3) which are shown in Figure 4.9:1.

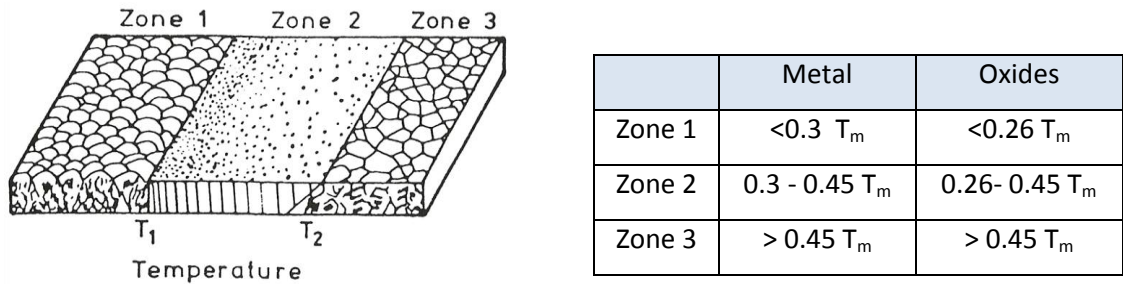


Figure 4.9:1 Structure zone model relating to evaporated films, after Movchan and Demchishin [106].

It is noticed from Figure 4.9:1 that the substrate temperature can greatly influence the structure of the coating (note in this figure the substrate temperature is expressed as a proportion of the melting temperature of the coating material).

In 1974, further work was conducted by Thornton, who investigated DC sputtered thick metal coatings (20-250 μm) at very high rates and managed to identify four zones (1, T, 2 and 3) which are shown in Figure 4.9:2 [128]. Thornton determined that pressure is a decisive operating parameter during sputtering, as it governs the mean free path of the sputtered atoms, hence effecting the surface energy distribution of the adatoms.

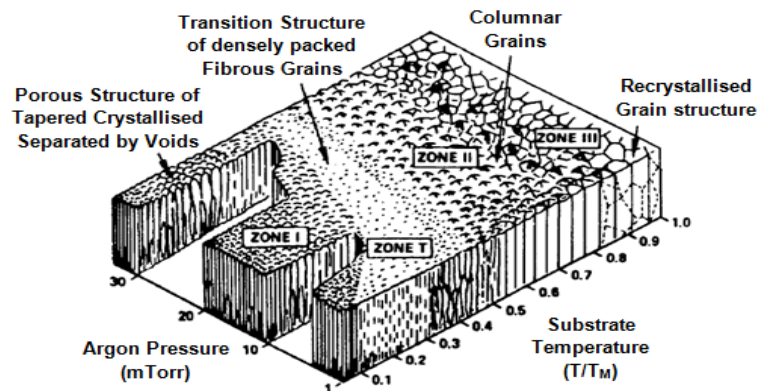


Figure 4.9:2 Structure zone model of sputter deposited materials

The MD and the Thornton model both include the Zone 1 structures for low temperature deposition. At low substrate temperatures, the sputtered atoms do not have enough energy to overcome the geometrical shadowing of the peaks and cannot diffuse into the valleys. As the argon pressure is increased, more collisions occur, further reducing the adatoms energy, which decreases the surface mobility and extends the Zone 1 region. The term used to describe the type of structure is 'Porous columnar'.

Thornton introduced Zone-T, which is the transition stage between Zone 1 to Zone 2 where the structure continues to grow due to the nucleation of the grains during sputtering deposition. The surface morphology of the Zone-T region is a densely packed fibrous grains and it is formed due to the energy of the bombardment sputtered atoms at low gas pressure. These energetic atoms have enough energy to overcome the geometrical shadowing and fill in the valleys [127].

In the Zone 2 region, the structure results from controlled surface diffusion growth. This enables the intercolumnar boundaries to become denser and the basic morphology of the intercolumnar structure to remain the same. This allows for the grains to increase in size and the surface features become smoother. The structure is described as 'dense columnar'.

In Zone 3, the substrate temperature is higher and allows the boundaries to sweep across to form mobile boundaries, which increase the bulk diffusion allowing recrystallisation and grain growth. This type of structure is termed 'fully dense equiaxed grain structures'.

Using physical vapour deposition processes at high biasing conditions, it was possible to replicate the re-crystallised grain structure that Thornton achieved [129-130]. Ross et al used the RF sputtering process to sputter amorphous hydrogenated silicon and demonstrated that argon ion bombardment is most effective during a high negative substrate bias at low gas pressure. He suggested that the biasing voltage should be added to the structure zone model instead of pressure [131]. Fountzoulas and Nowak [132] proposed another version of the SZM model by adding the ion energy as a parameter to the model.

Kelly and Arnell used the closed field unbalanced magnetron sputtering (CFUBMS) process to study the zone structures of aluminium, zirconium and tungsten coatings. Using this process suppressed the formation of porous structures and promoted the formation of fully dense structures at relatively low substrate temperatures. They developed a novel three-dimensional SZM to relate the homologous temperature, ion-to-atom ratio and the ion energy (represented by the biasing voltage). The novel 3-D SZM can be seen in Figure 4.9:3 [133].

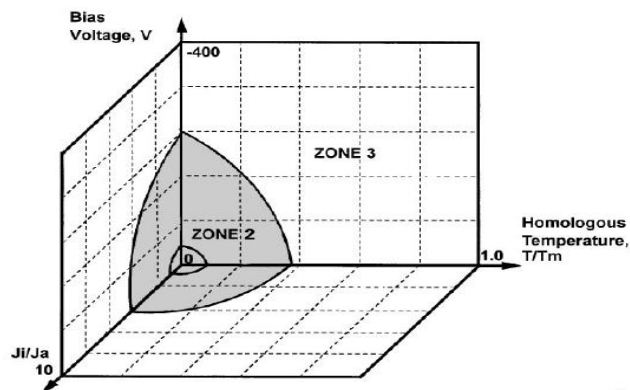


Figure 4.9:3 Novel SZM of the CFUBMS system, relating coating structure to the homologous temperature, ion-to-atom ratio and bias voltage [133].

The film structure of transparent conductive oxides influences the optical and the electrical behaviour, so it is important for the thin film to be of Zone 2 or Zone 3 structure in order to obtain good electrical and optical properties that will meet the needs of this project.

4.10 Summary and outlook

In this chapter, a concise overview of the basic concept of glow discharge, plasmas characteristics, along with characteristics and structural formations of thin films were introduced. The three types of plasma discharge were discussed and found that abnormal discharge is the point at which sputtering normally is carried out. Basic plasma characteristics were also reviewed and outlined the plasma sheath and the Debye length characteristics are very important characters in plasma physics and that the plasma is quasi-neutral except in the sheaths to electrodes or surfaces where the potential changes over several Debye lengths. The film structure of a deposited thin film depends greatly on the sputtered material, the substrate chemistry and morphology, the preparation of the substrate surface, the deposition process and the deposition parameters, it is important to create TCO that exhibit a film structure of zone 2 or zone 3.

PVD technology is primarily used for deposition of metal, metal-oxides and also some dielectrics materials. Key engineering and recent developments in magnetron sputtering, including the closed field unbalanced magnetron sputtering system made it possible to coat different types of materials such as metallic, ceramic and even insulating materials using high deposition rates

and good crystalline coatings. It also prompts the possibility of depositing onto substrates of complex geometry with a single to multi-layers along with competitive qualities

POWDER TARGETS

In the magnetron sputtering process, mainly solid or ceramic targets are used to sputter deposit thin films. Depending on the desired thin film, different targets such as pure elemental or compound targets are utilised to produce metallic or compound thin films. Alloy targets can also be used to sputter deposit thin films of different compounds. For research purposes, utilising such targets can be a costly process as solid targets can be expensive and several solid targets are required to investigate composition effect on thin films properties. Meanwhile, ceramic targets are fragile and crack under high deposition power, therefore capping the deposition rates, also sintering is required, therefore increasing process cost and lead-time.

In this chapter, the fabrication and operation of powder targets is examined including target discharge characteristics, hysteresis studies, compositional analysis and experimental parameters such as chamber pressure, sputtering power, pulsing frequency and duty cycles are carried out in order to optimise the deposition process and produce the desired thin films.

5.1 Introduction

In industry, the compositional ratio of the compound target is well defined in order to deposit optimised thin films. However producing a multi-compound material in a research laboratory can be an expensive approach requiring the purchase of several new alloy targets.

An alternative approach is using powder form materials that can easily be mixed and spread across a recessed plate to make a sputter target. Using blended powder targets offers a relatively cheap and highly versatile means of screening multi-component coating materials, compared to using solid targets. With solid targets, only a small area of the target (25-35%) is utilised during sputtering, which is the race-track area.

Blended powder targets have been used before to deposit different coatings such as doped zinc oxide coatings [88, 134-135], indium tin oxide (ITO) coatings [12], copper aluminium oxide coatings [51], and chromium boride-based coatings [136-137].

Sintered blended powder targets are not uncommon and have been reported by other researchers [138-140]. The blended powder target used in this project were all un-sintered. This decreases the process cost and decreases the lead-time for thin film production. The blending of the materials together to form the powder target is easier than sintering the target and it can always be re-spread to remove any racetrack, therefore increasing the utilisation of the target. Furthermore, the composition of the targets is easily varied and therefore it is a cheap means of assessing the effect of the target composition in order to optimise thin film properties.

5.2 Discharge stability

There are several parameters used to characterise and monitor the process stability during powder sputtering. These parameters include the discharge current, discharge voltage, reactive gas partial pressure, system pressure, deposition rate, film properties and light emitted from the plasma. It enables the investigation of the behaviour of the target during sputter deposition, and can give an indication to when the target is heated or when the target surface is oxidised, which can limit the deposition rate and influence the chemical composition of the sputtered film.

The discharge stability of each powder target is unique and depends on a number of influential factors such as the material particle size and its electrical and thermal conductivity. Giving the insulating nature of the powder targets, it is extremely difficult to strike a discharge using a DC power supply, therefore in this project an Advanced Energy Pinnacle Plus pulsed DC supply was used, which can drive the discharge at frequencies from 100 to 350 kHz with duty cycles from 50% to 95%. The discharge stability also depends on the degree of compaction of the blended powder surface. The powders are compacted or tamped to promote a better surface uniformity and improve thermal and electrical conductivity. Figure 5.2:1 presents two different powder targets; the left photo show a target tamped with a 100 g steel rod and the right photo for a target that tamped using a 1 kg steel rod. Both targets were sputtered using identical deposition process, the target shown in (a) was tamped very lightly which promoted for trapped air particles in the target and lead to aggressive out-gassing of the target and led to target arcing. Therefore

demonstrating, that to avoid arcing, it is important to ensure the tamping process is done with using an adequate weight.



(a)

(b)

Figure 5.2:1 Effect of tamping of the powder target, (a) target tamped with very light steel rod, (b) target tamped with 1 kg steel rod.

The discharge voltage of the powder targets was measured periodical during sputtering using a TDK P5100 voltage probe which was attached to the target and monitored using a Tektronix DPO3014 digital oscilloscope. It is important to note that each new powder target was conditioned in an argon atmosphere for an hour at constant power mode of 100 W. The power was then incremented at 20 W per five minutes to ensure no arcing occurred. When the powder target is conditioned, the target voltage is stabilised and target surface problems such arcing and out-gassing are eliminated.

Figure 5.2:2 presents the target voltage characteristics for conditioned powder targets as a function of the deposition period, including fluorine doped tin oxide (FTO), antimony tin oxide (ATO), copper aluminium oxide (CAO) and titanium (Ti) targets. The discharge was observed to be stable across the deposition period of one hour (i.e. no arcing was observed). However, a slight decrease was observed in the discharge voltage across all the powders. This

may be attributed to the thermal relaxation and/or the removal of contamination from the target surface. Another important factor that influences the discharge voltage is secondary electron emission yield, which varies for each material and determines how many electrons are released from the target for each incident ion. This accounts for the range of operating voltages displayed below.

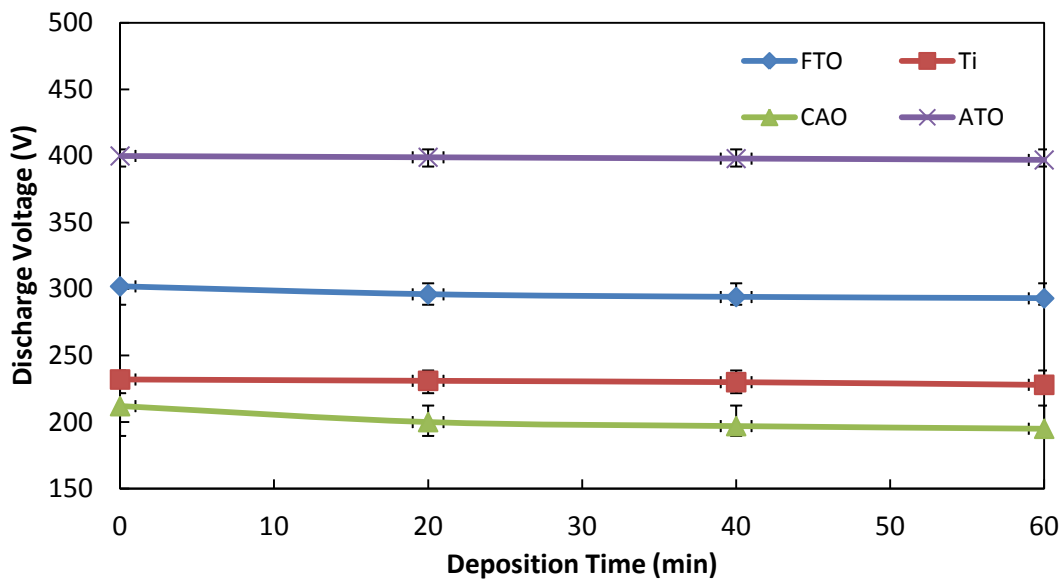


Figure 5.2:2 Discharge voltage stability as function of deposition period of loosely packed powder targets sputtered in argon and oxygen atmosphere.

During deposition, no target melting was observed for all the powder blends used as long as the target power was less than $P \leq 500$ W. Increasing the target power above 500 W, caused the powder target to deform and melt and then solidify as in the figure shown below. The copper aluminium powder target melted and solidified as the target power increased to 550 W.



Figure 5.2:3 Copper aluminium powder target surface state after being sputtered with 550 W.

5.2.1 Pulsed-DC reactive sputtering of dielectric powder targets

The DC reactive sputtering of oxide powder targets poses great difficulty in sustaining a stable discharge. As the powders are dielectrics, applying a DC signal to the target causes a charge build up on the target surface. If the charge reaches the breakdown voltage of the powder target, an arc will occur, which causes the powder to be ejected from the target holder, which effectively degrades the thin film quality. To overcome this problem, dielectric powder targets are sputtering using either a pulsed direct current (DC) [141-142] or a mid-frequency alternating current (AC) [143-144] technology. Both pulsed DC and mid-frequency AC use a voltage reversal at the dielectric target in order to offset the charge build up on the target surface. A schematic pulsed DC waveform is shown in Figure 5.2:4.

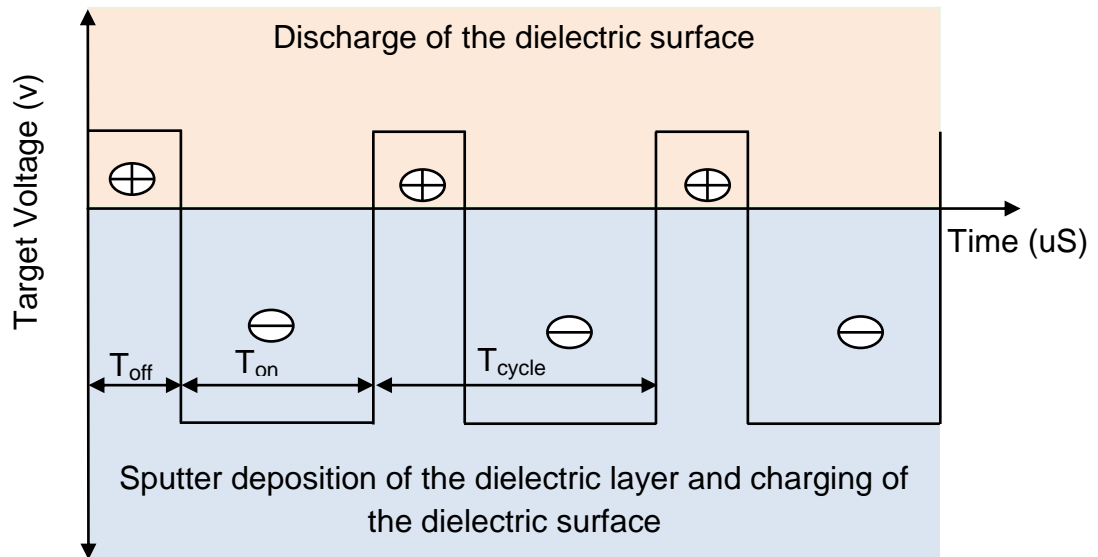


Figure 5.2:4 Schematic of an asymmetric bipolar-pulse DC waveform to power dielectric surface.

In a bipolar pulsed DC supply, the polarity of the voltage alternates between the negative and positive pulse, as observed from the figure above. The negative pulse duration and magnitude are normally longer than the positive pulse, this type of pulse is termed asymmetric pulse because the positive and negative pulses have different durations and magnitudes. During the negative pulse of the cycle, the ions are attracted to the target to eject the atoms from the target surface, while during the positive pulse, the electrons in the plasma are attracted to the target surface to discharge the positively charged regions [12].

During pulsed DC sputtering, there are two important factors; the pulse frequency and the duty cycle, which can be ranged from 20-350 kHz and 0.5-0.95, respectively. The duty cycle is defined as the negative pulse time divided by the cycle period ($T_{on}/(T_{on}+T_{off})$). These two important parameters affect the deposition conditions such as target voltage and current peaks, deposition rate and also the properties of the deposited thin films.

Another way for sputtering dielectric materials is using reactive mid-frequency (typically 40 kHz) AC sputtering arrangements. The plasma of the magnetron is only on for half the period, leaving the other half for undesired sputtering such as the chamber walls. To overcome this problem and to increase the deposition rate, the use of both halves of the periods are used and the single magnetron is replaced with two magnetrons, each connected to an opposite pole of a floating AC power supply. The necessity to replace a single magnetron with a dual magnetron increases the cost of the system, and also the nature of the system can lead to the increase in the substrate temperature which is very difficult to prevent [142].

5.2.2 Pulsing parameters and discharge behaviour

The sputtering of the powder target during this research was based on the pulsed DC power supply arrangements using a constant power mode. The constant power mode, allows the target voltage and current to vary to accommodate the target surface resistance, while securing a constant flux of energy to the target surface.

Pulsed DC sputtering of fluorine doped tin oxide (FTO) from a blended powder target is unique and novel, therefore, trial experiments were conducted using a variety of pulsing parameters, including pulse frequency and duty cycle as shown in Figure 5.2:5. These trial experiments were used to determine the optimum experimental conditions for a stable sputtering environment. Figure 5.2:5 demonstrates the different parameter arrays that were used to determine the deposition rate and the structure of the thin film.

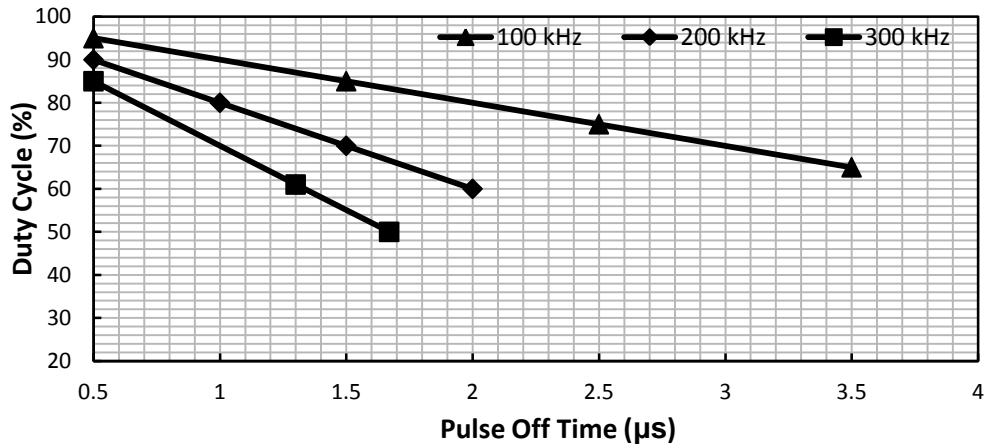
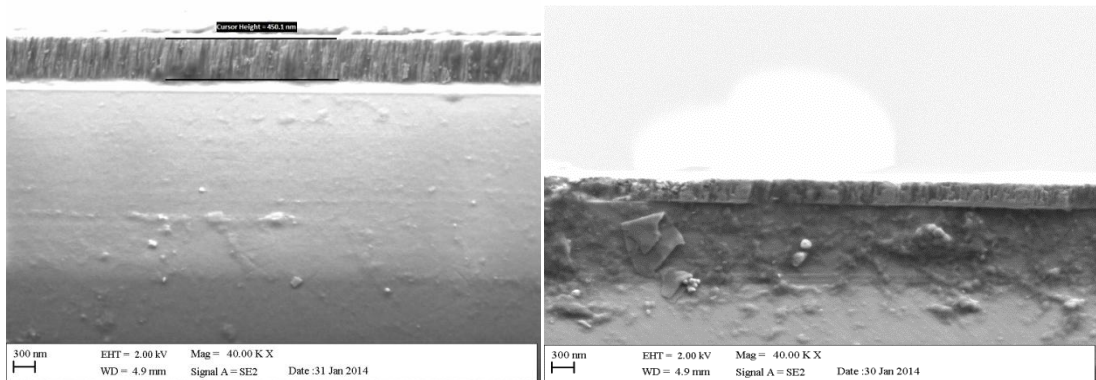
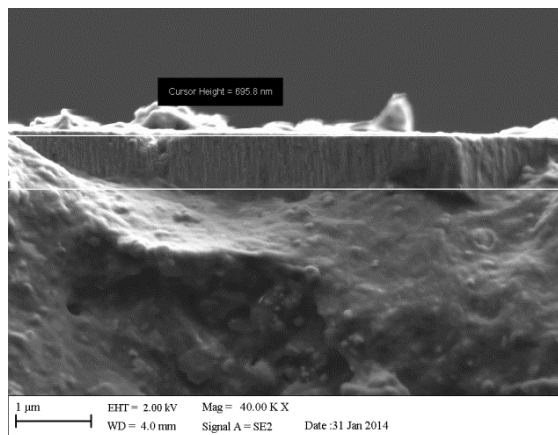


Figure 5.2:5 power supply trials conducted using different pulse frequency, pulse off time and duty cycle on FTO powder target.



(a) 300 kHz duty cycle 85% (b) 200 kHz duty cycle 85%



(c) 100 kHz duty cycle 85%

Figure 5.2:6 SEM fracture sections showing the effect of pulse frequency on structure and deposition thickness of the FTO thin films.

The deposition thicknesses and the structure of the deposited coatings were determined using the SEM, as observed in Figure 5.2:6. It was shown that the coatings based on a visual inspection, are well adhered and the morphology is the same as the widely accepted structure zone model of coatings grown using the pulsed DC sputtering technique, as reported by Kelly et al. [133]. During high pulse frequency such as (a) 300 kHz, the deposition thickness measured to 350 nm, meanwhile at (c) 100 kHz the thickness measured 696 nm.

The difference becomes clear when the target voltage waveforms found in Figure 5.2:7 are analysed.

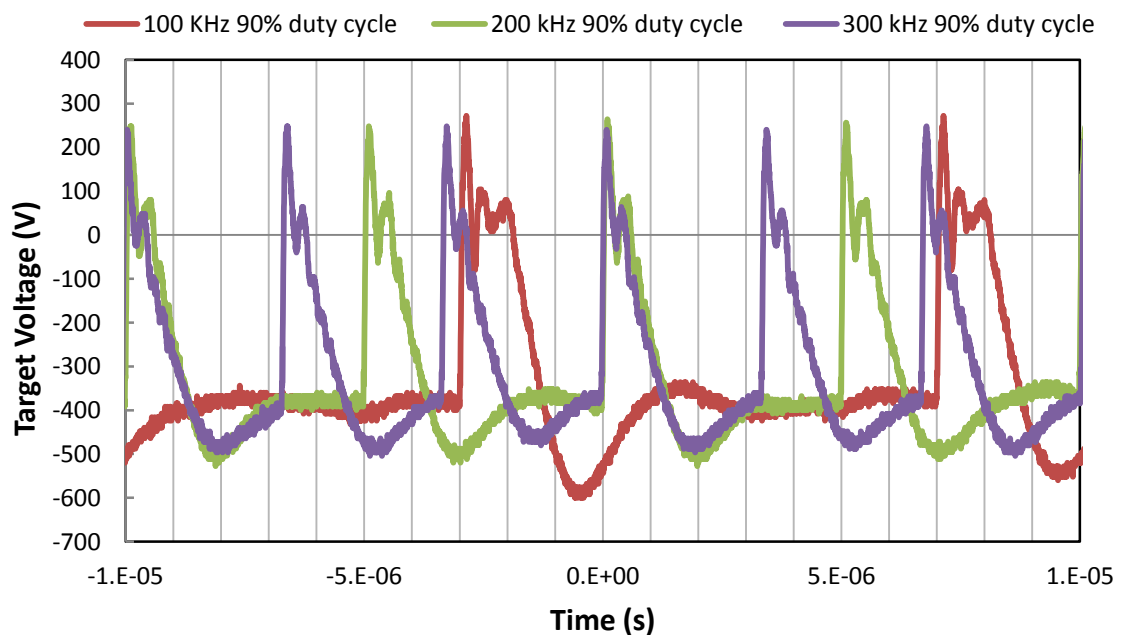


Figure 5.2:7 Effect of pulse frequency on FTO powder target voltage waveform 90% duty cycle using constant power mode at 400 W of sputtering power, in 10 sccm of Ar and 4.5 sccm of O₂, coating pressure of 0.55 Pa.

When operating at high pulse frequency, the plasma is effectively on for less time than during a pulsed frequency plasma. For instance, at 300 kHz pulse

frequency, there are 3 cycles for every one at 100 kHz. Thus, the time required to establish the plasma and for the target voltage to ramp to the discharge voltage over the same time period is three times longer in total than that of a 100 kHz pulse frequency, so as the frequency increases, the off time became an increasing proportion of the total cycle. This leads to the decrease in deposition rate; such behaviour was observed during the investigation using a FTO target as shown in Figure 5.2:8. The experimental conditions were set as follows; using a constant power mode of 400 W, 0.4 μ s pulse off time and 90% duty cycle. The Ar flow rate was set to 10 sccm and O₂ set to 4.5 sccm, chamber pressure of 0.55 Pa and substrate to target distance set to 11 cm.

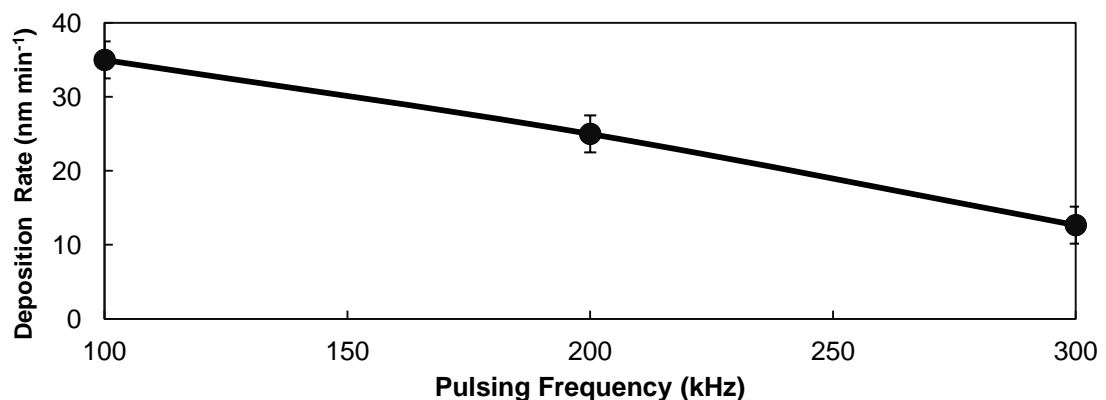


Figure 5.2:8 Effect of pulse frequency on the deposition rate of a FTO powder target (duty cycle = 90%).

As demonstrated, the target pulsing frequency has a significant influence on the deposition rate. An increase in the pulsing frequency was found to result in a decrease in the deposition rate. Another factor besides pulsing frequency is the pulsing duty cycle, which is an important variable. Figure 5.2:9 shows how the voltage waveform of a FTO powder target varies at a constant 200

kHz target pulse frequency and variable duty cycle (90, 70 and 50%) using constant power mode of 400 W, 10 sccm of Ar and 4.5 sccm of O₂, and a chamber pressure of 0.55 Pa.

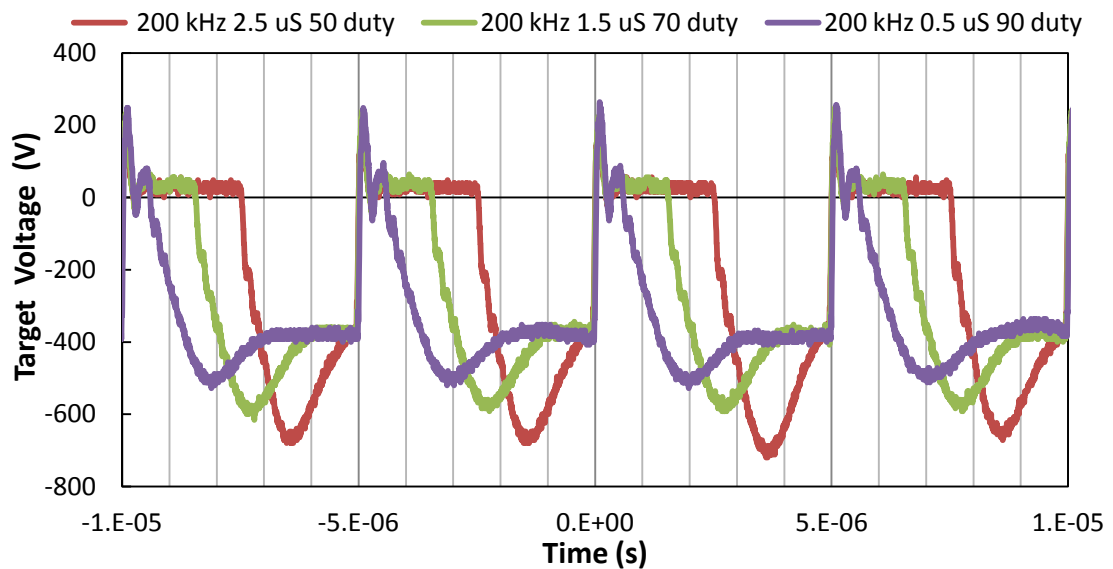


Figure 5.2:9 Effect of duty cycle on the FTO target voltage using 50, 70 and 90% duty cycle at 200 kHz pulse frequency.

At a higher duty cycle (90 %), the plasma was off for a very short moment; 0.5 μ s, hence the sputter efficiency of atoms removed from the target was very high and effectively yielded a high deposition thickness as shown in Figure 5.2:10. However, at a lower duty cycle (50 %) the plasma was off for a longer time at 3.5 μ s which allowed the plasma to decay through bipolar plasma distribution to the walls of the chamber. Therefore, a decrease in the deposition thickness was observed in the growth thickness of the FTO thin films (deposited at 400 W for a period of 20 minutes using a variety of pulse frequency ranging from 100-300 kHz) shown in Figure 5.2:10. All the powder targets were subject to a conditioning experiment, to ensure all the experimental conditions produced an arc free environment.

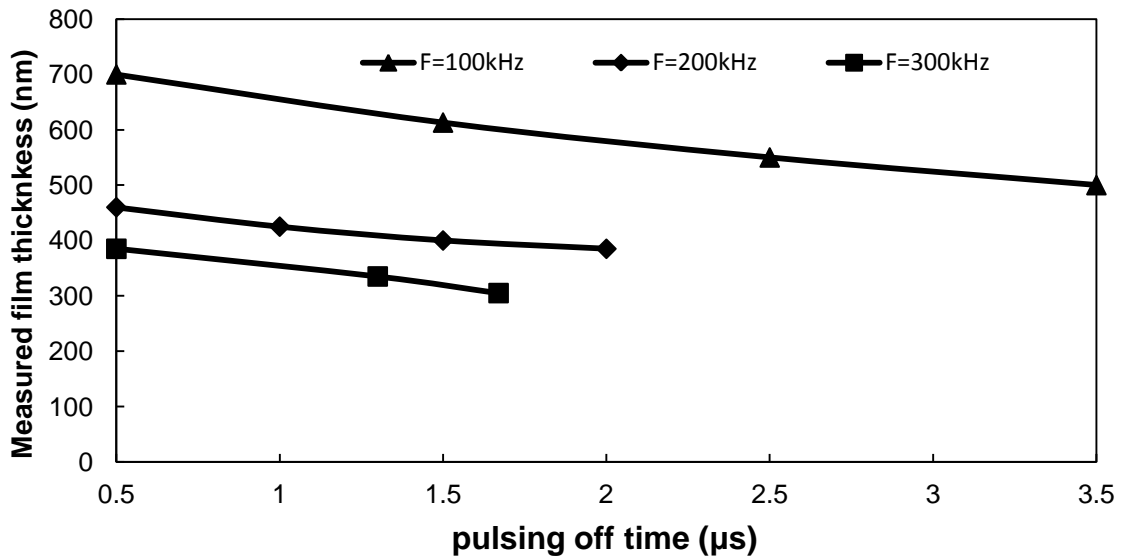


Figure 5.2:10 Effect of pulse time on the growth thickness of the FTO thin films using sputtering power of 400 W, sputtering period of 20 minutes using a variety of pulse frequency and a variety of pulse off time in 10 sccm of Ar and 4.5 sccm of O₂, coating pressure of 0.55 Pa.

During the conditioning of a newly spread FTO powder target, the power was introduced steadily at 50 W then incremented at 50 W per every 15 minutes, to ensure the powder target does not outgas very abruptly therefore causing target to be unstable and arc. Figure 5.2:11 presents the voltage characteristics of the FTO powder target during powder conditioning, measured using a digital oscilloscope attached directly beneath the target holder to eliminate any redundant noise signals. It was noted that during low power, the signal was observed to be noisy. The noise ripples were attributed to the change in the resistance of the powder target as it was conditioned. As the sputtering power increased above 100 W, the noise ripples decreased and disappeared during higher power indicating the powder target had stabilised. It is also important to note that the power delivered to the magnetron to

generate the plasma is realised mainly in the sputtering of the target material, but also can be lost through heating all surfaces, such as target, chamber walls and substrate [143]. The other point to note from Figure 5.2:11 is how the magnitude of the voltage increases with increasing power and how the voltage rises in the negative sense more quickly at higher powers, this observation show that the power supply is more stable at higher powers.

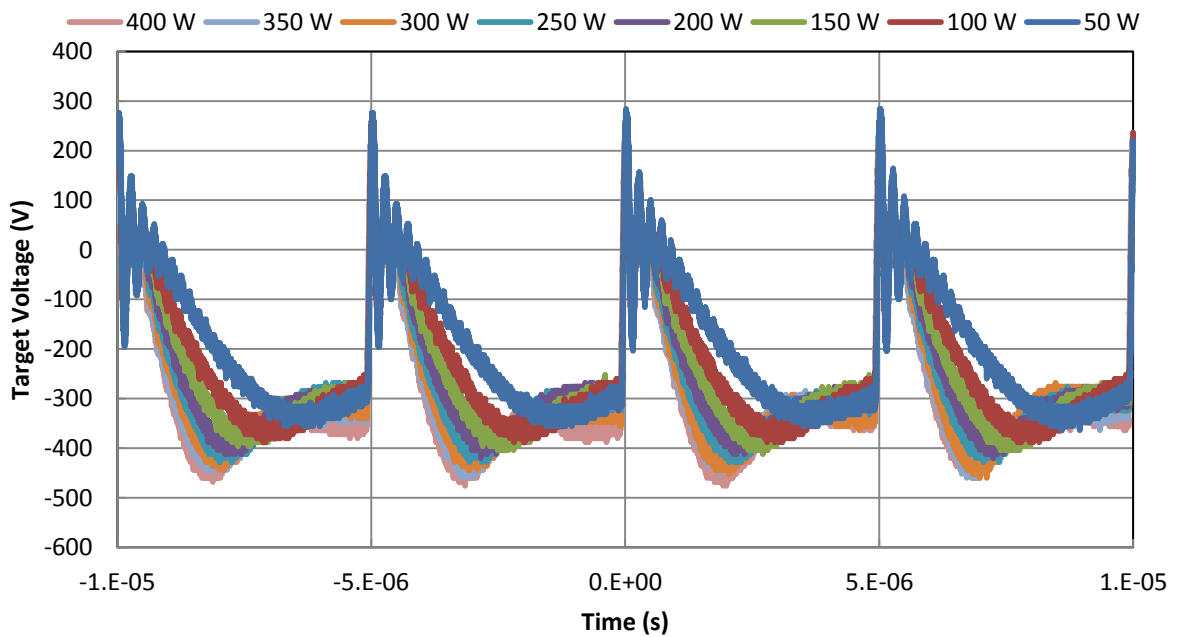


Figure 5.2:11 Effect of sputtering power on the FTO target voltage using a 90% duty cycle and 200 kHz pulse frequency in 20 sccm of Ar chamber pressure of 0.55 Pa.

The target voltage was measured in intervals of every five minutes across the 2.5 hours conditioning period, using a 90% duty cycle at 200 kHz pulse frequency and constant power mode, in 20 sccm of argon, chamber pressure 0.55 Pa; this is shown in Figure 5.2:12. At each new increment of power up to about 250 W, a new burst of outgassing from the target occurred until the adsorbed material was removed and the target voltage stabilised, and the size of the burst decreased with increasing power.

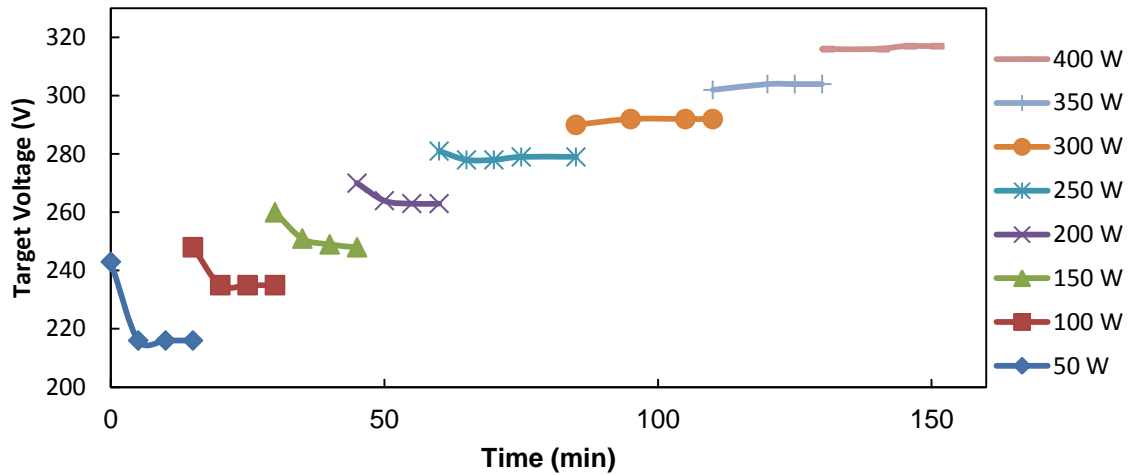


Figure 5.2:12 Average target voltage of FTO powder target conditioning measured across a period of 2 hours.

The chamber base pressure was also measured during the powder target conditioning using MKS a Baratron capacitance manometer vacuum gauge, connected to a PR4000 MKS pressure controller and readout. The chamber pressure increased from 0.55 Pa at 50 W to 0.59 Pa at 150 W, this slight increase in chamber pressure corresponds to the outgassing of the target. The chamber pressure observed to decrease to 0.56 Pa at 200 W then remained stable around the 0.55 Pa at 400 W. This indicated a stable target, clean from adsorbed materials. Oxygen gas at 4.5 sccm was added to the chamber and the diffusion pump valve was readjusted to give the desired operating pressure of 0.55 Pa after which the shutter situated between the target and the substrate holder was removed to resume sputtering. It is important to note that only newly formed powder targets followed such extensive and long conditioning procedure. Once the powder target has been used more than once, it stabilised and only 10 minutes was required to clean the target prior to deposition.

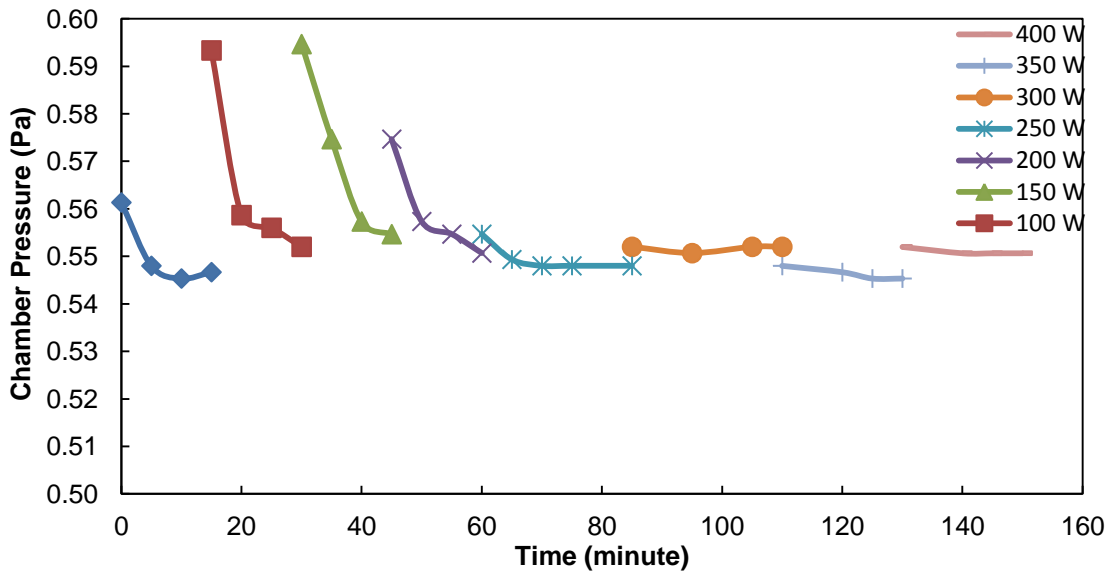


Figure 5.2:13 Chamber pressure variations during the FTO powder target-conditioning period of 2 hours.

The effect of the oxygen flow rate on the voltage characteristics of a pure tin oxide (SnO_2) target is demonstrated in Figure 5.2:14. The pure SnO_2 powder target was sputter cleaned in an argon atmosphere using constant power mode of 300 W, pulse frequency of 200 kHz and duty cycle of 90% at a chamber pressure of 0.54 Pa. The target was sputter cleaned to ensure that the target voltage was stable and not fluctuating. Oxygen gas was introduced to the chamber at increments of 2 sccm every five minutes. Sputtering in argon gas mode only, the target voltage was -363 V, as the oxygen gas was introduced to the chamber, the target voltage decreased in magnitude to -345 V and further decreased to -337 V as the oxygen was increased to 6 sccm. Introducing such a reactive gas into the plasma atmosphere reduced the discharge voltage; it implies that it is easier to sustain the magnetron discharge. This means the secondary electron coefficient must be higher for tin oxide, compared to tin. Therefore, the SnO_2 powder target does not require high energy to sustain the plasma.

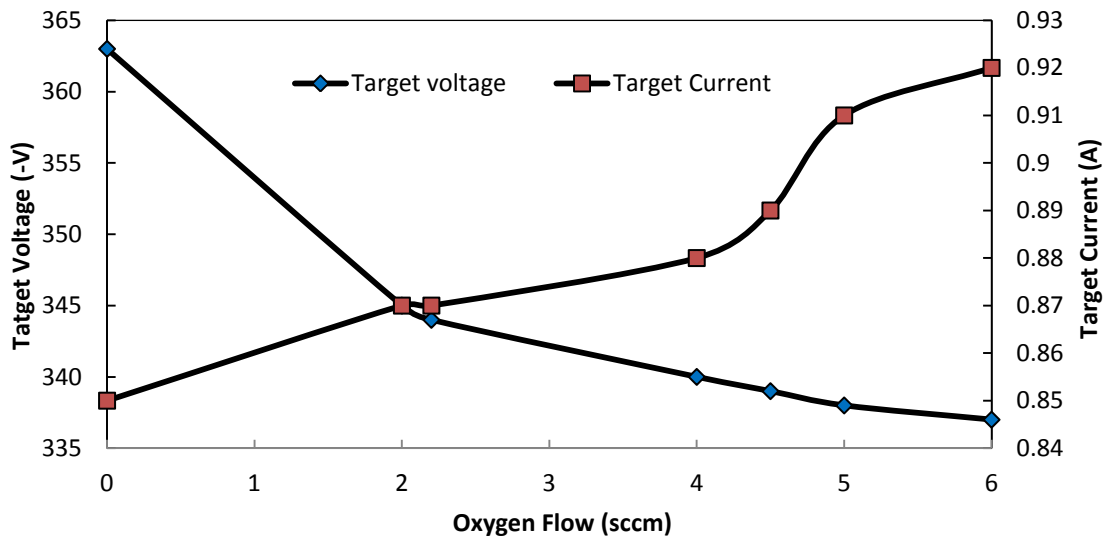


Figure 5.2:14 Effect of oxygen flow on the SnO₂ target voltage.

In general, the study of the deposition parameters such as duty cycle and pulse frequency helps to build a better understanding of how they affect the plasma and in growth of the coatings. The knowledge gained can be used to deposit coatings with specific deposition rates and with specific properties.

5.3 Target to substrate distance comparison

The distance (d_{t-s}) between the target and the substrate is another important experimental variable. This distance is the pathway the sputtered atoms travel to get to, and condense onto, the substrate surface. The longer the pathway, the longer the line of sight for the sputtered atoms to reach the substrate surface and vice versa is true. One thinks that using a short pathway will surely produce quicker deposition rate, true, but at the expense of producing defected stressed coatings. The stressed areas may lead to localised adhesion failure of the coating therefore causing the coatings to delaminate from the substrate surface.

Three set of experiments carried out on the FTO target at various target-to-substrate separations are shown in Table 5.3:1.

Table 5.3:1 Comparison experiments using different separation distances.

Exp. run	Separation distance (cm) d_{t-s}	Power supply set up	Run time (min)	O ₂ (sccm)	Ar (sccm)	Chamber pressure (Pa)
1	7	200 kHz 90%	15	4.5	10	0.55
2	9	200 kHz 90%	15	4.5	10	0.55
3	11	200 kHz 90%	15	4.5	10	0.55

The deposition conditions were kept the same and the run time was fixed at 15 minutes. A piece of kapton tape was placed on the glass substrate prior to sputtering and removed after the deposition to produce a step in the coating. The coating thickness was measured across six points and an average was calculated. The target separation produced large differences in coating thickness, as observed in the Figure 5.3:1. The coating thickness was found to decrease from 600 nm to 400 nm as the target-to-substrate separation (d_{t-s}) was increased from 7 cm to 11 cm. As the d_{t-s} is increased, the atom flux and the ion flux decreased; however, research has shown that the neutral atom flux decreases faster, therefore the ion-to-atom ratio actually increases. This implication was demonstrated by Kelly et. al. which showed that the ratio of ion-to-atom current density ($J_i:J_a$) increased twofold as the d_{t-s} was increased [145]. Although not measured during this study, it would suggest ion-to-atom ratio is a critical parameter in determining the film structure [135].

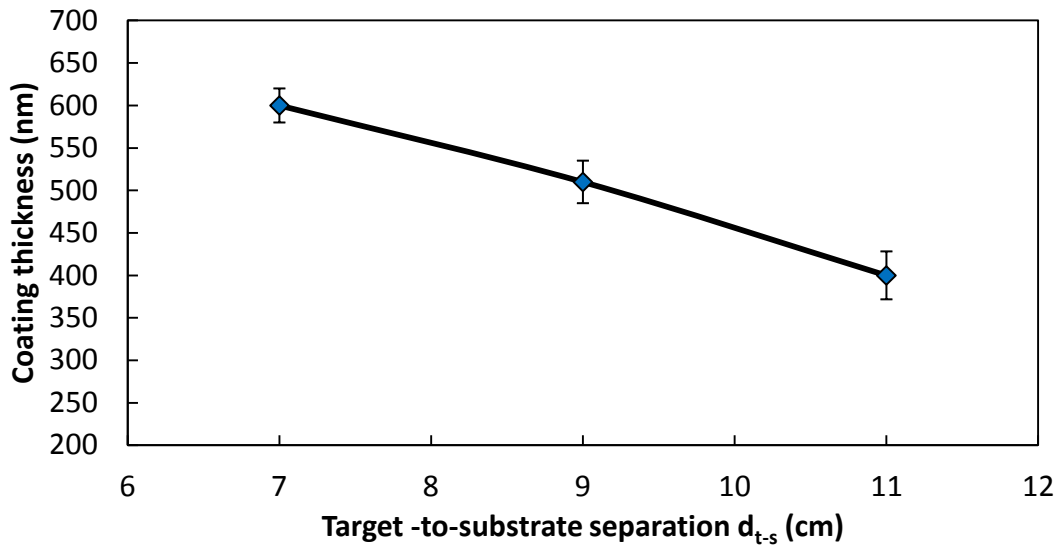


Figure 5.3:1. The effect of target-to-substrate separation (d_{t-s}) on the thickness of the coatings.

The relationship between the target-to-substrate separation and the electrical resistivity of the FTO thin films shown in Figure 5.3:2. It was observed that the further the away the substrate was from the target, the lower the electrical resistivity of the FTO coatings. This could be attributed to the higher ion-to-atom ratio. This implies that resistivity is optimised as the ion-to-atom ratio increases.

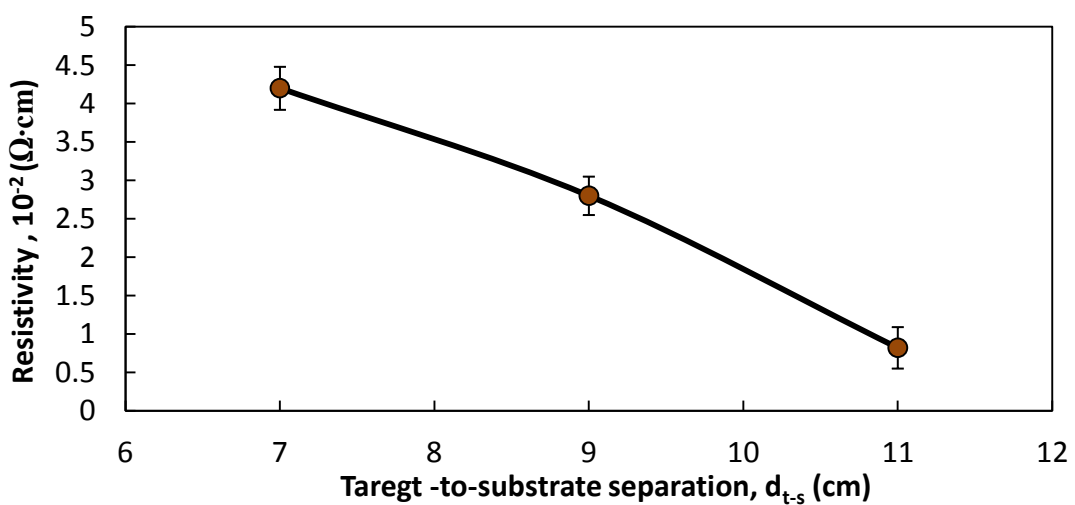
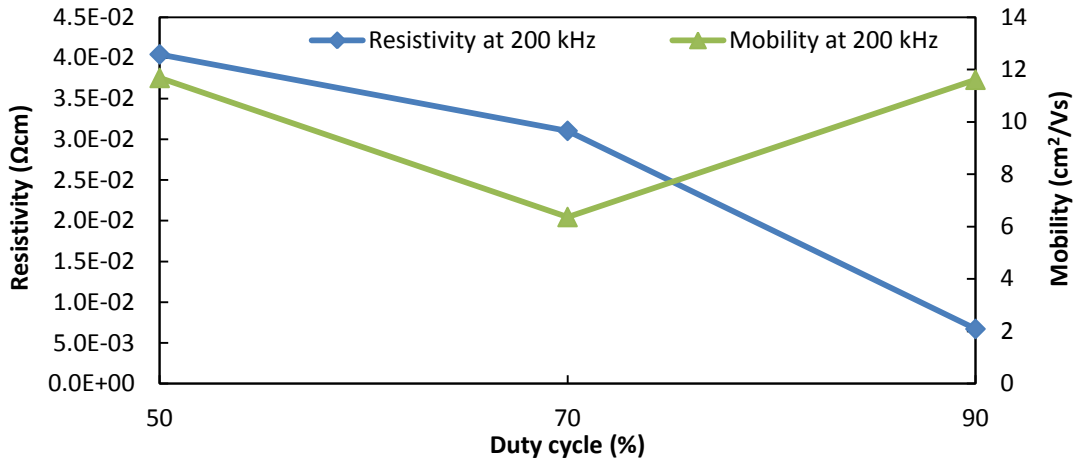


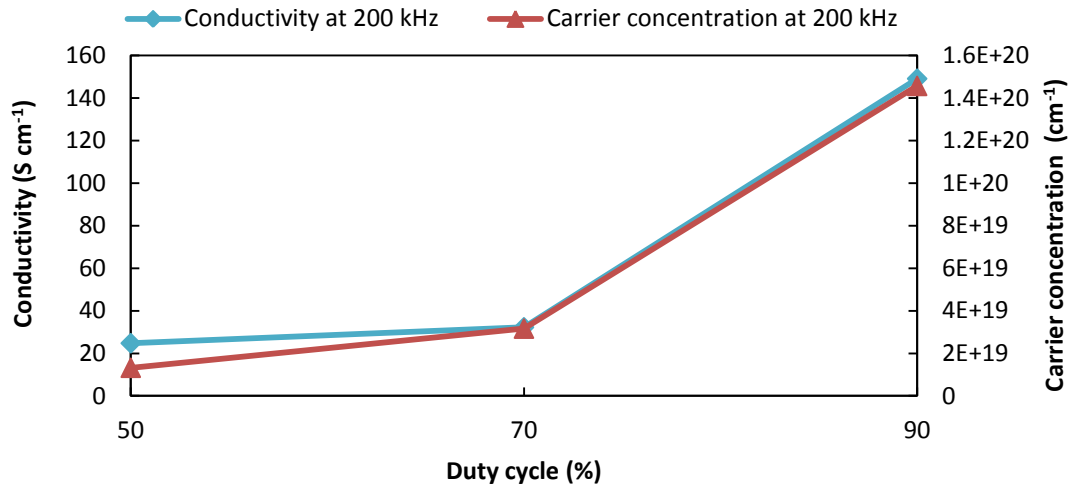
Figure 5.3:2 The effect of the target-to-substrate distance on the electrical resistivity of the FTO coatings.

5.4 Effect of pulse frequency and duty cycle parameters on electrical property of FTO

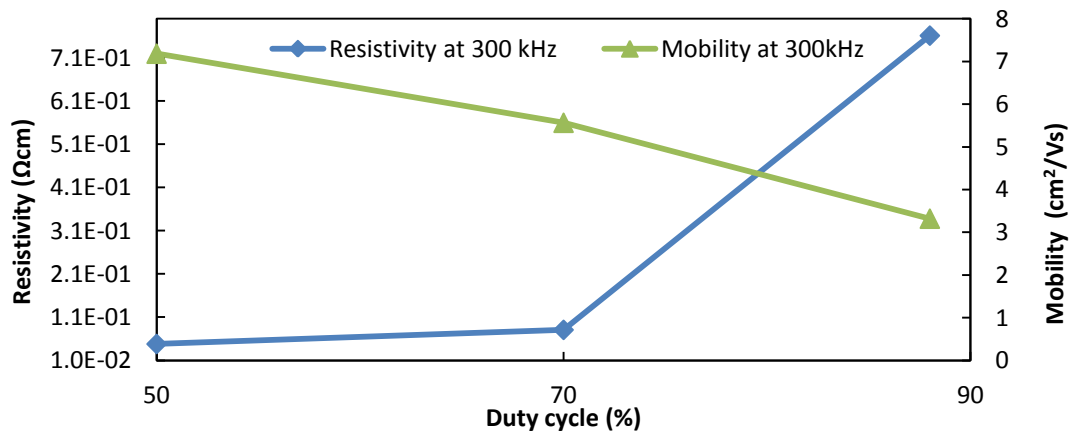
In this study, a set of experiments were designed to find the optimum pulse frequency and duty cycle for the deposition of FTO thin films. Based on the characteristic studies, two sets of frequencies were chosen; 200 and 300 kHz with different duty cycles; 50, 70, and 90%. The deposition period was carefully monitored in order to produce a consistent deposition thickness of 400 nm. The other operating conditions for each run were kept constant, including constant power mode of 400 W, 10 sccm of Ar and 4.5 sccm of O₂ and total pressure of 0.54 Pa was maintained during the deposition. The FTO powder target was optimised to a composition ratio of SnO₂:SnF₂ (6.6 at.% of fluorine) set to 52:9 grams. During the deposition at a pulse frequency of 200 kHz, the electrical properties of the FTO thin films were significantly improved as the duty cycle was increased from 50% to 90% as observed in Figure 5.4:1 (a-b). However, it was observed that increasing the pulse frequency to 300 kHz deteriorated the electrical properties of the FTO thin films as shown in Figure 5.4:1 (c-d). Therefore, this demonstrated that the optimum pulsing sputtering parameters were to use a high duty cycle of 90%, in combination with a pulse frequency of 200 kHz to yield the optimum electrical parameters.



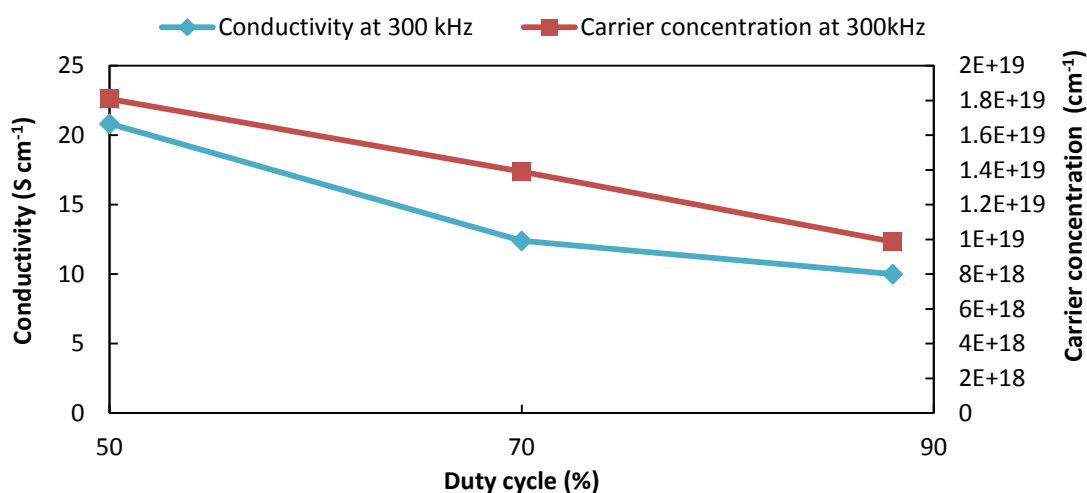
(a)



(b)



(c)

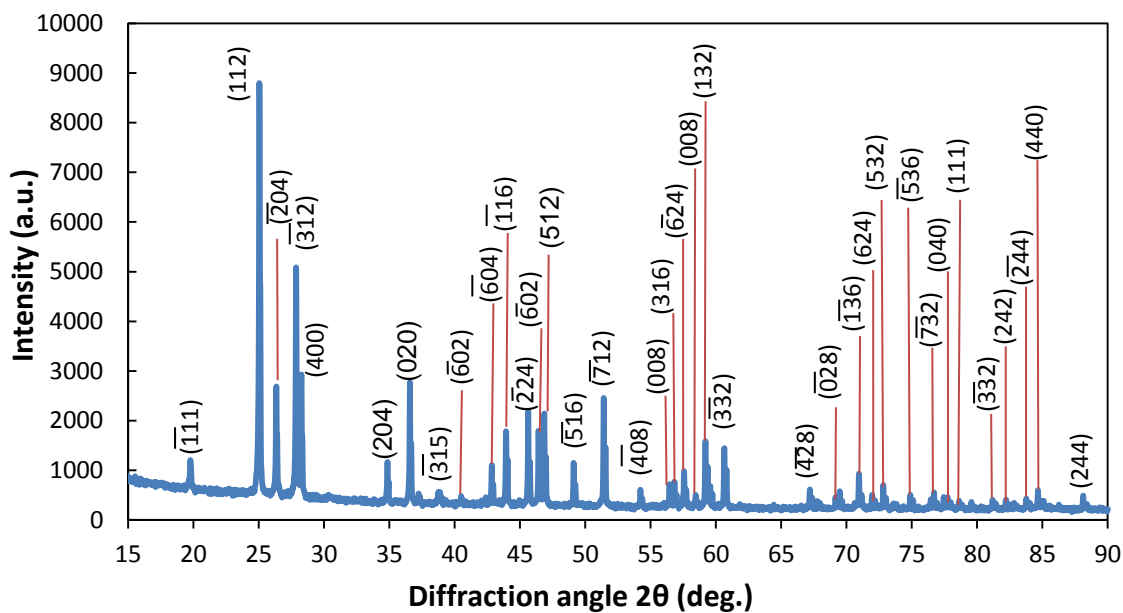


(d)

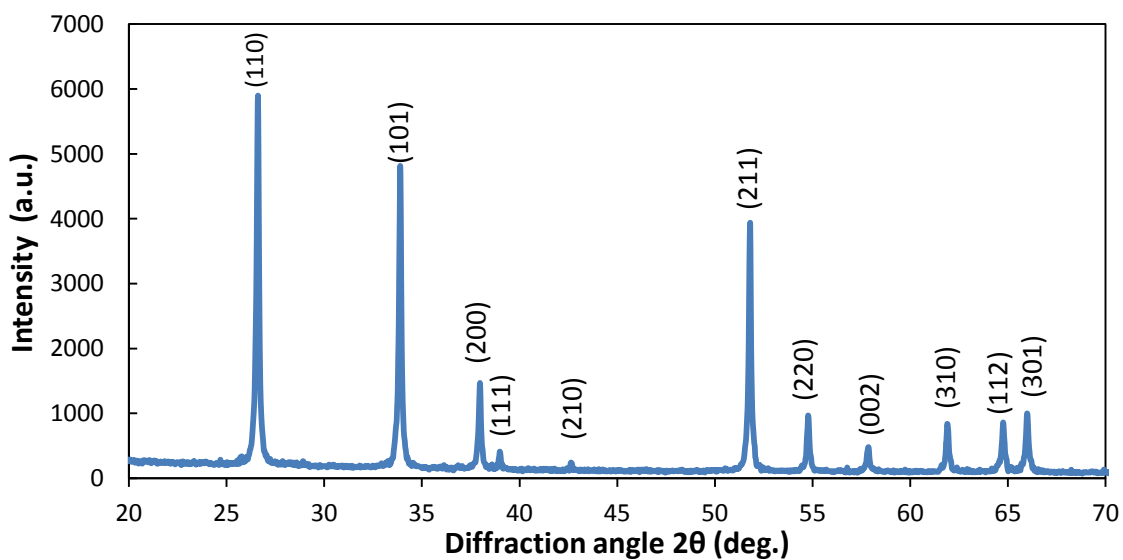
Figure 5.4:1 The effect of the pulse frequency of (a-b) 300 kHz (c-d) 200 kHz and duty cycle 50, 70, 90 % on electrical property of FTO thin films.

5.5 Crystallographic analysis of powder targets

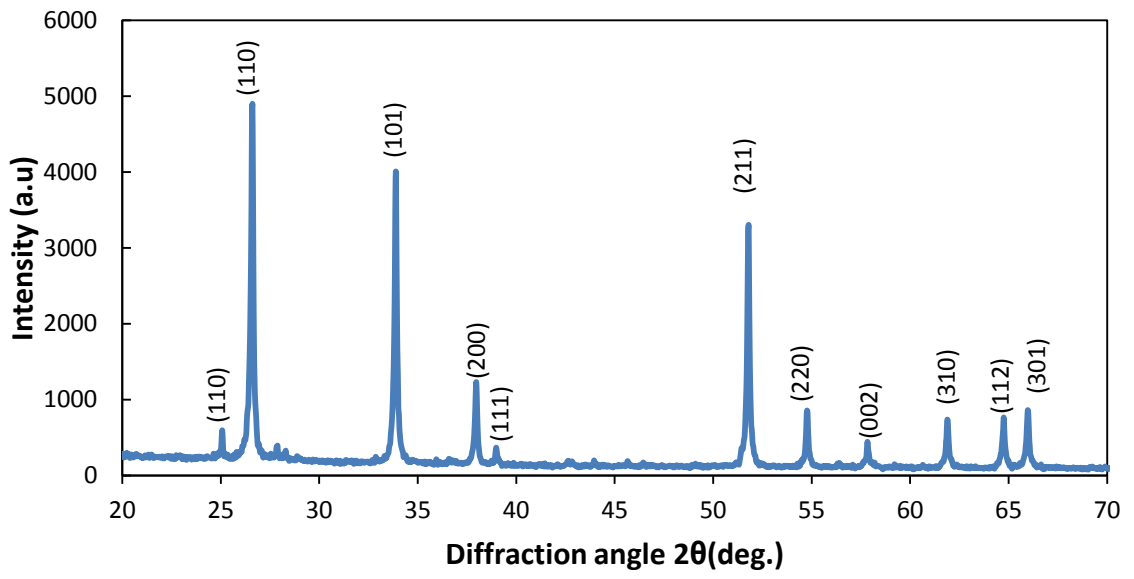
The crystallography of the powder targets was characterised using XRD (θ - 2θ configuration). The diffraction peaks were indexed to the intensity obtained from the JCPDS powder diffraction file to ensure the correct texture and phase identification of the powder target were achieved. These measured diffraction patterns were then used as reference patterns to compare against the diffraction pattern of the developed thin films to establish the possibility of peak shifts due to strain or stress that may have arisen due to the deposition process. The XRD diffraction pattern for SnF_2 , SnO_2 , $\text{SnO}_2:\text{SnF}_2$, Cu, Al, CuAl, Ti and $\text{Sb}_2\text{O}_5:\text{SnO}_2$ powder targets are shown in Figure 5.5:1. Each element or a compound has a unique crystal structure assembly and displays a X-ray diffraction pattern that is unique to its own structure and orientation.



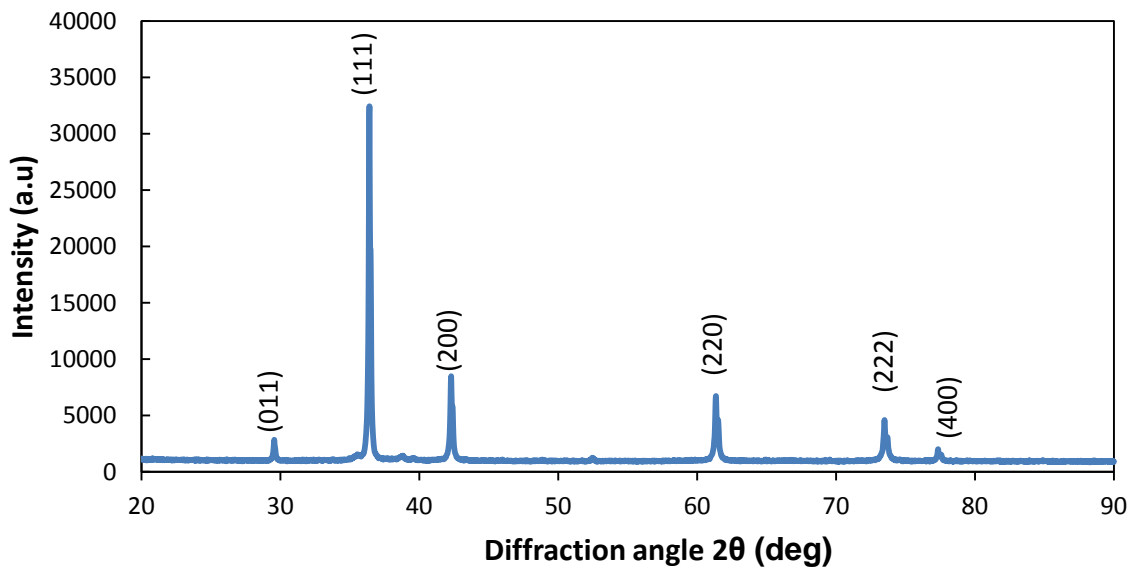
Tin fluoride



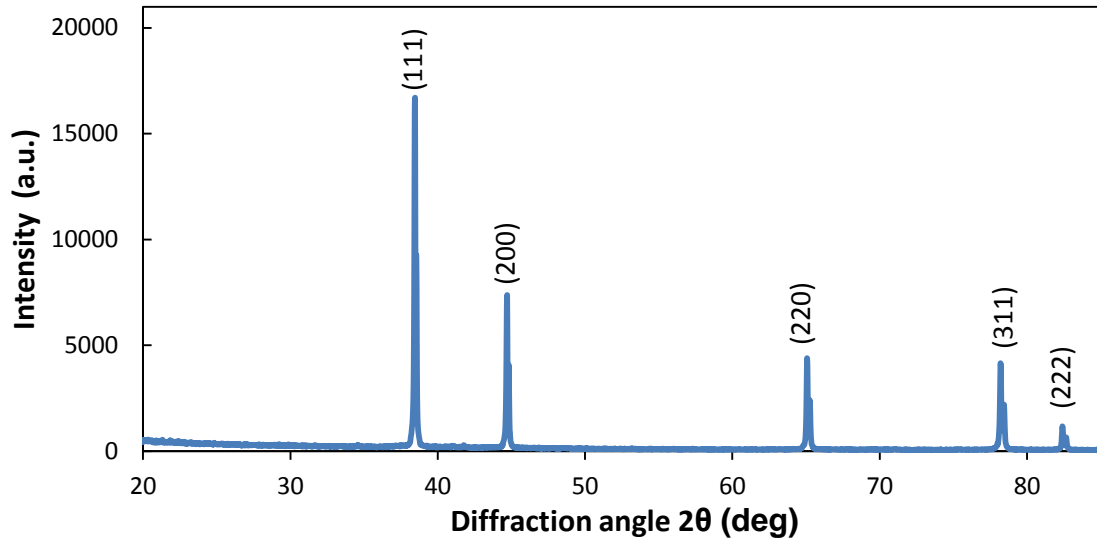
Tin oxide



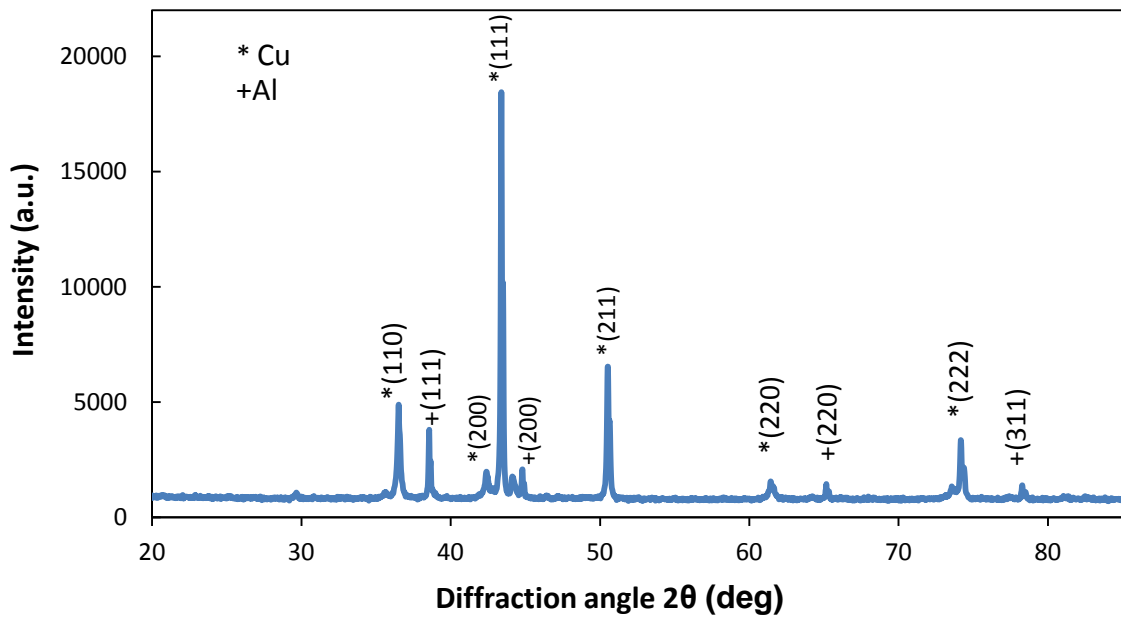
Fluorine doped tin oxide



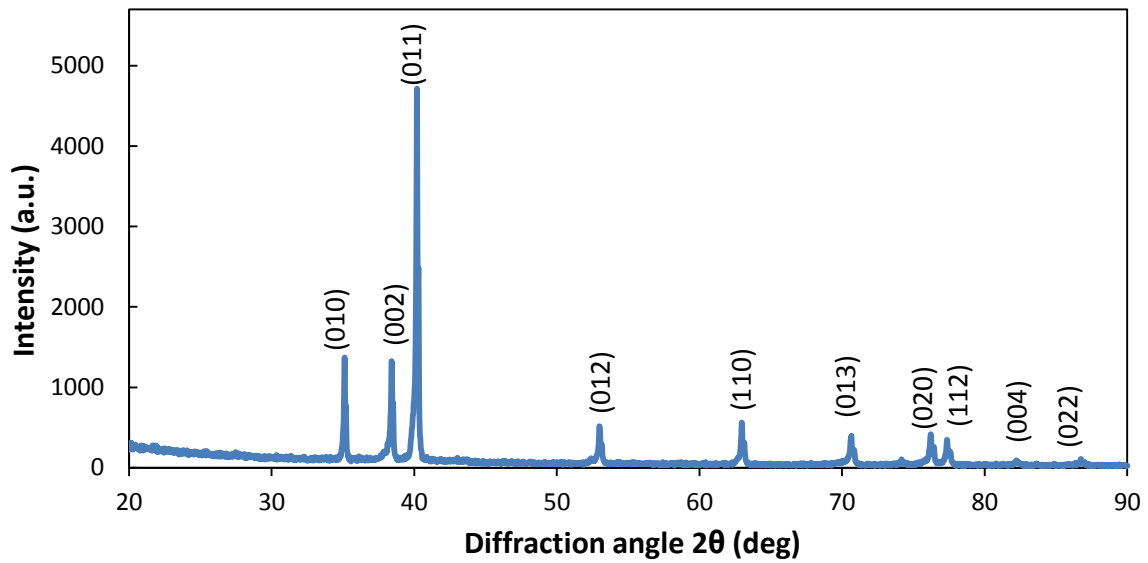
Copper metal base



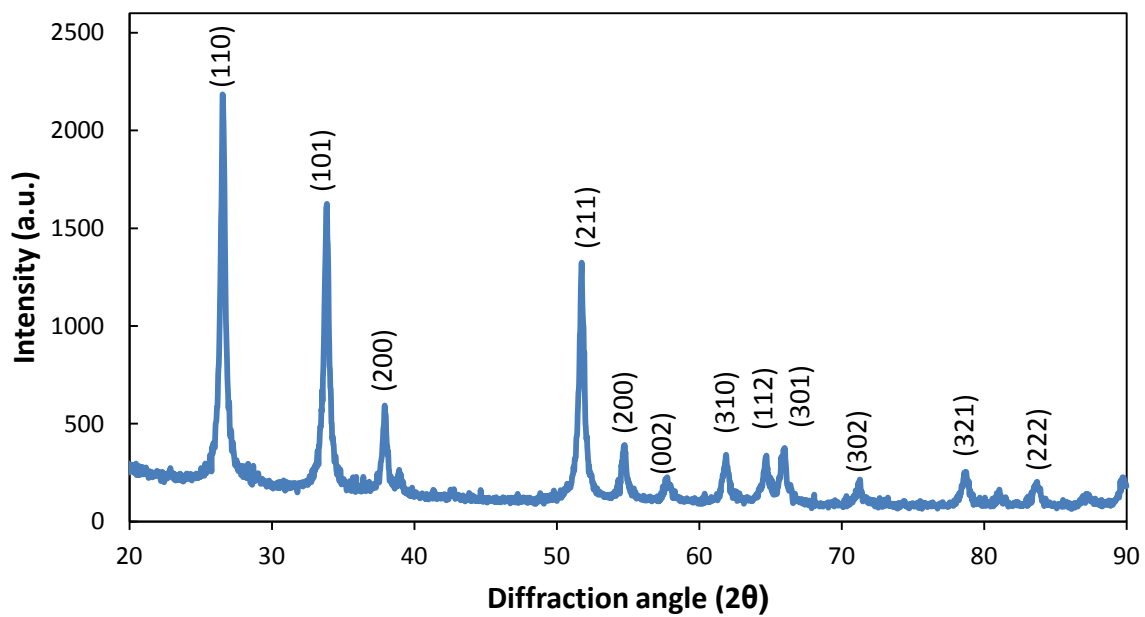
Aluminium metal base



Copper aluminium metal base



Titanium metal base



Antimony doped tin oxide

Figure 5.5:1 X-ray diffraction pattern for the powder targets used in this project

5.5.1 Target composition Vs sample composition

The chemical compositions of the FTO powder targets were obtained using SEM/EDS, using 10 kV as the accelerating voltage of the electron beam. The

EDS analysis of the tin oxide and the tin fluoride targets are shown below. The EDS analysis measurement shows a reasonable reproducibility of the chemical composition of the compound elements. The same powder sample was analysed four times and an error factor of +/- 3.5 at.% was calculated.

Table 5.5:1 The Compositional analysis of (a) SnO₂ and (b) SnF₂ powder targets prior to blending.

(a)			(b)		
Element	Weight %	Atomic %	Element	Weight %	Atomic %
O K	20.0	66.7	F K	28.4	67.3
Sn L	80.0	34.3	Sn L	71.6	32.7

The FTO targets were sputtered in argon and oxygen gas to yield a Ar/O₂ ratio of 9:1 at a total working pressure of 0.54 Pa. The power supply was set to a constant power mode of 400 W and a pulse frequency of 200 kHz and duty cycle of 90%. The total deposition run was 15 minutes to yield a 400 nm thin film. The EDS absolute data from the analysis of the FTO powder target and the subsequent films is given in Table 5.5:1. It is important to note that the oxygen arising from the glass substrate was not taken in to consideration during the analysis of this study because the energy of the EDS acceleration beam was optimised to 7 keV in order not to detect the elements of glass such as Si and Ca. The analysis of the un-doped tin oxide film are presented in Table 5.5:2. It was observed that there was 31.7 at.% tin and 68.4 at.% oxygen, which is close to stoichiometric SnO₂. It was observed that the fluorine content in the doped thin films was in the range of 0 - 7.4 at.%, which is low in comparison to the amount of fluorine incorporated into the powder

targets (0 - 13 at.%). This can be explained by the fact that fluorine is a light element ($Z=9$) and may be more readily scattered during gas phase transport through the high density plasma [146]. After all, as the sputtered particles move through the dense plasma, they will be scattered by the collisions with the argon and the oxygen gas atoms, and the mean free path decreases, therefore influencing the deposition profile.

Table 5.5:2 Compositional analysis of the powder targets and subsequent tin oxide and fluorine doped tin oxide.

Sample ID	Element at.% in targets			Element at.% in films		
	O	F	Sn	O	F	Sn
SnO ₂	66.7	0.0	33.4	68.4	0.0	31.7
SnO ₂ :F1	63.3	3.3	33.3	66.4	2.8	30.8
SnO ₂ :F2	60.0	6.6	33.3	64.0	5.3	30.7
SnO ₂ :F3	56.7	10.0	33.2	62.8	6.2	30.9
SnO ₂ :F4	53.4	13.0	33.3	60.1	7.4	32.5

5.5.2 Target composition Vs discharge voltage of CAO target

The composition of the Cu:Al metal base powder target was varied and the effect on the target voltage was investigated. The copper/aluminium powder targets were all sputtered at a fixed oxygen flow of 30 sccm (0.42 Pa), argon flow of 12 sccm (0.13 Pa), chamber pressure set to 0.55 Pa, the deposition period was set to 60 minutes. The power supply was set to 350 W using a pulse frequency of 100 kHz and duty cycle of 50%. Figure 5.5:2 shows the average target voltage of copper aluminium as a function of different target compositions. With a pure aluminium target, the average discharge voltage

was about -184 V. A pure aluminium metal base powder target has a very high oxidation rate, therefore when sputtered in a reactive environment, the target surface is immediately oxidised to Al_2O_3 . So the target tends to oxidise with higher content of oxygen, forming a dense oxidised layer, therefore effecting the sputter deposition rate [60]. When 25 at.% of Cu was introduced to the powder target content, the target discharge voltage increased to -225 V and further increased to -278 V at 50 at.% of Cu content. The discharge voltage was observed to further increase from -315 V to -470 V when the Cu concentration increased from 75 at.% to 100 at.%. The observed increase in the target voltage indicates that copper requires a higher potential to sputter the atom from the target.

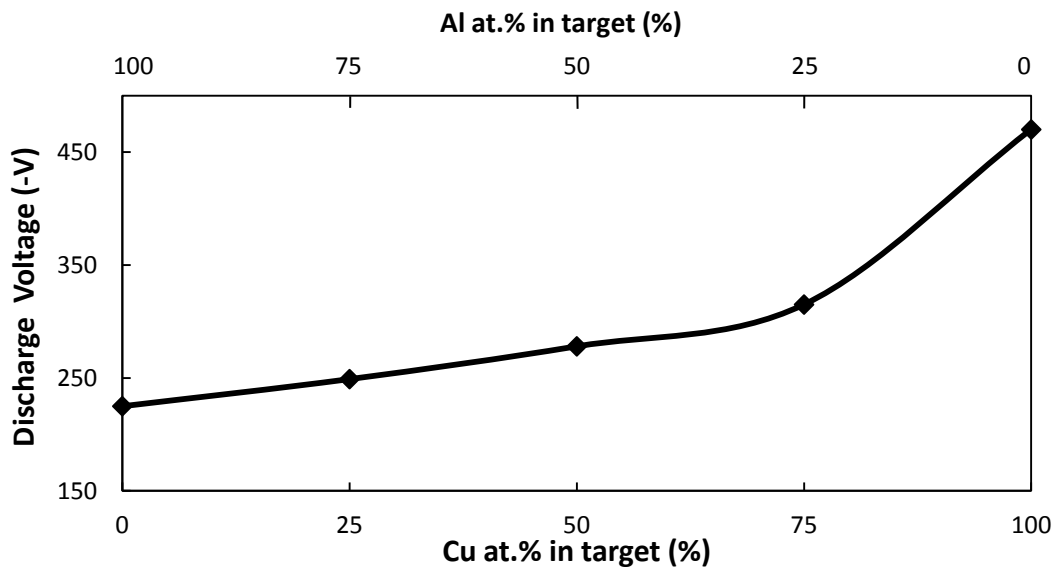


Figure 5.5:2 Average target voltage of a copper/aluminium target as a function of Cu at.% concentration deposited in oxygen environment.

The effect of the oxygen flow rate on the target voltage of a Cu:Al powder target with an atomic ratio of 75at.%Cu:25at.%Al and on the coating thickness were investigated. This study was carried in order to find the optimum oxygen

flow rate that would result in improving the optical transparency of the CAO coatings, while at the same time not decrementing the electrical properties. The relationship of the oxygen flow rate against the target voltage and the coating thickness is shown in Figure 5.5:3. It can be seen from the figure below, that the deposition rate decreases with increasing partial pressure, such behaviour was also reported in [60, 147]. The deposition rate can be obtained from the coating thickness and the relative deposition period of 60 minutes.

The deposition rate was observed to decrease as the oxygen gas was introduced to the chamber. Initially, sputtering in argon mode, the deposition rate achieved was $22 \text{ nm}\cdot\text{min}^{-1}$ at 0.13 Pa. when oxygen was introduced, the deposition rate reduced to $6 \text{ nm}\cdot\text{min}^{-1}$ at 0.41 Pa and a corresponding decrease in the target voltage was observed from -490 to -305 V. The decrease in the average target voltage can be attributed to the fact that as the O_2 is introduced to the deposition chamber, this increases the secondary electron coefficient, which in turn causes more ionisation of the sputtering gas and increases the ion current at the target, therefore, less potential is required to sustain the plasma discharge.

The decrease in the deposition rate may be attributed to the fact that O_2 chemisorbs on the target and forms a surface layer of adsorbed oxygen. This layer inhibits the sputtering of the target atoms and therefore reduces the deposition rate. In addition, with high content of O_2 in the deposition chamber, the Ar density is reduced. Since oxides have a lower sputter yield than metals, the net sputtering rate is reduced. Also the increase in the O_2 partial pressure,

increases the quantity of atoms in the chamber, which leads to more plasma collisions and therefore higher scattering of atoms to occur [60].

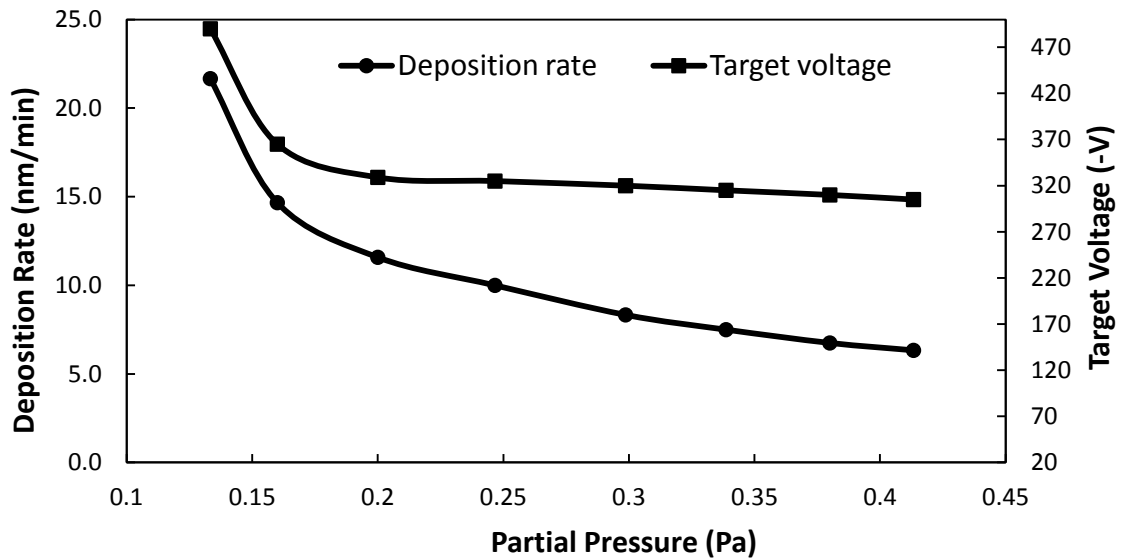


Figure 5.5:3 Deposition rate and the average target voltage as a function of oxygen partial pressure using a Cu:Al powder target.

5.5.3 Hysteresis studies of copper aluminium powder targets

To understand the effect of the reactive gas on metal-based powder targets, hysteresis studies were conducted using three powder targets using the same deposition parameters. Table 5.5:3 outlines the experimental parameters of the hysteresis trials including the composition ratio, oxygen flow rate and the total mass ratio of the powder target.

Table 5.5:3 Experimental parameters during the hysteresis study of Cu-Al powder target.

Target powder	Composition ratio (at.%)	Oxygen flow rate (sccm)	Total mass of target (g)
Cu	100	0-23	50
Al	100	0-23	50
Cu:Al	Cu:75,Al:25	0-10	Cu:43.2,Al:6.2

The first trial was for an aluminium powder target, the second was the copper powder target and the third trial was for a copper aluminium blended powder target. All the hysteresis trials were conducted with power set to 200 W and in a pulsed DC mode. The argon flow was set to 10 sccm, giving an initial base pressure of 0.12 Pa. The oxygen flow rate was set from 0-23 sccm and stepwise increased by 1 sccm every 2 minutes and the response of the target voltage (measured by an oscilloscope, connected directly to the magnetron) and the total pressure (measured by a Baratron capacitance manometer) were recorded. The measuring time intervals were sufficient to enable the target to stabilise. During the copper aluminium blended powder target trial, the oxygen flow was incremented at 0.2 sccm and the discharge voltage and the total pressure were recorded every 2 minutes.

The results of the hysteresis of the discharge voltage and the total pressure as a function of the oxygen flow rate for Al, Cu and CuAl blended powder targets are shown in Figure 5.5:4. It is apparent from Figure 5.5:4 (a) and (b) that an initial discharge voltage of -334 V and a total working pressure of 0.2 Pa was observed when sputtering in pure Ar. The cathode voltage remained stable until the O₂ flow rate was at 2 sccm due to getter effect of the Al target

surface, i.e. the adsorption of the O₂ molecules by the Al target surface. The target surface remained clean and the sputtered atoms were metallic. Other studies such as [148] have seen a slight increase in the discharge voltage prior to the transition state of the target surface. This can be due to formation of chemisorbed oxide layer which causes a decrease in the number of electrons emitted per incoming ion, also known as the ion secondary electron coefficient (γ_{ISEE}) [149]. However, in this study, such behaviour was not observed which suggests that it was due to the nature of the powder target which may have formed chemisorbed layers on the surface prior to sputtering.

As the flow of O₂ was increased to 5 sccm, the cathode voltage decreased to -163 V, corresponding to a metal oxide transition, a state where a target surface is fully oxidised and can no longer incorporate more O₂ atoms into its surface and it is sufficient enough to produce Al₂O₃. As the O₂ flow was increased from 5-22 sccm, the target surface entered the oxide steady state phase, which induces an increase in the γ_{ISEE} leading to a decrease in the cathode voltage to -160±10 V, and a corresponding partial pressure of 0.14 to 0.63 Pa was observed. No signs of unstable behaviour such outgassing was observed on the pressure measurements.

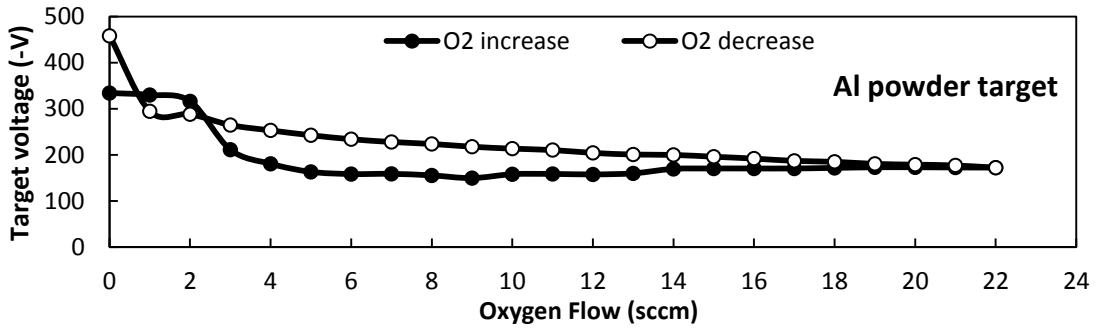
To complete the hysteresis loop, the O₂ flow rate was finally decreased using the 2 min. time interval between successive measurements. The cathode voltage began to increase at a steady rate of 6 V sccm⁻¹ from -172 V to -288 V as the O₂ decreased from 22 sccm to a critical value of 2 sccm. This slow increase in the cathode voltage corresponds to the transition stage between oxide and the metal mode. A further decrease in the O₂ flow to 0 sccm resulted in the cathode voltage increasing to -458 V, at which point the sputter

deposition returned to its original metal mode. The large spike in the discharge voltage as the target returns to the metallic mode cannot be interpreted as no reaction was observed in the pressure measurement, so the spike cannot be related to any gas related issues. So the increase of almost 100 V remains unclear, however, one interpretation could be related to a thermal matter i.e. the powder target was unable to dissipate heat directly, hence the observed increase in the target voltage. It is worth noting that the hysteresis loop did not follow a typical metal trend. One of the main reasons for this is due to the high oxidation state of Al. Other less prominent reasons could be due to the pumping speed of the pumps or the measured points are not stable enough, i.e. the 2 min. time interval between two measurements.

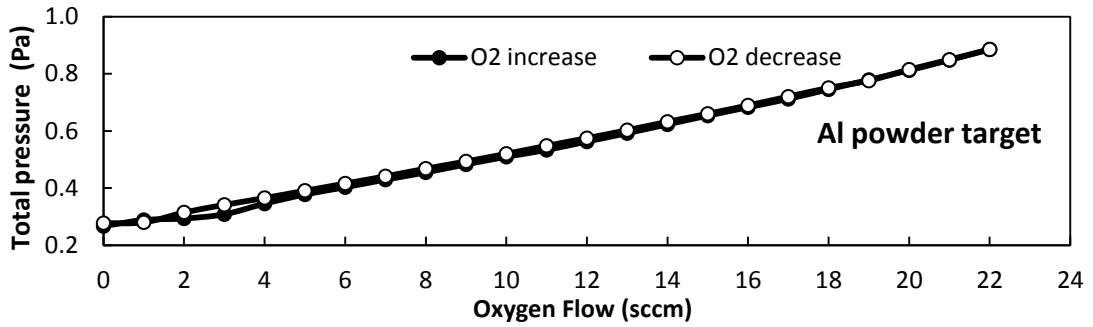
Figure 5.5:4 (c) and (d) shows the cathode voltage curve and total pressure of the O₂, respectively for the Cu powder target. Initially, when sputtering in argon mode, the cathode voltage was -460 V. As the O₂ flow increased to 5 sccm, the cathode voltage and the partial pressure slightly increased to -462 V and 0.11 Pa, respectively.

Due to the sputtering process, the target surface remains clean and the sputtered particles are of a metallic nature. Beyond 5 sccm of O₂, the target operates in a poisoned mode and the cathode voltage decreases to -316 V. It is apparent from the data that the cathode voltage continues to drop once the target has gone into poisoned mode. This is probably due to the fact that the 2 min. time interval was not sufficient for the target to adjust its surface composition to the new gas flow.

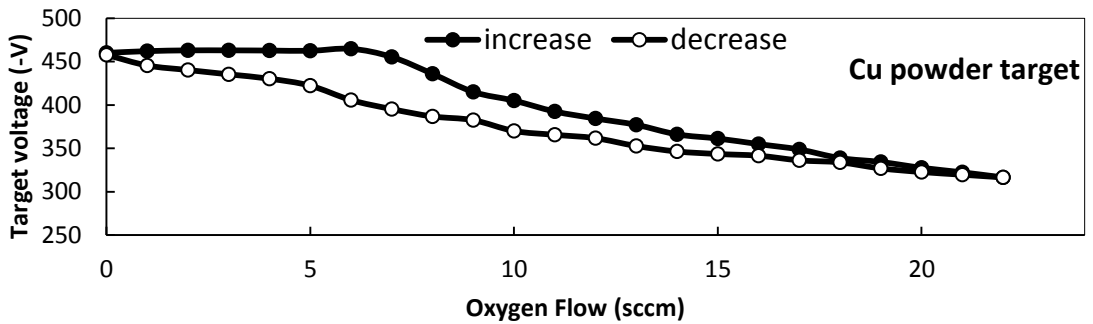
Figure 5.5:4 (d) and (e) shows the cathode voltage and the partial pressure of O_2 of for a Cu-Al powder target during the hysteresis trial. During this study, the O_2 flow was controlled from 0-9 sccm and step wise at 0.2 sccm every 2 min. The slow flow is required in order to allow the target to have enough time to react with the O_2 molecules. When the target was subject to an argon atmosphere, the cathode voltage was -428 V, which is 32 V lower than that of a pure Cu powder target. This can be attributed to the fact 25 at.% of the sputtered powder target was aluminium and therefore requires a lower voltage to be sputtered. It was noticed that as the oxygen flow was increased from 2-4 sccm, the voltage dropped from -390 to -320 V at a constant rate. This region can be classified as the transition mode of the target. As the oxygen gas was increased from 4-9 sccm, the cathode voltage decreased to -208 V at a slower rate, which indicated the formation of the oxide mode. To complete the hysteresis loop, the oxygen flow was decremented from 9-3 sccm and the measured cathode voltage increased at a slow rate from -208 to -322 V. The observed delay that the target requires to enter the transition mode maybe attributed to the formation of the oxide layer on top of the target surface which therefore required a longer time to sputter away. The oxygen flow was then decreased from 3-0 sccm and the voltage dropped to -422 V, which was lower than the cathode voltage at the start of the hysteresis. It was observed that the total pressure followed a linear relationship, as the oxygen gas was varied. This linear relationship suggests a stable sputtering system.



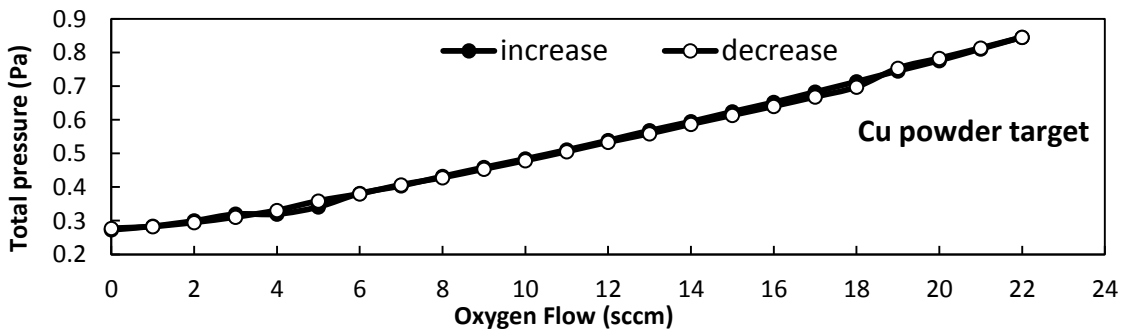
(a)



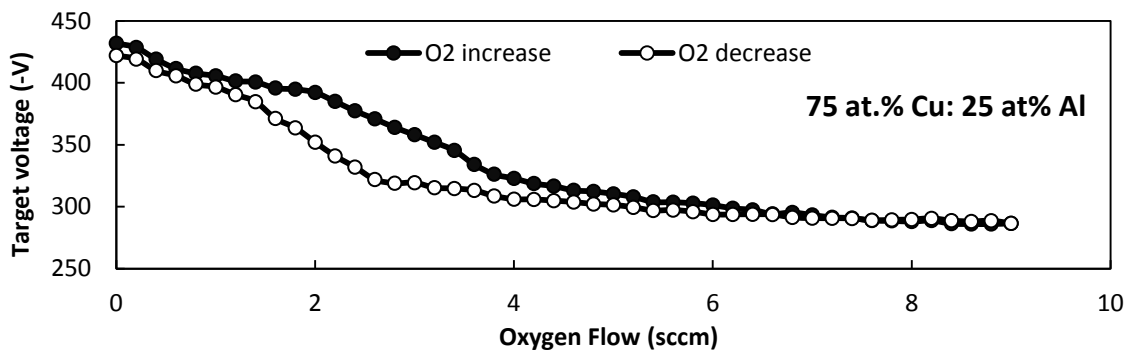
(b)



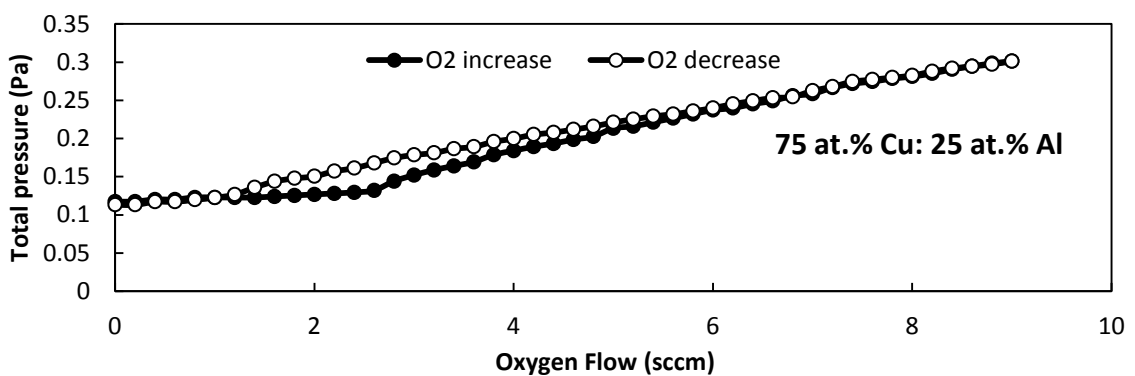
(c)



(d)



(e)



(f)

Figure 5.5:4 hysteresis analysis of pure metal powder target of (a-b) Al (c-d) Cu and (e-f) Cu:Al blended powder target.

5.5.4 Hysteresis study of titanium dioxide

A study of the effect of oxygen partial pressure on the titanium target voltage of a titanium powder target was also carried out. The oxygen flow rate was controlled using a MKS mass flow controller with a flow set from 0 sccm to 6 sccm, incremented in 0.2 sccm steps every 2 minutes. The target voltage was recorded from the pulsed DC power supply display control unit.

Prior to the input of the oxygen gas, the target was sputter cleaned in argon gas only at a chamber pressure of 0.36 Pa in order to remove the surface

oxide layer of the target. At each oxygen gas flow rate, sputtering took place until a constant target voltage was reached.

Table 5.5:4 Power supply experiment conditions during the Ti hysteresis study.

Power (W)	Frequency (kHz)	pulse off time (μ s)	Duty cycle (%) on
400	100	1	90

The chamber pressure was then adjusted to 0.6 Pa using the high-vac lever, after which the target voltage was measured. Following this, a given oxygen flow was introduced to the chamber and after a period of 2 minutes, the target voltage was measured, following this, the oxygen flow was incremented and target voltage re-measured.

Figure 5.5:5 outline the hysteresis behaviour of the titanium powder target while varying the oxygen flow rate. At low oxygen flow rates, almost all the reactive gas is gettered by the sputtered metal. This region is termed the metallic region. As a result, no changes in the base pressure of 0.6 Pa and average target voltage, -292 V, were observed. The metallic region persisted until the oxygen flow reached a critical value of 2 sccm at a base pressure of 0.6 Pa, where the flow rate of oxygen became higher than the gettering rate of the sputtered titanium, which led to a rise in the magnitude of the target voltage from -296 V to -322 V. This region is termed the transition region.

As the gas flow was increased from 4 sccm to 6 sccm, the base pressure increased from 0.59 Pa to 0.623 Pa while the target voltage increased in magnitude from -322 V to -348 V, which is the point at which the system entered the reactive or poisoned region. At this point, the target surface was

fully poisoned with oxygen and the target voltage reached equilibrium (the target voltage saturating at -348 V).

The oxygen gas flow was then reduced from 6 sccm to 4 sccm at 0.2 steps per every 2 minutes and it was noticed that the target voltage decreased in magnitude from -348 V to -343 V. As the oxygen flow was further decreased from 4 sccm to 2 sccm, the target voltage dropped from -343 V to -298 V. The oxygen was further reduced from 2 sccm to 0 sccm and the target voltage decreased in magnitude from -298 V and settled at -289 V. The reason for the delayed target voltage change compared to that when increasing the oxygen flow is mainly due to the low sputtering rate of titania compared to titanium, which means the oxygen flow rate has to be reduced to a point where it can no longer maintain the compound layer which was being continuously sputtered. At this point, the poisoned target is 'cleaned' again.

When the target is completely poisoned, any further increase in the reactive gas flow will result in a linear increase in the base pressure.

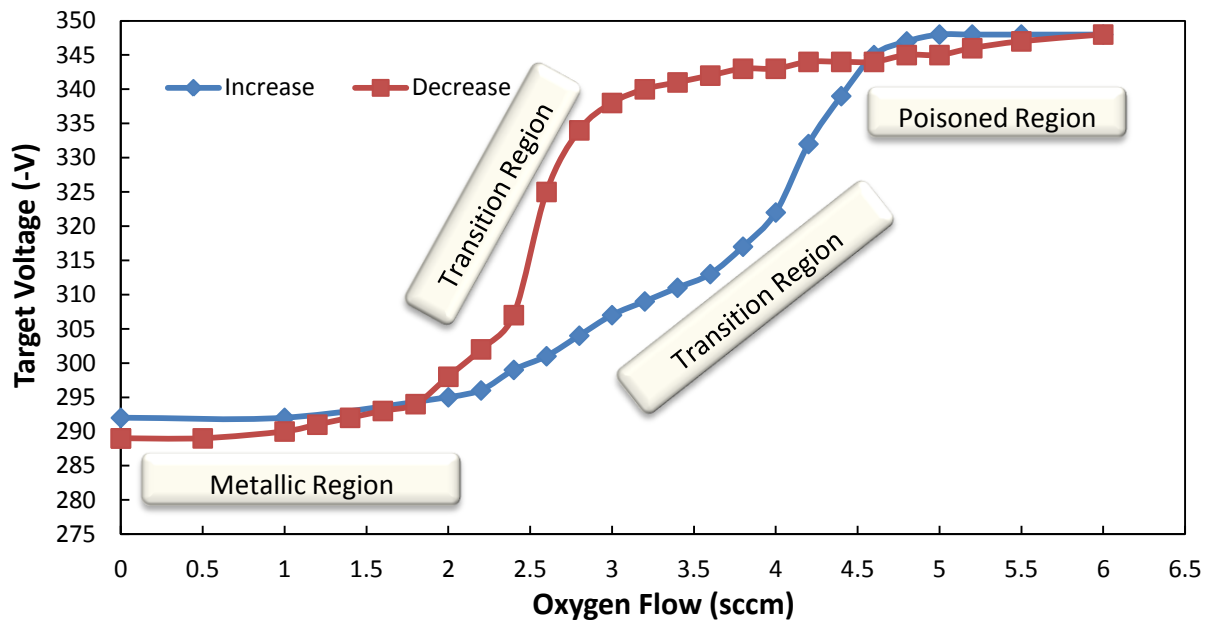


Figure 5.5:5 Hysteresis study of Ti metal base powder.

5.6 Effect of base pressure on target voltage of titanium target

To understand the effect of the base pressure on the target voltage of titanium, an experiment was prepared using the same conditions illustrated in Table 5.5:4.

Initially the argon flow was used to maintain a constant base pressure into the continuously pumped chamber and then used to initiate the plasma. The argon flow was set from 0 to 7 sccm (7 sccm is the full range scale) then the high-vac valve was used to increase the chamber pressure up to 0.6 Pa. The chamber pressure was increased at 0.067 Pa per every 2 minutes and the target voltage was recorded.

Initially, the argon gas flow was set to 0 sccm, at which point no plasma was initiated and target voltage was reading -663 V, this is effectively an open circuit voltage. As the argon pressure was increased to 1 sccm which corresponds to 0.06 Pa, the plasma was activated and the target voltage decreased in magnitude from -663 V to -387 V and began to decrease even further as the chamber pressure was increased. Figure 5.6:1 illustrates the behaviour of the target voltage as the chamber pressure was increased. It can be observed from Figure 5.6:1 that at low chamber pressure, the target voltage is higher than that compared to operating at a higher pressure. The decrease in the discharge voltage with pressure is a result of a reduced probability of electron recapture, yielding to higher ionisation.

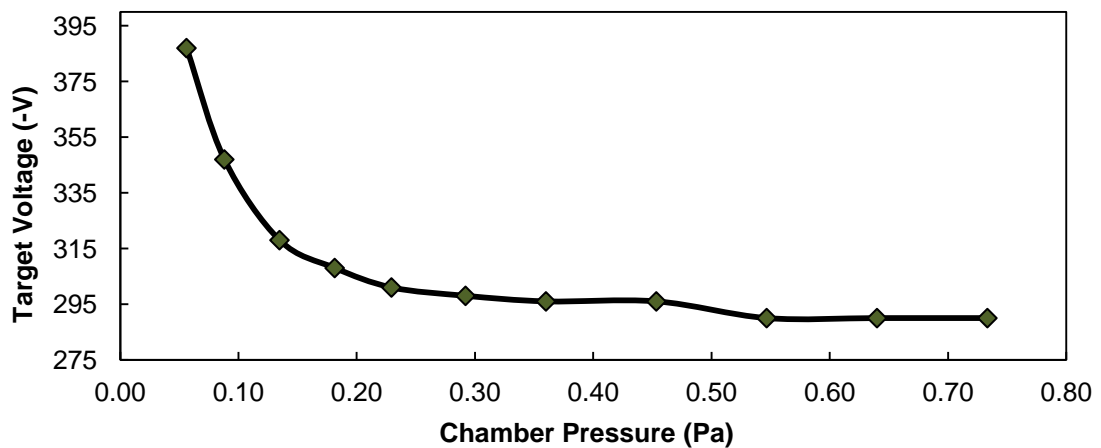


Figure 5.6:1 Effect of chamber pressure on target voltage for titanium powder.

A plot of the operating frequency against the time averaged target voltage is shown in Figure 5.6:1. The experiments were carried using the operating conditions shown in Table 5.5:4, at chamber pressure of 0.60 Pa. The plot outlines the fact operating at lower frequencies will increase the sputtering

rate as more energy is available to excite the sputtered particles, therefore the sputter yield is proportional to the target voltage.

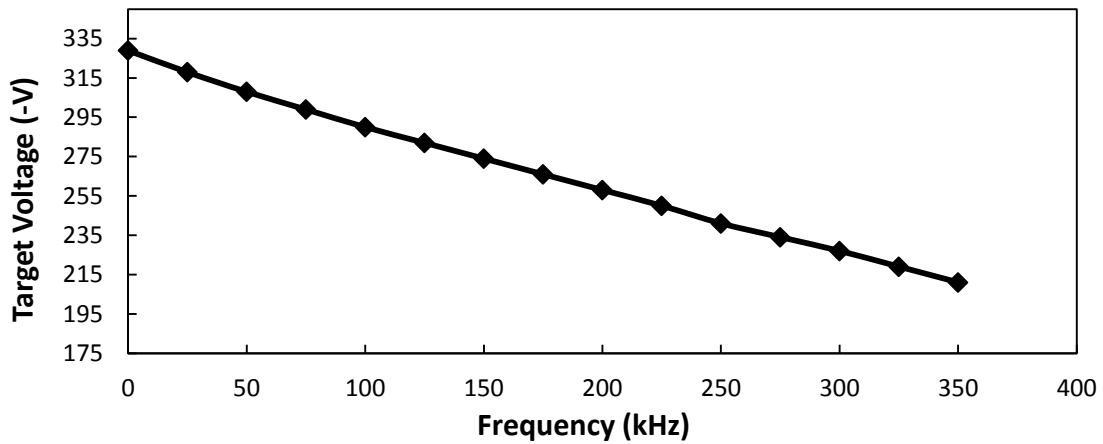


Figure 5.6:2 Effect of frequency on time averaged target voltage for titanium powder target.

5.7 Effect of oxygen flow rate on titanium target discharge voltage

A study of the effect of oxygen flow rate on the target voltage has been carried out. The oxygen flow rate was varied from 0 sccm to 8 sccm and the target voltage was recorded. Each experiment run was for a period of 2 hours using the conditions shown in Table 5.7:1Table 5.5:4. The average target voltage was recorded according to the Pinnacle Plus power supply display unit.

Table 5.7:1 Experimental parameters of oxygen partial pressure affect on target voltage.

Frequency (kHz)	Power (W)	Pulse off time (μ s)	Duty cycle (% on)	Ar flow (sccm)	O ₂ flow (sccm)
250	400	2	50	7	0 to 8

The use of a reactive gas such as oxygen will cause the formation of a compound layer on the target surface. It can be observed from Figure 5.7:1, that when sputtering in metallic mode, i.e. with no oxygen flow to the chamber, the target voltage was lower in comparison to that when increasing the oxygen flow. The increase in the oxygen flow, results in the oxidation of the titanium target surface, therefore additional discharge voltage is required in order to sustain the plasma discharge.

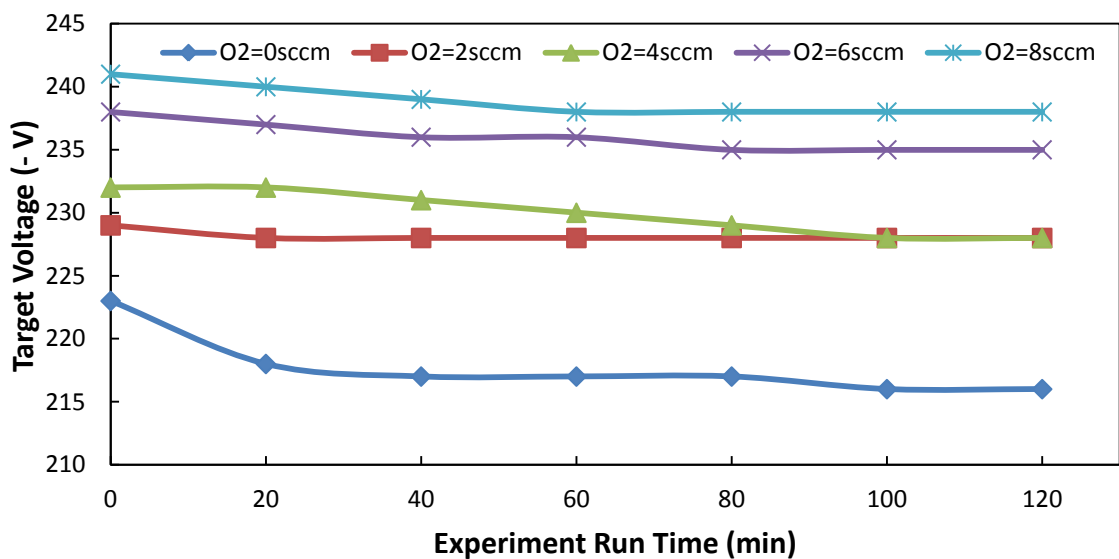


Figure 5.7:1 Target voltage Of Ti target at different oxygen flow rates.

5.8 Deposition rate in a titanium/oxygen system

Figure 5.8:1 outlines the variation of the deposition rate of titanium powder target as a function of oxygen flow rate. It can be observed that the deposition rate has a negative linear relationship as the oxygen rate was increased. This rapid decrease in the deposition rate was due to the oxidation of the target surface, resulting in a lower sputtering yield of the oxide [150]. This

phenomenon has been related to the chemical reaction occurring between the target surface and the oxygen gas [151].

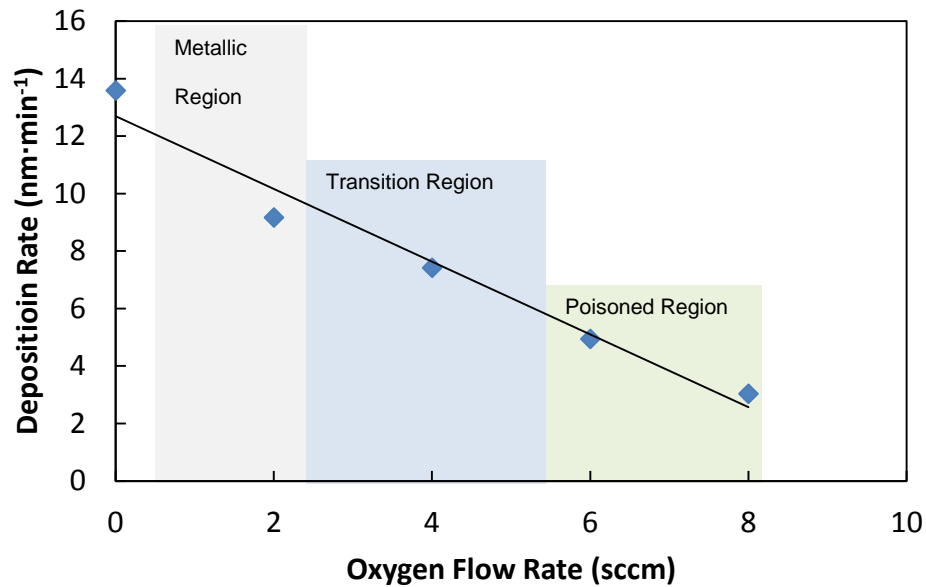


Figure 5.8:1 Deposition rate of a titanium target at different oxygen flow rates.

5.9 Summary and outlook

In Chapter 5 the fabrication and the characterisation of the powder targets were demonstrated. During the fabrication process, it is important to ensure the tamping of the powder targets is carried out using a heavy load, in order to yield a better thermal conductivity and therefore limit the arcing probability.

Using powder targets limits the use of high sputtering power due to the thermal instability; therefore, 500 W is the maximum power that can be used in this powder sputtering system.

Owing to the insulating nature of the powder target, the use of the pulsed DC bipolar configuration is necessary in order to offset the charge build up on the

target surface. Using such configuration yielded a well adhered and dense structured coatings.

The target-to-substrate separation (d_{t-s}) study conducted on the FTO powder target showed that 11 cm was the optimum separation distance needed to produce optimum electrical properties.

A compositional analysis conducted on the FTO powder target and the FTO coating showed a variation in the composition atomic percentage. This is attributed to the fact that as the sputtered particles travel through the dense plasma, light elements such as fluorine are easily scattered by collisions with the gas atoms which significantly influence the deposition profile.

The hysteresis study on the Cu:Al metal base powder as a function of the oxygen flow demonstrated that the metal target surface began to transition from the metallic mode to oxide mode between 2-4 sccm. The cathode voltage continued to drop once the target has gone into the oxide mode, This is possibly due to the fact that the measured points are not stable points, i.e. the 2 minutes interval between the measurement was not sufficient enough for the target to adjust its surface composition to the new gas flow.

Optimisation experiments were carried to study the influence of the base pressure, pulsing frequency and oxygen flow rate on the target voltage of titanium metal base powder target. It was observed that using low operating pressures resulted in higher target voltages. This is maybe attributed to the fact that titanium target was oxidised and requires a higher discharge voltage to sustain the plasma. Also reported, operating at lower frequencies increases the sputtering rate, as more energy is available to excite the sputtered

particles. It was determined from the optimisation of Ti experiments that the oxygen flow rate should be in the range of 2 to 4 sccm in order to produce transparent coatings. However the initial electrical tests show that the coatings were very resistive as it was not possible to measure them using the Hall probe system.

ANALYTICAL TECHNIQUES

The development of thin film coatings and devices requires the measurement and the study of their properties. In this research, it is important to characterise the thin films developed in terms of their electrical, optical, structural and compositional arrangement. The techniques involved were; the Van der Pauw technique (using the Hall effect measurement system), spectrometry (using the USB2000+ spectrometer), scanning electron microscopy (SEM), X-ray diffraction (XRD) and energy dispersive X-ray (EDX). The thickness of the thin films were measured by surface profilometry (Dektak ST stylus surface profilometer).

6.1 Introduction

The advancement of analytical techniques has been growing owing to the increasingly interdisciplinary field of thin films applications. The deposition of thin films under varying growth conditions, play the most significant role on the properties of the thin films. The variation in the structure of the thin films can be characterised structurally, chemically, optically and electrically. Each technique employs a unique way of analysing the thin film, for instance the structural and chemical analysis of a thin film provides information from the first few layer of the surface via applying an incident electron, ions or photon beams. These interact with the surface and emit a combination of secondary beams of electrons, ion or photons, which are captured by the analytical system for structural and chemical analysis of the thin film.

This chapter will only address the characterisation techniques relevant to this project for composition, morphology structure and film thickness.

6.2 Analysis of electrical properties

To understand the conductivity behaviour of the TCO coating that will be developed, four parameters will be investigated, these are charge carrier density, N_d , mobility, μ , the resistivity, ρ , and conductivity, σ . As the conductivity does not distinguish between hole and electron conduction, a Hall Effect study of the carriers is required to determine whether the coating developed is an n-type or a p-type; the carrier density will be used to determine this fact.

Conductivity, σ , is a measure of the electric current density, J , passing through the material at a given electric field, E . It is measured in $S \cdot cm^{-1}$ and it is given by the following equation;

$$\sigma = \frac{E}{J} \quad \text{Eq. 6.2:1}$$

The reciprocal of conductivity is known as the electrical resistivity, ρ , with units of $\Omega \cdot cm$. For a given dimension of the coating (l = length, b = width, t = thickness, R = resistance), the electrical resistivity is given by the following equation;

$$\rho = R \times \left(\frac{b \times t}{l} \right) \quad \text{Eq. 6.2:2}$$

If the coating has a square dimension i.e. $b=l$, then equation Eq.6.2:2 becomes;

$$\rho = Rt = \rho_s \quad \text{Eq. 6.2:3}$$

ρ_s , is known as the sheet resistivity, which refers to the conductivity of one square of the film and it represents the resistance between two sides of the square and it is independent of the square size with units of Ω/square . It can be seen from equation 6.2.2 that the electrical resistivity is greatly influenced by the thickness of the coating. As a result, this will affect the conductivity of the coating.

Charge carrier density and mobility can be measured by employing the magnetic and the electric field. The force that relates the two factors is termed the Lorentz force, F , which is the total force exerted on a charged particle travelling at velocity, V , through a magnetic field, B , and the electric field, E ;

$$F = -e \cdot V \cdot B \quad \text{Eq. 6.2:4}$$

Figure 6.2:1 outlines the vector direction of the instantaneous velocity of the electrons and the magnetic field;

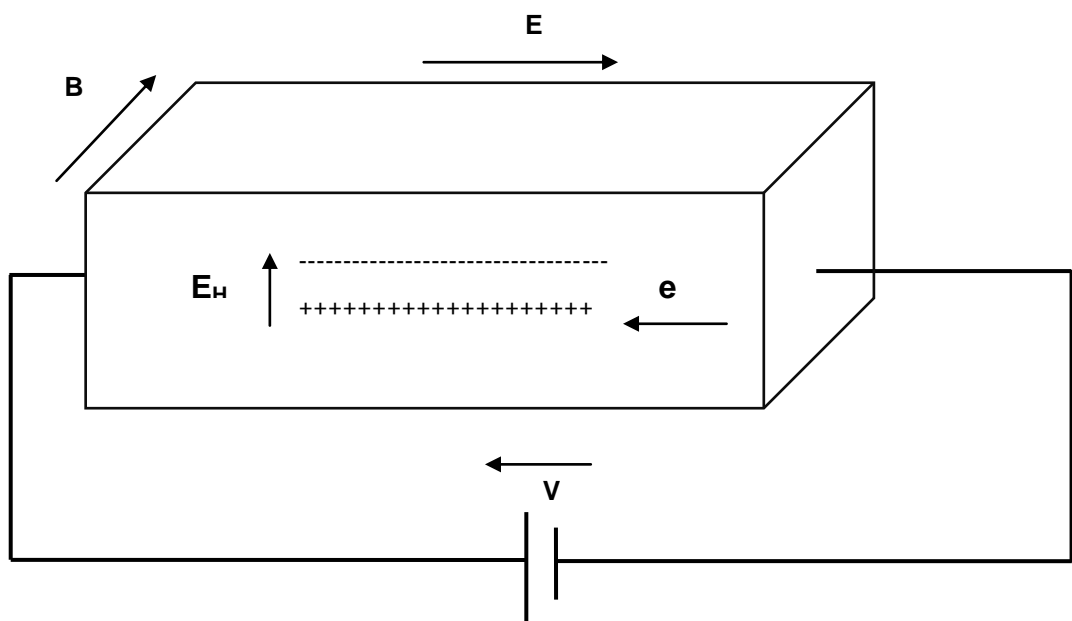


Figure 6.2:1 Schematic of the Hall effect.

The direction of the Lorentz force is determined using the right-hand-rule (obtained by pointing the right thumb in the direction of the current and the fingers curl in the same sense as the magnetic field). The electron direction is determined by the Lorentz force and as a result, the electrons are pushed and

mounted upwards while the other side becomes depleted of electrons, this produces the Hall field, E_H as can be observed in Figure 6.2:1. The measurable difference in the potential is termed the Hall voltage, V_H . The Hall field acts on the electrons with the same magnitude as the Lorentz force but in the opposite direction.

Since, E , E_H , and, B , are mutually perpendicular and given that the instantaneous velocity, V , equal to the drift velocity, V_d , as the thermal velocities, V_{th} , of a charged particles in all direction are equated to zero, hence, the Hall field can be given by the following equation;

$$E_H = V_d \cdot B \quad \text{Eq. 6.2:5}$$

Given that drift velocity is the product of the electron mobility, μ , and electric field, E ,

$$v_d = \mu \cdot E \quad \text{Eq. 6.2:6}$$

Therefore the Hall field is;

$$E_H = \mu \cdot E \cdot B \quad \text{Eq. 6.2:7}$$

It can be deduced from the above equation that the Hall field is a product of the mobility of the charged particle, the electric field and the magnetic field.

6.2.1 Hall effect measurement system

In 1879, Edward Hall determined the sign of the moving charges that form the electrical current by studying the effect when he applied a magnetic field perpendicular to the direction of the current flowing through a conductor and observed that the electrical field is created in a direction that is perpendicular to both. The Hall effect is important in the analysis of semiconductors to determine their electrical characterisation.

The Hall Effect Measurement System (HEMS) is a system used to make electrical measurements of the deposited thin films. It utilises the Van der Pauw's technique to measure the charge carrier density, N_d , Hall mobility, μ , resistivity, ρ , and conductivity, σ , of the thin film. The HEMS used to determine the electrical properties during this research is the HEMS-3000 system manufactured by ECOPIA.

6.2.2 Van der Pauw technique

The Van der Pauw method was used to measure the resistivity of the TCO coatings. Four Ohmic contacts are placed on the periphery of the TCO coated sample as shown on Figure 6.2:2,

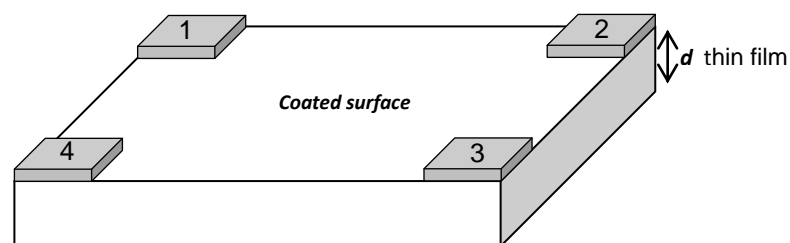


Figure 6.2:2 Ohmic contact placement on TCO thin film

Initially, the Van der Pauw technique is used to measure the sheet resistance, R_s , of the coated sample. There are two characteristic resistances; R_A , and R_B , associated with the four terminals, which Van der Pauw demonstrated with the following two equations [152];

$$R_A = \frac{V_{43}}{I_{12}} \quad \text{Eq. 6.2:8}$$

$$R_B = \frac{V_{14}}{I_{23}} \quad \text{Eq. 6.2:9}$$

Where;

V_{43} Is the measured voltage across contact terminals 4 and 3.

V_{14} Is the measured voltage across contact terminals 1 and 4.

I_{12} Is the measured current across contact terminals 1 and 2.

I_{23} Is the measured current across contact terminals 2 and 3.

The characteristic resistances, R_A , and, R_B , are found by applying a dc current, I , across contact terminal 1 and out of contact terminal 2 and measuring the voltage across contact terminals 4 and 3 (V_{43}). The same process is repeated by applying dc current, I , across contact terminal 2 and out of contact terminal 3 while measuring the voltage across contact terminals 1 and 4 (V_{14}). R_A , and, R_B , can then be calculated using equations 6.2:8 and 6.2:9 respectively.

The characteristic resistances, R_A , and, R_B , are related to the sheet resistance of the thin film through the Van der Pauw equation;

$$e^{\left(-\pi \frac{R_A}{R_S}\right)} + e^{\left(-\pi \frac{R_B}{R_S}\right)} = 1 \quad \text{Eq. 6.2:10}$$

Equation 6.2:10 can be solved numerically for, R_S , and the resistivity, ρ , can be calculated using the following equation:

$$\rho = R_S d \quad \text{Eq. 6.2:11}$$

The sheet carrier density, n_s , can be determined using the Van der Pauw's technique by measuring the Hall voltage, V_H . The Hall voltage is obtained by forcing the dc current through the opposing pair of the terminal contacts 1 and 3, and measuring the Hall voltage, V_H , across the terminal contacts 2 and 4 (V_{24}) and continuing to taking a series of voltage measurements at a constant current, I , and constant magnetic field, B , that is applied perpendicular to the thin film sample. Once the Hall voltage is determined, the sheet carrier density can be calculated using the following equation;

$$n_s = \frac{IB}{q|V_H|} \quad \text{Eq. 6.2:12}$$

Then the bulk carrier density can also be calculated using the following equation;

$$n = \frac{n_s}{d} \quad \text{Eq. 6.2:13}$$

To ensure the consistency of the results, the following factors must be considered;

- The quality and size of the ohmic contacts
- The size of the ohmic contact compared to the size of the measured thin film sample
- The uniformity and accuracy in thickness measurement

6.3 Analysis of optical properties

The optical analysis is a quantitative measurement of the thin film to determine the transparency and the reflection as a function of wavelength, typically in the range of 200-2500 nm to cover the UV-VIS-IR spectrum.

The optical analysis of a sample is determined using a spectrometer device which transmits light through an optical fibre over a range of wavelengths, which strikes the sample surface where the light is either transmitted (T), reflected (R) or absorbed (A). The total output light should sum to 1, therefore adding the three factors, realises the following relationship,

$$T + R + A = 1 \quad \text{Eq. 6.3:1}$$

The light transmitted through the fibre optics consists of a stream of photons that interact with molecules of the thin films, which absorb the photon, and therefore reduce the intensity of the penetrating light beam.

During this research, the optical properties of the developed thin films were measured by an Ocean Optics USB200+ spectrometer system. To minimise the system errors and incoherence during the measurements, the intensity of the light passing through a microscope glass slide identical to the sample substrate was measured and taken as a reference. The reference provided the absorption of light by the glass slide. A reference spectrum is a spectrum taken with the light source on, and when the light source is blocked in the sampling region. The reference measurements are then stored and used as way of calibrating the instrument prior to the optical analysis of the thin film samples. A typical schematic diagram for the transmission, absorption and the reflection configurations are demonstrated in the figure below;

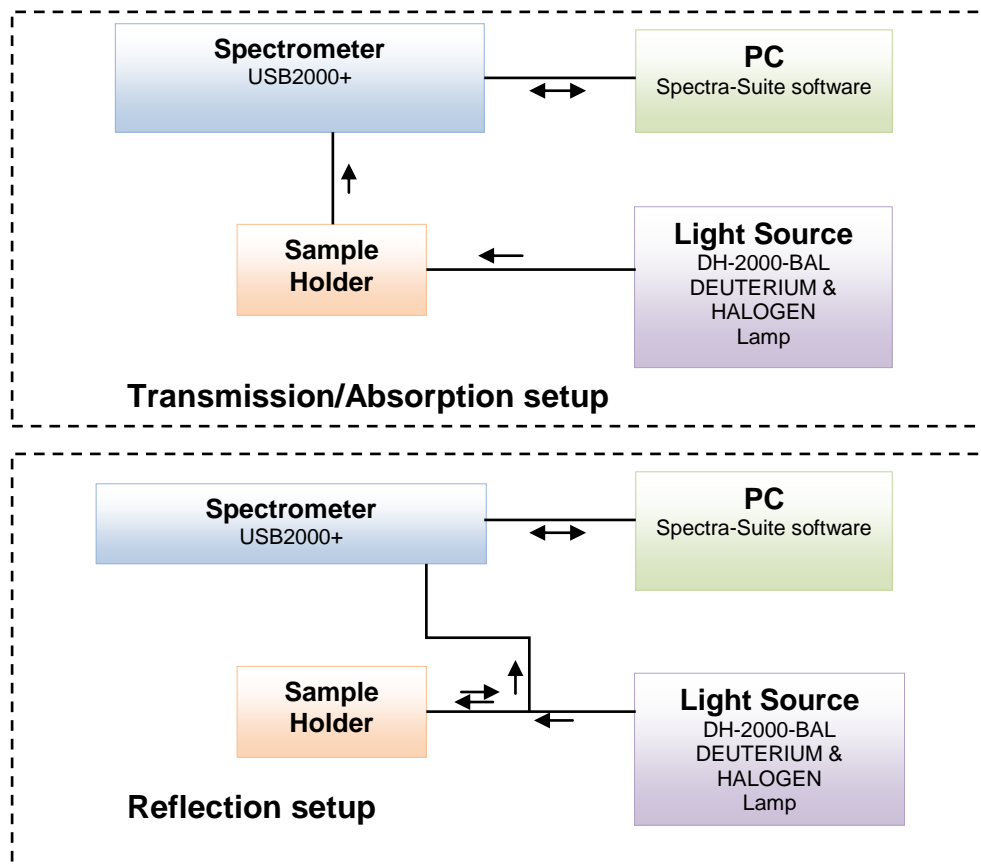


Figure 6.3:1 The instrumental setup for measuring the Transmission, absorption and the reflection of the coating.

The transmission is expressed as a percentage (T %) and it is defined as the percentage of the light energy that is transmitted through the thin film sample relative to the amount that passes through the reference. The Spectra-Suite software calculates the T% using the following equation;

$$T = \frac{S-D}{R-D} \times 100\% \quad \text{Eq. 6.3:2}$$

Where: S is the sample intensity at a specific wavelength, D is the dark intensity at a specific wavelength and R is the reference intensity at a specific wavelength

Absorption is a measure of how much light a coating can absorb. In general, absorption is related to the thickness of the coating, as the thicker the coating, the higher the chances of the molecules of the coating obstructing the photons pathway and absorbing the photon, hence reducing the intensity of the light passing through the coating. Spectra-Suite calculates the absorbance (A) using the following equation;

$$A = -\log\left(\frac{S-D}{R-D}\right) \quad \text{Eq. 6.3:3}$$

The transmission and absorption setup is the same, the light source transmits light (wavelength 300-950 nm) via an optical fibre cable onto the sample holder. The light waves interact with the coating and the transmitted light from

the sample is fed through another optical fibre cable to the spectrometer where the light waves are converted into digital data which are transmitted to the computer via a USB bus.

Reflection is expressed as a percentage (R%), relative to the reflection from a standard reference sample. Reflection is defined as the light energy which is reflected from the thin film sample without changing its wavelength.

Depending on the surface of the coating, reflection can be specular, meaning the angle of incidence is equal to the angle of reflection, or it can be diffuse, meaning the angle of incidence is not equal to the angle of reflection. Some coatings have a glossy finish, which provides more specular reflection than diffuse reflection. Spectra-Suite software determines the R% as follows;

$$R = \frac{S-D}{R-D} \times 100\% \quad \text{Eq. 6.3:4}$$

In a reflection setup, the light source transmits the light energy via the optical fibre cable onto the sample, the sample holder holds the optical fibre at a 90 degree angle to the coated sample and the output of the reflection probe carries the light from the sample to the spectrometer via an optical fibre. The spectrometer converts the received light intensity into digital data and sends it to the computer via the USB bus.

6.4 Structural analysis

It is important to determine the morphology and topology of the coating surface, the crystal structure, grain size, and composition. The analysis techniques will include scanning electron microscopy (SEM), energy dispersive X-ray spectroscopy (EDS) and X-ray diffraction (XRD). The SEM system to analyse the topography of the films was manufactured by Carl Zeiss Ltd, model number Supra 40VP and the software used was SmartSEM. The EDS systems used in this research was manufactured by EDAX Inc, model number Apollo 40SDD and the software used was Genesis.

6.4.1 Scanning electron microscopy

The scanning electron microscope (SEM) is the most frequently used technique for the study of the morphology of thin films. The SEM can give very detailed images, which can be used to study the adhesion, surface topography, surface defects and structure of the coating. The SEM can also be used to study the chemical composition of the coating by changing the mode of the SEM to energy dispersive X-ray spectroscopy (EDX) or to wavelength dispersive X-ray (WDX) spectroscopy, which acts as an electron probe micro analyser (EPMA). When the SEM is in the EPMA mode, it strikes the sample surface atoms with high energy electrons and during the process, X-rays characteristic of the sample atoms are emitted and collected (the energy of the electrons was set to 7 KeV in order not to detect the elements of the glass substrate). These can then be identified and counted, which gives information regarding the concentration of the atoms in the sample and therefore the coating composition.

In a typical SEM configuration, an electron is thermionically emitted from a cathode filament (usually tungsten or LaB₆) and it is attracted to an anode. The electrons are focused into a fine spot size of circa 5 nm by using two condenser lenses. As the electrons are condensed onto a fine spot size, an objective lens, which contains a pair scanning coils, is used to deflect the beam in a linear or raster fashion onto an area of the sample surface.

The energy of the electrons can be accelerated from a few thousand electron volts to 50 keV. As the fast moving electrons strike the sample surface, the primary electrons decelerate, and begin to lose energy inelastically to the sample atomic electrons and the lattice. After some time, the beam begins to spread across the sample surface due to random scattering events, creating a huge number of electron excitation and a teardrop shaped dimension is formed. The excited electrons leave the sample surface and emit X-rays, light, and heat. The appropriate detectors on the SEM detect and differentiate these signals to convert into an image.

The characterisations that will be included in this research are as follows;

SEM micro images of the coatings will be used to determine the surface topography and if there are any surface defects such as pin holes or micro stress which may introduce surface stress on the coating after a period of time.

Also, chemical characterisation will be compiled by studying the atomic weight ratio of the coatings to determine the composition ratio of the coating.

6.4.2 X-ray diffraction

X-ray diffraction is a non-destructive technique used to determine the crystalline phases and the structure (strain state, grain size, defect structure, epitaxy, phase composition, preferred orientation) in crystalline materials [153].

In a typical X-ray diffraction system, the sample is exposed to a beam of monochromatic X-rays, and as a result, the atomic lattice of the sample diffracts the beam at specific angles producing a unique diffraction pattern, as shown in Figure 6.4:1. The diffraction pattern produced includes the angle of diffraction and the intensities of the diffracted beam, which can be represented using Bragg's equation,

$$AB + BC = n\lambda \quad \text{Eq. 6.4:1}$$

Consider the length of the incident and the reflected beams are equal,

$$AB = BC$$

Therefore,

$$n\lambda = 2AB$$

Using simple geometry, yields,

$$\sin\theta = \frac{AB}{d}$$

$$2d\sin\theta = n\lambda$$

The diffraction angles can be used to calculate the interplanar atomic spacing (d-spacing) using the Bragg's law equation shown below;

$$n\lambda = 2d_{hkl}\sin\theta_{hkl} \quad \text{Eq. 6.4:2}$$

Where, d , is the distance between atomic layers in the crystal structure, θ , is the angle of incidence of the reflected X-ray beam, n , is an integer, λ , is the wavelength of the incident X-ray beam usually of value 0.154 nm for a copper X-ray source. A schematic representation of Bragg's law is shown in Figure 6.4:1. The important point is that the path length is the same, therefore the diffracted beam is in phase and there is constructive interference, rather than the destructive interference which occurs at all angles other than the Bragg angle.

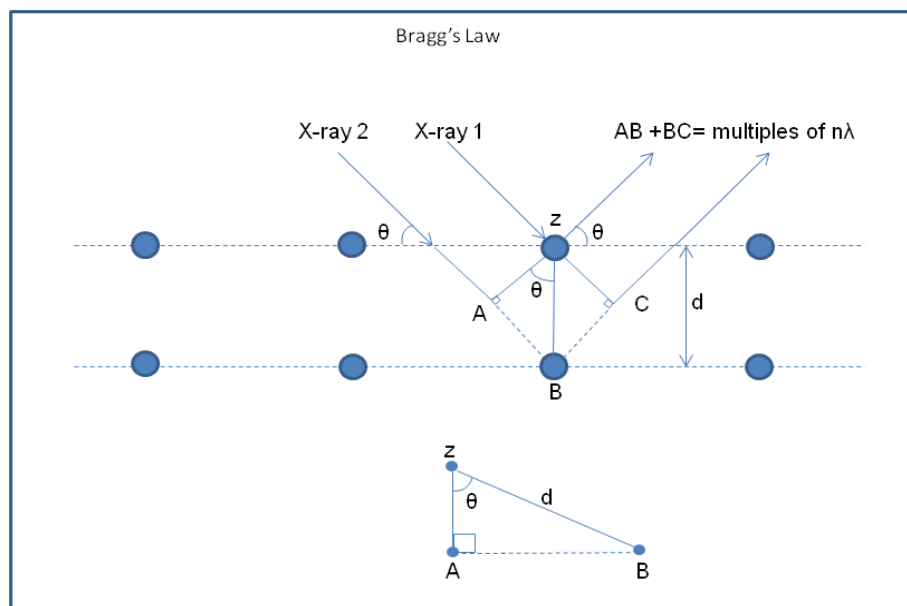


Figure 6.4:1 Schematic representation of X-ray diffraction operating in the θ - 2θ mode.

The interatomic distances of the material, also known as the d -spacing are used to characterise the type of the material. This is done by comparing the XRD trace with that published by the Joint Committee for Powder Diffraction

Standards (JCPDS). The measured XRD trace can also give information about the preferred orientation (texture of the material), defect structure (such as strain analysis), phase composition and grain size of the crystallites in the sample

The atom arrangement within a crystalline lattice can also be found from the position of the diffraction peak and the intensity of the peak can be used to assess any preferred orientation in the structure. The diffraction peak widths are used to obtain an accurate estimate of the grain size using the Scherrer equation shown below [154];

$$D = 0.9 \times \left(\frac{\lambda}{\beta \sin \theta} \right) \quad \text{Eq. 6.4:3}$$

Where, D , is the grain size, λ , is the wavelength of the X-ray source (0.154178 nm for copper radiation), β , is the width of the diffraction peaks at full wave half maximum in rads (FWHM) and, θ , is the diffraction angle measured in radians. Due to the deposition nature of PVD techniques, PVD coatings tend to show strong textures because the coating flux arrives from a limited set of directions. Low energy lattice arrangements are usually formed which results in preferred planes (111), (110) etc. laying parallel to the surface. A unique peak appears on the XRD data collector only when the reflected data meets Bragg's law. This unique peak is used to analyse the nature of the lattice such as the orientation and the texture.

Generally, the XRD patterns of thin films measured using the conventional θ - 2θ scanning mode generally produce a weak signal from the thin film and an intense signal from the substrate. One way to avoid the strong signal from

the substrate and to achieve a stronger diffraction signal from the thin film is to perform the Grazing Incident X-ray diffraction method (GIXRD). The method is based on the fact that at X-ray energies, the refractive index of the materials is less than 1.0. One can then achieve total external reflection from the surface if the incident angle is set to a small value typically in the range of 0.3-3°. At this point, the path length of the X-ray beam through the thin films increases and the substrate is not visible to the X-ray beam, but only evanescent waves penetrate into and scatter from it. The strongest X-ray signal intensity is therefore achieved at the surface as desired. This gives a dramatic increase in the films signal-to-background ratio since the path length increases when the grazing incidence angle is used, the diffraction volume increase proportionally.

The grazing incident and the diffracted beams are made nearly parallel to substrate by means of narrow slit (put along the incident beam) and mirror slits (put along the Soller slit on the detector side). During the collection of the diffraction spectrum, only the detector rotates through a set angle (usually 20-70°, 2θ range), and keeping the incident angle, the path length and irradiated area constant. The Soller slit on the receiving side, allows for beams that are nearly parallel to the surface to arrive to the detector, this adds to the advantage of reducing sensitivity to sample displacement from the rotation axis. The schematics of the GIXRD are shown below.

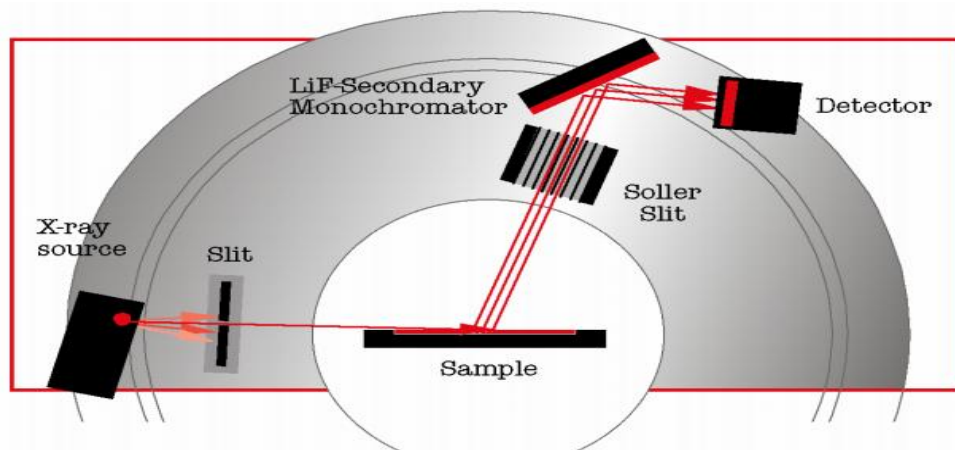


Figure 6.4:2 GIXRD device setup.

During the analysis of the data, it is important to consider instrumental effects such as the instrumental broadening of the X-ray beam, this can be estimated by analysing a calibration sample such a Si or an Al sample, which then the collected data is compared to the JCPDs data and the instrumental broadening is calculated. This broadening is the same for all the samples, so it is subtracted during the calculation of the grain size estimation.

During this research, the PANalytical Xpert³ MRD X-ray diffraction system was used. The anode material used during the XRD scans was Cu with K_{α} wavelength of 0.1541874 nm. Due to thickness of the thin films, Grazing incidence XRD (GIXRD) thin film analysis was used for phase identification.

The XRD patterns for the measured thin films, were analysed using HighScore Plus software developed by PAN analytical. The following treatments were carried on each XRD pattern.

- Determining the background;

In order to carry any phase analysis or peak search, HighScore Plus determines the background of the anchor scan,

- Peak search;

Peak search automatically locate the peak position and the peak intensity. It is also able to determine the $K\alpha_1$ and $K\alpha_2$ peaks,

- $K\alpha$ stripping;

The $K\alpha$ is a doublet consisting of $K\alpha_1$ and $K\alpha_2$ radiation. This function is used to eliminate the $K\alpha_2$ from the scanned XRD pattern. $K\alpha_2$ is the emission line given by the electron transition to the innermost “ K ” shell (quantum number 1) from the $2p$ orbital of the second or the, L shell (with quantum number 2). $K\alpha$ is by far the strongest x-ray spectral line for an element bombardment because it attains enough energy to cause a maximally intense X-ray emission.

- Profile fitting

It is a function used to characterise the peak profiles of the XRD pattern by applying a range of mathematical profile functions to determine the peak characteristics such as the position, intensity, width and shape.

- Line profile analysis (LPA)

It is a function used to determine the microstrain and the crystallite size for a single or a range of peaks. LPA uses the integral breadth (defined as the net peak area / peak height) as a measure of the peak width and the shape of the peak Φ (defined as the FWHM / integral breadth) to describe the peak variation. The algorithm deconvolutes the profile into a mathematical Gaussian and a Lorentzian part. The line profile automatically calculates the

instrumental broadening values *LORENTZ* $B_{instr.}$ and *GAUSS* $B_{instr.}$ and effectively calculates the strain and the crystallite size accordingly.

Crystallite size and the lattice strain calculations can also be done manually using the Scherrer calculator function available in high score software. The basis of simple size or strain analysis are the following two equations;

The Scherrer equation defined as,

$$crystallite\ size\ (average) = K\lambda / (B_{size} \cos\theta) \quad \text{Eq. 6.4:4}$$

And the lattice strain defined as,

$$Lattice\ strain\ (mean\ lattice\ distortion) = B_{strain} / (4\tan\theta) \quad \text{Eq. 6.4:5}$$

Where B is the structural broadening, which is the difference in the integral profile width between the standard and the sample measured. The following two equation are used to calculate the B value for the crystallite size and the lattice strain,

$$B_{(size)} = B_{obs.} - B_{std.} \quad \text{Eq. 6.4:6}$$

$$B_{(strain)} = \sqrt{(B_{obs.}^2 - B_{std.}^2)} \quad \text{Eq. 6.4:7}$$

Where $B_{obs.}$ And $B_{std.}$ is the observed broadening of the sample measured and the standard broadening.

6.5 Summary and outlook

The developed thin films during this research are subject to optical, morphological, structural and electrical characterisation using standard techniques in order to quantify the effect of the variables on the thin film properties such as the effect of doping or the effect of experimental parameters such as power or pulse frequency. The optimised n-type and p-type thin films are then used to devise a p-n heterojunction diode, which is subject to electrical testing to measure the efficiency of the device as a current generating device.

EXPERIMENTAL DETAILS

This chapter presents the experimental arrays and setup for each developed thin film. The methods and procedures used for target preparation and substrate cleaning and the deposition details are also presented.

7.1 Introduction

The aim of this project is to deposit n-type and p-type semiconductors for use in a p-n hetero junction power generating diode by magnetron sputtering from powder blended targets. The preparation of the powder targets are defined in the next subsection.

A traditional one variable method was used in the dopant trials, in which the composition of the fluorine doped tin oxide (FTO) and the copper aluminium (CA) metal base powder targets were varied and the effect on the optical, electrical properties and the morphology of the developed thin films were studied.

Other variables such as the pulse frequency and duty cycle and their effect on the thickness and the deposition rate of the thin films were also studied.

7.2 Preparation of the powder targets

The sputter powder rig used during this research was designed by Postill for the development of novel applications. The full design of the powder rig can be found in [155] and [114].

In this project, single and compound based powder targets were deployed to create thin films that are optimised for the of p-n junction diode device. The powders were all sourced from Alfa Aesar and the purities ranged from 97.95% to 99.99%. The total mass of the powder was set to approximately 60 g which is appropriate to cover all of the copper backing plate and depending on the density of the powder, the total mass was reduced in order to keep the powder target thickness similar. The mass distribution of the powder blend was calculated based on the atomic percent concentration (at.%). Using

loosely packed powder targets permits the ability to prepare targets that contain different compositional ratios. The composition of the powder targets were based on changing the at.% of the dopant. Table 7.2:1 presents the at.% of the fluorine in the tin oxide and aluminium at.% in the copper powder target. Research has shown that fluorine plays a significant role in the optical and electrical properties of the tin oxide [48, 71, 83, 156-157], meanwhile the aluminium affects the optical properties of the copper thin films [51, 158-159].

Table 7.2:1 Atomic percent ratio of the dopants for the SnO₂:F and Cu:Al powder targets.

Target name	Atomic percentage of dopant at.%
SnO ₂ :F1	5
SnO ₂ :F2	10
SnO ₂ :F3	15
SnO ₂ :F4	20
CAO7525	25
CAO5050	50
CAO2575	75

The molecular masses (M) of SnO₂, SnF₂, Cu and Al are 150.706 g·mol⁻¹, 156.706 g·mol⁻¹, 63.55 g·mol⁻¹ and 26.98 g·mol⁻¹, respectively. The amount of powder target required to cover the surface area of the backing plate was 60g and therefore the at.% calculation was based on the total mass of 60g.

The following example illustrates the atomic percent calculation for the SnO₂:F3 powder target.

The at.% of fluorine is determined by the number of fluorine atoms n(F) divided by the total number of all atoms in the powder target

$(n(\text{Sn}), n(\text{O}), n(\text{Sn}), n(\text{F}))$. It is important to note that the number of atoms of Sn found in the SnO_2 is different than the one found in the SnF_2 as the molar mass ratios between the two compounds are different.

The atomic percentage (at.%) of, F , needed in the $\text{SnO}_2:\text{F}_3$ target is 15%,

$$\text{at. \%} = \frac{n(\text{F})}{n1(\text{Sn})+n(\text{O})+n2(\text{Sn})+n(\text{F})} \quad \text{Eq. 7.2:1}$$

And from the chemical formula of SnO_2 , the Sn is be defined as;

$$n1(\text{Sn}) = 0.5n(\text{O}) \quad \text{Eq. 7.2:2}$$

And from the chemical formula of SnF_2 , the Sn is defined as;

$$n2(\text{Sn}) = 0.5n(\text{F}) \quad \text{Eq. 7.2:3}$$

Substituting Eq.7.2:2 and Eq.7.2:3 into Eq.7.2:1 gives,

$$0.15 = \frac{n(\text{F})}{1.5n(\text{O}) + 1.5n(\text{F})}$$

$$n(\text{F}) = 0.15(1.5n(\text{O}) + 1.5n(\text{F}))$$

Therefore the fluorine to oxygen ratio is defined as,

$$n(\text{F}) = \frac{9}{31}n(\text{O})$$

The above ratio is also correct for the ratio between the SnF_2 and the SnO_2 ,

$$n(\text{SnF}_2) = \frac{9}{31}n(\text{SnO}_2)$$

To calculate the mass of SnF_2 and the SnO_2 needed to make the total mass of 60g,

total mass = mass of (SnF₂) + mass of (SnO₂)

$$60\text{g} = m(\text{SnF}_2) + m(\text{SnO}_2)$$

$$60\text{g} = n(\text{SnF}_2) \times M(\text{SnF}_2) + n(\text{SnO}_2) \times M(\text{SnO}_2)$$

$$60\text{g} = \frac{9}{31} n(\text{SnO}_2) \times M(\text{SnF}_2) + n(\text{SnO}_2) \times M(\text{SnO}_2)$$

$$n(\text{SnO}_2) = \frac{60\text{g}}{\left(\frac{9}{31} M(\text{SnF}_2) + M(\text{SnO}_2)\right)}$$

$$n(\text{SnO}_2) = \frac{60\text{g}}{\left(\frac{9}{31} \times 156.71\text{g/mol} + 150.71\text{g/mol}\right)}$$

$$n(\text{SnO}_2) = \frac{60\text{g}}{\left(\frac{9}{31} \times 156.71\text{g/mol} + 150.71\text{g/mol}\right)}$$

$$n(\text{SnO}_2) = 0.3058 \text{ mol}$$

Therefore, it is possible to calculate the mass for the SnO₂ powder target that is required,

$$m(\text{SnO}_2) = n(\text{SnO}_2) \times M(\text{SnO}_2) \quad \text{Eq. 7.2:4}$$

$$m(\text{SnO}_2) = n(\text{SnO}_2)\text{mol} \times 150.706\text{g/mol}$$

$$m(\text{SnO}_2) = 0.3058\text{mol} \times 150.706\text{g/mol}$$

$$m(\text{SnO}_2) = 46.09\text{g}$$

Therefore the total mass required for the SnF₂ to produce 15 at.% of F,

$$m(\text{SnF}_2) = 60\text{g} - 46.09\text{g}$$

$$m(\text{SnF}_2) = 13.91\text{g}$$

To ensure the calculation was accurate, the number of moles for each element was calculated using $m(\text{SnO}_2) = n(\text{SnO}_2) \times M(\text{SnO}_2)$

Eq.7.2:4 by using the calculated mass of SnO_2 and the SnF_2 .

$$\text{amount of substance in the compound} = \frac{\text{mass of element}}{\text{molar mass}}$$

Using the equation above, the following table was created and the mass percentage for each element was calculated.

Table 7.2:2 Calculation for mass % of elements in $\text{SnO}_2:\text{F}_3$ powder target

	Element				Total number
	F_2	Sn (n2)	Sn (n1)	O_2	
Number of mol	0.177	0.089	0.306	0.612	1.184
Calculated at. %	14.95	7.52	25.84	51.69	100

Based on the equations above, the rest of the composition for the $\text{SnO}_2:\text{F}$ powder targets were calculated and are shown in Table 7.2:3.

The atomic mass percentage of the copper aluminium powder was also calculated, and demonstrated below is the target composition ratio of 50 at. %:Al and 50 at. %Cu. The total mass of the powder target was set to 50g and the molar mass of Cu and Al is 63.55 and $26.98 \text{ g}\cdot\text{mol}^{-1}$, respectively. The atomic mass percentage is defined as the number of mols (n) for that particular element divided by the total number of mols (n_T) within in that compound, this can be shown as follows;

$$\text{at. \%} = \frac{n}{n_T} \quad \text{Eq. 7.2:5}$$

The total mass of the compounds needed to make 50g is defined as,

$$m(\text{Cu}) + m(\text{Al}) = 50\text{g} \quad \text{Eq. 7.2:6}$$

The $m(\text{Cu})$ is the mass of copper and is defined as,

$$m(\text{Cu}) = n(\text{Cu}) \times M(\text{Cu}) \quad \text{Eq. 7.2:7}$$

And $m(\text{Al})$ is the mass of aluminium and is defined as,

$$m(\text{Al}) = n(\text{Al}) \times M(\text{Al}) \quad \text{Eq. 7.2:8}$$

Since,

$$n(\text{Cu}) = n(\text{Al})$$

Therefore, substituting the value of $M(\text{Cu})$ and $M(\text{Al})$ into Eq 7.2:6 becomes,

$$50\text{g} = n(\text{Cu}) \times [M(\text{Cu}) + M(\text{Al})]$$

$$n(\text{Cu}) = \frac{50\text{g}}{90.53\text{g}\cdot\text{mol}^{-1}}$$

$$n(\text{Cu}) = 0.552 \text{ mol}$$

The mass of Cu is therefore,

$$m(\text{Cu}) = n(\text{Cu}) \times M(\text{Cu})$$

$$m(\text{Cu}) = 0.552\text{mol} \times 63.55\text{g}\cdot\text{mol}^{-1}$$

$$m(\text{Cu}) = 35.10\text{g}$$

Therefore, the mass of the Al can easily be calculated from the total mass of the powder target,

$$50\text{g} = m(\text{Cu}) + m(\text{Al})$$

$$m(\text{Al}) = 14.51\text{g}$$

Using the same method shown above, the rest of the composition ratios were calculated and are shown in Table 7.2:3.(b).

Table 7.2:3 The total mass of the blended powder targets (a) fluorine doped tin oxide, (b) copper aluminium oxide and (c) titanium and antimony doped tin oxide.

(a)

powder target ID	compound powder target mass (g)	
	tin oxide	tin fluoride
SnO ₂	60.0	0
SnO ₂ :F1	57.5	2.5
SnO ₂ :F2	52.7	7.3
SnO ₂ :F3	46.1	13.9
SnO ₂ :F4	43.2	16.8

(b)

powder target ID	compound powder target mass (g)	
	copper	aluminium
CA2575	21.98	28.01
CA5050	35.09	14.90
CA7525	43.79	6.21

(c)

powder target ID	Other powder target mass (g)
titanium Ti	60
antimony doped tin oxide Sb ₂ O ₃ :SnO ₂ (10:90 at.%)	60

Regardless of the powder target material, the preparation method was kept the same. The mass of the powder was measured to two decimal places using an Oertling OB152 scale. The powder target material was inserted into a glass bottle, which was placed on a tumble rotator for several hours to

ensure the blending of the powders. As described in Chapter 5, the powder blend was then distributed across the 2 mm recessed backing plate and was tamped down using a 1 kg steel cylinder to ensure uniformity of the target surface and also to ensure the powder is dense for better thermal and electrical conductivity. No additional adjustments were carried on the target surface such as sintering the powders or pressing with excessive force. The purity, particle size and the hazard of the powder materials are given in Table 7.2:4. During the handling of the powder targets, safety measures were carried out such as wearing protective gloves and breathing masks to ensure the protection against skin irritation and the inhalation of dust metal particles. The powder targets were placed in a safe cupboard to ensure the safety of other students.

Prior to sputtering, each powder target surface was sputter cleaned using an Advanced Energy DC Pinnacle Plus power supply with operating conditions; pulsing frequency of 200 kHz, duty cycle of 90 % and sputtering power density of 0.2 Wcm^{-2} for a period of 10 minutes. After the cleaning process, the oxygen gas was introduced to the chamber to yield a known Ar/O₂ ratio.

Table 7.2:4 Purity, particle size and hazard of the powder targets.

Compound	Purity (%)	Mesh size	Hazard warning
tin oxide (SnO ₂)	99.99	-325	skin and eyes irritation.
tin fluoride (SnF ₂)	97.95	-325	Corrosive, poison, burns eyes and skin.
antimony oxide (Sb ₂ O ₃)	99.999	-325	Irreversible effects do not breathe dust, wear suitable protection.
titanium (Ti)	99.95	-325	Irritates skin and eyes.
copper powder (Cu)	99.99	-325	Highly flammable, risk of impaired fertility.
aluminium powder (Al)	99.95	-325	Highly flammable in air, irritates skin and eyes.

7.3 Deposition techniques

7.3.1 Substrate cleaning

The thin films were initially deposited on standard microscope glass slides which were used to characterise the thin films, then deposited on the final 10cm² float glass substrate. The glass substrates were cleaned very thoroughly to remove all traces of any contamination such as fingerprints, grease/oil, which can create negative effects on the thin film surfaces. The substrates were initially cleaned for a period of 10 minutes using a transistorised ultrasonic tank. This ultrasonic cleaner uses transducers that are mounted at the bottom of the tank to create high frequency sound waves, which causes tiny cavities that are formed in the liquid of the tank. As these cavities implode with the substrate surface a large energy is realised to the surface, which cause the removal of dirt, stains, and other particles. The substrates were then dried using a jet of compressed air and immediately attached to the substrate holder and placed in the deposition chamber. The substrates were subject to an RF sputter clean using a power supply fixed to the substrate holder. The holder was insulated from the chamber and connected to a RF power supply (RFX-600, Advanced Energy), which was set to 0.13 Wcm⁻² for a period of 10 minutes to further clean any contamination from the substrate via plasma etching prior to deposition.

7.3.2 Sputtering equipment

During this research, all the developed coatings were deposited using a mid-frequency pulsed DC magnetron sputtering technique from loosely packed powder targets. The magnetron, which is strongly unbalanced, has a diameter

of 180 mm to provide a reasonable area of uniform deposition on the substrate. Full schematics of the sputtering system and a detailed schematic of the discharge are given in Figure 4.5:6, further description of the deposition system has been given previously [88, 134, 136, 141]. In order to control the properties of the developed coatings the following experimental parameters were monitored;

- Discharge voltage: The power supply used to strike the discharge was an Advanced Energy DC Pinnacle Plus power supply, which was set to constant power mode in order to allow for constant input of energy to the target, therefore attaining constant discharge plasma.
- Base pressure: The base pressure is the pressure of the deposition chamber prior to introducing any sputtering ambience. To ensure the level of impurities in the chamber was kept to a minimum, the base pressure was ensured to be 2.1×10^{-4} Pa.
- Working pressure: This is the pressure of the sputter chamber prior to the initiation of the glow discharge. The gas flow rates of Ar and O₂ were controlled using Ar and O₂ mass flow controller (MFC) with flow range of 25 sccm and 50 sccm, respectively. The MFCs were set and maintained using a two-channel mass flow controller power supply/readout (PR4000B by MKS). The Ar:O₂ ratio inside the sputtering system was calculated by adjusting the relative flow rate of each gas,

$$\text{Ratio of Gas 1} = \frac{(\text{flow rate of gas 1})}{(\text{flow rate of gas 1}) + (\text{flow rate of gas 2})} \quad \text{Eq. 7.3:1}$$

The working pressure was adjusted to 0.24 Pa using Ar gas in order to perform the substrate and target surface cleaning process.

7.3.3 Deposition conditions

On the completion of the substrate and target cleaning processes, the chamber working pressure was readjusted by varying the argon to give 0.4 Pa and at the same time, the O₂ gas was fed in to the chamber depending on the specific run conditions in order to maintain the coating stoichiometry and compensate for any lost O₂ during the deposition runs.

During this research, the main variable was the target composition, therefore, based on previous characterisation studies (Chapter 5), other deposition conditions were kept the same, such as the target to substrate separation, Ar:O₂ ratio, power, pulse frequency and duty cycle.

The best FTO thin films (prepared using SnO₂:F2 powder target) in terms of the electrical and optical behaviour were prepared in an Ar and O₂ atmosphere with a constant flow rate of 23 and 4.5 sccm, respectively, which gave a coating pressure of 0.54 Pa. During deposition, the shutter was opened and the magnetron discharge was pulsed at 200 kHz using an Advanced Energy DC Pinnacle Plus power supply which was operated in constant power mode to provide a power density of 1.6 Wcm⁻², at 90% duty cycle (pulse off time set to 0.5 μs). These conditions were chosen to produce stable arc free deposition conditions. The deposition period of all the experiments was set to 15 min. The optimum deposition rate of 27 nm·min⁻¹ was achieved through a trial of different pulsing frequency, duty cycle and target to substrate distance, using the SnO₂ powder target as described earlier. The deposition rate for the different powder targets was not found to vary significantly during this study. The synthesis temperature during the

deposition of the thin film was measured to be below 170 °C at the substrate using a platinum thermal resistor sensor.

Copper aluminium oxide (CuAlO₂) thin films, were deposited onto standard microscope glass substrates by using pulsed DC magnetron sputtering technique using the copper and aluminium metal base powder blended target. The powder blended targets were formed as described in earlier chapter.

The operating conditions were chosen through an array of experimental trials to produce arc free operating and to produce the desired p-type CAO thin film. During the trial depositions, the power supply was set to constant power mode, with pulse frequency set to between DC, 100, 250, 350 kHz, using duty cycle of 50% and power set to 250 W and then to 350 W. The deposition time was set to 150 minutes. Depending on the discharge sputtering power and frequency used, the variation in the deposition thickness were recorded and shown in the table below.

Table 7.3:1 Deposition conditions and corresponding deposition rates of CuAlO₂ thin films.

Sample ID	Frequency (kHz)	Duty cycle on (%)	Discharge Power (W)	Thickness (nm)	Deposition rate (nm·min ⁻¹)
7525CAO#8	350	61	350	620	4.13
7525CAO#7	225	55	350	633	4.22
7525CAO#6	100	55	350	1090	7.27
7525CAO#5	0	0	350	579	3.86
7525CAO#4	350	61	250	417	2.78
7525CAO#3	225	55	250	415	2.76
7525CAO#2	100	55	250	600	5.0
7525CAO#1	0	0	250	430	2.86

The deposition was prepared in an Ar and O₂ atmosphere with constant flow rates of 13 and 30 sccm, respectively, which gave a coating pressure of 0.4 Pa. The diffusion pump speed was controlled in order to increase the coating pressure to 0.6 Pa as it gave a stable and dense plasma.

Trial experiments were conducted on antimony doped tin oxide (ATO) and titanium metal base powder (Ti) targets to explore its structural, optical and electrical properties. The preparation of the powder targets followed the same procedure as mentioned in the previous subsection. The experimental conditions for the ATO and the Ti powder target are shown below.

Table 7.3:2 Standard deposition parameter for (a) antimony doped tin oxide powder target and (b) titanium metal base powder target.

(a)

Power (W)	Frequency (kHz)	Pulse time_off (uS)	Duty cycle (%)	Ar (sccm)	O ₂ (sccm)	Chamber pressure (Pa)	Deposition run (min)
300	200	0.5	90	23	4.5	0.50	40

(b)

Power (W)	Frequency (kHz)	Pulse time_off (uS)	Duty cycle (%)	Ar (sccm)	O ₂ (sccm)	Chamber pressure (Pa)	Deposition run (min)
400	100	1	90	23	1.75	0.60	120

The top and the back side electrical contacts were made using silver and copper metal targets. The sputtering depositions were performed using DC mode power supply, therefore promoting high deposition rates. The following table outlines the deposition condition,

Table 7.3:3 Standard deposition parameters for Cu and Ag targets.

Material	Power (W)	Frequency (kHz)	Ar (sccm)	O ₂ (sccm)	Chamber pressure (Pa)	Deposition run (min)
Cu	500	DC	17	0	0.3	120
Ag	500	DC	17	0	0.3	120

7.4 Fabrication of p-n junction diodes

To demonstrate the applicability of the SnO₂:F thin films, the CuAlO₂ thin films and the metallic contacts, a simple p-n heterojunction diode was fabricated. The device was fabricated, by depositing a 400 nm FTO film onto copper contact pads, then p-type CAO film grown to a 1 μm was deposited on to the FTO layer. Then a silver metallic contact was then deposited onto the CAO film to create the device. Finally, a 1 μm titanium dioxide thin film was grown on top of the silver contacts as a protective layer for the device. The fabrication process of the p-n junction is shown in Figure 7.4:1.

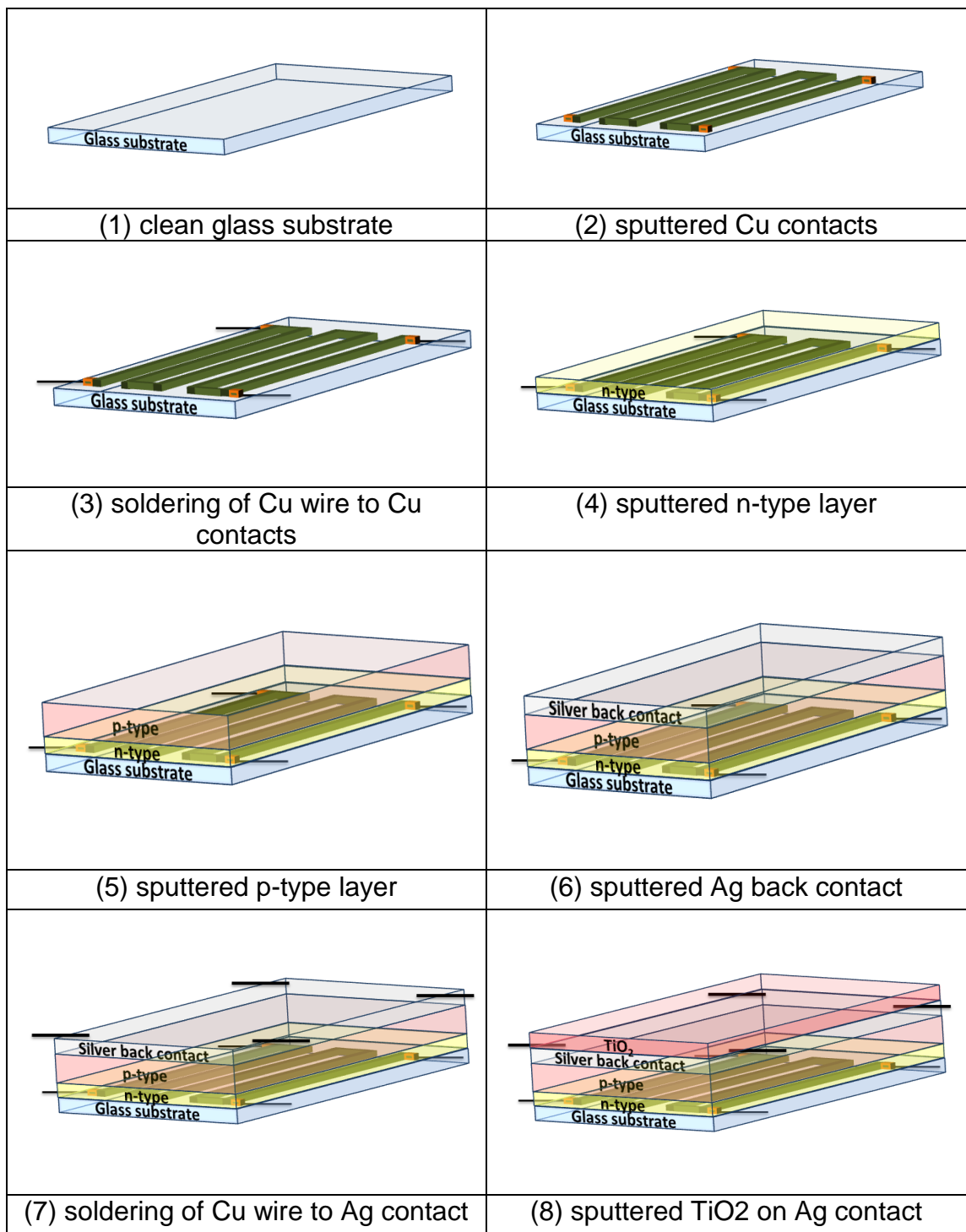


Figure 7.4:1 Schematic fabrication process of p-n junction solar diode

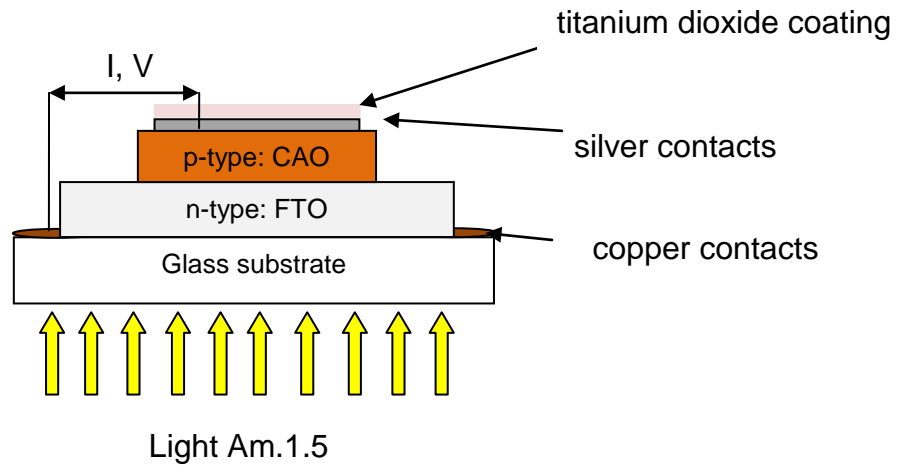


Figure 7.4:2 Cross section schematic diagram of multi p-n heterojunction diode configuration.

To extract the photoelectrons from the diode, the n-type copper metallic contacts were deposited through a mask that was customised to specifically allow maximum sun light while maximising the coverage area for the collection of charged carriers. Figure 7.4:3 outlines the mask and the corresponding deposition of the copper metal contacts. The copper contacts were grown to 1 μm thick which gave an electrical resistivity (using the Hall effect measurement system) to be less than $3.3 \times 10^{-6} \Omega \cdot \text{cm}^{-1}$.

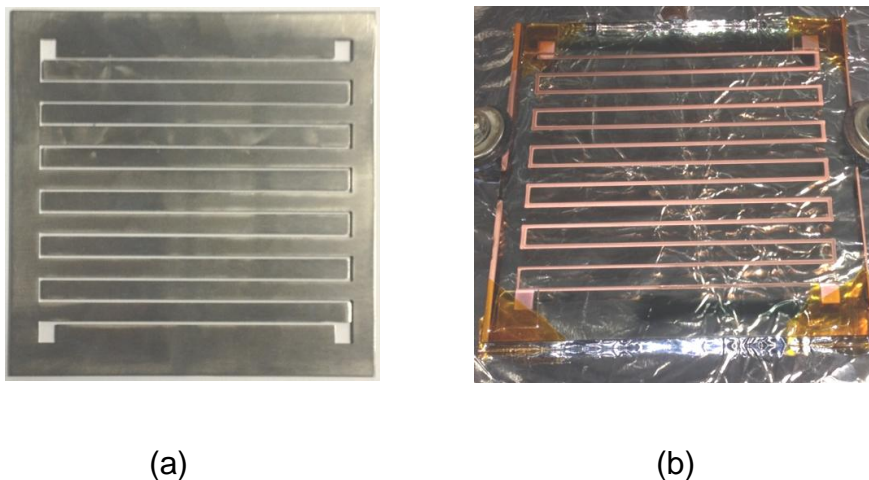


Figure 7.4:3 (a) The mask design and (b) the corresponding copper metal contact for the n-type FTO thin film.

The FTO thin film was deposited onto the copper contacts using a second mask that only exposed the grid of the copper contacts but not the electrical soldering contacts points.

To complete the diode configuration, the p-type CAO thin film was deposited on top of the FTO thin film using a third mask that had a smaller dimension to the n-type mask, in order to stop any short circuit problems occurring. Silver contacts were deposited on top of the CAO using a fourth mask that had a smaller dimension to that of the p-type thin film. Finally, a titanium dioxide coating was deposited onto the silver contacts to protect the device from any damage caused by scratches etc. The Cross section schematic diagram of the complete p-n heterojunction diode configuration is shown in Figure 7.4:2.

7.5 Summary and outlook

The powder target preparation has been discussed along with the mathematical calculation for the atomic percentage content for the mixed powder targets. Target conditioning prior to sputtering deposition has two main advantages; firstly, it is an important step to extract any contaminations and trapped gaseous atoms from within the powder particles; secondly it stabilises the powder target and reduces the abrupt arcing problems that powder targets suffer from. The powder target approach is a cheap and efficient means of investigating and optimising the properties of multi-component materials, compared to using metallic or ceramic targets regardless of the powder target material, the preparation method was kept the same. Paying attention to experimental parameters such as the target

voltage, chamber pressure and the gas flow ratio is very important in order to be able to the repeat the experiment and develop thin films that attain consistent optoelectrical properties. The schematic of the p-n heterojunction was demonstrated.

CHARACTERISATION OF THIN FILMS

This chapter presents the electrical, optical, topographical, and morphological analysis for the n-type and p-type thin films. To demonstrate the applicability of the SnO₂:F/CuAlO₂ thin films, a simple p-n heterojunction diode was fabricated and a typical J-V rectifying characteristics of the resultant device was demonstrated.

8.1 Fluorine doped tin oxide

8.1.1 Introduction

In this work, fluorine doped tin oxide coatings were produced from blended SnO₂ and SnF₂ powder targets and the effect of different fluorine doping levels was investigated. The chemical composition, structural, electrical and optical properties of the FTO coatings sputtered in an argon/oxygen gas mixture at different deposition conditions is reported.

8.1.2 Elemental analysis of SnO₂:F thin films

The EDS absolute data from the analysis of the FTO films is given in Table 8.1:1. The EDS accelerated energy beam was optimised to be 7 KeV in order not to detect the elements of glass such as Si and Ca. The analysis of the undoped tin oxide film shows a composition of 31.7 at.% tin and 68.4 at.% oxygen which is close to stoichiometric SnO₂. It was observed that the fluorine content in the doped thin films is in the range of 0-7.4 at.%, which is low in comparison to the amount of fluorine incorporated into the powder targets (0-13 at.%). This can be explained by the fact that fluorine is a light element (Z=9) and may be more readily scattered during gas phase transport through the high density plasma [146].

Table 8.1:1 Compositional analysis of the powder targets and subsequent tin oxide and fluorine doped tin oxide.

Sample ID	Element at.% in targets			Element at.% in films		
	O	F	Sn	O	F	Sn
SnO ₂	66.7	0.0	33.4	68.4	0.0	31.7
SnO ₂ :F1	63.3	3.3	33.3	66.4	2.8	30.8
SnO ₂ :F2	60.0	6.6	33.3	64.0	5.3	30.7
SnO ₂ :F3	56.7	10.0	33.2	62.8	6.2	30.9
SnO ₂ :F4	53.4	13.0	33.3	60.1	7.4	32.5

Figure 8.1:1 depicts the relationship between the fluorine and oxygen atomic contents incorporated in the film, as functions of the fluorine content of the target. It was observed that the fluorine to oxygen ratio increased with the increase in the fluorine content in the thin film. This implies that the fluorine is successfully incorporated into the tin oxide, as each F⁻ anion substitutes an O⁻² anion in the lattice. This is attributed to the fact that fluorine is the most favoured oxygen substitute, because the ionic size of fluorine (F⁻:0.133 nm) is closely matched to that of oxygen (O⁻²:0.132 nm) [160].

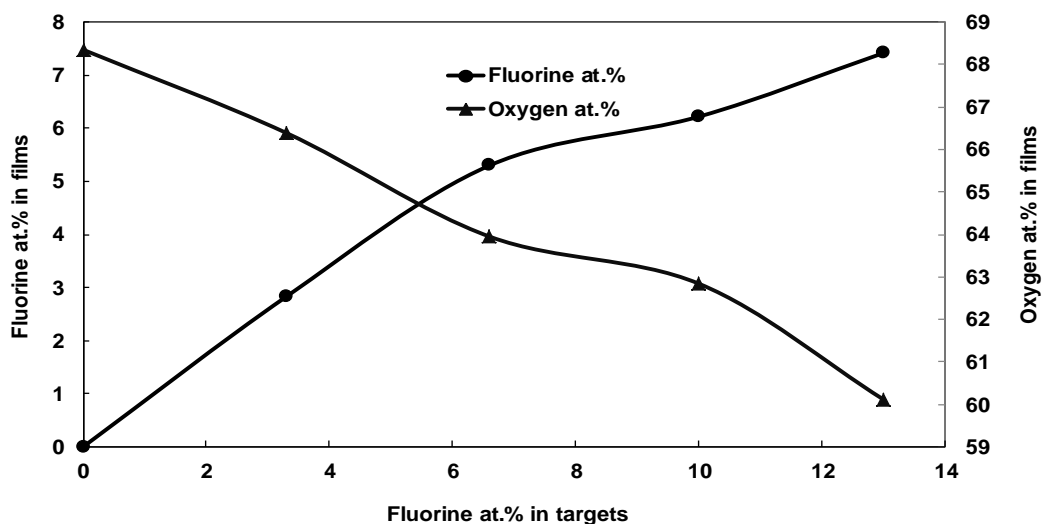


Figure 8.1:1 EDS analysis of fluorine and oxygen atomic content in the FTO films as a function of fluorine atomic content in the target.

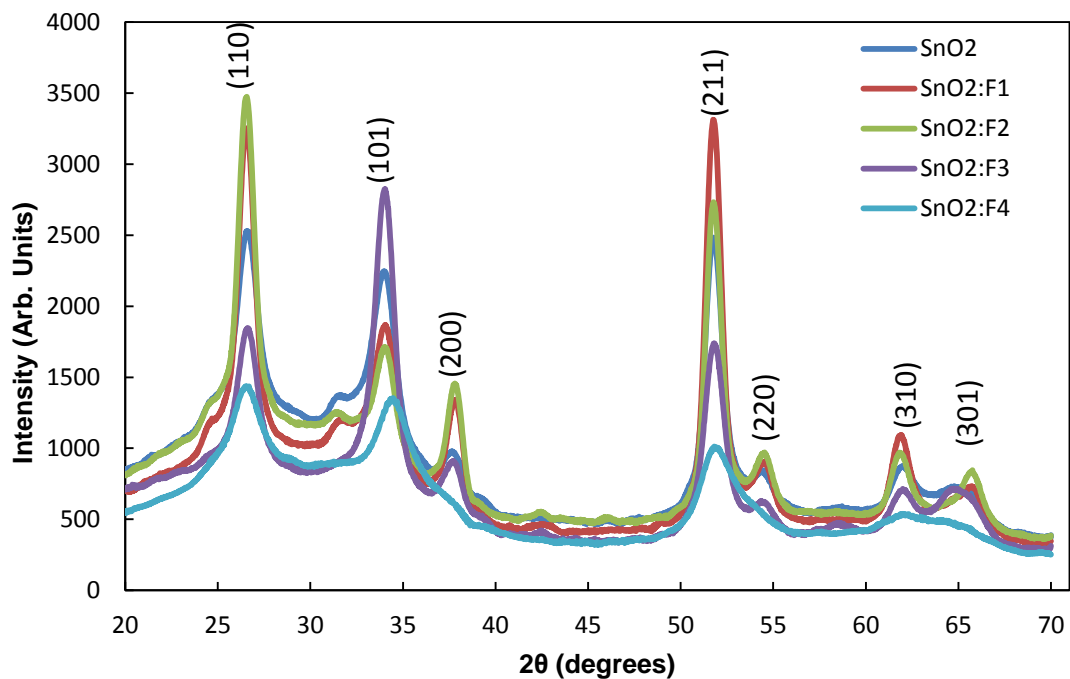
8.1.3 Structural properties of SnO₂:F thin films

The crystal structures of the SnO₂ and SnO₂:F thin films were analysed using X-ray diffraction over the range 20° to 70° 2θ. The XRD patterns for the undoped SnO₂ and the doped SnO₂:F films are presented in Figure 8.1:2. The diffraction angle (2θ), Miller indices (hkl), grain size (D) and texture coefficient for all the thin films are presented in Table 8.1:2.

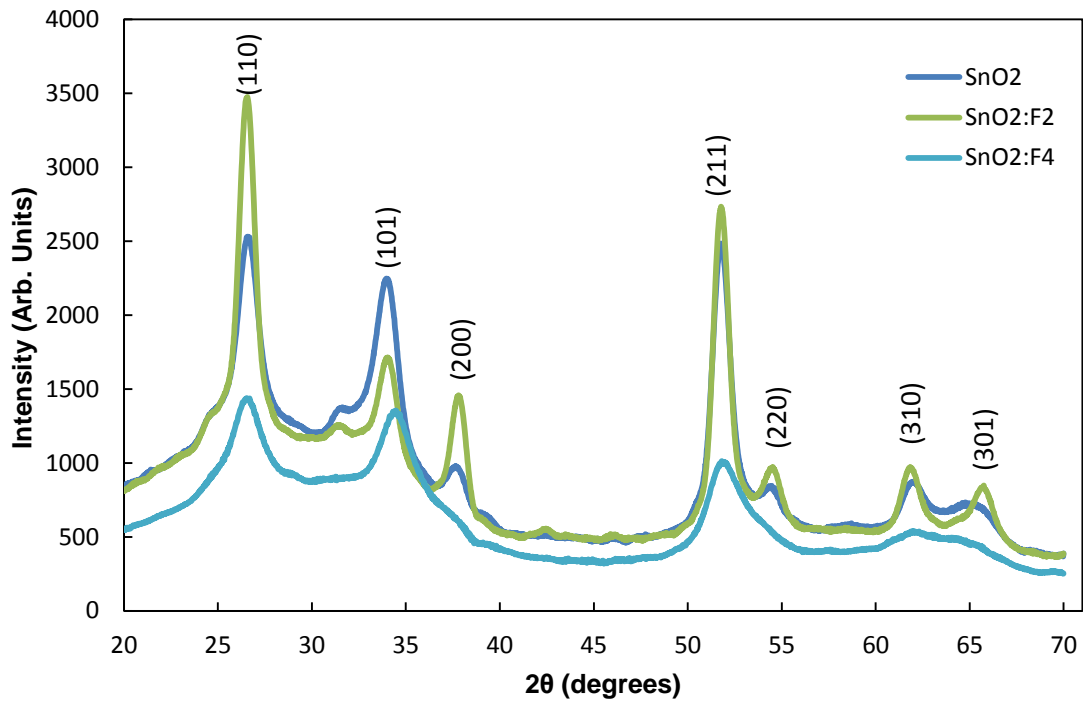
It can be observed from Figure 8.1:2 that the films exhibited XRD patterns with diffraction peaks corresponding to the (110), (101), (200), (211), (301), and (310) peaks of the rutile SnO₂ pattern [161]. The presence of these peaks indicates that all the films were found to be of the cassiterite type with a polycrystalline structure. No other diffraction lines that correspond to other tin oxide or tin fluoride structures were detected. In addition, there was no significant shift in the peak positions of all the developed thin films, which probably implies that fluorine doping did not introduce any significant stress in the films. For comparison reason, the XRD pattern for SnO₂, SnO₂:F2 and SnO₂:F4 were plotted on a separate Figure 8.1:2 (b) to give the reader a clear observation of the effect of the fluorine doping. It is apparent from Figure 8.1:2 (b) that the undoped SnO₂ sample has a lower intensity in comparison to the more sharper, more intense peaks of the SnO₂:F2 sample. In other words, the crystallinity of the SnO₂ samples were improved with the fluorine incorporation (2.8 to 5.4 at.%). In the present investigation, the intensity of the (200) plane ameliorates with the increase in the fluorine concentration up to 5.4 at.% and then deteriorated with fluorine concentration up to 7.4 at.% (sample SnO₂:F4), a similar behaviour was observed by Moholkar et al [13]. It is therefore

concluded that the fluorine content strongly effects the structure of the SnO₂, as observed elsewhere [83].

Thin films deposited via magnetron sputtering, usually exhibit a preferred orientation because the sputtered atoms arrive at the substrate via limited pathways, therefore promoting the formation of a columnar microstructure. A preferred orientation can also be affected by experimental parameters, such as the growth temperature [162-163], coating thickness [58] and fluorine doping level [44, 46].



(a)



(b)

Figure 8.1:2. XRD diffraction pattern for (a) all FTO diffraction patterns (b) diffraction pattern of SnO₂, SnO₂:F1 and SnO₂:F4.

The intensity of the hkl reflection pattern can be utilised to determine the orientation of the grains or the volume of crystallites within that particular hkl plane parallel to the surface sample.

The degree of the preferred orientation of the thin films can be estimated by comparing the relative intensities of the measured peaks. A texture coefficient $TC(hkl)$ is calculated using the Harris analysis technique shown in Eq 8.1:1 [164].

$$TC_{(hkl)} = \frac{I_{(hkl)}}{I_o(hkl)} \times \left[\frac{1}{n} \sum_{i=1}^n \frac{I_{(hkl)}}{I_o(hkl)} \right]^{-1} \quad \text{Eq. 8.1:1}$$

Where I is the measured intensity of the peak, I_o is the theoretical intensity obtained from the JCPDS powder diffraction file and n is the number of peaks.

The texture coefficients for the (110), (200) and (211) peaks are shown in Table 8.1:2. It is apparent from Table 8.1:2 that the coatings tend to have a (211) preferred orientation or texture ($TC > 1$). FTO coatings grown by other techniques suggest that the (200) peak was most influenced by fluorine doping [18]. Although the TC of the (200) peak varies with fluorine content, becoming a maximum of 1.11 at 5.3 at.% F, it still remains below the TC for the (211) peak.

The grain sizes of the crystallites were calculated using the Scherrer equation for the (110), (211) and (200) peaks [165]. It is important to note that a lattice strain de-convolution was not considered during the calculation. The calculated values are presented in Table 8.1:2.

Table 8.1:2 Diffraction angle (2θ), the miller indices (hkl), grain size (D) and the texture coefficient (P) of FTO thin films.

Sample ID	$2\theta(^{\circ})$	Peak	Grain size D	Texture coefficient P
		(hkl)	(nm)	
SnO₂	26.6	110	15	0.48
	37.7	200	24	0.42
	51.7	211	22	1.27
SnO₂:F1	26.5	110	28	0.73
	37.8	200	23	0.95
	51.6	211	34	1.48
SnO₂:F2	26.5	110	31	0.77
	37.8	200	38	1.11
	51.7	211	33	1.31
SnO₂:F3	26.6	110	13	0.47
	37.7	200	14	0.6
	51.6	211	15	1.01
SnO₂:F4	26.6	110	9	0.3
	51.4	211	7	0.49

The average of the grain sizes for the (110), (200) and (211) peaks is shown in Figure 8.1:3. It was observed that the mean crystallite size followed a progressive incremental trend with increasing fluorine content up to 5.3 at.% (from 20 nm to 34 nm), beyond which there was a reduction in the crystallite size, which may be due to the excess fluorine within the tin oxide lattice. The implication being that 5.3 at.% of fluorine in the lattice was the optimum composition, of those tested, for grain growth. The calculated values for the lattice parameters 'a' and 'c' for SnO₂ thin films are 4.74 Å and 3.35 Å for the (110) peak which are in reasonable agreement with the standard data (a = 4.73 Å, c = 3.18 Å) [161].

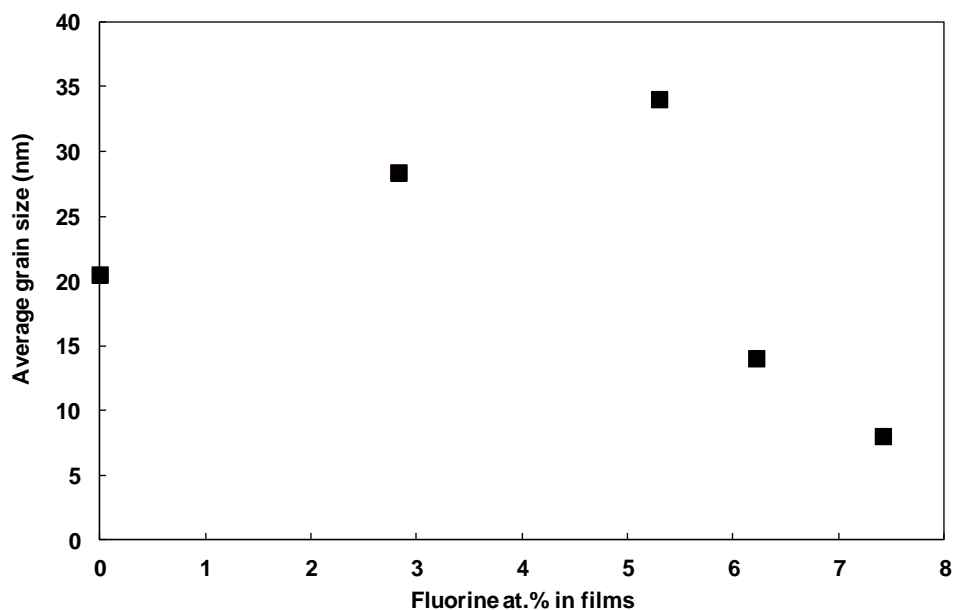


Figure 8.1:3 Average grain size as a function of fluorine atomic content in the FTO thin films.

8.1.4 Electrical properties of SnO₂:F thin films

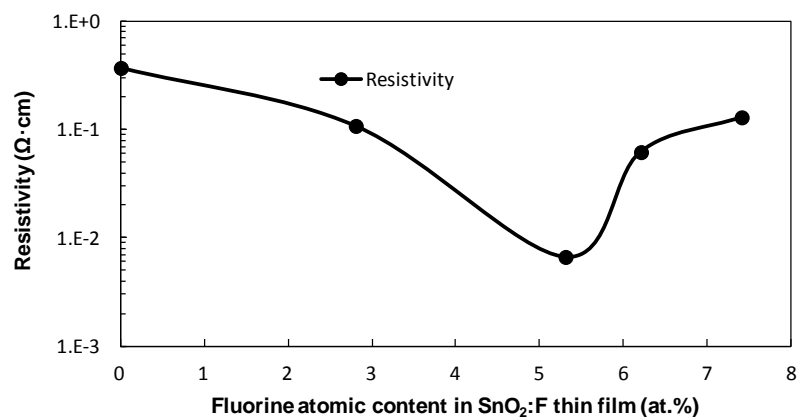
To characterise the electrical properties of the thin films, Hall effect probe measurements in a Van der Pauw configuration at room temperature were

employed [152]. Figure 8.1:4 presents the electrical behaviour of the thin films as a function of the fluorine content. The values for the carrier concentration (N_d) were reported to be negative, indicating n-type semiconductor behaviour however, the absolute value was plotted to present the trend of the data.

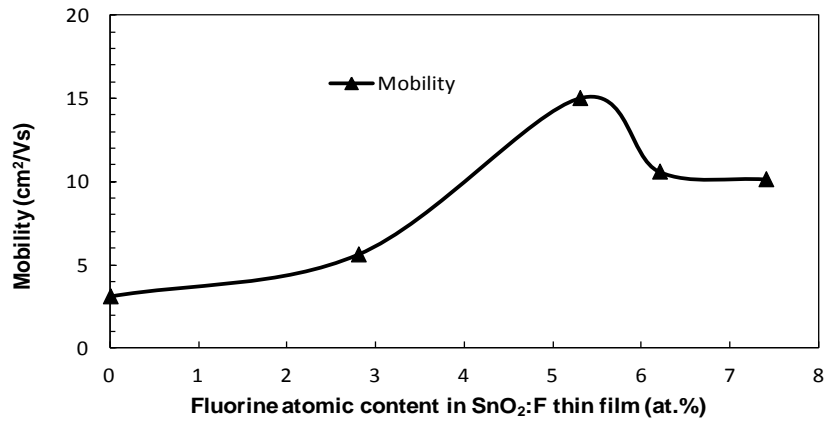
Resistivity and mobility values of $3.71 \times 10^{-1} \Omega \cdot \text{cm}$ and $3.1 \text{ cm}^2/\text{Vs}$ and a corresponding carrier concentration (N_d) of $5.5 \times 10^{18} \text{ cm}^{-3}$ were obtained for un-doped SnO_2 . These values are similar to those reported elsewhere [45, 47]. It was observed from the carrier concentration (N_d) data that the FTO thin films exhibit n-type conductivity, which is also achieved by other deposition techniques including spray pyrolysis and PLD [37], [44].

It was observed from Figure 8.1:4, that the best electrical properties were achieved with a fluorine concentration of 5.3 at.%, corresponding to a resistivity of $6.71 \times 10^{-3} \Omega \cdot \text{cm}$, mobility of $15.1 \text{ cm}^2/\text{Vs}$ and a carrier concentration (N_d) of $1.46 \times 10^{20} \text{ cm}^{-3}$ for the films. Similar results were achieved by PLD at a deposition temperature of 300°C [44]. The improvement in the electrical properties is attributed to the larger grain size observed at this composition [44]. In addition, the hybrid orbital configuration of fluorine and oxygen are $2S^22P^5$ and $2S^22P^4$, respectively, indicating that fluorine atoms promote one free electron/ molecule when it sits in place of oxygen. As the ionic radius of F (1.36 \AA) is slightly lower than that of O^{2-} (1.40 \AA), so the fluorine atoms are more electronegative than the oxygen atoms, therefore the fluorine substitutes the oxygen sites more easily [166]. This phenomenon leads to higher carrier concentration, which is shown in Figure 8.1:4. Similar trends were observed in [39].

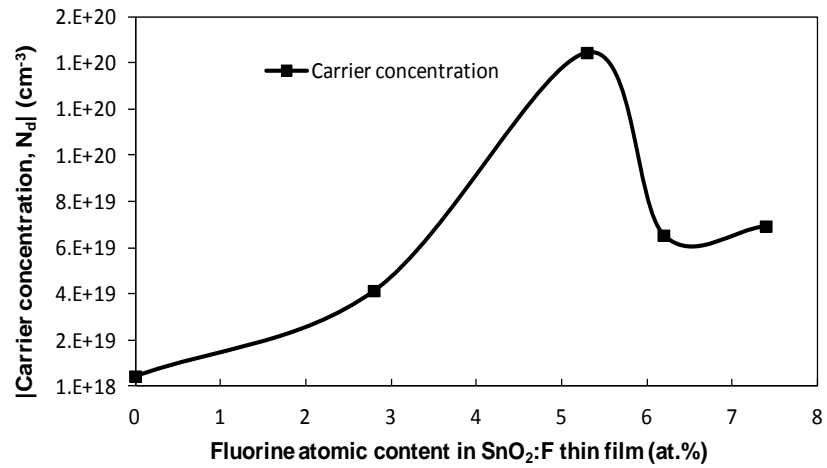
Increasing the fluorine content in the film beyond 5.3 at.% resulted in a degradation of the electrical properties. This is probably attributed to the solubility limit of fluorine into the tin oxide lattice [11], and probably the cause for the reduction in the grain size, as observed in Table 8.1:2 [38]. The excess fluorine atoms do not occupy the correct position within the lattice, which leads to disorder of the structure, grain boundary scattering and therefore to a decrease in the free carrier concentration (N_d) and mobility and an increase in the resistivity ($7.04 \times 10^{19} \text{ cm}^{-3}$, $10.15 \text{ cm}^2/\text{Vs}$ and $1.31 \times 10^{-1} \text{ } \Omega \cdot \text{cm}$, respectively). The effect of the fluorine content on the electrical properties of FTO was investigated by Elangovan et al, who reported the degradation in the electrical properties is probably due to the solubility limit of fluorine content in the thin film [11]. Kim et al found that a saturation carrier concentration (N_d) is achieved due to the formation of Sn-F complexes in the grain boundaries when using higher than 10 wt.% of SnF_2 in target [9]. The electrical results depicted in this study indicate that the mobility and the carrier concentration (N_d) were limited by the solubility limit of fluorine content in the film. This behaviour is also observed by Elangovan et. al [11].



(a)



(b)



(c)

Figure 8.1:4 Variation of (a) resistivity in logarithmic scale, (b) mobility and (c) absolute carrier concentration of FTO thin films as a function of fluorine atomic content.

8.1.5 Optical properties of SnO₂:F thin films

The optical transmittance and the direct band-gap properties of SnO₂:F films as a function of the fluorine content in the thin films are presented in Figure 8.1:5 and Figure 8.1:6, respectively. The transmittance data of each sample

was recorded three times and an average taken. The optical transmittance (T) was averaged over the wavelength range of 300-900 nm, and the absorption coefficient (α) was determined by using Eq. 8.1:2

$$T \approx e^{-\alpha t} \quad \text{Eq. 8.1:2}$$

Where, t , is the thickness of the film. The absorption refers to the excitation of an electron from the valence band to the conduction band. The absorption coefficient was then used to estimate the direct optical energy band-gap (E_g) using the relation shown in Eq 8.1:3.

$$\alpha h\nu = C(h\nu - E_g)^{1/2} \quad \text{Eq. 8.1:3}$$

Where, h , is Planck's constant, ν , is the frequency of the incident photon, C , is a constant for direct transition and, α , is the absorption coefficient. The direct optical energy band-gap (E_g) was estimated by extrapolating the linear portion of the curve $(\alpha h\nu)^2$ against $(h\nu)$ for direct allowed transition to the point where $\alpha h\nu = 0$ [25].

The optical transmission spectra recorded in the wavelength range of 300 to 900 nm are presented in Figure 8.1:5. High transparency in the visible range ($82\% < T_{\text{vis}} < 85\%$) was observed, in accordance with the requirements for TCO applications (80%) [167]. This can be associated with good structural homogeneity. It is evident from the Figure 8.1:5; that the average visible transmittance is not influenced much for different doping levels of fluorine; similar behaviour was also observed in [166] and [168]. However, a slight decrease in the transmission is probably due to the decrease in the oxygen

vacancies as perceived in the EDS data shown in Table 8.1:1. The insert in Figure 8.1:5 is for the convenience of the reader to give a quick average view of the transmission and the direct optical band-gap against the change in the fluorine concentration in the thin film. The sharp decrease in the transmission in the UV range of the spectrum is related to the light absorption edge [169]. It is also possible to notice that both the un-doped and the doped films showed interference fringe patterns suggesting the thickness of the coating being greater than 100 nm.

The direct band-gap for un-doped tin oxide was estimated to be 3.70 eV, which increased slightly to a value of 3.77 eV at a fluorine content of 5.4 at.% in the film as observed in Figure 8.1:6. The direct band-gap values obtained in this work are slightly higher than the direct band-gap values of 3.17-3.45 eV reported in [46] and slightly lower than the band-gap values of 4.0-4.25 eV reported in [44]. This variation is probably attributed to the different concentration of fluorine used in the film, the thickness variation and the experimental variables such as working pressure and deposition temperature.

Generally, the band-gap energy for doped metal oxides films is higher than that of the un-doped type. This is because the energy gap between the valence band and the lowest empty state in the conduction band is found to increase due to the filling of low lying energy levels in the conduction that is caused by the increase in the carrier concentration (Burstein-Moss effect) [167]. The shift in the band-gap can also be related to the variation in the mean crystallite size, the internal stress or due to the free carrier concentration [170].

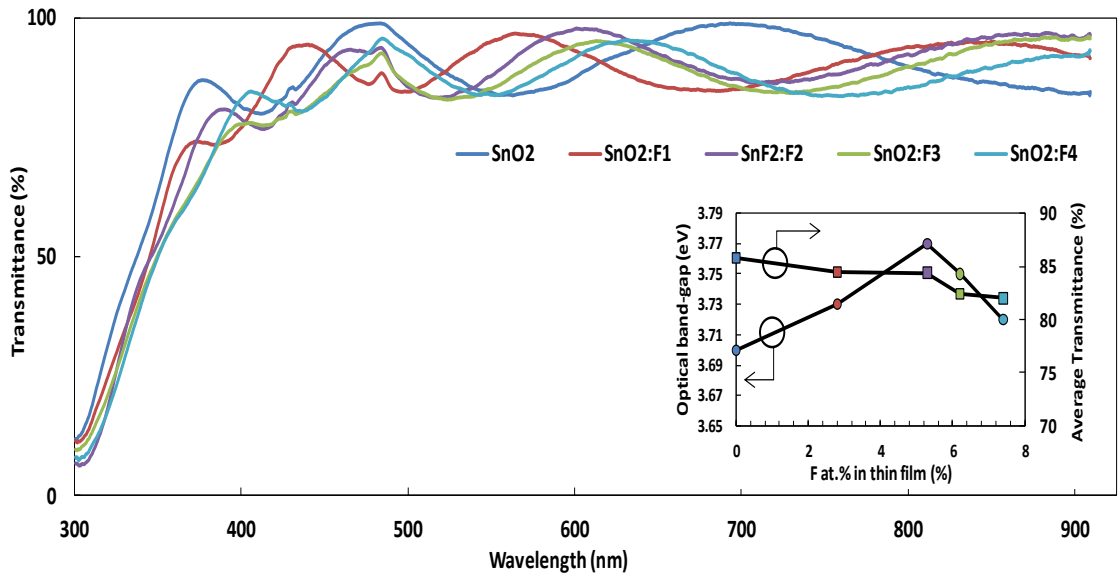


Figure 8.1:5. The optical transmittance of FTO thin films as a function of fluorine atomic content. The insert shows the variation in optical band-gap and the average transmittance across the $300 \leq \lambda \leq 900$ nm with change in fluorine concentration in thin film.

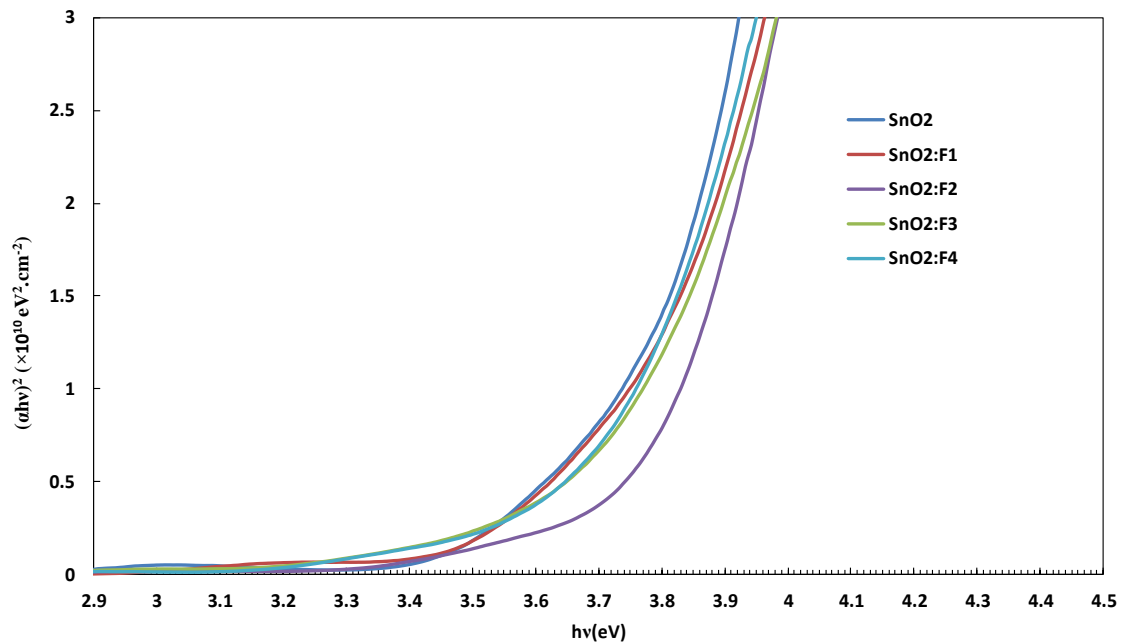
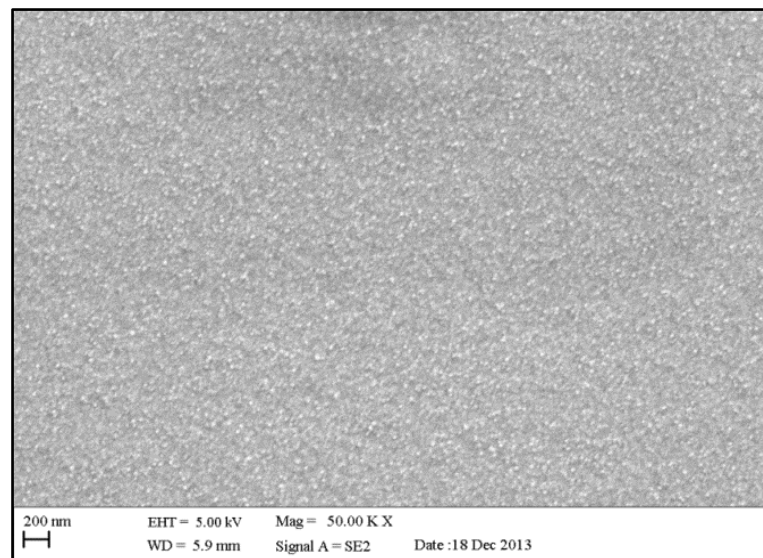


Figure 8.1:6. The direct allowed transition of FTO thin films as a function of fluorine atomic content.

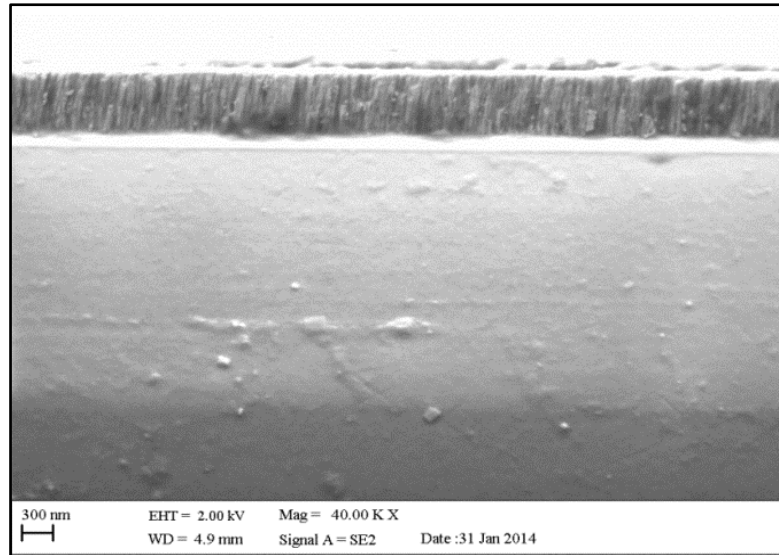
8.1.6 Morphological properties of SnO₂:F thin films

Figure 8.1:7 (a) and (b) shows the surface area and the cross-section SEM morphologies of the SnO₂:F₂ film, respectively. The film has a compact and dense homogenous surface characterised by small grains. The small grains observed in Figure 8.1:7 (a) are probably a result of the low deposition temperature. Consonni et al. studied the effect of deposition temperature and observed an increase in the mean grain size from 60-127 nm as the growth temperature raised from 360-460 °C.

The thickness of the film was measured to be about 410 nm, which is in good agreement with the Dektak profilometer measurements. The cross-sectional images show that the thin film has a dense columnar grained structure normal to the surface of the substrate.



(a)



(b)

Figure 8.1:7. (a) Surface topography, (b) Cross-sectional morphologies of SnO₂:F₂ thin film.

8.1.7 Conclusions

Transparent conductive oxide SnO₂:F thin films have been deposited on glass substrates by the pulsed DC magnetron sputtering technique in a Ar/O₂ atmosphere using loosely packed blended powder targets. The thin films were grown at a deposition rate of 27 nm·min⁻¹ and a deposition temperature below 170 °C. It was determined that 5.3 at.% of fluorine incorporated into the film gave the best electrical behaviour. In addition, the XRD structural analysis showed that the crystallinity of the SnO₂ samples were improved with the fluorine incorporation and the intensity of the (200) plane ameliorated with the increase in the fluorine concentration up to 5.3 at.% found in the thin film. The average optical transmittance achieved for this coating was 83% across a range of 300 ≤ λ ≤ 900 nm. The detailed analysis of the electrical properties of

the thin film as a function of the fluorine doping level revealed that, a resistivity as low as $6.71 \times 10^{-3} \Omega \cdot \text{cm}$ was obtained with a fluorine content of 5.3 at.%.

This work has shown the ability to grow transparent conductive oxide $\text{SnO}_2:\text{F}$ thin films using a cost effective (no post annealing of samples, and high deposition rate) and environmentally friendly method (no fluorine gas is used and no toxic effluent is produced). This technique is of great advantage for studying the properties of multicomponent materials and identifying optimum compositions.

Future work will include evaluating the long-term performance of the developed TCO coatings, including the susceptibility to delamination through electrochemical corrosion and accelerated weather trials. The effect of thickness variation to the optical and the electrical performance of the TCO will also be investigated.

8.2 Antimony doped tin oxide

8.2.1 Introduction

Antimony doped tin oxide (ATO) thin films can be deposited using a variety of deposition techniques, such as vapour deposition methods, including magnetron sputtering [171], pulsed laser deposition [172] molecular beam epitaxy [173]. The deposition conditions such as the working gas pressure, target size, system geometry and the deposition power, play an important role on the quality of the ATO. The effect of the deposition power can certainly influence the $(\text{Sn}+\text{Sb})/\text{O}$ ratio of the developed thin films by changing the deposition rate and the deposition ratio of the sputtered atoms/ reactive oxygen. Therefore, this is a good opportunity to the study the effect of

deposition power on the properties of the developed thin films including the electrical, optical and structural properties of the thin films.

During the deposition process, the discharge current and the discharge power were recorded and illustrated in Figure 8.2:1. It can be observed that the discharge current increased linearly with the increase in the discharge power, this suggests that the energy and the number of atoms arriving at the substrate increase due to the increase in the discharge power, similar trends were observed during the deposition of aluminium zinc oxide via magnetron sputtering [174]. The increase in the energy can be used to promote the sputtered atoms to grow in a particular direction or order. Also, the increase in the number of the sputtered atoms, at a fixed Ar:O₂ ratio during the deposition can lead to the change in the stoichiometry of the thin films.

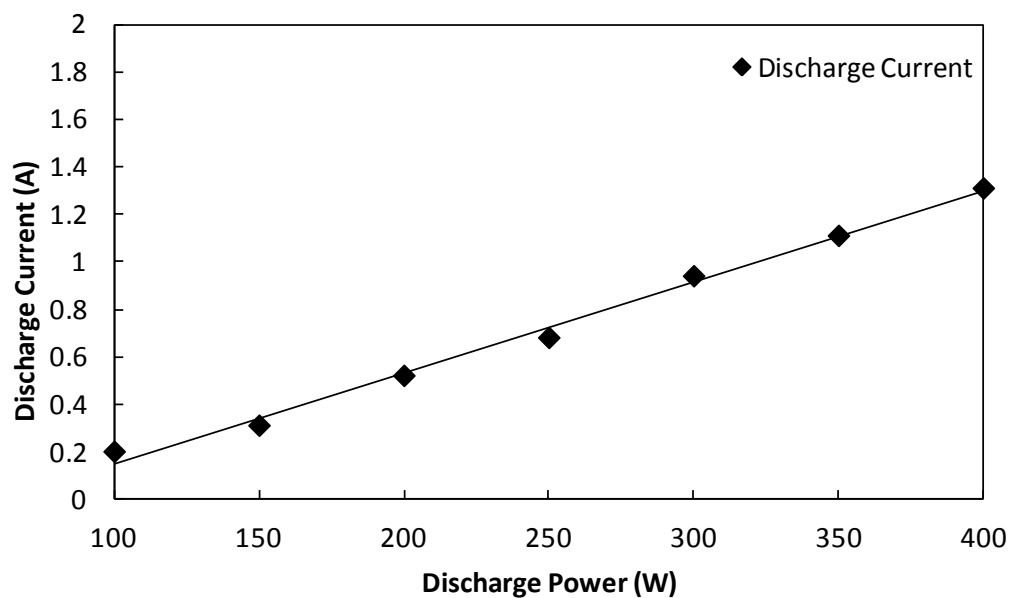


Figure 8.2:1 Discharge of power–current curve for a working pressure 0.5 Pa for a ATO powder target.

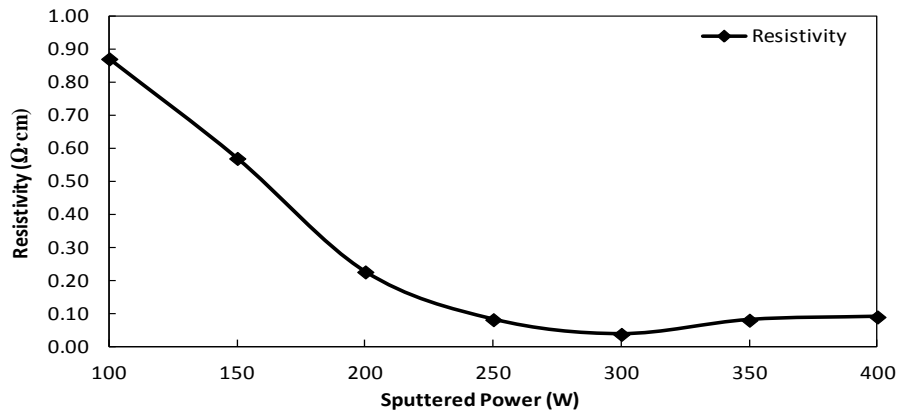
8.2.2 Electrical properties of antimony doped tin oxide

A Hall probe measurement system was used to measure the electrical characteristics of the as-deposited (no post annealing) antimony doped tin oxide ($\text{Sb}_2\text{O}_5:\text{SnO}_2$, ATO) thin films, using only one target composition of 10:90 wt.% $\text{Sb}_2\text{O}_5:\text{SnO}_2$. All the electrical measurements were based on a coating thickness of 400 nm, which was measured using the surface profilometer.

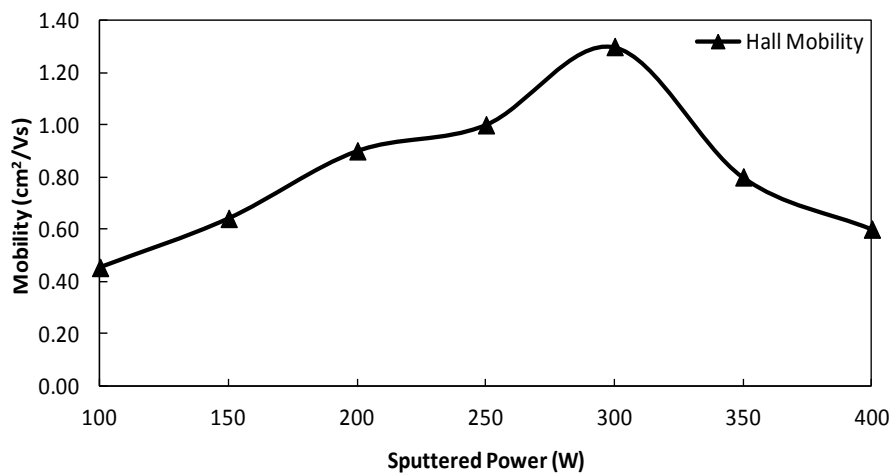
During the ATO trial experiments, it was found that the target power was the major influence on the transparency and the electrical resistivity of the thin films, so it was chosen to be the prime factor during this investigation. The effect of the discharge power was varied from 100 W to 400 W using a constant chamber pressure of 0.5 Pa, and a constant deposition period of 90 minutes. Varying the target discharge power also varied the deposition rate, therefore varying the thickness of the thin films. The film thickness has a major influence on the electrical resistivity and the optical transparency of thin films, and can affect the surface morphology and the crystallinity of the thin film [52]. Thus, a careful measure was made to ensure that during each experiment, a coating thickness of circa 400 nm was produced (this was achieved by varying the deposition run time).

Figure 8.2:2 (a) and (b) outlines the variation of the electrical resistivity and the Hall mobility as a function of varying the target discharge power for the thin films deposited on a standard microscope glass. The results show that all the films are of n-type conductivity. It can be observed from the figure that as the target power increased from 100 W to 150 W, the electrical resistivity

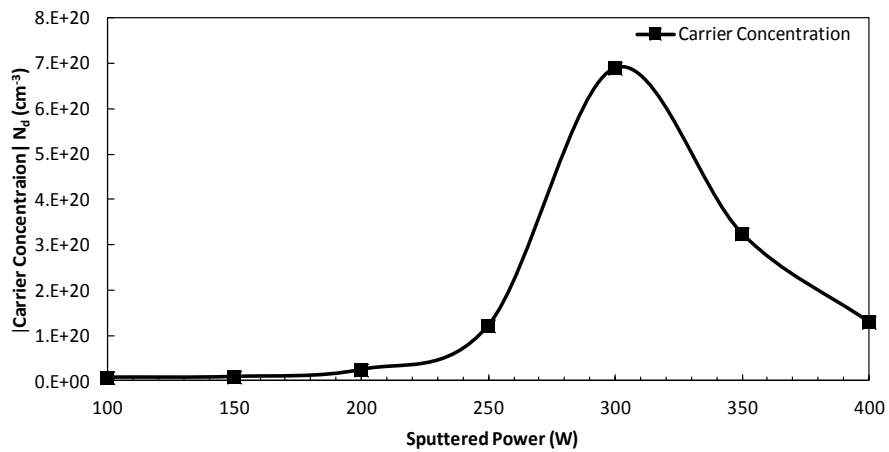
decreased from 8.71×10^{-1} to 5.70×10^{-1} $\Omega \cdot \text{cm}$, at the same time, the mobility increased from 0.53 to 0.64 cm^2/Vs . This can be attributed to the enhancement of the crystallinity as the target power was increased. As the target power was increased from 150 W to 300 W, the resistivity decreased from 5.70×10^{-1} to 3.75×10^{-2} Ωcm , while the mobility increased from 0.64 to 1.30 cm^2/Vs . The improvement in the electrical resistivity and the Hall mobility is due to the reduction in the density of the grain boundaries, which are the transitional regions between different neighbouring crystallites. This causes less carrier scattering to take effect which resulted in the increase in Hall mobility, similar trends were observed in [55] and [175]. As the power was further increased from 300 W to 400 W, the resistivity increased from 3.75×10^{-2} to 9.02×10^{-2} $\Omega \cdot \text{cm}$ and the mobility decreased from 1.30 to 0.60 cm^2/Vs . This sudden change in the electrical resistivity and the Hall mobility is due to the fact that higher target power causes an increase in the deposition rate which therefore can limit the growth of the crystalline grains and can lead to strong boundary scattering for carrier which results in the increased resistivity [54]. Similar trends were observed by Montero et al [55]. Research has shown that antimony doped tin oxide grown by other methods such as DC and RF magnetron sputtering [52, 55], were a subject to in situ annealing or deposited at very high substrate temperatures which promoted the enhancement in the electrical properties of the thin film.



(a)



(b)



(c)

Figure 8.2:2. Variation of the electrical (a) resistivity, (b) hall mobility and (c) carrier concentration of $\text{SnO}_2\text{:Sb}$ thin films with varying target power.

8.2.3 Optical properties of ATO thin films

Figure 8.2:3 presents the optical transmittance in the visible wavelength range of the ATO thin films deposited on a microscope glass substrate as a function of target discharge power. The average transmittance of the ATO film deposited at a target discharge power of 100 W was 67%. Increasing the target discharge power from 100 W to 250 W reduced the optical transmittance to 59%. However, at a target discharge power of 300 W the average optical transmittance improved to 70%. By increasing the target sputtering power to 400 W, the average optical transmittance reduced to 60%. The improvement in the average optical transmittance at a target sputtering power of 300 W is closely related to the film structure. Moreover, the surface morphology also affects the thin films transmittance, as the bigger the grain size, the less light is scattered due to the decrease in the grain boundaries. The improvement in the crystalline structure can also be observed from the XRD data shown in Figure 8.2:4.

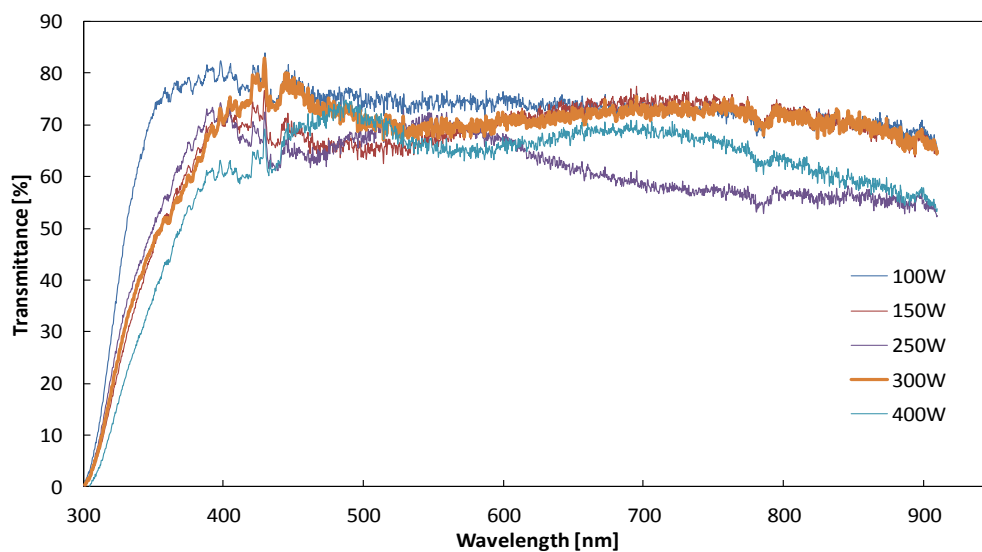


Figure 8.2:3 Optical transmittance of ATO thin films as a function of the discharge power.

8.2.4 Structural properties of ATO thin films

In order to understand the effect of the discharge sputtering power on the crystal structure of the ATO thin films, X-ray diffraction analyses were done over the range 20° to 70° 2θ . The XRD patterns for the ATO thin films as a function of the discharge power is shown in Figure 8.2:4. It is shown that, during a low discharge sputtering power of 100 W, the grown films have been shown to have amorphous structures. This may be attributed to the sputtered atoms not having enough energy to form a crystalline structure, therefore the random structure is created which is of an amorphous nature. It is observed that the increase in the discharge sputtering power to 300 W, resulted in a sharp increase in the (110) peak, and the weak trace of the (101), (200), (211), (220), (310) and (301). Increasing the discharge power to 400 W resulted in the noticeable decrease in the intensity of the main (101) peak which may be attributed to the increase in the deposition rate, a similar trend was observed by Montero et al. [55]. The progressive increase in the (110) peak can be related with the increase in the concentration of the charge carriers [176].

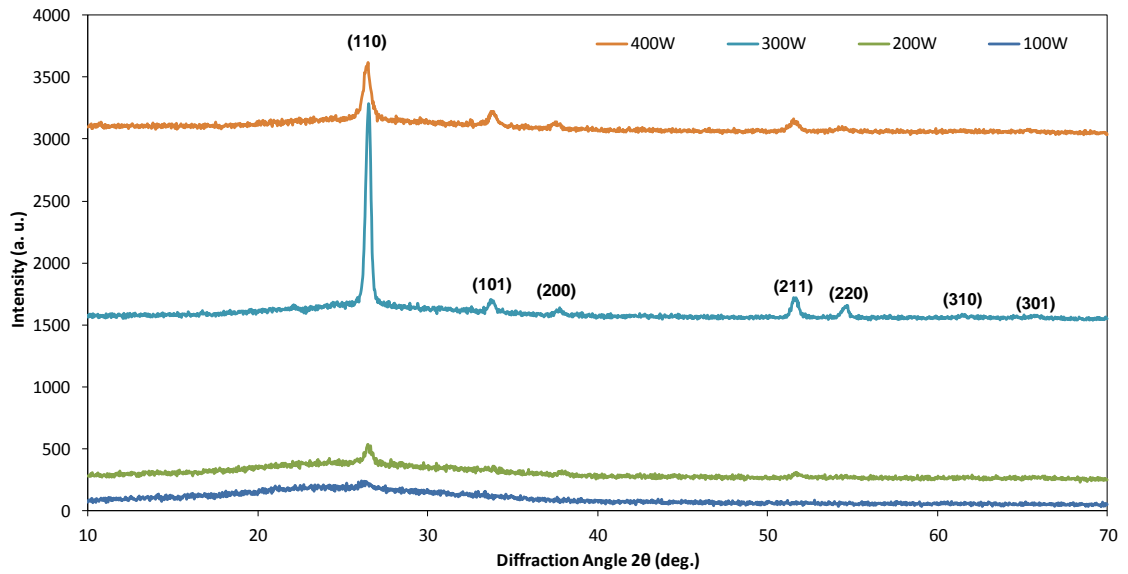


Figure 8.2:4 The XRD pattern for ATO thin films as function of discharge power.

The mean crystalline size of the ATO thin films is shown in Figure 8.1:3. The average grain size for the (110) main peak was measured using the Scherrer formula. It was not possible to measure the crystallite size for the 100 W XRD trace as the (110) had no significance. Figure 8.1:3 shows that the average grain size increases from 5 nm to 15 nm with the increase in the discharge sputtering power from 200 to 300 W. The increase promotes the decrease in grain boundaries and, therefore the decrease in the number of scattering centres for carriers, giving an enhancement in the electrical resistivity the enhancement in the grain size subject to the increase in the discharge sputtering power maybe related to the generation of lattice imperfections as the results of increasing the deposition rate. The increase in the deposition rate can promote the generation of donor carriers in the thin film and therefore enhancing the active growth of the crystalline grains.

Therefore, it is concluded that at the appropriate discharge sputtering power of 300 W, the electrical properties of the ATO thin films were enhanced. However, excessive supply of the discharge sputtering power over 300 W caused the degradation in the (110) preferred orientation, resulting in the decrease in the grain size as shown below. The decrease in the grain size increases the grain boundary scattering, therefore decreasing the Hall mobility and the carrier concentration of the ATO thin films, which causes the poor electrical properties.

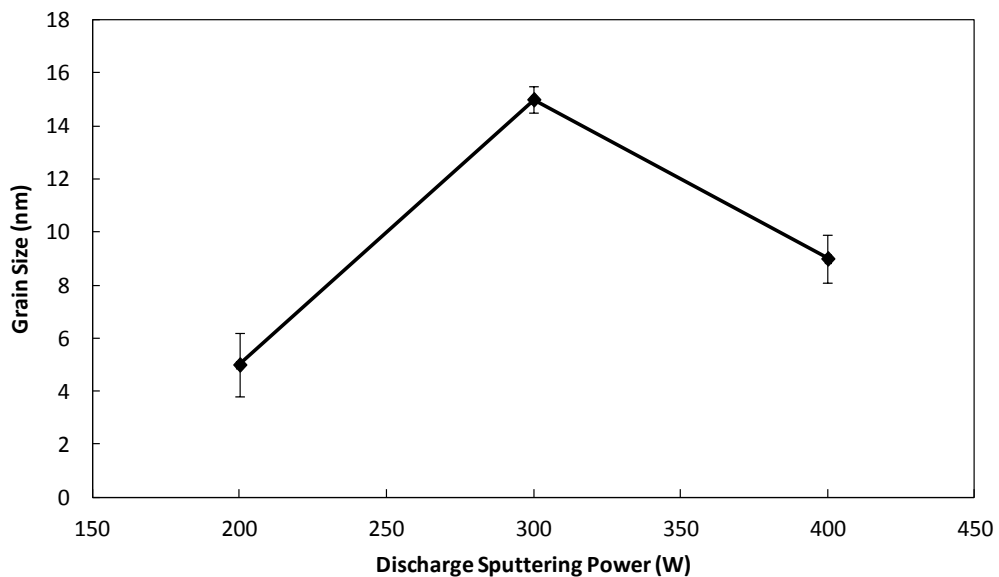


Figure 8.2:5. Average grain size for the ATO thin films as a function of the discharge sputtering power.

8.2.5 Conclusion

The optimisation process of antimony doped tin oxide ($\text{Sb}_2\text{O}_5:\text{SnO}_2$, ATO) at a target atomic ratio of 10:90 at.%, $\text{Sb}_2\text{O}_5:\text{SnO}_2$ was performed by varying the target discharge sputtering power and investigating the effect on the structure, electrical and optical properties of the ATO thin films. The crystallinity of the

thin films improved with increasing sputtering discharge power up to 300 W, this is supported by the XRD patterns. Moreover, the increase in the sputtering power improved the structural properties of the thin film which led to the increase in the Hall mobility by increasing the crystallinity of the thin film. Consequently, the electrical resistivity was reduced due to the decrease in carrier scattering attributed to the improved crystallinity of the coating. Therefore, at a sputtering power of 300 W, ATO thin film was deposited onto a microscope glass substrate with an electrical resistivity of $3.75 \times 10^{-2} \Omega\cdot\text{cm}$ and an average of 70% transmission in the visible range of the spectrum was achieved.

8.3 Copper aluminium oxide

8.3.1 Introduction

In general, two general conditions define a metal oxide TCOs; (1) to have a band-gap higher than 3 eV to be able to transmit 80% of light in the visible spectrum, (2) capability to degenerate doping in order to embrace carrier concentration higher than 10^{20} cm^{-3} [56].

Previous research has been conducted by Alkoy et al. [51] on CuAlO_2 thin films using pulsed DC magnetron sputtering power using oxide powder targets, however no previous work has been reported on using powder form metal base targets. This research used Cu and Al metal based powder target at different composition ratios and deployed excessive oxygen flow rates to the plasma in an attempt to oxidise the thin films and studied the optical

properties of the CAO thin films. In addition, the effect of the discharge sputtering power and the pulse frequency was also report.

8.3.2 Elemental analysis of the CAO thin films

Compositional analysis was carried out on Cu-Al-O thin films that were produced using three powder targets that contained different composition ratios of Cu:Al. The deposition conditions of each trial run were kept identical to minimise the effect of experimental errors (as ascribed in section 7.3.3). It can observed from Table 8.3:1 that the composition analyses of the Cu-to-Al atomic ratio increased from 0.5 to 1.2 with the increase in the Cu atomic content in the powder target. In addition, the Cu, Al and O elements were successfully incorporated in the lattice structure of the deposited thin films, indicating the formation of the Cu-Al-O structure based thin films.

Table 8.3:1 Composition analysis of CAO thin films produced using different powder targets.

Sample ID	Cu (at.%)	Al (at.%)	O (at.%)	Cu/Al ratio
CAO2575	10.5	20.8	68.7	0.5
CAO5050	15.6	12.5	71.9	1.2
CAO7525	31.6	15.52	52.8	2.0

The effect of the discharge sputter power on the compositional ratio of the Cu-Al-O thin films was carried out using the CA7525 powder target.

An Al metal base powder targets are well known to oxidise to form Al_2O_3 under the presence of oxygen partial pressures and that the oxide requires a lower formation energy in comparison to that of CuO_2 [66]. And since Al is

less dense than Cu, it is required to use more content of the Al material during the making of the target, therefore the surface area of Al is greater than that of Cu. The use of a high content of oxygen (oxygen flow rate of 30 sccm) during deposition led to the formation of an oxide layer on top of the Cu:Al powder target surface, which resulted in a decrease of the sputter yield. The formation of the oxide layer, led to the production of two types of sputtered species, the oxides and the metals. Oxides targets have lower sputter yields in comparison to metal targets, as the former have stronger chemical bonds [177].

Table 8.3:2 Composition of Cu-Al-O thin film deposited using various discharge sputtering power.

Sample ID	Cu (at.%)	Al (at.%)	O (at.%)	Cu/Al ratio
CAO 250 W	31.5	15.9	52.6	1.9
CAO 350 W	31.5	15.5	52.8	2.0

The effect on the Cu:Al in the thin film as a function of the various pulsed frequency at a discharge power of 350 W is shown in Figure 8.3:1 and the results are summarised in Table 8.3:3. It can be observed that sputtering in DC mode produced a thin film with Cu-to-Al ratio of 1.9 and increasing further to 2.3 at pulsed frequency of 350 kHz. The effect of varying the pulsed frequency on the composition of the deposited thin film is very little and the observed influence on Cu-to-Al atomic ratio indicated that the pulsed frequency process parameter does not alter the affects the sputter yield of Cu-to-Al ratio.

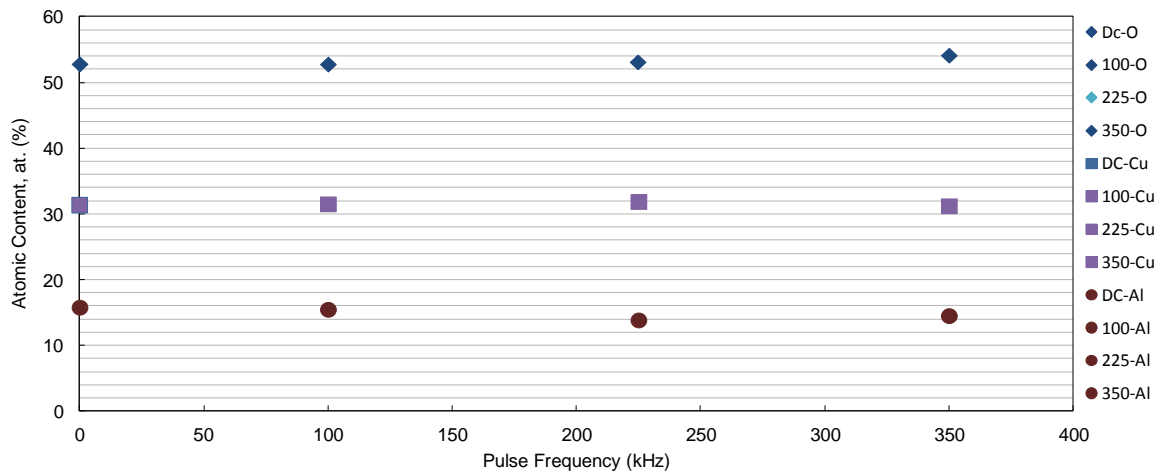


Figure 8.3:1 The effect of pulse frequency on the atomic ratio of a CuAlO_2 thin films.

Table 8.3:3 Effect of pulse frequency on the composition ratio of CuAlO_2 thin films sputtered at 350 W.

Pulse Frequency (kHz)	Cu (at.%)	Al (at.%)	O (at.%)	Cu/Al ratio
0	31.3	15.8	52.8	1.9
100	31.6	15.5	52.8	2.0
225	31.3	14.5	54.2	2.1
350	31.9	13.9	53.1	2.3

8.3.3 Deposition growth rate

Experimental parameters can greatly affect the deposition rate of powder targets. Some of the parameters include the discharge sputter power, pulse frequency and flow rate of the reactive gas. The deposition rate under 250 W and 350 W of discharge sputter power and varying pulse frequencies of DC 100 225 and 350 kHz are shown in Figure 8.3:2. It was observed that using a high discharge sputter power of 350 W produced the highest deposition rate. It can be reasoned that higher discharge power can provide higher flux to the

Ar ions in the plasma, therefore increasing the bombardment on the powder target per second [178].

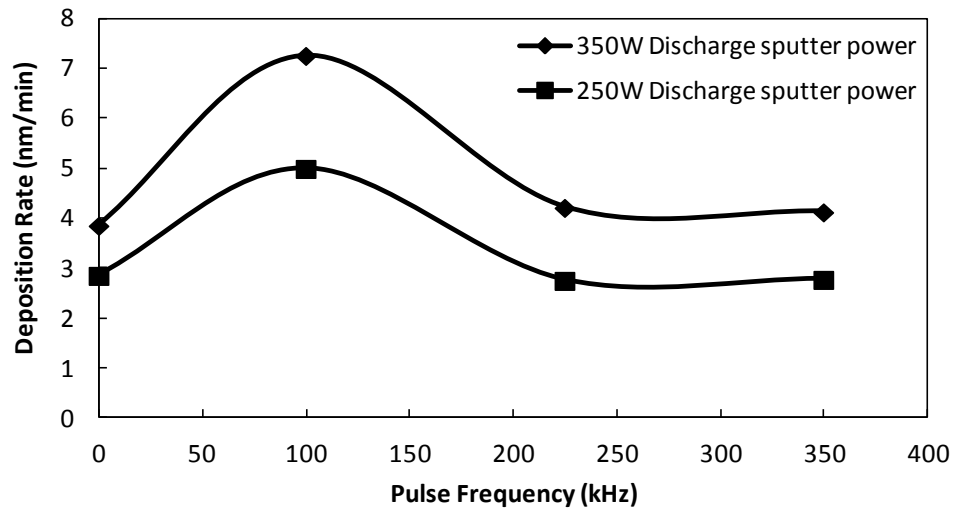


Figure 8.3:2 Deposition rate of Cu-Al-O thin film as a function of various pulse frequency and discharge sputter powers.

The effect of the oxygen flow rate on the film thickness was investigated out using experimental conditions shown in Table 8.3:4. The variation of film thickness as a function of oxygen flow rate was then plotted as shown in Figure 8.3:3. The film thickness decreased with an increase in the oxygen flow rate fed into the chamber. This could be due to the poisoning of the powder metal target occurring at higher oxygen flow rates (also evident from the hysteresis experiments that showed the poisoning of the target at 8 sccm of oxygen flow). In addition, the target contained Al, therefore the formation of the Al_2O_3 on the target surface occurred during the sputtering process, therefore causing an effect on the deposition rate.

Table 8.3:4 Dependence of CuAlO₂ thickness on the O₂ flow rate.

Powder target ID	O ₂ Flow rate (sccm)	Discharge power (W)	Pulse frequency (kHz)	Duty cycle (%)	Deposition period (min)	Film thickness (nm)
CA7525	0	350	100	55	60	1300
CA7525	10	350	100	55	60	450
CA7525	20	350	100	55	60	432
CA7525	30	350	100	55	60	380

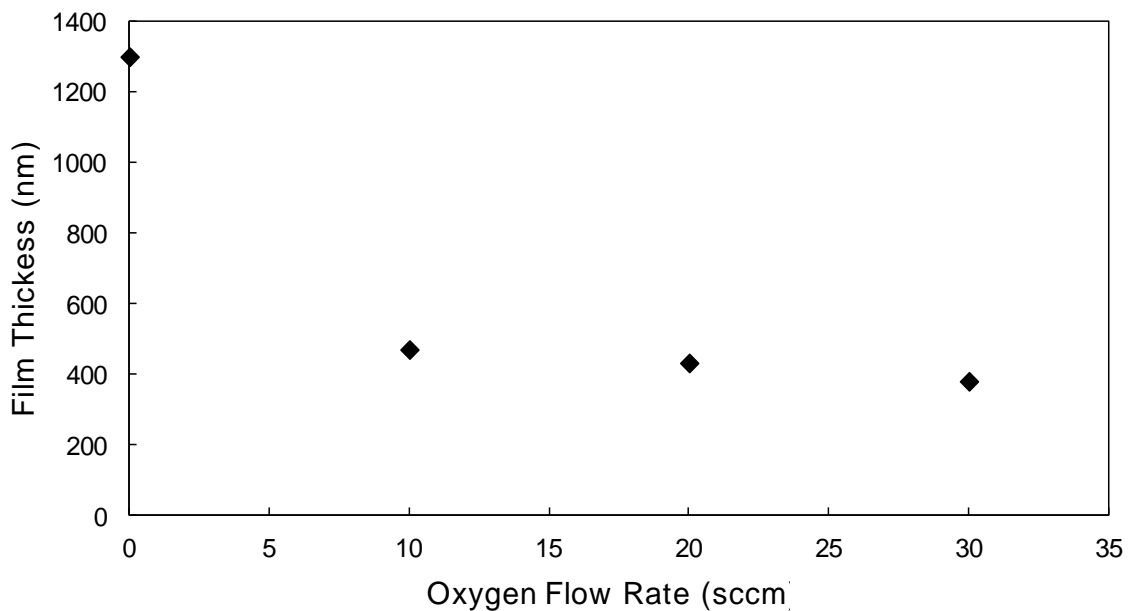


Figure 8.3:3 Effect of the oxygen flow rate on the film thickness of the CuAlO₂ coatings.

8.3.4 Structural properties of CAO thin films

The crystallographic structure and the phase composition of the Cu-Al-O thin films have been shown previously to be greatly influenced by the deposition and the annealing conditions [51]. Figure 8.3:4, shows the XRD patterns of the Cu-Al-O thin films deposited under various discharge powers of 250 W

and 350 W and varying pulsed frequencies of DC, 100 kHz, 225 kHz and 350 kHz.

It was observed from Figure 8.3:4 (a) that sputtering at 250 W using DC mode produced an amorphous structure film. A similar amorphous structure was observed by Reddy et. al when using copper aluminium alloy metal target and sputtered in Ar/O₂ environment using low substrate temperature and DC magnetron sputtering mode [68]. However, as the magnetron discharge was pulsed, and set to 100 kHz, the film structure became crystalline CuAlO₂ with a peak at diffraction 2θ angle of 37.5°, corresponding to the (012) plane. The results are consistent with the standard JCPDS data [179]. It is important to note that no other peaks corresponding to the Cu or the Al metal base target formed in the as-deposited CAO thin films, suggesting single-phase films. This indicates the ability to produce coatings of CAO with no residual metal remainder in the film. Similar results were reported by Alkoy et al. who deposited CAO coatings in an argon only atmosphere using copper oxide and aluminium oxide powder targets, and managed to achieve a delafossite structure with a peak at 37.5° corresponding to the (012) plane [51].

As the pulse frequency was changed to 225 kHz and 350 kHz, the intensity of the (012) peak was reduced considerably. This maybe simply due to lower thickness achieved, 630 nm at 225 kHz and 620 nm at 350 kHz, as can be observed in Table 7.3:1.

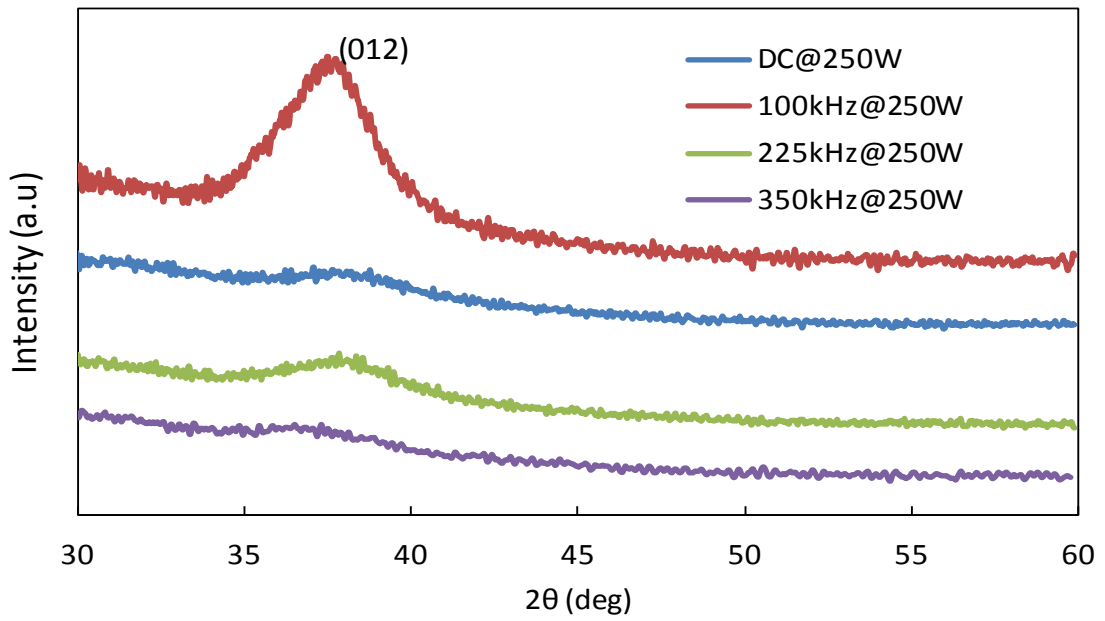
Figure 8.3:4 (b) shows the XRD patterns of the CAO thin films deposited using a sputter discharge power of 350 W and varying pulse frequencies of DC, 100 kHz, 225 kHz and 350 kHz. It can be observed that 350 W improved

the crystallinity of the coatings as the increase in the power effectively increased the deposition rate and raised the deposition temperature. It is important to note that during sputtering at 100 kHz, the intensity of the (012) became more intense and the appearance of the (110) peak in comparison to other pulsed frequency parameters. This could be attributed to the fact that pulsing at 100 kHz produced an optimum amount of ion to atoms ratio during sputtering, to produce a crystalline film.

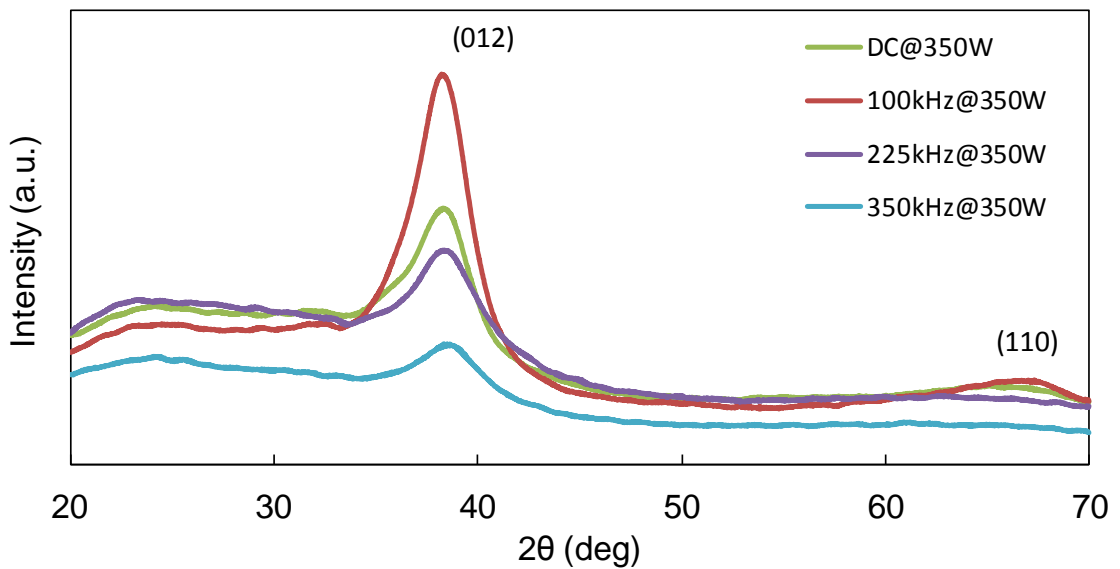
To understand the effect of the discharge sputter power onto the crystallinity of the thin films, the crystallite size of the films was calculated. The analysis of crystallite is performed by measuring the broadening of the (012) diffraction peak. The crystallite size (D) of the as-deposited CAO thin films are calculated using the Scherrer equation (as described earlier) and are presented on Table 8.3:5. For the films deposited at a discharge power of 250 W, it was not possible to measure the crystallite as the peaks were very small apart from the film deposited at 100 kHz, which was approximately of 13.4 nm. At a discharge power of 350 W, the crystallite size was approximately of 13-14 nm. It was not possible to report a great improvement in the crystallinity of the deposited thin film. This suggests that the increase in the discharge power from 250-350 W produced a noticeable difference in the (012) peak of the film. It is important to note that due to the nature of the powder target, the discharge power was limited to 350 W, as increasing the power further resulted in the melting of the aluminium powder particles in the target. Hsieh et. al [66], observed an increase in the grain size from 50-150 nm along with the RF power at 300 W; however, it is important to note that the dimension of the magnetron was 0.1 cm in thickness and 1 cm in diameter as published in

[177], which is considerably smaller in comparison to the size of the magnetron used in during this research, 0.2 cm thickness and 18 cm in diameter.

The EDX data of the thin film deposited at 100 kHz and discharge power of 350 W provided an argument that the Cu-to-Al ratio was found to be 2-to-1 with respect to the oxygen concentration that was introduced during the deposition. Such composition ratio can produce different phase compounds such as Cu_2O with a diffraction peak (111) corresponding to diffraction angle of 34.5° and CuO with a diffraction peak ($\bar{1}11$) corresponding to a diffraction angle of 36.5° . In the literature, it is suggested during the oxidation of Cu, initially Cu_2O is formed during low deposition temperature, and that CuO starts forming with deposition temperatures above 300°C and with increasing oxidation [180]. The deposition temperature of pulsed DC magnetron sputtering using powder target was measured in previous work and it was shown to be 170°C [181], and it is therefore assumed that only Cu_2O can be a possible phase in the as-deposited Cu-Al-O structure, but in weak intensities, or even existing in an amorphous structure. Hence, it was not possible to detect using the XRD diffraction technique. It is therefore possible to conclude that the as-deposited CAO thin film deposited by the pulsed DC magnetron sputtering technique can be composed of possibly two types of structures, an amorphous and nanocrystalline structure.



(a)



(b)

Figure 8.3:4 XRD pattern of the CAO thin films deposited using various discharge power (a) 250 W and (b) 350 W using various pulse frequency of DC, 100, 225 and 350 kHz.

Table 8.3:5 The grain size of the as-deposited CAO thin films.

Target power (W)	Pulse frequency (kHz)	Grain size (nm)
350	DC	13.4
	100	14
	225	13.1
	350	13.3
250	DC	-
	100	13.4
	225	-
	350	-

8.3.5 Electrical properties of CAO thin films

The electrical resistivity of the as-deposited CAO thin films prepared with different Cu-to-Al ratios is shown in Figure 8.3:5. The resistivity of the 0.5 Cu-to-Al coating was 4.20 MΩ·cm. The resistivity was further optimised with the increase in the Cu-to-Al ratio 2.0 down to 4.35 Ω·cm. Increase the copper atomic content from 10.5 at.% to 31.6 at.% in the coating lattice promotes for more free carriers and therefore improved the electrical resistivity of the coating by six orders of magnitude. The hole carrier concentration of the 0.5 and the 2.0 Cu-to-Al ratios were $6.44 \times 10^{11} \text{ cm}^{-3}$ and $4.19 \times 10^{17} \text{ cm}^{-3}$, respectively. The corresponding hole mobilities were 1.35 cm²/Vs to 3.42 cm²/Vs. It can be observed that with high content of Al incorporated into the thin film, it effectively substitutes the Cu ions and distorts the lattice and consumes some of the native holes [177]. A similar effect was observed by Ong et al. who measured an electrical resistivity of 4.8 MΩ·cm at Al content higher than 6.8 at.% in the film. The high resistivity was attributed to the formation of the Al₂O₃ phase in the lattice.

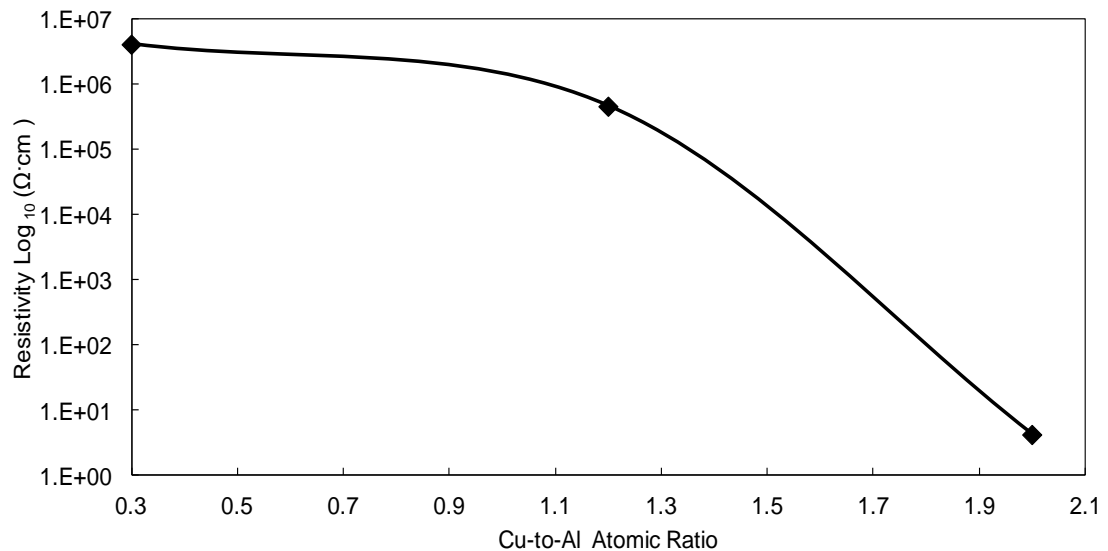


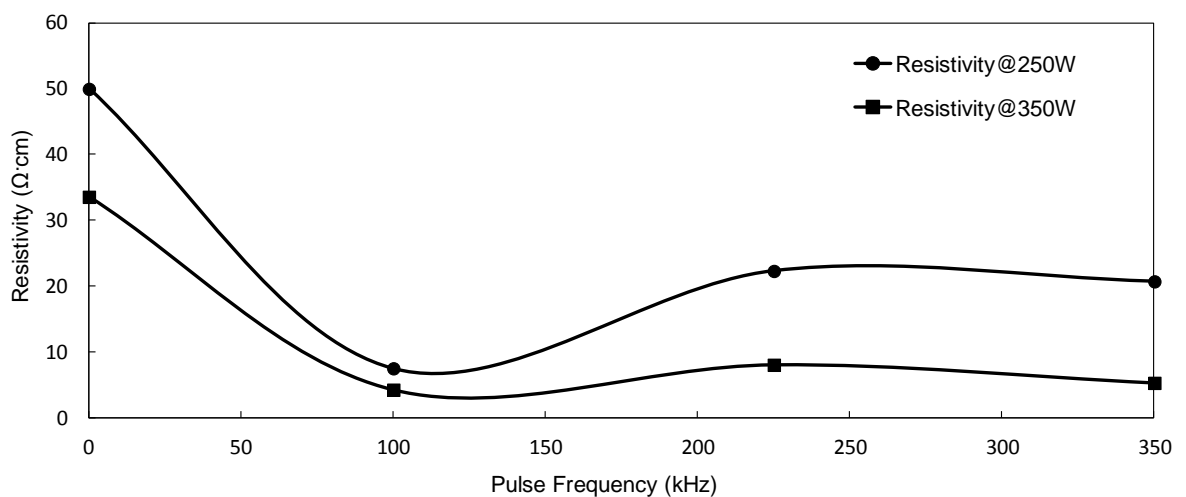
Figure 8.3:5 Effect of Cu-to-Al ratio on the electrical resistivity of the CAO thin film.

The effect of the pulse frequency and the discharge power on the electrical resistivity (ρ), Hall mobility (μ) and hole carrier concentration (n) are shown in Figure 8.3:6. It can be observed from Figure 8.3:6 (a) that the resistivity at 250 and 350 W using DC pulse frequency were 50 and 30 $\Omega\cdot\text{cm}$ respectively. The drop in the resistivity could possibly be related to the difference in the deposition rate between the sputter discharges powers (as observed in Figure 8.3:2), therefore promoting for thicker coatings. In addition, sputtering at higher power promotes for higher energetic atoms and therefore greater thermal energised atoms to impinge onto the substrate. The electrical resistivity decreased to a lowest value of 17.6 $\Omega\cdot\text{cm}$ and 4.35 $\Omega\cdot\text{cm}$ at discharge sputter power of 250 W and 350 W using a pulsed frequency of 100 kHz. The increase in the pulsed frequency to 350 kHz in both discharge powers did not influence the electrical resistivity any further. This gives the indication that sputtering the Cu-Al powder target at a pulse frequency of 100 kHz using 350 W of sputter discharge power; results in the lowest electrical

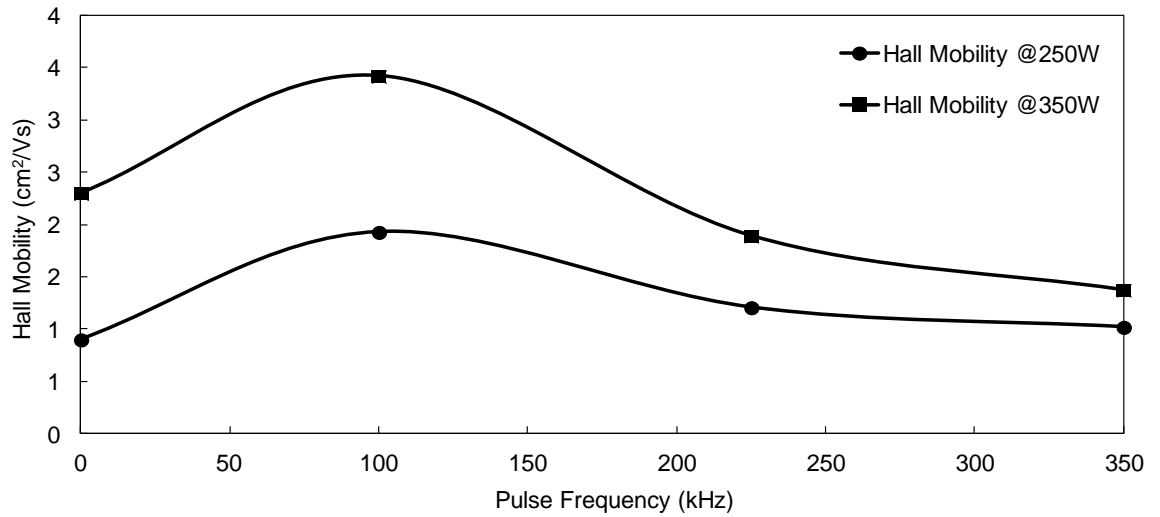
resistivity. The low electrical resistivity of $4.35 \Omega \cdot \text{cm}$ obtained was very closely matched to the of Alkoy et. al who reported resistivities in the range of 5-10 $\Omega \cdot \text{cm}$ using pulsed DC magnetron sputtering with oxide base powder targets. The achieved value of $4.45 \Omega \cdot \text{cm}$ was lower than the $1.9 \text{ k}\Omega \cdot \text{cm}$ for deposition by RF magnetron sputtering and the $10.5 \Omega \cdot \text{cm}$ reported for pulsed laser deposition [62] and the $12 \Omega \cdot \text{cm}$ obtained for DC sputtered films [59]. However Wang et. al reported the lowest resistivity of $0.14 \Omega \cdot \text{cm}$ using plasma enhanced chemical vapour deposition [64].

The Hall mobility and the carrier concentration of the as-deposited CAO thin films were measured against the varying discharge sputter power and the pulse frequency, the results are shown in Figure 8.3:6 (b-c). The positive value obtained for the carrier concentration indicates the majority of the carriers in the thin film are of positive charge and therefore it was determined that the required p-type characteristic was achieved. The results showed that using a discharge power of 350 W and a pulse frequency of 100 kHz produced a Hall mobility of $3.42 \text{ cm}^2/\text{Vs}$ in comparison to $1.93 \text{ cm}^2/\text{Vs}$ achieved during a discharge power of 250 W and pulse frequency of 100 kHz. It can be clearly observed that increasing the discharge power from 250 to 350 W influenced the Hall mobility and the carrier concentration of the as-deposited CuAlO_2 thin films. However it was not possible to increase the power any further. Other literature suggests that the improvement in the Hall mobility and the carrier concentration can be attributed to the improvement in the grain size and hence the decrease in the grain boundaries and minimising the trapping/scattering of the charge carriers at the grain boundaries [68, 182]. However, in this research, the crystallite size did not vary along the (012)

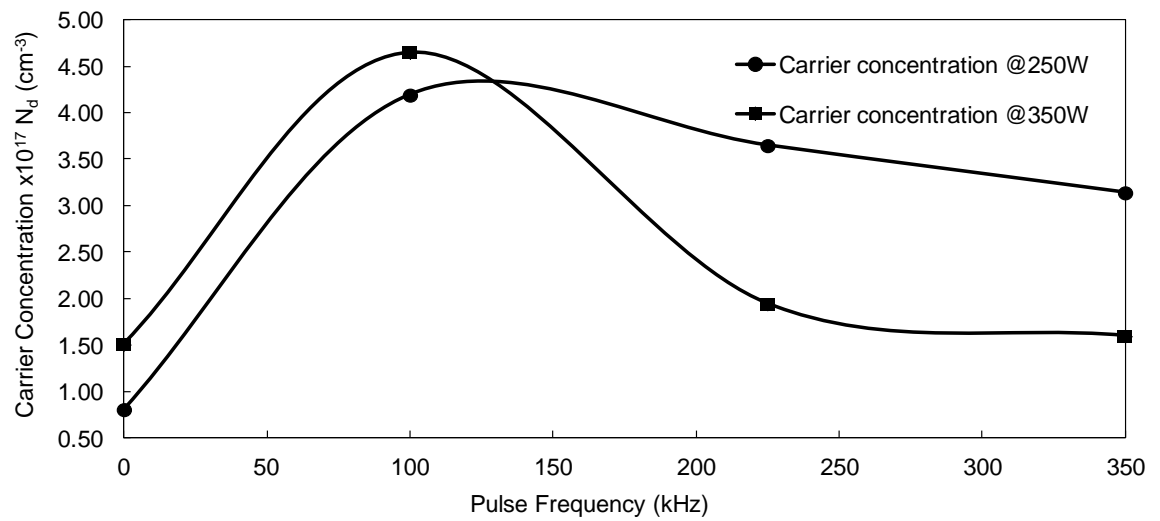
diffraction peak with respect to the change in the discharge power or the pulse frequency. This may be attributed to the weak diffraction signal of the immature nanocrystalline CAO thin film. Hence, the need to use further analytical techniques such RBS (Rutherford backscattering spectroscopy) and XPS (X-ray photoelectron spectroscopy) to determine the composition structure and valence of the elements, respectively. This will give a clearer understanding of the influence of the oxygen valency on the conduction mechanism of the CAO coatings and the effect of the excess oxygen vacancies on the conduction mechanism of the as-deposited thin films. Lan et. al reported that the electrical properties of the CAO thin films is dependent on the oxygen concentration and reported an enhancement in the electrical resistivity by an order of one magnitude to a minimum value of $217 \Omega \cdot \text{cm}$ at a partial pressure of 0.4 Pa of oxygen [183].



(a)



(b)



(c)

Figure 8.3:6 Electrical properties (a) resistivity, (b) Hall mobility and (c) carrier concentration of CAO thin films using various pulse frequency and discharge sputtering power.

The effect of the oxygen flow rate on the metal based copper aluminium powder target with atomic composition of 75at.%Cu:25at.%Al were investigated by depositing the films under different oxygen concentration of, 2 sccm, 4 sccm, 20 sccm 30 sccm. The electrical resistivity of the thin films were measured. The base pressure was kept at 0.6 pa with constant argon flow of 13 sccm. The pulse frequency was kept at 100 kHz with duty-cycle 55 % and a discharge power of 350 W.

The films deposited at oxygen flows of 2 to 4 sccm showed a very high electrical resistivity of 39 K Ω ·cm and 10 K Ω ·cm, respectively. Increasing the oxygen flow from 6 to 10 sccm decreased the electrical resistivity from 241 Ω ·cm to 20 Ω ·cm respectively. The electrical resistivity decreased further from 18.5 Ω ·cm to 4.35 Ω ·cm as the oxygen flow was increased from 12-30 sccm, respectively. The maximum oxygen flow rate of the mass flow controller was reached and it was not possible to increase the oxygen flow any further. The results shown in Figure 8.3:7 indicate that the lowest electrical were achieved with oxygen flow rate of 30 sccm, indicating that the electrical resistivity of the as-deposited thin film is sensitive to the oxygen concentration.

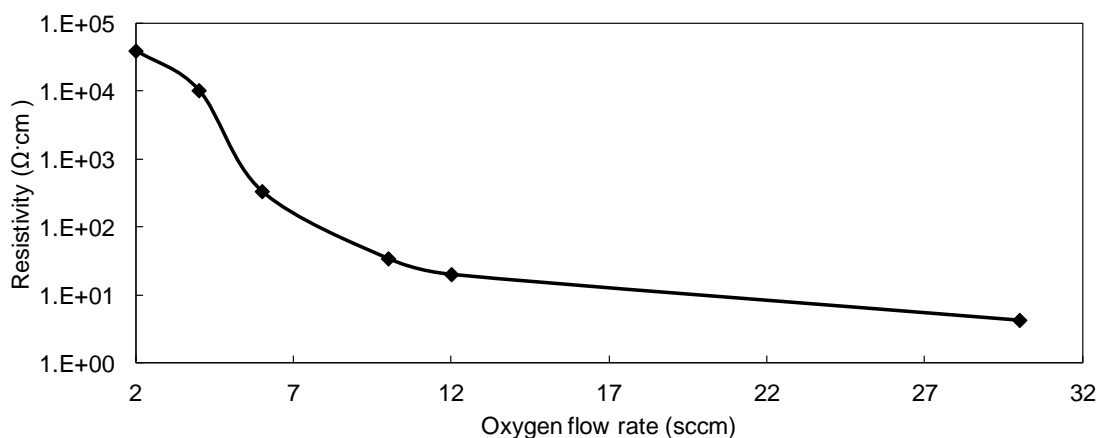


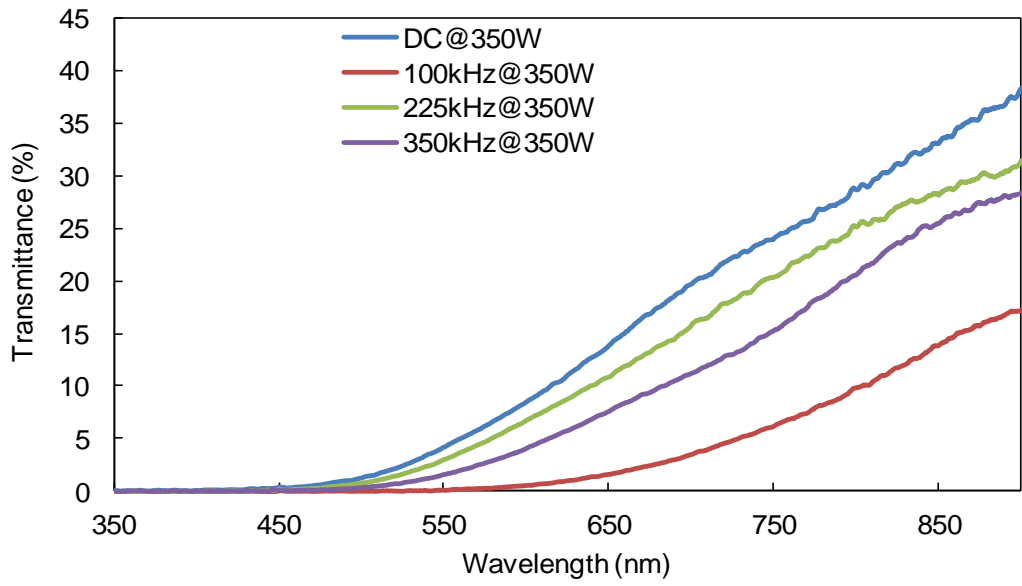
Figure 8.3:7 Effect of the oxygen flow rate on the CAO thin films.

8.3.6 Optical properties of CAO thin films

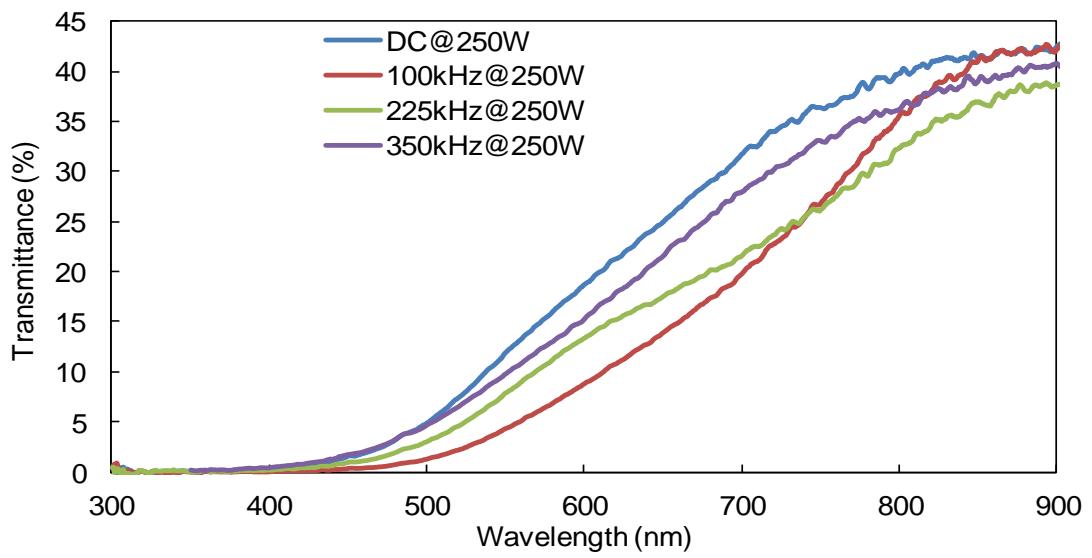
The optical transmissions of the as-deposited CAO were recorded for 300 nm to 900 nm wavelength range, taking a similar glass substrate as reference, and hence the spectrum gave transmittance of the films only. The optical transmittance of the samples sputtered using 250 W and 350 W at varying pulse frequencies are shown in Figure 8.3:8 (a) and (b) and the average Transmittance between 300-900 nm as a function of the varying pulse frequency is shown in Figure 8.3:8 (c). As can be observed, the transmission is found to be very small in the lower wavelength of visible regions, this can be attributed to the fact that the films contained high atomic percent of copper metal atoms, and metal elements are opaque in the visible region [60].

The average transmittance was found to decrease from 27.5% to 14 % with the increase in the discharge power from 250 W to 350 W. Higher discharge power promotes thicker films, therefore degradation in the film transmission can be attributed to the difference in film thickness.

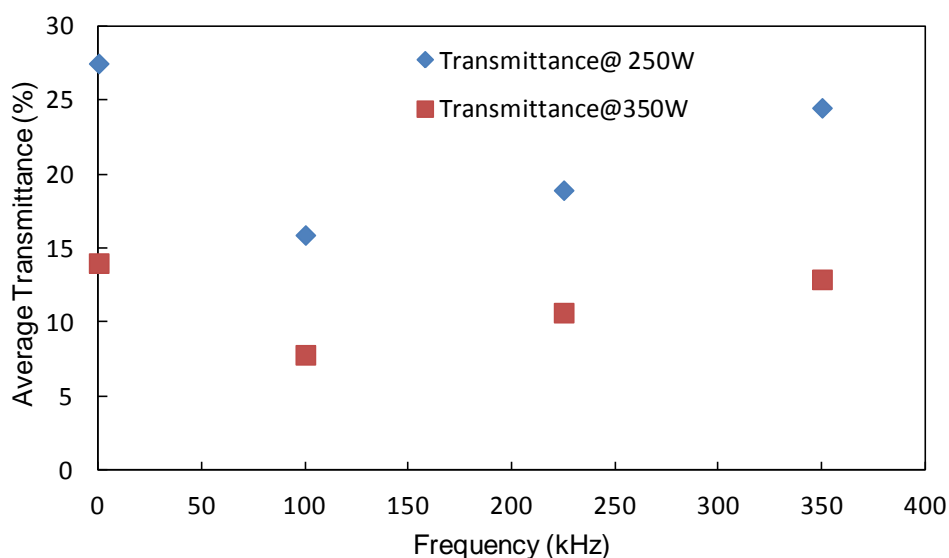
Regardless of the sputter power used, 100 kHz pulse frequency promoted for the lowest transmittance of 15.9% and 7.8% for 250 W and 350 W of discharge power, respectively. Therefore concluded that deposition conditions such as the discharge power and the pulsing frequency plays an important role on the deposition thickness of the thin film and effectively on the performance of the films.



(a)



(b)



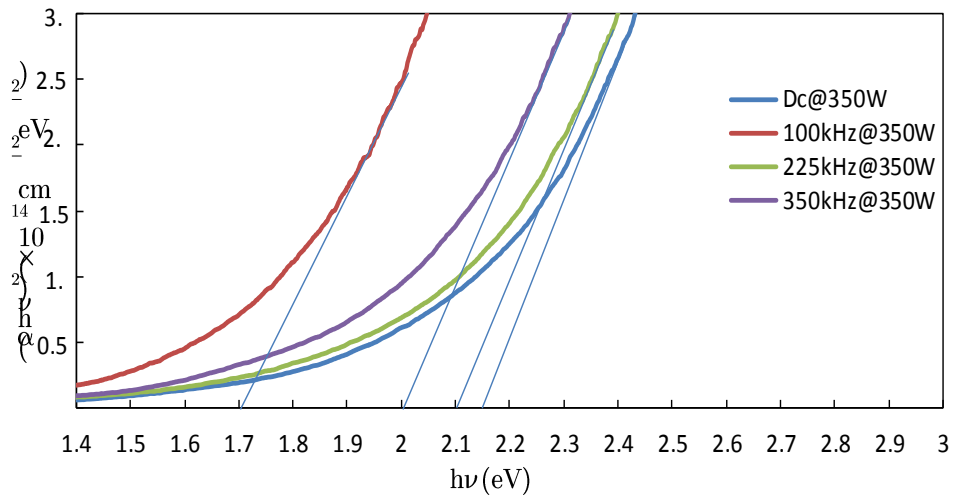
(c)

Figure 8.3:8 Optical transmittance of CAO thin films grown using (a) 350 W (b) 250 W sputter discharge power (c) average transmittance across 350-900 nm at various pulsed frequency and discharge sputter power.

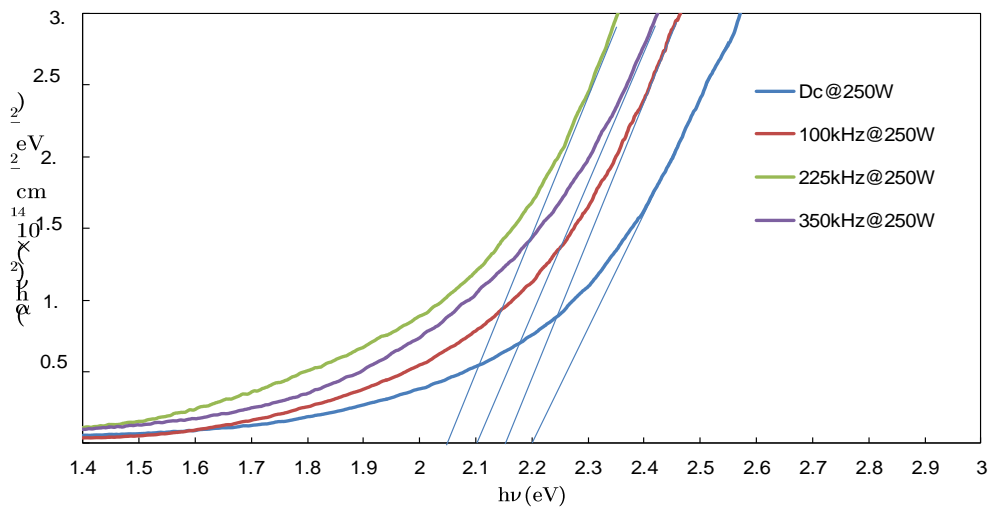
The optical band-gap (E_g) of the CAO films was determined from the transmission spectra and calculated using Tauc method described in the earlier section. Based on previous reports, the optical band-gap of CAO thin films were reported to exhibit a direct band-gap, in the range of 3.4-3.7 eV and located the indirect band-gap in the range of 1.65-2.1 eV [183-185]. All the calculations were based on direct transition, for this, the band-gap was calculated from the spectra of $(ah\nu)^2$ Vs $h\nu$ plot by extrapolating the linear portion of the curve to the, $h\nu$, axis, as shown in Figure 8.3:9. The results of this study were summarised in Table 8.3:6. The highest optical band-gap achieved was 2.2 eV at discharge power of 250 W DC. The achieved optical direct band-gap is not within range of other reported values such as that of Lan et al. who reported a direct band-gap of 3.47eV and that of Fang et al.

who reported a direct band-gap of 3.5 eV and of Yin et al. who reported band-gap of 3.26 eV [158, 183, 185]. This disparity could be due to the different growth conditions and to post deposition treatments. Also, the nano sized particles (average of 13 nm particle size) achieved during this study are much lower than that reported by other techniques such as 50 nm reported by Reddy [68] et al. and 33 nm reported by Rwei et al. [158]. Therefore, the increase in the scattering of the incident photon could be a factor in narrowing the absorption edge and therefore reducing the optical direct band-gap.

Another useful technique in determining the optical band-gap of semiconductor is the use of photoluminescence technique. When a valence electron is given the right amount of energy to overcome the electrostatic potential, the valence electrons of a semiconductor material transit from the valence band (ground state) to the conduction band (excited state) where the electrons are unstable. The electrons then transit back to the ground state and emit a photon. By measuring the wavelength of the photon, the band-gap can be estimated [158]. In other published work, photoluminescence analysis studies showed that the band-gap of the CAO thin film decreased from 3.84-3.60 eV as the average grain size of the thin film increased from 30-60 nm [59]. Alivisatos reported that the absorption edges shifts to higher energy (blue-shift) as the particle size was reduced [186]. Another reason that may affect the absorption edge is the high content of the Cu metal particles within the lattice, therefore absorbing most the photon and causing the reduction in the optical direct band-gap.



(a)



(b)

Figure 8.3:9 The direct optical band-gap of CAO thin films as a function of discharge power at (a) 350 W and (b) 250 W with varying pulse frequencies

Table 8.3:6 Average optical transmittance and energy band-gap of CAO thin films grown using various pulse frequency and discharge sputtering power

Discharge Power (W)	Pulsing Frequency (kHz)	Direct Band-gap (eV)	Average optical Transmittance (350-900 nm) (%)	Film Thickness (nm)
250	DC	2.20	27.50	430
	100	2.15	15.90	600
	225	2.05	18.90	415
	350	2.15	24.50	417
350	DC	2.15	14.0	580
	100	1.70	7.80	1090
	225	2.10	10.65	633
	350	2.0	12.90	620

8.3.7 Conclusion

CAO thin films were successfully deposited on glass substrate using loosely packed *Cu* and *Al* metal base powder targets deposited by pulsed DC magnetron sputtering. The influence of pulsing frequency and discharge sputter power and oxygen flow rate were demonstrated. The best electrical properties were achieved using at duty cycle of 55% with pulse frequency of 100 kHz, discharge power of 350 W and oxygen flow rate of 30 sccm. The optimised conditions produced a CAO thin film with diffraction peaks at 2θ angles of 37.5° and 66.5° , corresponding to the (012) and the (110) planes. A p-type semiconductor was grown to 1 μm and obtained electrical resistivity of $4.35 \Omega \cdot \text{cm}$, a hole carrier concentration of $4.6 \times 10^{17} \text{ cm}^{-3}$ and average optical transmittance of 7.8% and optical band-gap of 2.1 eV. The low optical properties were attributed due to the nano-size particle size and the high content of the Cu atoms. The results showed that the developed p-type CAO

can be used as p-type semiconductor layer in the heterojunction configuration that will be developed in this research.

8.4 Photovoltaic response of p-n junction

The photovoltaic response of the developed p-n junction diode was characterised by measuring the current-voltage behaviour of the device in dark and under illumination. The intensity of the incident light was 100 mWcm⁻² (AM1.5) provided by a halogen lamp that was placed 10 cm directly above the device under test (DUT). The J-V characteristics were then determined by measuring the current density and the voltage. All measurements were taken at room temperature.

The AM1.5 J-V characteristics curves of the p-n junction diode device were collected using an Abet Technologies Ltd. Solar simulator with light power density calibrated using a LOT Oriel GaAs reference cell was used. To generate the voltage sweep between -1 V to 1 V, a Keithly source meter was used, whilst measuring the current densities of the device both in the dark setup and under light illumination. A visual basic program was used to generate the J-V curve and calculate the parameters of efficiency, short circuit current (I_{sc}) density, open circuit voltage (V_{oc}) and the fill factor (FF). The J-V characteristics of the device are shown in Figure 8.4:2.

When the light shines at the cell, it resulted in the flow of the drift current due to the minority electrons and holes, which flow from the n-FTO to the p-CAO. This produced a light-generated current I_L . The photovoltage that is generated from the I_L in the forward bias mode, reduces the junction's potential energy

barrier, resulting in a diffusion current that flows in the opposite direction to that of the I_L . Since the magnitude of the I_L is bigger than the forward biased diffusion current, the net current flows from the n-side to the p-side (opposite to that of the forward biased diode current). Hence, when the light shines on the cell, the current flows in the opposite to the direction of the generated voltage. Over all, when the light shines onto the cell, the J-V curve shifts downwards in the current-voltage axis as shown in Figure 8.4:2.

During forward bias measurements, the holes in the CAO and the electrons in the FTO are pushed to the junction, which reduces the thickness of the depletion region and lowers the barrier of the p-n junction. When the bias voltage is further increased, the depletion region becomes low enough to disable the zone's electric field from the counteracting charge carrier motion across the p-n junction, therefore reducing the electrical resistance [187]. During the reverse bias, the holes in the CAO and the electrons in the FTO are pulled away from the junction, which promotes an increase in the depletion region. This consequently raises the voltage barrier, which causes high electrical resistance to the flow of the charge carriers [187]. This indicates that the absorption of light by the active layer generates carriers, which therefore contributes to the photocurrent due to the production of excitations and their subsequent dissociation into the free charge carriers at the junction barrier indicating the observed rectification. It was expected that the photovoltaic characteristics of the CAO and the FTO would originate a rectifying behaviour due to the depletion region formed at the interface.

The characteristic of the p-n junction solar cell diode are determined in terms of the open circuit voltage (V_{oc}), the short circuit current density (I_{sc}) and the fill

factor (FF). The V_{oc} is defined as the maximum voltage that can be obtained from the p-n junction solar cell device when its terminals are left open. It corresponds to the amount of forward bias of the p-n junction due to the light-generated current (I_L), and at this voltage, the (I_L) becomes equal and opposite to the forward bias diffusion current of the p-n junction solar cell diode. The short circuit current is defined as the maximum current produced by the p-n junction solar cell diode when its terminals are shorted, i.e. when the voltage is zero, which is equal to the photon current (I_{ph}). The V_{oc} and I_{sc} were determined from the I-V curve to be 0.40 V and 65.3 $\mu\text{A}/\text{cm}^2$ respectively, which give an ideal power (P_o) of 26.1 $\mu\text{W}/\text{cm}^2$. Other photovoltaic devices, such as the Au/ZnO:Co/n-Si produced a maximum V_{oc} of 0.195 V and I_{sc} of 2.63 μA . The low performance of the device, was attributed due to the short life-time of the photo-carriers due to the number of traps [188].

The maximum power (P_m) was also calculated from the I-V curve shown in Figure 8.4:3, by measuring the maximum voltage (V_{max}) and the maximum current (I_{max}) which were 0.25 V and 45 $\mu\text{A}/\text{cm}^2$, yielding a maximum power density of 11.3 $\mu\text{W}/\text{cm}^2$. The fill factor, FF , was then determined which is a measure of the power conversion efficiency of the J-V characteristics and it is always less than one. It is the ratio of the maximum power (P_m) that can be extracted from the device to the ideal power (P_o), it is given by the following equation [189],

$$FF = \frac{P_m}{P_o} = \frac{[V_m \times I_m]}{[V_{oc} \times I_{sc}]} \quad \text{Eq. 8.4:1}$$

The FF was calculated to 43.2%. The most important figure or merit of the p-n junction device is the power conversion cell efficiency (η), which is the ratio of the power output to the power input and it is defined as [189],

$$\eta = \frac{P_m}{P_{rad}} = \frac{FF \times V_{oc} \times I_{sc}}{P_{in}} \quad \text{Eq. 8.4:2}$$

The power output is the maximum power point P_m of the cell, and the input power is the power of the light spectrum incident upon the p-n junction device P_{rad} , which is 100 mW/cm². The efficiency of the device was calculated to be 0.045 %. Other p-n junction devices fabricated from Cu₂/TiO₂ produced efficiencies of 0.01% and attributed the low efficiency was attributed to the poor contacts and small junction area of their device [190]. The performance of the device are summarised in the table below.

Table 8.4:1 Photovoltaic parameters of n-FTO/p-CAO p-n junction solar cell device

Device Performance	Value
$J_{sc}(\mu A)$	65.3
$V_{oc}(V)$	0.4
FF	0.43
η (%)	0.0452
$V_m(V)$	0.25
$I_m(\mu A)$	45
Cell area (cm ²)	0.25

The developed photovoltaic performance is similar to that developed by Ocak et. al who developed a heterojunction devices by DC-sputtering a n-ZnO thin film onto p-InP substrate and observed a good rectification with $FF = 32$ %

and η of 0.0754 % and attributed the low efficiency of the device due to the high series resistance [191]. The achieved photovoltaic parameters are very low for practical applications which could be due to the fundamental reasons (limited by the material properties) or due to the technological reason (limited by cell processing capabilities). When the energy of incident photons onto the device have less energy than the band-gap energy of the device they do not contribute to the generation of the hole-electron pair generation. This type of loss is referred to as transmission loss and it almost equals to 23% of the losses in single junction p-n junction solar cells [192]. If the photon energy is higher than the band-gap energy of the device, the excess energy is given off as heat to the material, this type of loss is referred to as thermalisation loss, which contributes to about 33 % of a single junction solar cells [192].

Other unavoidable losses in the solar cells that contributes to the loss in the conversion efficiency is the parasitic resistance such as the series resistance R_s and the shunt resistance R_{sh} [191]. The equivalent circuit of a real solar cell device is shown in Figure 8.4:1. The R_{sh} represents the resistive losses that are caused by the current leakage across the diode and at the edge of the device. The effect of the impurities and the crystal defects in the depletion region of the p-n junction also contributes to the R_{sh} of the device.

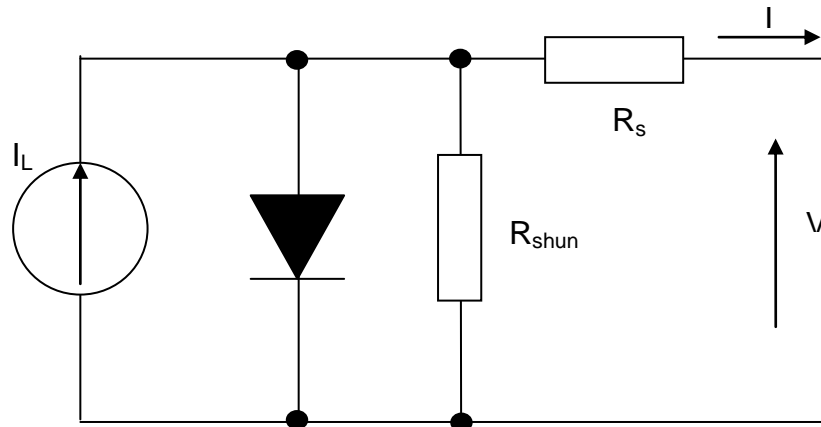


Figure 8.4:1 The equivalent electrical circuit of a real pn-junction solar cell.

As mentioned in the previous sub-chapter, the electrical resistance of the deposited n-FTO was about 150Ω , which acts as a loss in the current efficiency of the device. Meanwhile, the p-CAO films suffered from high resistance $+100 \text{ K}\Omega$ and from small grain size ($<10\text{nm}$) which may act as carrier traps to the excited electrons, therefore increasing the recombination effect and decreasing the flow of the current. The recombination processes play an important role in the device performance as the photogenerated charges can recombine before reaching the electrodes of the device. The recombination effect mainly reduces the V_{oc} of the device, which as consequence reduces the FF . Another factor that decreases the efficiency of the device is the shunt resistance which arises due to the leakage across the p-n junction due to the crystal defects of the material in the junction region [192].

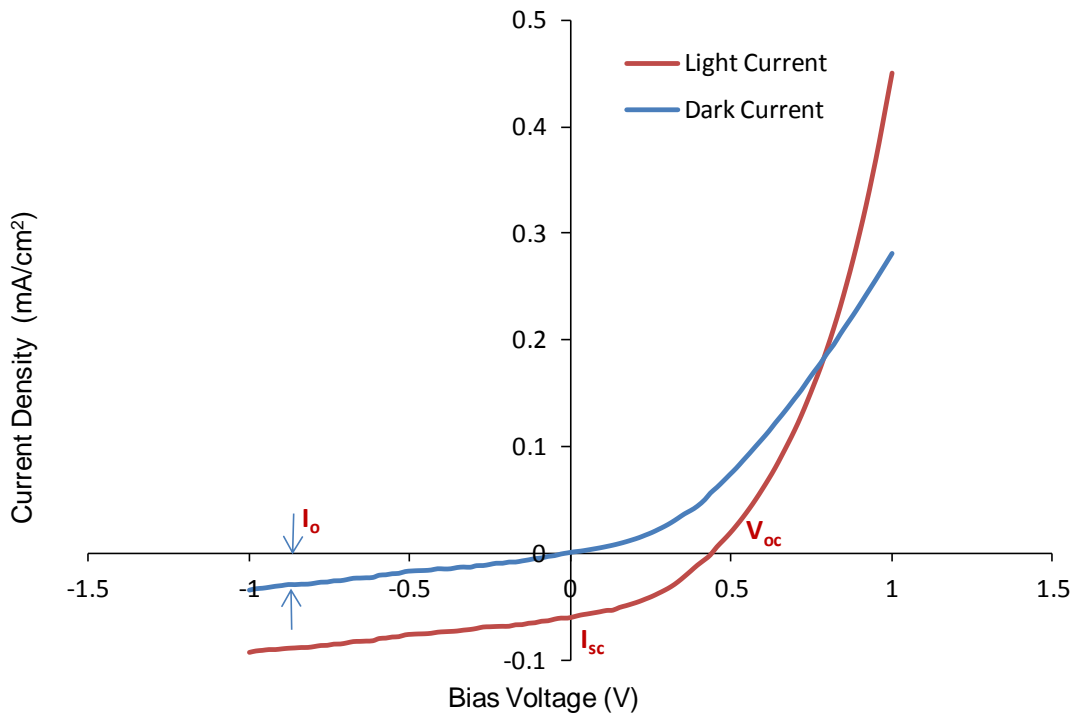


Figure 8.4:2: Electrical I-V characterisation of the p-n heterojunction device in dark and under illumination.

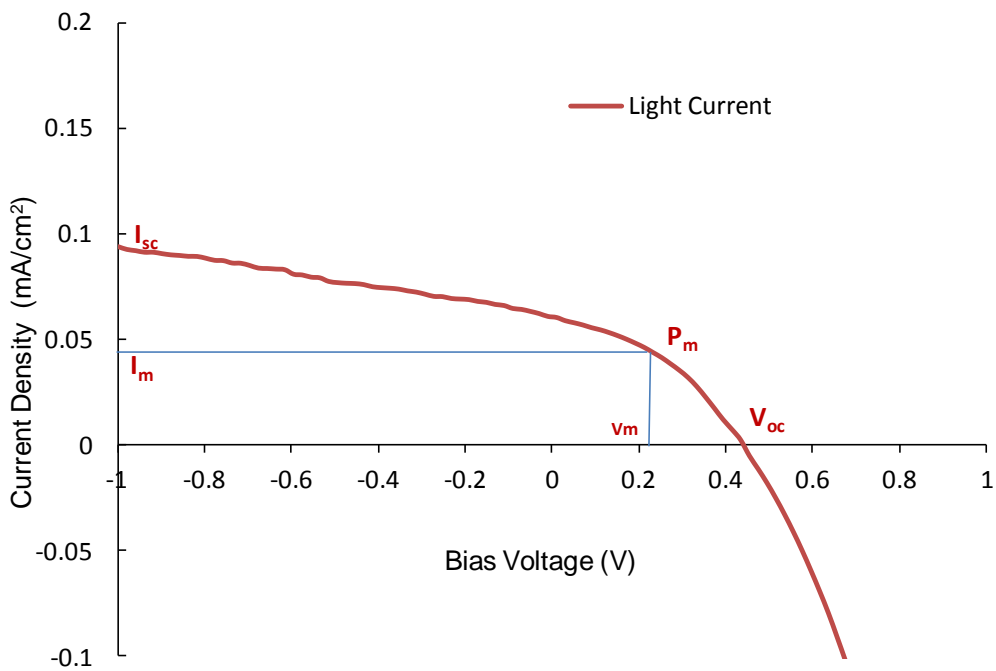


Figure 8.4:3 I-V curve and the parameters used to calculate the device performance.

The fabrication process of the electrical contacts for the n-FTO layer followed a number of trials using different device configurations in order to optimise the device performance in terms of efficiency and device reproducibility. In terms of the device efficiency, the size of the device was constructed to accommodate an area of 10 cm² in order to capture the most amount of sun light energy therefore harvesting increasing the efficiency of the device. The initial device configuration was set up to use Ag as the electrical contacts for the n-FTO, however, the design was not successful because the silver kept delaminating from the glass substrate and it was also very difficult to solder onto the contact pads. In addition, two separate deposition runs were needed to complete the design of the contacts, this added to the production process time. Figure 8.4:4 outlines the design layout for the bottom contact layer of the n-type layer and the stress related problem that were encountered after the deposition of the n-FTO onto the Ag contacts.



(a)



(b)



(c)

Figure 8.4:4 n-FTO Ag electrical contacts (a) Mask design (b) complete Ag contact design, (c) problems encountered after FTO deposition onto the Ag contacts.

8.4.1 Conclusion

A p-n junction power generating diode was successfully fabricated using pulsed DC magnetron sputtering technique using a combination of un-sintered loosely packed powder targets. The main parameters of the n-FTO/p-CAO heterojunction illumination such as the short circuit current density (J_{sc}) $65.3 \mu A/cm^2$, open circuit voltage (V_{oc}) 0.4 V, fill factor (FF) 0.43 and power conversion efficiency 0.043% were determined. The device showed that the current at a given voltage for the device under illumination is higher than that in the dark. This indicates that the absorption of the light by the active layer generates carrier contributing photocurrent. This is due to the production of excitants and their subsequent dissociation into the free charge carriers at the p-n junction interface. Consequently, a successful generation of a photovoltaic solar cell have been achieved. Further improvements in the photovoltaic properties can be realised by:

- Optimising the thickness of the p-type CAO layer
- Investigation of other material as a substitute to the P-CAO candidates
- Improving the growth conditions of the device.

OVERALL CONCLUSIONS

The aim of this project was to use un-sintered loosely packed powder targets as a deposition source for pulsed DC magnetron sputtering to create a p-n junction solar generating diode. In retrospect, this thesis can be divided into five parts, *i)*, a general historical background of solar cell, *ii)*, theory of semiconductors and p-n junctions, *iii)*, a general description of PVD and magnetron sputtering, *iv)* development of n-type and p-type thin films and the electrical contacts for the p-n junction device, *v)* performance of the developed thin films and the p-n junction device.

The field of photovoltaic solar cells technology has witnessed a rapid increase of demand as a producer of electricity using very low cost materials and technology for large-scale production. This has pushed thin film solar cell technology to be the perfect candidate and for the magnetron sputtering technique to be the prime technology for the production of thin film solar cells. Because no silicon materials are required, relatively high deposition rate can be produced and the technology is available for large area production volumes.

The conclusion of this research can be summarised as follow,

- Pulsed DC magnetron sputtering from blended powder targets has been shown to be very viable, highly versatile technique for the production of the thin films for the production of the p-n junction solar cell diodes.
- The deposition system can be used to deposit either single or multi-component thin films.
- Provided the powder targets are well mixed, it offers a good control over the film composition.
- The film structure of a deposited thin film depends greatly on the sputtered material, the substrate chemistry and morphology, the preparation of the substrate surface, the deposition process and the deposition parameters.
- It is important to create TCO that exhibit a film structure of zone 2 or zone 3.
- SEM micro images of the thin films showed the production of dense columnar with defect-free thin films at deposition temperatures lower than 170 °C and at relatively high deposition rate.

- Owing to the insulating nature of the powder target, the use of the pulsed DC configuration with negative cathode voltage is necessary in order to offset the charge build up on the target surface. Using such configuration yielded well adhered and densely structured coatings.
- Using the pulsed DC magnetron sputtering technique in combination with powder targets promotes for a cost effective (no post annealing of samples, and high deposition rate) and environmentally friendly method (no fluorine gas is used and no toxic effluent is produced). This technique is of great advantage for studying the properties of multicomponent materials and identifying optimum compositions.
- Using powder targets limits the use of high sputtering power due to the thermal instability therefore 500 W is the maximum power that can be used in powder sputtering.
- Substrate-to-target distance was proven to be influential on the electrical properties of the as-deposited thin films.
- Process conditions, including, the base pressure, pulse frequency and oxygen flow rate influenced the target voltage of a Ti powder target. Low operating pressure results in higher target voltage and the increase in the probability of sputtered atom transport from target to substrate surface due to the lowering of the gas scattering rate between the background gas and the sputtered atom. Also, lower pulsing frequency results in higher deposition rate because more of the pulse on time is available to sputter the target.
- To enhance the optical and electrical property of the TCO, a controlled concentration of a dopant is added. The addition of the dopant to the

semiconductor was to enhance the carrier concentration of the free charge carriers. Excess doping concentration can cause serious scattering effect which in turn lowers the carrier mobility, effectively increasing the electrical resistivity of the coating.

- Sputtering deposition conditions optimised for FTO yield a deposition rate of $27 \text{ nm}\cdot\text{cm}^{-1}$ and deposition temperature at $170 \text{ }^\circ\text{C}$.
- The EDS analysis showed a compositional variation between the fluorine doped tin oxide (FTO) powder target and the FTO thin film because light elements can suffer from scattering issues due to collision with gas atoms, which significantly influences the deposition profile. It was determined that 5.3 at.% of fluorine incorporated into the tin oxide thin film lattice promoted an enhancement in the electrical properties from $3.71\times 10^{-1} \text{ }\Omega\cdot\text{cm}$ to $6.71\times 10^{-3} \text{ }\Omega\cdot\text{cm}$.
- Antimony doped tin oxide (ATO) was also investigated as a possible n-type semiconductor and showed relatively high resistivity of $3.75 \times 10^{-2} \text{ }\Omega\cdot\text{cm}$ and an average of 70 % transmission in the visible range of the spectrum.
- The optimisation of the deposition conditions of the Cu:Al metal base powder target yielded a single phase CAO p-type thin film with optical transparency of 7.8 % and electrical resistivity of $4.35 \text{ }\Omega\cdot\text{cm}$.
- The successful production of p-n junction solar generating diode with V_{oc} and I_{sc} determined from the I-V curve to be 0.40 V and $65.3 \text{ }\mu\text{A}/\text{cm}^2$ respectively, which give an ideal power (P_o) of $26.1 \text{ }\mu\text{W}/\text{cm}^2$. The maximum power (P_m) was calculated to be $11.3 \text{ }\mu\text{W}/\text{cm}^2$ using the I_{max} $45 \text{ }\mu\text{A}/\text{cm}^2$ and V_{max} 0.25 V that were also determined from the I-V curve. The fill factor and the power conversion efficiency were calculated to be 0.43 and 0.045 %

respectively. The device showed that the current at a given voltage for the device under illumination is higher than that in the dark. This indicates that the absorption of the light by the active layer generates carrier-contributing photocurrent.

RECOMMENDATIONS FOR FUTURE WORK

Further to the work described in this thesis, a number of questions remain and more studies are needed in order to further develop the investigated work.

- To install a better cooling system for the powder target to enable the use of a higher deposition power to increase the deposition rate.
- To develop a better system to blend the loosely powder target to ensure the homogenous distribution of the mixed powders target.
- To install an extra magnetron to the system in order to enable the deposition of the n-type and the p-type thin films using the same deposition run without the exposure of the coating to air. This will further enhance the p-n junction region by extracting any impurities that may have been added due to the exposure of the device to air during the change of the powder target.

- The performance of the p-n junction solar cell can be improved by optimising the p-type film thickness.
- To investigate further possible p-type materials, and improving the deposition growth conditions of the device.
- To deposit the p-n junction onto a ceramic tile and study the effect of the substrate onto the performance of the device.

Appendix-A

PUBLICATIONS AND CONFERENCE CONTRIBUTIONS

A.1 Publications

- Banyamin, Z.Y.; Kelly, P.J.; West, G.; Boardman, J. Electrical and Optical Properties of Fluorine Doped Tin Oxide Thin Films Prepared by Magnetron Sputtering. *Coatings*, **2014**,*4*, 732-746.

A.2 Conference contribution

- Banyamin, Z.Y.; Kelly, P.J.; West, G. Functional P-type and N-type semiconductor thin films for the use in p-n junction diodes grown by closed field magnetron sputtering, Coventry 2013, *Functional Thin Films*, (oral)
- Banyamin, Z.Y.; Kelly, P.J.; West, G. Optoelectrical characterisation of fluorine doped tin oxide thin film grown by pulsed DC magnetron

sputtering technique, Coventry 2012, Nanostructured Metal Oxide Thin Films (poster)

- Banyamin, Z.Y.; Kelly, P.J.; West, G. Effect of fluorine doping onto the optoelectrical properties of tin oxide thin films prepared by magnetron sputtering technique, Strasburg, EMRS-2013, advanced inorganic materials and structures for photovoltaic, TCO materials and structures. (poster)

Reference

1. Becquerel, A.E., *Mémoire sur les effets électriques produits sous l'influence des rayons solaires*. acad sci, 1839. **9**: p. 2.
2. Adams, W.G. and R.E. Day, *The Action of Light on Selenium*. Philosophical Transactions of the Royal Society of London, 1877. **167**: p. 313-349.
3. Green, M.A. *Photovoltaics: coming of age*. in *Photovoltaic Specialists Conference, 1990., Conference Record of the Twenty First IEEE*. 1990.
4. Fritts, C.E., *New form of selenium cell, with some remarkable electrical discoveries made by its use*. Science, 1883. **2**(30): p. 283.
5. Grondahl, L.O., *The Copper-Cuprous-Oxide Rectifier and Photoelectric Cell*. Reviews of Modern Physics, 1933. **5**(2): p. 141-168.
6. ohl, R., *light sensitive elcetric device*, in *US patent: 2402662*. 1946: USA.
7. Riordan, M. and L. Hoddeson, *The origins of the pn junction*. Spectrum, IEEE, 1997. **34**(6): p. 46-51.
8. Martin A, G., *Photovoltaic principles*. Physica E: Low-dimensional Systems and Nanostructures, 2002. **14**(1-2): p. 11-17.
9. Razykov, T.M., et al., *Solar photovoltaic electricity: Current status and future prospects*. Solar Energy, 2011. **85**(8): p. 1580-1608.
10. Bädeker, K., *Über Die Elektrische Leitfähigkeit und Die Thermoelektrische Kraft Einiger Schwermetallverbindun- gen*. Annalen Der Physik, March 1907. **22**(4): p. 749-766.
11. *Comprehensive Characterization of DC Sputtered AZO Films for CIGS Photovoltaics*. Journal of The Electrochemical Society, 2011. **158**(5): p. H510.
12. Zhou, Y. and P.J. Kelly, *The properties of tin-doped indium oxide films prepared by pulsed magnetron sputtering from powder targets*. Thin Solid Films, 2004. **469–470**(0): p. 18-23.
13. Moholkar, A.V., et al., *Effect of fluorine doping on highly transparent conductive spray deposited nanocrystalline tin oxide thin films*. Applied Surface Science, 2009. **255**(23): p. 9358-9364.
14. Szyszka, B., et al., *Recent developments in the field of transparent conductive oxide films for spectral selective coatings, electronics and photovoltaics*. Current Applied Physics, 2012. **12**, **Supplement 4**(0): p. S2-S11.
15. Piprek, J., *Chapter 1 - Introduction to Semiconductors*, in *Semiconductor Optoelectronic Devices*, J. Piprek, Editor. 2003, Academic Press: Boston. p. 3-11.
16. Bellingham, J.R., W.A. Phillips, and C.J. Adkins, *Electrical and optical properties of amorphous indium oxide*. Journal of Physics: Condensed Matter, 1990. **2**(28): p. 6207.
17. He, B., et al., *The effect of substrate temperature on high quality c-axis oriented AZO thin films prepared by DC reactive magnetron sputtering for photoelectric device applications*. Superlattices and Microstructures, 2013. **64**(0): p. 319-330.
18. Zhang, Y., et al., *Structural and opto-electrical properties of Cu–Al–O thin films prepared by magnetron sputtering method*. Vacuum, 2014. **99**(0): p. 160-165.
19. Heavens, O.S., *Optical Properties of Thin Solid Films*. 1955 London: Butterworths Scientific Publications.
20. Ohring, M., *The materials science of thin films*. 1991: academic press limited.

21. Rancourt, J.D. and E. Society of Photo-optical Instrumentation, *Optical thin films [electronic resource] : user handbook*. 1996, Bellingham, Wash. (1000 20th St. Bellingham WA 98225-6705 USA): SPIE. 1 online resource (xii, 289 p. : ill.) : digital file.
22. Pugalenti, A.S., et al., *Effect of thickness on the structural, optical and electrical properties of RF magnetron sputtered GZO thin films*. Materials Science in Semiconductor Processing, (0).
23. Granqvist, C.G., *Transparent conductors as solar energy materials: A panoramic review*. Solar Energy Materials and Solar Cells, 2007. **91**(17): p. 1529-1598.
24. Castañeda, L., *Present Status of the Development and Application of Transparent Conductors Oxide Thin Solid Films*. Materials Sciences and Applications, 2011. **2**(9): p. 1233-1242.
25. Tauc, J., R. Grigorovici, and A. Vancu, *Optical Properties and Electronic Structure of Amorphous Germanium*. physica status solidi (b), 1966. **15**(2): p. 627-637.
26. *Electronic Structures and Optical Properties of ZnO, SnO₂ and In₂O₃*. Japanese Journal of Applied Physics, 1999. **38**(6A): p. 3453.
27. *Optoelectronic studies of sol-gel derived nanostructured CdO-ZnO composite films*. Journal of Alloys and Compounds, 2011.
28. Kawazoe, H., et al., *Transparent p-Type Conducting Oxides: Design and Fabrication of p-n Heterojunctions*. MRS Bulletin, 2000. **25**(08): p. 28-36.
29. Vanaja, K.A., et al., *Pulsed laser deposition of p-type α -AgGaO₂ thin films*. Thin Solid Films, 2008. **516**(7): p. 1426-1430.
30. Hosono, H., M. Yasukawa, and H. Kawazoe, *Novel oxide amorphous semiconductors: transparent conducting amorphous oxides*. Journal of Non-Crystalline Solids, 1996. **203**(0): p. 334-344.
31. Calnan, S. and A.N. Tiwari, *High mobility transparent conducting oxides for thin film solar cells*. Thin Solid Films, 2010. **518**(7): p. 1839-1849.
32. Kılıç, Ç. and A. Zunger, *Origins of Coexistence of Conductivity and Transparency in SnO₂*. Physical Review Letters, 2002. **88**(9): p. 095501.
33. Kim, H., et al., *Electrical, optical, and structural properties of indium-tin-oxide thin films for organic light-emitting devices*. Journal of Applied Physics, 1999. **86**(11): p. 6451-6461.
34. Ellmer, K., *Resistivity of polycrystalline zinc oxide films: current status and physical limit*. Journal of Physics D: Applied Physics, 2001. **34**(21): p. 3097.
35. Piprek, J., *Chapter 4 - Optical Waves*, in *Semiconductor Optoelectronic Devices*, J. Piprek, Editor. 2003, Academic Press: Boston. p. 83-120.
36. Cachet, H., *Chapter 22 - Films and powders of fluorine-doped tin dioxide*, in *Fluorinated Materials for Energy Conversion*, N. Tsuyoshi and G. Henri, Editors. 2005, Elsevier Science: Amsterdam. p. 513-534.
37. Subba Ramaiah, K. and V. Sundara Raja, *Structural and electrical properties of fluorine doped tin oxide films prepared by spray-pyrolysis technique*. Applied Surface Science, 2006. **253**(3): p. 1451-1458.
38. Tesfamichael, T., et al., *Optical and electrical properties of nitrogen ion implanted fluorine doped tin oxide films*. Nuclear Instruments and Methods in Physics Research Section B: Beam Interactions with Materials and Atoms, 2003. **201**(4): p. 581-588.
39. Kim, et al., *Texture control of fluorine-doped tin oxide thin film*. Thin Solid Films, 2011. **519**(10): p. 3081-3085.

40. Gerhardinger, P.F. and R.J. McCurdy, *Float line deposited transparent conductors - implications for the PV industry*. 1996. p. 399-410.
41. Sankara Subramanian, N., et al., *Studies on Spray Deposited SnO₂, Pd:SnO₂ and F:SnO₂ Thin Films for Gas Sensor Applications*. Synthesis and Reactivity in Inorganic, Metal-Organic, and Nano-Metal Chemistry, 2006. **36**(1): p. 131-135.
42. Yadav, A.A., et al., *Electrical, structural and optical properties of SnO₂:F thin films: Effect of the substrate temperature*. Journal of Alloys and Compounds, 2009. **488**(1): p. 350-355.
43. Sheel, D.W. and J.M. Gaskell, *Deposition of fluorine doped indium oxide by atmospheric pressure chemical vapour deposition*. Thin Solid Films, 2011. **520**(4): p. 1242-1245.
44. Kim, H., R.C.Y. Auyeung, and A. Piqué, *Transparent conducting F-doped SnO₂ thin films grown by pulsed laser deposition*. Thin Solid Films, 2008. **516**(15): p. 5052-5056.
45. Mientus, R. and K. Ellmer, *Structural, electrical and optical properties of SnO₂-x:F-layers deposited by DC-reactive magnetron-sputtering from a metallic target in Ar-O₂/CF₄ mixtures*. Surface and Coatings Technology, 1998. **98**(1-3): p. 1267-1271.
46. Elangovan, E. and K. Ramamurthi, *Studies on micro-structural and electrical properties of spray-deposited fluorine-doped tin oxide thin films from low-cost precursor*. Thin Solid Films, 2005. **476**(2): p. 231-236.
47. Gorley, P.M., et al., *SnO₂ films: formation, electrical and optical properties*. Materials Science and Engineering: B, 2005. **118**(1-3): p. 160-163.
48. Maruyama, T. and H. Akagi, *Fluorine-Doped Tin Dioxide Thin Films Prepared by Radio-Frequency Magnetron Sputtering*. Journal of The Electrochemical Society, 1996. **143**(1): p. 283-287.
49. Martel, A., et al., *Discharge diagnosis and controlled deposition of SnO_x:F films by DC-reactive sputtering from a metallic tin target*. Surface and Coatings Technology, 1999. **122**(2-3): p. 136-142.
50. Exarhos, G.J. and X.-D. Zhou, *Discovery-based design of transparent conducting oxide films*. Thin Solid Films, 2007. **515**(18): p. 7025-7052.
51. Alkoy, E.M. and P.J. Kelly, *The structure and properties of copper oxide and copper aluminium oxide coatings prepared by pulsed magnetron sputtering of powder targets*. Vacuum, 2005. **79**(3-4): p. 221-230.
52. Yang, W., et al., *Properties of Sb-doped SnO₂ transparent conductive thin films deposited by radio-frequency magnetron sputtering*. Thin Solid Films, 2013. **542**(0): p. 285-288.
53. Batzill, M. and U. Diebold, *The surface and materials science of tin oxide*. Progress in Surface Science, 2005. **79**(2-4): p. 47-154.
54. Shokr, E.K., et al., *Sb-doping effects on optical and electrical parameters of SnO₂ films*. Journal of Physics and Chemistry of Solids, 2000. **61**(1): p. 75-85.
55. Montero, J., C. Guillén, and J. Herrero, *Discharge power dependence of structural, optical and electrical properties of DC sputtered antimony doped tin oxide (ATO) films*. Solar Energy Materials and Solar Cells, 2011. **95**(8): p. 2113-2119.
56. Tadatsugu, M., M. Toshihiro, and N. Jun-ichi, *Impurity-doped ZnO Thin Films Prepared by Physical Deposition Methods Appropriate for Transparent Electrode Applications in Thin-film Solar Cells*. Semicond. Sci. Technol., 2005. **20**(4): p. s35.

57. Betz, U., et al., *Thin films engineering of indium tin oxide: Large area flat panel displays application*. Surface and Coatings Technology, 2006. **200**(20–21): p. 5751-5759.
58. Agashe, C., et al., *Physical properties of highly oriented spray-deposited fluorine-doped tin dioxide films as transparent conductor*. Solar Energy Materials and Solar Cells, 2009. **93**(8): p. 1256-1262.
59. Banerjee, A.N. and K.K. Chattopadhyay, *Recent developments in the emerging field of crystalline p-type transparent conducting oxide thin films*. Progress in Crystal Growth and Characterization of Materials, 2005. **50**(1–3): p. 52-105.
60. Zhang, Y., et al., *Effect of oxygen partial pressure on the structure and properties of Cu–Al–O thin films*. Applied Surface Science, 2012. **258**(14): p. 5354-5359.
61. Neumann-Spallart, M. and R. Pinto, *Growth conditions of CuAlO₂ films — Thermodynamic considerations*. Thin Solid Films, 2011. **520**(4): p. 1299-1302.
62. Kawazoe, H., et al., *P-type electrical conduction in transparent thin films of CuAlO₂*. Nature, 1997. **389**(6654): p. 939-942.
63. Stauber, R.E., et al., *Thin film growth of transparent p-type CuAlO₂*. Electrochemical and Solid-State Letters, 1999. **2**(12): p. 654-656.
64. Wang, Y., et al., *Optical and electrical properties of p-type transparent conducting Cu–Al–O thin films prepared by plasma enhanced chemical vapor deposition*. Materials Science and Engineering: B, 2001. **85**(2–3): p. 131-134.
65. Banerjee, A.N. and K.K. Chatopadhyay, *Reactive Sputtering*, D.Depla and S.Mahieu, Editors. 2008, Springer Press: Berlin. p. 413.
66. Hsieh, P.-H., Y.-M. Lu, and W.-S. Hwang, *Effects of RF power on the growth behaviors of CuAlO₂ thin films*. Ceramics International, 2014. **40**(7, Part A): p. 9361-9366.
67. Sun, Z., et al., *Effect of Al components on the properties of CuAlO₂ thin films deposited by RF magnetron sputtering*. Journal of Alloys and Compounds, 2013. **581**(0): p. 488-493.
68. Reddy, A.S., et al., *Effect of substrate temperature on the physical properties of dc magnetron sputtered CuAlO₂ films*. Journal of Alloys and Compounds, 2009. **474**(1–2): p. 401-405.
69. Elmer, K., *Magnetron Sputtering of Transparent Conductive Zinc Oxide. Relation between the Sputtering Parameters and the Electronic Properties*,. Journal of Physics D: Applied Physics, January 2000. **33**: p. 45-47.
70. Hiramatsu, M., et al., *Transparent conducting ZnO thin films prepared by XeCl excimer laser ablation*. Journal of Vacuum Science & Technology A, 1998. **16**(2): p. 669-673.
71. J. W. Bae, S.W.L.a.G.Y.Y., *“Doped-Fluorine on Electrical and Optical Properties of Tin Oxide Films Grown by Ozone-Assisted Thermal CVD,”*. Journal of The Electrochemical Society, March 2007. **154**: p. D34-S37.
72. Acosta, D.R., et al., *About the structural, optical and electrical properties of SnO₂ films produced by spray pyrolysis from solutions with low and high contents of fluorine*. Thin Solid Films, 1996. **288**(1–2): p. 1-7.
73. Soliman, M., et al., *Effect of fluorine doping and spraying technique on the properties of tin oxide films*. Renewable Energy, 2001. **23**(3–4): p. 463-470.
74. Thangaraju, B., *Structural and electrical studies on highly conducting spray deposited fluorine and antimony doped SnO₂ thin films from SnCl₂ precursor*. Thin Solid Films, 2002. **402**(1–2): p. 71-78.

75. H. Agura, H.S., T. Matsushita, T. Aoki and M. Okuda, "Low Resistivity Transparent Conducting Al- Doped ZnO Films Prepared by Pulsed laser Deposition," *Thin Solid Films*, July 2006. **445**(2): p. 263-267.
76. S. M. Park, T.I.a.K.E., *Effects of Substrate Temperature on the Properties of Ga-Doped ZnO by Pulsed Laser Deposition,* *Thin Solid Films*, August 2006. **513**: p. 90-94.
77. Woodward, H.M.a.P.M., "Electronic Structure Studies of Main Group Oxides Possessing Edge- Sharing Octahedra: Implications for the Design of Transparent Conducting Oxides," *Chemistry of Materials*, November 2004. **16**(25): p. 5233-5248.
78. P. Ebert, Z.Z., F. Kluge, M. Simon, Z. Zhang and K. Urban, "Importance of Many-Body Effects in the Clustering of Charged Zn Dopant Atoms in GaAs," *Physical Review Letters*, July 1999. **38**(4): p. 757-760.
79. T. Pisarkiewicz, K.Z.a.E.L., "Scattering of Charge Carriers in Transparent and Conducting Thin Oxide Films with a Non-Parabolic Conduction Band," *Thin Solid Films*, July 1989. **174**: p. 217-223.
80. Makino, H., et al., *P-7: Ga-Doped ZnO Transparent Conductive Film as Substitution for ITO Common Electrode in TFT-LCDs*. SID Symposium Digest of Technical Papers, 2009. **40**(1): p. 1103-1106.
81. Yang, W. and J. Joo, *Effects of pulsed sputtering frequency on the uniformity of Al:ZnO's transparent conductive oxide properties for solar cell applications*. *Journal of Vacuum Science & Technology A: Vacuum, Surfaces, and Films*, 2009. **27**(6): p. 1310-1315.
82. Angusmaclod, H., *1 - Recent developments in deposition techniques for optical thin films and coatings*, in *Optical Thin Films and Coatings*, A. Piegari and F. Flory, Editors. 2013, Woodhead Publishing. p. 3-25.
83. Bilgin, V., et al., *Electrical, structural and surface properties of fluorine doped tin oxide films*. *Applied Surface Science*, 2010. **256**(22): p. 6586-6591.
84. *Stability in a high humidity environment of TCO thin films deposited at low temperatures*. *physica status solidi (a)*, 2007.
85. Kelly, P.J. and R.D. Arnell, *Magnetron sputtering: a review of recent developments and applications*. *Vacuum*, 2000. **56**(3): p. 159-172.
86. Ocal, T., et al., *High quality ITO thin films grown by dc and RF sputtering without oxygen*. *Journal of Physics D: Applied Physics*, 2010. **43**(5): p. 055402.
87. *RF Sputtered ITO Thin Film with Improved Optical Property*. *MRS Proceedings*, 2012. **1447**.
88. Zhou, Y., et al., *The characteristics of aluminium-doped zinc oxide films prepared by pulsed magnetron sputtering from powder targets*. *Thin Solid Films*, 2004. **447-448**(0): p. 33-39.
89. Sanghun, L., et al., *Combined effect of the target composition and deposition temperature on the properties of ZnO:Ga transparent conductive oxide films in pulsed dc magnetron sputtering*. *Semiconductor Science and Technology*, 2011. **26**(11): p. 115007.
90. Bosio, A., N. Romeo, and V. Canevari, *Chapter 23 - Doped transparent conducting oxides suitable for the fabrication of high efficiency thin film solar cells*, in *Fluorinated Materials for Energy Conversion*, T. Nakajima and H. Groult, Editors. 2005, Elsevier Science: Amsterdam. p. 535-548.

91. Liao, B.-H., et al., *FTO films deposited in transition and oxide modes by magnetron sputtering using tin metal target*. Applied Optics, 2014. **53**(4): p. A148-A153.
92. Owings, R.R., et al., *Process enhanced polaron conductivity of infrared transparent nickel–cobalt oxide*. Thin Solid Films, 2005. **483**(1–2): p. 175-184.
93. Sato, H., et al., *Transparent conducting p-type NiO thin films prepared by magnetron sputtering*. Thin Solid Films, 1993. **236**(1–2): p. 27-31.
94. Cao, L., et al., *Highly transparent and conducting fluorine-doped ZnO thin films prepared by pulsed laser deposition*. Solar Energy Materials and Solar Cells, 2011. **95**(3): p. 894-898.
95. Izumi, H., et al., *Electrical properties of crystalline ITO films prepared at room temperature by pulsed laser deposition on plastic substrates*. Thin Solid Films, 2002. **411**(1): p. 32-35.
96. Sima, C. and C. Grigoriu, *Study on TiO₂ thin films grown by advanced pulsed laser deposition on ITO*. Thin Solid Films, 2009. **518**(4): p. 1314-1317.
97. Huang, Y., et al., *Transparent conductive p-type lithium-doped nickel oxide thin films deposited by pulsed plasma deposition*. Applied Surface Science, 2012. **258**(19): p. 7435-7439.
98. Chih-Tang, S., R.N. Noyce, and W. Shockley, *Carrier Generation and Recombination in P-N Junctions and P-N Junction Characteristics*. Proceedings of the IRE, 1957. **45**(9): p. 1228-1243.
99. Moll, J.L., *The Evolution of the Theory for the Voltage-Current Characteristic of P-N Junctions*. Proceedings of the IRE, 1958. **46**(6): p. 1076-1082.
100. Razeghi, M., *Semiconductor p-n and Metal-Semiconductor Junctions*, in *Fundamentals of Solid State Engineering*. 2009, Springer US. p. 1-56.
101. Sze, S.M., K.K. Ng, and MyLibrary, *Physics of semiconductor devices*. 3rd ed. ed. 2007, Hoboken, N.J.: Wiley-Interscience. x, 815 p. : ill. ; 25 cm.
102. Cooke, M., *Semiconductor Devices*. 1990: prentice Hall international
103. Quintino, L., *1 - Overview of coating technologies*, in *Surface Modification by Solid State Processing*, R. Miranda, Editor. 2014, Woodhead Publishing. p. 1-24.
104. Geng, H., *Semiconductor manufacturing handbook : [wafer processing technologies ; nanotechnology and MEMs ; fab yield, operations, and facilities]*. 2005, New York, NY [u.a.]: McGraw-Hill.
105. Deshpandey, C.V. and R.F. Bunshah, *II-2 - Evaporation Processes*, in *Thin Film Processes*, J.L.V. Kern, Editor. 1991, Academic Press: San Diego. p. 79-132.
106. Mattox, D.M. and Knovel, *Handbook of physical vapor deposition (PVD) processing: film formation, adhesion, surface preparation and contamination control*. 1998, Westwood, N.J: Noyes Publications.
107. Mattox, D.M., *Chapter 6 - Vacuum Evaporation and Vacuum Deposition*, in *Handbook of Physical Vapor Deposition (PVD) Processing (Second Edition)*, D.M. Mattox, Editor. 2010, William Andrew Publishing: Boston. p. 195-235.
108. Steckelmacher, W., *Handbook of plasma processing technology: Fundamentals, etching, deposition and surface interactions: Edited by S M Rossnagel, J J Cuomo and W D Westwood*, Noyes Publications, NJ, USA, 1990. Vacuum, 1991. **42**(12): p. 779.
109. Langmuir, I., *Oscillations in Ionized Gases*. Proceedings of the National Academy of Sciences of the United States of America, 1928. **14**(8): p. 627-637.

110. Ohring, M., *Chapter 4 - Discharges, plasmas, and ion-surface interactions*, in *Materials Science of Thin Films (Second Edition)*. 2002, Academic Press: San Diego. p. 145-202.
111. Scott G. Walton, J.E.G., *Chapter 2 - Plasmas in Deposition Processes*, in *Handbook of Deposition Technologies for Films and Coatings (Third Edition)* R.F. Bunshah, Editor. 2010, NOYES PUBLICATIONS: Boston. p. 32-92.
112. Donald M, M., *Ion plating — past, present and future*. Surface and Coatings Technology, 2000. **133–134**(0): p. 517-521.
113. Musil, J., J. Vlcek, and P. Baroch, *Chapter 3 - Magnetron Discharges for Thin Films Plasma Processing*, in *Materials Surface Processing by Directed Energy Techniques*, Y. Pauleau, Editor. 2006, Elsevier: Oxford. p. 67-110.
114. Zhou, Y., *The Production and Properties of TCO Coatings Prepared by Pulsed Magnetron Sputtering from Powder Targets*, in *Institute of Materials Research*. 2004, University of Salford: Manchester. p. 201.
115. Rosnagel, S.M. and J.J. Cuomo, *Ion beam bombardment effects during films deposition*. Vacuum, 1988. **38**(2): p. 73-81.
116. Window, B. and N. Savvides, *Charged particle fluxes from planar magnetron sputtering sources*. Journal of Vacuum Science & Technology A: Vacuum, Surfaces, and Films, 1986. **4**(2): p. 196-202.
117. Kelly, P.J. and R.D. Arnell, *The influence of substrate temperature on the properties of Al, Zr and W coatings deposited by closed-field unbalanced magnetron sputtering*. Vacuum, 1998. **49**(1): p. 43-47.
118. Kelly, P.J. and R.D. Arnell, *The influence of deposition parameters on the structure of Al, Zr and W coatings deposited by closed-field unbalanced magnetron sputtering*. Surface and Coatings Technology, 1996. **86–87, Part 1**(0): p. 425-431.
119. Teer DG, U.p.N., USA patent No. 5 554 519, European patent No. 0 521 045.
120. Depla, D., S. Mahieu, and J.E. Greene, *Chapter 5 - Sputter Deposition Processes*, in *Handbook of Deposition Technologies for Films and Coatings (Third Edition)*, P.M. Martin, Editor. 2010, William Andrew Publishing: Boston. p. 253-296.
121. Lieberman, M.A., Lichtenberg, Allan J. , *Principles of Plasma Discharges and Materials Processing*, ed. S. Edition. 2005.
122. Mott-Smith, H.M. and I. Langmuir, *The Theory of Collectors in Gaseous Discharges*. Physical Review, 1926. **28**(4): p. 727-763.
123. Clements, R.M., *Plasma diagnostics with electric probes*. Journal of Vacuum Science & Technology, 1978. **15**(2): p. 193-198.
124. Vook, R.W. and C.H. Chung, *Ag films formed simultaneously on (111) and (100) NaCl*. Thin Solid Films, 1976. **37**(3): p. 461-473.
125. Wasa, K., M. Kitabatake, and H. Adachi, *1 - Thin Film Materials and Devices*, in *Thin Film Materials Technology*. 2004, William Andrew Publishing: Norwich, NY. p. 1-16.
126. Grünbaum, E., *Epitaxial growth of metal single-crystal films*. Vacuum, 1974. **24**(4): p. 153-164.
127. Mattox, D.M., *9 - Atomistic Film Growth and Some Growth-Related Film Properties*, in *Handbook of Physical Vapor Deposition (PVD) Processing*. 1998, William Andrew Publishing: Westwood, NJ. p. 472-568.
128. Thornton, J.A., *High Rate Thick Film Growth*. Annual Review of Materials Science, 1977. **7**: p. 239.

129. Bunshah, R.F. and R.S. Juntz, *The Influence of Ion Bombardment on the Microstructure of Thick Deposits Produced by High Rate Physical Vapor Deposition Processes*. Journal of Vacuum Science and Technology, 1972. **9**(6): p. 1404-1405.
130. Enomoto, Y. and K. Matsubara, *Structure and mechanical properties of ion-plated thick films*. Journal of Vacuum Science and Technology, 1975. **12**(4): p. 827-829.
131. Ross, R.C. and R. Messier, *Microstructure and properties of rf-sputtered amorphous hydrogenated silicon films*. Journal of Applied Physics, 1981. **52**(8): p. 5329-5339.
132. Fountzoulas, C. and W.B. Nowak, *Influence of ion energy and substrate temperature on the structure of copper, germanium, and zinc films produced by ion plating*. Journal of Vacuum Science & Technology A: Vacuum, Surfaces, and Films, 1991. **9**(4): p. 2128-2137.
133. Kelly, P.J. and R.D. Arnell, *Development of a novel structure zone model relating to the closed-field unbalanced magnetron sputtering system*. Journal of Vacuum Science & Technology A: Vacuum, Surfaces, and Films, 1998. **16**(5): p. 2858-2869.
134. Kelly, P.J., Y. Zhou, and A. Postill, *A novel technique for the deposition of aluminium-doped zinc oxide films*. Thin Solid Films, 2003. **426**(1–2): p. 111-116.
135. Kelly, P.J. and Y. Zhou, *Zinc oxide-based transparent conductive oxide films prepared by pulsed magnetron sputtering from powder targets: Process features and film properties*. Journal of Vacuum Science & Technology A: Vacuum, Surfaces, and Films, 2006. **24**(5): p. 1782-1789.
136. Audronis, M., et al., *The structure and properties of chromium diboride coatings deposited by pulsed magnetron sputtering of powder targets*. Surface and Coatings Technology, 2005. **200**(5–6): p. 1366-1371.
137. Audronis, M., et al., *The effect of pulsed magnetron sputtering on the structure and mechanical properties of CrB₂ coatings*. Surface and Coatings Technology, 2006. **201**(7): p. 3970-3976.
138. Piekoszewski, J., et al., *RF-sputtered CuInSe₂ thin films*. Solar Energy Materials, 1980. **2**(3): p. 363-372.
139. Greene, J.E., *Epitaxial crystal growth by sputter deposition: Applications to semiconductors. Part I*. Critical Reviews in Solid State and Materials Sciences, 1983. **11**(1): p. 47-97.
140. Face, D.W., et al., *Preparation of superconducting thin films of bismuth strontium calcium copper oxides by reactive sputtering*. Applied Physics Letters, 1988. **53**(3): p. 246-248.
141. P. J. Kelly and Y. Zhou, *Zinc oxide-based transparent conductive oxide films prepared by pulsed magnetron sputtering from powder targets: Process features and film properties*. Vac Sci Technol A 2006. **24**((5)): p. 1782-1785.
142. Belkind, A., A. Freilich, and R. Scholl, *Pulse duration effects in pulse-power reactive sputtering of Al₂O₃*. Surface and Coatings Technology, 1998. **108–109**(0): p. 558-563.
143. Belkind, A., et al., *Mid-frequency reactive sputtering of dielectrics: Al₂O₃*. Surface and Coatings Technology, 2003. **174–175**(0): p. 88-93.
144. Este, G. and W.D. Westwood, *A quasi-direct-current sputtering technique for the deposition of dielectrics at enhanced rates*. Journal of Vacuum Science & Technology A, 1988. **6**(3): p. 1845-1848.

145. Kelly, P.J. and R.D. Arnell, *The influence of magnetron configuration on ion current density and deposition rate in a dual unbalanced magnetron sputtering system*. Surface and Coatings Technology, 1998. **108–109**(0): p. 317-322.
146. Čada, M., et al., *Measurement of energy transfer at an isolated substrate in a pulsed dc magnetron discharge*. Journal of Applied Physics, 2007. **102**(6): p. 063301.
147. Sundaram, K.B. and A. Khan, *Characterization and optimization of zinc oxide films by r.f. magnetron sputtering*. Thin Solid Films, 1997. **295**(1–2): p. 87-91.
148. Thomann, A.L., et al., *Energy transferred to the substrate surface during reactive magnetron sputtering of aluminum in Ar/O₂ atmosphere*. Thin Solid Films, 2013. **539**(0): p. 88-95.
149. Depla, D., S. Mahieu, and SpringerLink, *Reactive sputter deposition [electronic resource]*. 2008, Berlin: Springer. 1 online resource (xviii, 570 p.) : ill. (some col.).
150. Gurumurugan, K., et al., *Structural, optical, and electrical properties of cadmium oxide films deposited by spray pyrolysis*. physica status solidi (a), 1994. **143**(1): p. 85-91.
151. Mohamed, S.H., et al., *Correlation between structure, stress and optical properties in direct current sputtered molybdenum oxide films*. Thin Solid Films, 2003. **429**(1–2): p. 135-143.
152. Pauw, L.J.V.d., *A method of measuring specific resistivity and hall effect of discs of arbitrary shape*. February 1958, philips research reports: Eindhoven netherlands. p. 334.
153. Ingham, B. and M.F. Toney, *1 - X-ray diffraction for characterizing metallic films*, in *Metallic Films for Electronic, Optical and Magnetic Applications*, K. Barmak and K. Coffey, Editors. 2014, Woodhead Publishing. p. 3-38.
154. Patterson, A.L., *The Scherrer Formula for X-Ray Particle Size Determination*. Physical Review, 1939. **56**(10): p. 978-982.
155. Postill, A., *Development of a rig to sputter powders for novel applications*, in *Institute for materials research*. 2004, University of salford: Manchester.
156. Gao, Q., et al., *Improved mechanical properties of SnO₂:F thin film by structural modification*. Ceramics International, 2014. **40**(2): p. 2557-2564.
157. Jäger, T., et al., *Thin films of SnO₂:F by reactive magnetron sputtering with rapid thermal post-annealing*. Thin Solid Films, 2014. **553**(0): p. 21-25.
158. Yu, R.-S. and H.-H. Yin, *Structural and optoelectronic properties of p-type semiconductor CuAlO₂ thin films*. Thin Solid Films, 2012. **526**(0): p. 103-108.
159. *Ion Energy Distributions in Magnetron Sputtering of Zinc Aluminium Oxide*. Plasma Processes and Polymers, 2009: p. NA.
160. Elangovan, E., M.P. Singh, and K. Ramamurthi, *Studies on structural and electrical properties of spray deposited SnO₂:F thin films as a function of film thickness*. Materials Science and Engineering: B, 2004. **113**(2): p. 143-148.
161. *Joint Committee on Powder Diffraction Standards (JCPDS), International Centre for Diffraction Data*, in *Card No. 41-1445*. 1997.
162. Consonni, V., et al., *Preferential orientation of fluorine-doped SnO₂ thin films: The effects of growth temperature*. Acta Materialia, 2013. **61**(1): p. 22-31.
163. Fukano, T. and T. Motohiro, *Low-temperature growth of highly crystallized transparent conductive fluorine-doped tin oxide films by intermittent spray pyrolysis deposition*. Solar Energy Materials and Solar Cells, 2004. **82**(4): p. 567-575.

164. Barratt, C.S. and T.B. Massalski, *Structure of Metals*. 1980, Pergamon: Oxford.
165. Mamazza Jr, R., D.L. Morel, and C.S. Ferekides, *Transparent conducting oxide thin films of Cd₂SnO₄ prepared by RF magnetron co-sputtering of the constituent binary oxides*. *Thin Solid Films*, 2005. **484**(1–2): p. 26-33.
166. Bhuvanewari, P.V., et al., *Effect of fluorine doping on the structural, optical and electrical properties of spray deposited cadmium stannate thin films*. *Materials Science in Semiconductor Processing*, 2013. **16**(6): p. 1964-1970.
167. Guillén, C. and J. Herrero, *TCO/metal/TCO structures for energy and flexible electronics*. *Thin Solid Films*, 2011. **520 31** (1): p. 1-17.
168. Arefi-Khonsari, F., et al., *Deposition of transparent conductive tin oxide thin films doped with fluorine by PACVD*. *Thin Solid Films*, 2003. **427**(1–2): p. 208-214.
169. Shanthi, S., et al., *Effect of fluorine doping on structural, electrical and optical properties of sprayed SnO₂ thin films*. *Journal of Crystal Growth*, 1998. **194**(3–4): p. 369-373.
170. Elangovan, E. and K. Ramamurthi, *A study on low cost-high conducting fluorine and antimony-doped tin oxide thin films*. *Applied Surface Science*, 2005. **249**(1–4): p. 183-196.
171. Körber, C., P. Ágoston, and A. Klein, *Surface and bulk properties of sputter deposited undoped and Sb-doped SnO₂ thin films*. *Sensors and Actuators B: Chemical*, 2009. **139**(2): p. 665-672.
172. Kim, H. and A. Piqué, *Transparent conducting Sb-doped SnO₂ thin films grown by pulsed-laser deposition*. *Applied Physics Letters*, 2004. **84**(2): p. 218-220.
173. White, M.E., et al., *Electron transport properties of Sb:SnO₂ single crystalline thin films grown by plasma-assisted molecular beam epitaxy*. *Journal of Applied Physics*, 2009. **106**(9): p. 093704-093704-6.
174. Kwak, D.-J., M.-W. Park, and Y.-M. Sung, *Discharge power dependence of structural and electrical properties of Al-doped ZnO conducting film by magnetron sputtering (for PDP)*. *Vacuum*, 2008. **83**(1): p. 113-118.
175. Shanthi, E., et al., *Electrical and optical properties of undoped and antimony-doped tin oxide films*. *Journal of Applied Physics*, 1980. **51**(12): p. 6243-6251.
176. Stjerna, B., E. Olsson, and C.G. Granqvist, *Optical and electrical properties of radio frequency sputtered tin oxide films doped with oxygen vacancies, F, Sb, or Mo*. *Journal of Applied Physics*, 1994. **76**(6): p. 3797-3817.
177. Hsieh, P.-H., et al., *Effect of Al content on electrical conductivity and transparency of P-type Cu-Al-O thin film*. *Surface and Coatings Technology*, 2010. **205, Supplement 1**(0): p. S206-S209.
178. Lu, Y.M., et al., *Effect of RF power on optical and electrical properties of ZnO thin film by magnetron sputtering*. *Materials Chemistry and Physics*, 2001. **72**(2): p. 269-272.
179. *JCPDS- International Centre for Diffraction Data, Card No. 09-0185*.
180. Ghosh, S., et al., *Deposition of thin films of different oxides of copper by RF reactive sputtering and their characterization*. *Vacuum*, 2000. **57**(4): p. 377-385.
181. Banyamin, Z., et al., *Electrical and Optical Properties of Fluorine Doped Tin Oxide Thin Films Prepared by Magnetron Sputtering*. *Coatings*, 2014. **4**(4): p. 732-746.

182. Chan, K.-Y. and B.-S. Teo, *Investigation into the influence of direct current (DC) power in the magnetron sputtering process on the copper crystallite size*. Microelectronics Journal, 2007. **38**(1): p. 60-62.
183. Lan, W., et al., *The effect of oxygen on the properties of transparent conducting Cu–Al–O thin films deposited by rf magnetron sputtering*. Materials Science and Engineering: B, 2007. **139**(2–3): p. 155-159.
184. Trani, F., et al., *Band structures of delafossite transparent conductive oxides from a self-consistent GW-approach*. Physical Review B, 2010. **82**(8): p. 085115.
185. Fang, M., et al., *Optical properties of p-type CuAlO₂ thin film grown by rf magnetron sputtering*. Applied Surface Science, 2011. **257**(20): p. 8330-8333.
186. Alivisatos, A.P., *Semiconductor Clusters, Nanocrystals, and Quantum Dots*. Science, 1996. **271**(5251): p. 933-937
187. Li, Y., et al., *I–V characteristics of the p–n junction between vertically aligned ZnO nanorods and polyaniline thin film*. Synthetic Metals, 2010. **160**(5–6): p. 499-503.
188. Yakuphanoglu, F., *Electrical and photovoltaic properties of cobalt doped zinc oxide nanofiber/n-silicon diode*. Journal of Alloys and Compounds, 2010. **494**(1–2): p. 451-455.
189. Rogel-Salazar, J., *Advances in Thin-Film Solar Cells, by I.M. Dharmadasa*. Contemporary Physics, 2013. **54**(2): p. 117-117.
190. Li, D., et al., *Prototype of a scalable core–shell Cu₂O/TiO₂ solar cell*. Chemical Physics Letters, 2011. **501**(4–6): p. 446-450.
191. Ocak, Y.S., et al., *Analysis of electrical and photoelectrical properties of ZnO/p-InP heterojunction*. Journal of Alloys and Compounds, 2011. **509**(23): p. 6631-6634.
192. Solanski, C.S., *Solar photovoltaics : fundamentals, technologies and applications*. 2009, New Delhi: PHI Learning.